Consejo Superior de Investigaciones Científicas
Universitat de València
IFIC - INSTITUTO DE FISICA CORPUSCULAR

Image Reconstruction and Correction Methods for Madpet-II based on Monte Carlo Techniques

Irene Torres Espallardo

Departament de Física Atòmica, Molecular y Nuclear, IFIC
Universitat de València - CSIC

VNIVERSITAT DE VALÈNCIA Facultat de Física

Magdalena Rafecas López, Investigadora Ramón y Cajal del Departamento de Física Atómica, Molecular y Nuclear de la Universitat de València, y

Sibylle I. Ziegler, Investigadora jefe del grupo de Instrumentación de la *Nuklearmedizinische Klinik und Poliklinik, Klinikum rechts der Isar der Technische Universität München* en Múnich (Alemania)

Certifican:

Que la presente memoria, IMAGE RECONSTRUCTION AND CORRECTION METHODS FOR MADPET-II BASED ON MONTE CARLO TECHNIQUES, ha sido realizada bajo su dirección en la *Nuklearmedizinische Klinik und Poliklinik, Klinikum rechts der Isar der Technischen Universität München* y el Instituto de Física Corpuscular de València por *Irene Torres Espallardo*, y constituye su Tesis para optar al grado de Doctora en Ciencias Físicas.

Y para que así conste, en cumplimiento de la legislación vigente, presentan en la Universitat de València la referida Tesis Doctoral, y firman el presente certificado, en

Burjassot, 1 de Diciembre de 2009

Magdalena Rafecas López

Sibylle I. Ziegler

Contents

Prólogo

La memoria que se presenta a continuación recoge el trabajo de investigación llevado a cabo entre el *Klinikum rechts der Isar* y el Instituto de Física Corpuscular de Valencia para optar al grado de doctora en Ciencias Físicas. El trabajo se enmarca dentro del campo de Imagen Médica y más concretamente en el de tomógrafos PET dedicados a animales pequeños.

Bajo el título Reconstrucción de la Imagen y Correcciones para MADPET-II usando Técnicas de Montecarlo hemos englobado diversos temas relacionados con la obtención de imágenes y correcciones necesarias para obtener información cuantitativa del escáner MADPET-II. En particular se han investigado las correcciones de coincidencias accidentales y la normalización para dicho sistema. MADPET-II, que viene de *Munich Avalanche photoDiode PET*, es un escáner para el estudio de animales pequeños desarrollado en el departamento de Medicina Nuclear del Klinikum rechts der Isar en Múnich. Sus rasgos más característicos son la distribución de los cristales centelleadores en dos capas radiales y la lectura individual de cada uno de sus cristales por un fotodiodo de avalancha (APD). En el capítulo 2 se discute con más detalle y profundidad el diseño y las características de este escáner. MADPET-II permite obtener una alta sensibilidad, manteniendo una alta resolución espacial. La alta sensibilidad se consigue usando un campo de visión (FOV) tan grande como el diámetro interno del escáner, reduciendo el umbral energético e introduciendo sucesos triples[1], producidos cuando uno de los fotones ha depositado su energía en más de un cristal. Al mismo tiempo, se logra una alta resolución espacial porque se proporciona información de la profundidad de interacción del fotón en el cristal (DOI) y las imágenes son reconstruídas usando algoritmos iterativos tridimensionales basados en histogramas de líneas de respuesta, junto con una matriz del sistema generada a traves de técnicas Montecarlo. Dos capítulos de esta tesis se han reservado al estudio de dos de los elementos mencionados previamente, la creación de una matriz del sistema basada en Montecarlo (capítulo 3) y la introducción de los sucesos triples (capítulo 5).

En general, los escáneres PET para animales pequeños se dedican a estudios radiofarmaceúticos. En este tipo de estudios es muy importante que las imágenes

[1]Un fotón de 511 keV puede depositar toda su energía en un cristal o a través de sucesivas interacciones Compton ir dejando la energía en diferentes cristales. Gracias a la lectura individual de los cristales de MADPET-II y cuando la energía depositada en los distintos cristales cae dentro de la ventana energética, es posible detectar más de un suceso asociado con un solo fotón. Por tanto, se puede producir y detectar un suceso triple proveniente de los dos fotones de la aniquilación.

reconstruídas proporcionen información cuantitativa sobre la actividad emitida por el sujeto en estudio. Varias correcciones se deben de aplicar para obtener estimaciones realistas de la distribución de actividad. Entre estas correcciones, esta tesis se ha centrado en la corrección debida a las coincidencias aleatorias (capítulo 4) y la normalización (capítulo 6).

Todos los capítulos de esta tesis tienen un denominador común que es el uso de simulaciones basadas en técnicas Montecarlo. Nos hemos beneficiado de las ventajas que ofrecen las técnicas de Montecarlo, pero también hemos sufrido sus limitaciones. Empezando con las ventajas, hemos podido simular un escáner cuya geometría es bastante compleja debido a su configuración en doble capa. Otra ventaja de las técnicas de Montecarlo es que permite estudiar efectos de parámetros que no pueden ser medidos en la práctica. Particularizando para nuestro caso, gracias a esta capacidad pudimos validar los métodos para la estimación de las coincidencias aleatorias usando la información relacionada con la aniquilación que proporciona el programa de simulación. Ademas, como es un modelo computacional, es posible activar o desactivar ciertos efectos según nuestros intereses. Por ejemplo, en las simulaciones para el estudio de las coincidencias aleatorias no fueron incluidas la dispersión y la atenuación debidas al objeto, para podernos centrar en los efectos debidos al sistema y a los detectores. En cambio, para el estudio de normalización, necesitamos una simulación lo más cercana posible a la medida de normalización, por tanto, simulamos la fuente dentro de el continente de plástico, incluyendo la atenuación y la dispersión del objeto, junto con la atenuación de la actividad con el tiempo. Una limitación importante de las técnicas Montecarlo es el tiempo de computación necesario para hacer una simulación. Para resolver este problema hemos recurrido a las simetrías del escáner y a la granja de ordenadores que hay en la instalación de Grid en el IFIC.

Después de los capítulos de introducción y de la descripción del escáner MADPET-II, el esquema de este trabajo se presenta a continuación:

- Capítulo 3 presenta la generación de la matriz del sistema basada en las técnicas de Monte Carlo.
- Capítulo 4 investiga la estimación y corrección de coincidencias aleatorias.
- Capítulo 5 incluye los sucesos triples para obtener imágenes.
- Capítulo 6 estudia diferentes propuestas para la normalización.

Al final de cada capítulo se encuentran las correspondientes conclusiones. Éstas se encuentran resumidas en el último capítulo en castellano. Por tanto, salvo *la introducción a PET dedicados a animales pequeños* que viene a continuación y *las conclusiones finales*, el resto de la tesis está escrita en inglés. De esta forma se cumplen los requisitos exigidos por la normativa del Doctorado Europeo.

A mis queridos padres,
Pepe y Virtudes,
por sus continuos ánimos.

Breve Introducción sobre tomógrafos PET dedicados a animales pequeños

La tomografía por emisión de positrones, *Positron Emission Tomography* (PET), es una técnica de diagnóstico por imagen que usa sustancias radiactivas para obtener imágenes fisiológicas del cuerpo. Entre otros, las imágenes de PET pueden visualizar el metabolismo de la glucosa, el flujo sanguíneo o concentraciones de receptores. Con estas imágenes se puede detectar tumores, localizar áreas del corazón afectadas por enfermedad coronaria o identificar zonas del cerebro afectadas por drogas. Por esta razón, las imágenes que se obtienen a través de la PET se llaman funcionales, a diferencia de otras, como la tomografía computerizada, que produce imágenes anatómicas.

El primer paso en un estudio de PET es la producción del radiofármaco apropiado para visualizar la enfermedad en cuestión. El radiofármaco es una sustancia formada por radionúclidos emisores de positrones (los más usados son ^{15}O, ^{13}N, ^{11}C y ^{18}F) incorporados a moléculas biológicamente interesantes para el estudio a realizar. Posteriormente, el radiofármaco se introduce en el cuerpo, bien por inyección o inhalación. La calidad de las imágenes mejora con la cantidad de radiofármaco administrado, pero la radiación que reciben los órganos internos del paciente pone un límite a la dosis administrada. El radioisótopo con el que se ha marcado el radiofármaco emite positrones y éstos se aniquilan emitiendo dos fotones de 511 keV en la misma dirección y sentidos opuestos. Estas emisiones salen del cuerpo del paciente en todas las direcciones a una tasa proporcional a la concentración local de radioármaco, y son detectados por el sistema PET, que rodea al paciente. El sistema de adquisición guarda la información sobre la posición y dirección del par de fotones que se ha detectado. Estos datos se organizan en histogramas, donde cada bin corresponde a una pareja de detectores. El histograma resultante contiene medidas de las proyecciones. Las imágenes tomográficas no se pueden ver directamente, sino que se calculan a partir de las proyecciones en un proceso llamado reconstrucción de la imagen. El método convencional de reconstrucción de la imagen es una técnica llamada retroproyección filtrada de Fourier, *Fourier filtered backprojection* (FBP). La FBP es una técnica de reconstrucción analítica, es decir, la solución a la reconstrucción se puede escribir explícitamente. Esto es posible gracias a que estos métodos no consideran el ruido estadístico, ni

otros factores físicos que complican la descripción del proceso de imagen. Frente a las ténicas analíticas, en los últimos años, han emergido las denominadas técnicas iterativas, como los algoritmos Maximum-Likelihood Expectation-Maximization (MLEM) y Ordered-Subsets Expectation-Maximization (OS-EM). Los métodos iterativos, que se usan para implementar estimaciones estadísticas, permiten incluir en el proceso de reconstrucción factores que describen la emisión y detección del par de fotones, produciendo imgenes de PET de mayor calidad.

La PET, como otras técnicas de diagnóstico a través de la imagen, se está usando en laboratorios con animales pequeños. Una de las ventajas que ofrece la PET es que permite utilizar el mismo animal varias veces, pues no es necesario sacrificar el animal, como por ejemplo en la autorradiografía. Esta ventaja es importante ya que se evitan variaciones debidas a diferencias entre distintos animales de la misma especie, también permite el seguimiento de una terapia y el estudio de la evolución de una enfermedad. El resultado final es que se reduce el número de animales usados en el laboratorio, se acelera la obtención de resultados y se mejora la calidad de los resultados.

Un gran número de compuestos marcados con emisores de positrones se han sintetizado [8] abriendo la posibilidad a que se puedan medir cuantitativamente un amplio rango de procesos biológicos no invasívamente y repetidamente con PET. Combinado junto con la alta especificidad de los radiotrazadores, permite poder estudiar encimas específicos, proteínas, receptores y genes, haciendo la técnica PET tremendamente atractiva para estudios en laboratorios con animales. Por último, otra gran ventaja de usar la PET con animales pequeños (para hacer modelos de enfermedades) es que las imágenes producidas proporcionan un puente entre el modelo del animal y estudios con humanos. El ratón se ha convertido en el animal elegido para crear modelos de enfermedades humanas y para intentar entender la biología de los mamíferos. Esto se debe, fundamentalmente, a que los ratones tienen una alta tasa de reproducción y que genética y fisiológicamente son similares a los humanos. Para estudios cerebrales, tradicionalmente se ha utilizado la rata por el tamaño de su cerebro (3.3 g el de la rata y 0.45 g el del ratón).

Hay un gran número de cuestiones que se deben de considerar cuidadosamente en el caso de los estudios PET con animales pequeños. Algunas de ellas son comunes al diseño y optimización de escáneres PET para humanos; otras, son específicas de este tipo de escáneres. El objetivo fundamental es obtener el mayor número de cuentas posible y localizarlas con tanta precisión como sea posible. El determinar con exactitud la posición donde se ha generado el par de fotones depende, fundamentalmente, de la resolución espacial de los detectores y de la habilidad para quitar o corregir sucesos dispersados, coincidencias aleatorias y otros fenómenos físicos de degradación de la imagen. Aumentar el número de cuentas detectadas requiere aumentar la dosis suministrada, hasta llegar a un máximo que vendrá determinado por la masa del animal y la actividad específica del radiofármaco. También se pueden aumentar los sucesos detectados aumentando la eficiencia de los detectores y cubriendo el máximo ángulo sólido.

En cuanto a la resolución espacial, la diferencia fundamental entre un escáner

PET para humanos y uno dedicado a animales pequeños viene de los diferentes tamaños físicos entre humanos (70 kg) y ratas o ratones (30-300 g). Por tanto, para alcanzar la misma calidad de imagen, la resolución espacial se ha de mejorar en comparación con la que tiene un escáner PET de humanos. Si se tiene una resolución espacial de 10 mm en estudios de cuerpo entero con escáneres clínicos, se ha de obtener una resolución en la imagen menor de 1 mm en todas las direcciones para los estudios con animales.

La sensibilidad absoluta de detección del sistema de imagen, es decir, la fracción de desintegraciones radiactivas que producen un suceso detectado, debe ser al menos tan buena como la de un escáner PET típico. El número de cuentas detectadas por elemento de imagen determina directamente el nivel de señal respecto del ruido de las imágenes reconstruídas. Si el criterio de sensibilidad no se satisface, el ruido estadístico en las imágenes reconstruídas hace que se necesite un suavizado espacial que degradará la resolución espacial. Escáneres PET para humanos detectan del orden de 0.3-0.6% de los fotones de aniquilación en modo bidimensional (2D) y 2-4% en modo de adquisición tridimensional (3D), [10], [11]. Basándonos en el mismo argumento de escala que en el caso de la resolución espacial, y para preservar el número de cuentas por elemento de imagen, la sensibilidad de un sistema de imagen dedicado a ratones tendría que mejorar en un factor 1000 respecto al del humano, lo que técnicamente no es posible. Aunque esta reducción en sensibilidad se puede arreglar inyectando mayores cantidades de radioactividad, existen ciertas limitaciones que discutiremos en el siguiente párrafo. Una solución para compensar el problema de la sensibilidad es el uso de algoritmos de reconstrucción más sofisticados, que hagan mejor uso de las cuentas disponibles. Los algoritmos iterativos, que modelan con mayor precisión la física del escáner y la estadística de los datos antes de ser procesados, juegan un papel importante en los estudios PET de alta resolución. Esto es debido a que estos algoritmos producen mejoras tanto en la resolución espacial como en la relación señal-ruido respecto a los algoritmos analíticos.

Para concluir con los desafíos de las cámaras PET para animales pequeños, dedicamos unas palabras a la cantidad de dosis y masa que se puede utilizar con estos animales. Se podría pensar que los animales de laboratorio, al no estar sujetos a la misma reglamentación y procedimientos respecto a exposiciones radioactivas que los humanos, la dosis inyectada por unidad de masa se puede aumentar hasta el punto que el aumento de cuentas resuelva el problema de la sensibilidad en estos sistemas. Sin embargo, hay que tener en cuenta que ésta es una técnica que sigue el principio del trazador, lo que implica que los niveles de trazador son lo suficientemente bajos para no perturbar el sistema biológico que se estudia. Hay varias circunstancias en las que la masa del trazador limitará la cantidad de radiación que se puede inyectar a un ratón. Por tanto, en cada caso se debe determinar la cantidad de masa que se puede inyectar sin violar los principios del trazador. En casos en los que se puedan inyectar grandes cantidades de masa, el tiempo muerto del escáner y su comportamieto a actividad altas serán los factores limitantes.

List of Figures

List of Tables

Chapter 1

Small Animal PET scanners

1.1 Basics of PET

Positron Emission Tomography (PET) is a non invasive imaging modality that belongs to the nuclear medicine field and provides three-dimensional (3D) tomographic images of radiotracer distribution within a living subject [1]. Molecular probes can be labeled with positron-emitting nuclides (^{11}C, ^{13}N, ^{15}O, ^{18}F, ^{64}Cu, etc) and administered into subjects via different routes. These proton-rich radionuclides spontaneously suffer a β^+ decay, in which a proton is converted into a neutron, resulting in the emission of a positron and a neutrino. The emitted positron, equal in mass and opposite in charge to an electron, slows down through a series of collisions with the surrounding matter, then it combines with an electron before both annihilate. The mass of positron and electron (m_e) is converted in two high energy photons of 511 keV which travel in approximately opposite directions [2]. The two gamma rays are sensed at two detectors at roughly the same time. Therefore, it can be inferred that a decay event occurred along the line that joins both detectors. This line is usually referred as line of response (LOR). Coincidence detection of these gamma rays, which are highly penetrating and can escape from the subject, and reconstruction of the location of the annihilation events using analytical or statistical methods form the basis of PET. With its dynamic capability, PET provides both spatial and temporal measurements of the distribution of the biomolecules within a living subject. Combined with kinetic modelling, PET provides quantitative measurements of biological processes in vivo. This unique feature and the wide variety of biomolecules that can be labeled with positron-emitting nuclides of different half-lives make PET an extremely powerful tool to study normal development and diseases in humans, the pharmacokinetics of new drugs, and animal models of human diseases.

1.1.1 Instrumentation

Detector Technology

The highly penetrating nature of 511 keV gamma rays requires PET detectors to have sufficient stopping power to effectively detect the signal. At this en-

ergy, gamma rays interact with detectors primarily through Compton scatter and photoelectric interaction. The photoelectric interaction is the preferred mechanism for detection because the energy of the incoming gamma ray is completely absorbed, which allows energy discrimination to reject gamma rays that have undergone Compton scatter in the subject. Therefore, it is interesting to have detectors made of high atomic number (Z) and high-density material to maximize the photoelectric cross-section and detector efficiency for PET applications. Coincidence detection of the annihilation gamma rays further requires the detectors to a have quick timing response to minimize the effects of accidental or random coincidences.

Random coincidences occur when two gamma rays from different annihilation events are detected by two detectors within a predetermined timing window [3] (random events in figure 1.1). Random coincidences introduce statistical noise in the data and may become the primary limiting factor of system performance at high counting rate applications [4]. The number of random coincidences is directly proportional to the width of the predetermined timing window and increases as the square of the activity. An improvement in detector timing response can extend the operation of a PET system to high-activity experiments, resulting in a wider dynamic range and better counting rate performance.

Another degradation factor is scatter, which occurs when one of the annihilation gamma rays undergoes a Compton scattering inside the subject (like the scattered events in the figure 1.1) or the detectors. Intra-subject scatter reduces the contrast of the image and can be significant for a large subject, such as a human, in a 3D PET system. Scattered event is indistinguishible from a true event except on the basis of its energy. At 511 keV, forward scatter, in which only a small amount of energy is lost in the interaction, is favoured. If PET detectors only accept events with an energy of 511 keV, all scattered events could be eliminated. But this would require a detector with a perfect energy resolution. PET detectors have a finite energy resolution and it is necessary to acquire the events with an energy window, which takes scattered and true events. Improving the energy resolution of the scanner will reduce the detected scatter.

Inorganic scintillators with high density, high Z, and quick decay time have been the dominant detector technology for PET. The physical and optical properties of the commonly used scintillation materials are shown in the table 1.1.1. The scintillation mechanism depends on the energy states of the crystal lattice of the material. The 511 keV gamma rays interact with the scintillation crystal and produce photoelectrons or Compton electrons. These energetic electrons produce a large number of electron-hole pairs that can drop into the impurity sites within the crystal lattice. Electrons at the excited states release energy through fluorescence to produce light photons, which are then detected by secondary photon detectors (light detectors).

Scintillation detectors require a secondary detector to convert the scintillation light into an electric signal. For PET applications, this secondary detector needs to be sensitive to the emission spectrum of the scintillator, to provide adequate signal amplification, and to have quick timing response. The most common

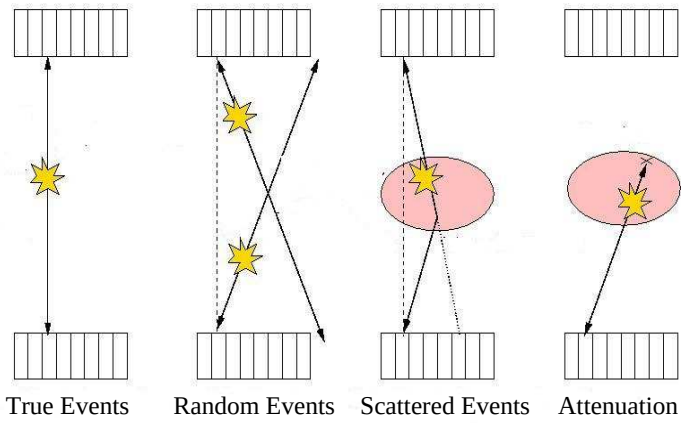

Figure 1.1: The various events associated with coincidence detection of the annihilation photons coming from positron-emitting radionuclides, illustrated for two opposed modules of coincidence detectors.

light detector is the photomultiplier tube (PMT). PMT provides several stages of charge amplification to achieve a typical gain of higher than 10^6. It also provides excellent timing response, which is ideal for PET applications. The disadvantages of PMT are the relatively low quantum efficiency of the photocathode, its sensitivity to magnetic fields, and its bulky size. Nevertheless, it is still the most widely used light detector in PET to date and provides the highest performance in terms of timing resolution for all scintillation-based detectors.

Avalanche photodiodes (APD) are semiconductor detectors that convert light photons to electron-hole pairs. The electrons are accelerated sufficiently so that when they collide with atoms on their way toward the anode, they generate more electron-hole pairs. The collection of charge carriers is slower in APD than in PMT, thus the timing performance is inferior. With relatively low gain (typically from 101 to 103) that strongly depends on the applied electric field, APD-based detectors require a highly regulated power supply and low-noise electronics compared to PMT-based systems. This technology has been used in small animal PET and in dedicated PET brain insert for a magnetic resonance scanner. The main advantages of APD is its compactness and its insensitivity to magnetic fields [12], which increases flexibility in design of high-resolution PET detectors and systems. With higher quantum efficiency, APD-based detectors can have superior energy resolution compared to PMT-based detectors.

A new light detector, the silicon photomultiplier (SiPM), has recently been introduced [13] [14] [15]. It consists of an array of small APD cells (p-n-junctions) with a density of approximately 1000 units per mm^2. These individual cells operate in Geiger mode, whereas the entire detector can be seen as an analog device with its output proportional to the number of light photons detected. The internal amplification is typically approximately 105-106. The quantum efficiency

Table 1.1: Physical and optical properties of commonly used scintillation materials in PET [55]

Scintillation material	Density (g/cm^3)	Effective Atomic Number (Z)	Primary Decay Constant (ns)	Emission Intensity (% relative to NaI)	Emission wave-length (nm)	Attenuation coefficient at 511 keV (cm^{-1})
NaI(Tl)	3.67	51	230	100	410	0.35
LSO	7.40	65	40	75	420	0.86
GSO	6.71	59	60	30	430	0.70
BGO	7.13	75	300	15	480	0.95
YAP	5.55	32	27	40	350	0.37
BaF2	4.88	53	2	12	220, 310	0.45
YSO	4.45	36	70	45	550	0.36
LGSO	7.23	65	60	40	420	0.84
LuAP	8.34	64	17	30	365	0.87

Table 1.2: Half life, maximum positron energy, and average positron range in soft tissue of isotopes commonly used in PET

Isotope	Half-Life (min)	Maximum Positron Energy (MeV)	Average Positron Range in soft tissue (mm)
^{11}C	20.3	0.96	1.52
^{13}N	9.97	1.19	2.05
^{15}O	2.03	1.7	3.28
^{18}F	109.8	0.64	0.83
^{82}Rb	1.26	3.15	7.02

is similar to vacuum PMT (20%-30%), and its timing response is less than 100 ps, significantly faster than conventional APD. Its potential in PET applications is currently being explored.

Detector Design

Coincidence detection of the annihilation gamma rays is an indirect measurement of the positron origin. The spatial resolution of a PET system is known to be limited by three factors: (a) positron range, (b) acolinearity of positron annihilation, and (c) detector intrinsic resolution. A positron travels a short distance from its origin before it annihilates. Depending on the radionuclide, the average positron range varies from a few hundred micrometers to a few millimeters (table 1.2). The effect of the positron range on the system spatial resolution has been deeply studied in [56] for the most common PET isotopes.

The positron also does not come to a complete stop at the instant of annihilation. To preserve the momentum and energy, the two emitted gamma rays travel at directions that deviated slightly from 180^o. The angular distribution of

the deviation was reported to have a mean of 0.5^o FWHM [5]. The uncertainty in identifying the source of origin is also proportional to the distance between a pair of detectors in coincidence. This can be expressed as FWHM(acolinearity, mm)= 0.0022D, where D is the distance between a pair of detectors in cm [6].

The sensitivity of a PET system is determined by the geometric efficiency of the system and the intrinsic detection efficiency of the detectors. The geometric efficiency of a system is the probability of the annihilating gamma rays intercepting the detectors, which corresponds to the solid angle coverage of the detectors. The closer a detector is positioned to the source, the larger the solid angle it can cover. The intrinsic efficiency of a detector is the probability of detection when a gamma ray intercepts the detector, a factor related to the composition and thickness of the detector material. The probability of interaction grows as the thickness increases. But, when a gamma ray enters a detector, the depth of interaction (DOI) may introduce in uncertainty in the identification of the origin of the gamma rays ([7]). This uncertainty is higher when the crystal is thicker and the position of the source is closer to the detectors. This effect is illustrated in figure 1.2 and it will be explained in section 1.1.3.

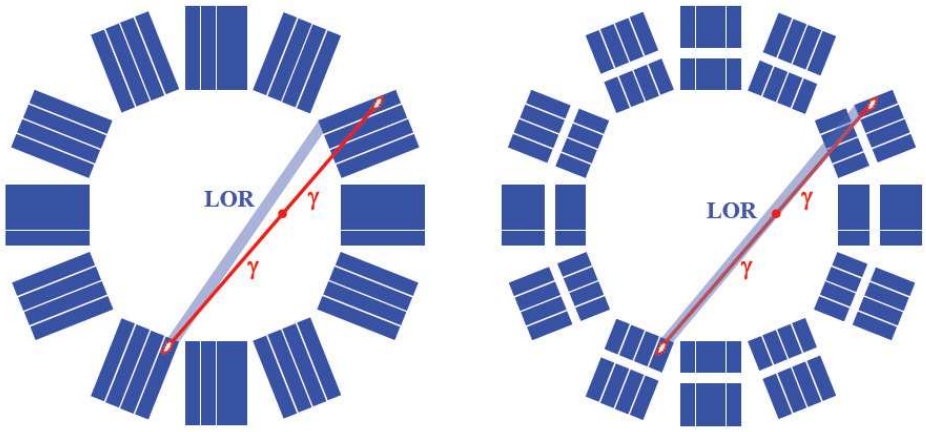

Figure 1.2: Depth of interaction information. On the left, a system without DOI is shown, one can see that the assigned LOR does not correspond to the photon pair path. On the contrary, at the right side, a system with a quantized DOI information can provide the LOR that overlaps the photon pair path.

Combining these factors, one would see that a small system radius leads to higher geometric efficiency at the cost of loss of radial resolution. Reducing the depth of the detector crystal can reduce the DOI effect and preserve the image resolution, but at the cost of lower intrinsic detection efficiency. Many PET systems are designed with some of these parameters compromised in exchange for image resolution, system sensitivity, and/or imaging field of view (FOV).

Scintillation crystal-based PET detectors can be divided into three categories: continuous crystal, block detector, and pixelated crystal, as illustrated in figure 1.3. In the three cases, the detectors can be configured as full rings that com-

pletely surround the patient or as partial rings with rotational motion to obtain the needed angular sampling.

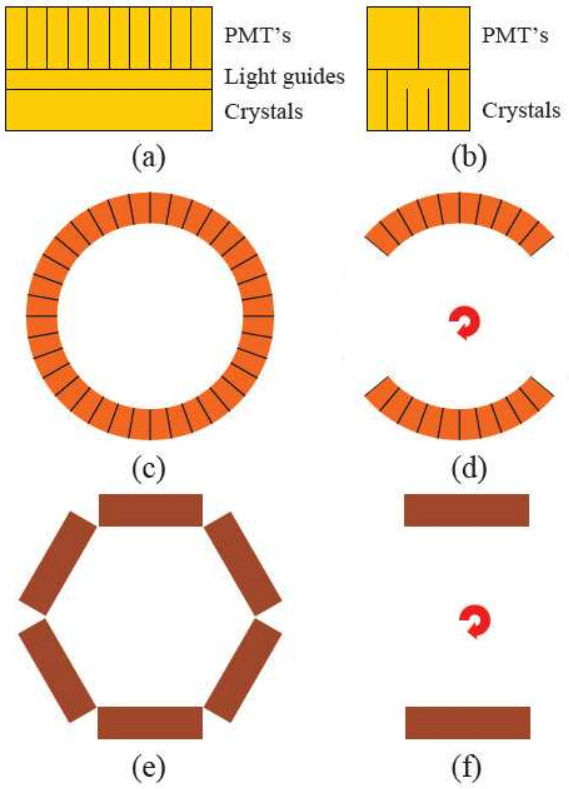

Figure 1.3: The major crystal-PMT decoding geometry and designs commonly used in scintillation-crystals-based PET. (a) Continuous crystal read out by an array of PMTs sensitive to position. (b) Block detector uses pixelated crystals and PMTs. (c) Full ring of discrete crystals configured as small blocks or larger detector modules. (d) Partial ring of detector blocks that rotates. (e) Array of large detectors, either continuous or discrete crystals. (f) Partial array of large detector that rotates.

Depending on the design of the scanner, PET data can be acquired in either 2D or 3D mode (see figure 1.4). Traditionally, PET data acquisitions were based on plane-by-plane LOR detection (2D mode). Direct and cross planes originated from LORs detected within the same ring (ring difference 0) or the two adjacent rings (ring difference ± 1), respectively. To shield out-of-plane coincidence photons that are emitted obliquely, annular septa composed of lead-tungsten separate the rings. Working in 2D mode, system sensitivity is constrained to a defined value by geometric acquisition conditions and by electronic collimation fixed between adjacent planes. A large increase in sensitivity can be obtained by collecting all possible LORs; this is possible if the septa are removed. In this approach, called 3D mode, the sensitivity is 3-4 times higher than in 2D mode (figure 1.4). However, this gain is associated with an increase in random and

scatter coincidences, and the increased counting rate can result in loss of events due to the dead time. To fully take advantage of the 3D mode, faster coincidence detection is required, along with higher computing power to manage the very high counting rate.

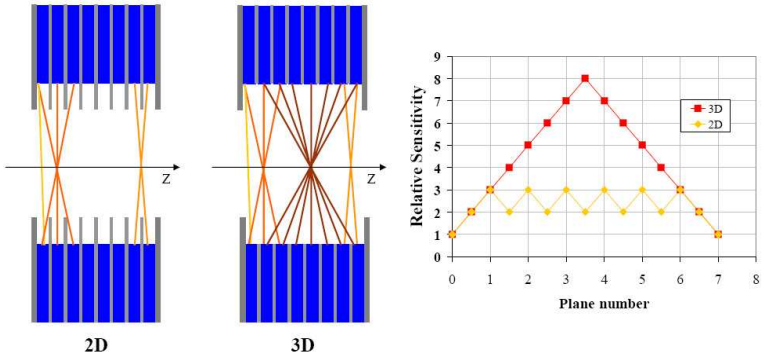

Figure 1.4: Comparison between the sensitivity in 2D (with septa) and 3D (without septa) modes [19]

1.1.2 Image Reconstruction

After the two gamma rays have been detected, the next step is to compute, or reconstruct, images from these data. This section is dedicated to explain the main reconstruction algorithms employed in PET.

Acquisition and Organization of Data

A conventional PET scanner counts coincidence events between pairs of detectors. As we have already mentioned, the straight line connecting the inner face centers of two detectors is called a line of response. In the same way, the parallelepiped joining the two detectors defines the volume of response (VOR) (figure 1.5). In the absence of physical effects such as attenuation, scattered and accidental coincidences, and detector efficiency variations, the total number of coincidence events detected will be proportional to the total amount of tracer contained in the hypothetical tube of VOR (shown by the shaded area in figure 1.5b. Because photon counting from radioactive decay is a random process, the expectation operator for each pair of detectors (in this example, detector 1 and 2) is

$$E\{\text{photons detected per second}\} = \iiint_{VOR} s(\mathbf{x}) f(\mathbf{x}) dx \tag{1.1}$$

where $s(\mathbf{x})$ is the detection sensitivity within the tube at $\mathbf{x}$ and $f(\mathbf{x})$ is the three dimensional distribution of radiotracer activity inside the patient.

For the LOR definition, a scanner comprising multiple small detectors was considered. Scanners based on large-area, position-sensitive detectors can be described similarly if viewed as consisting of large number of very small virtual detectors.

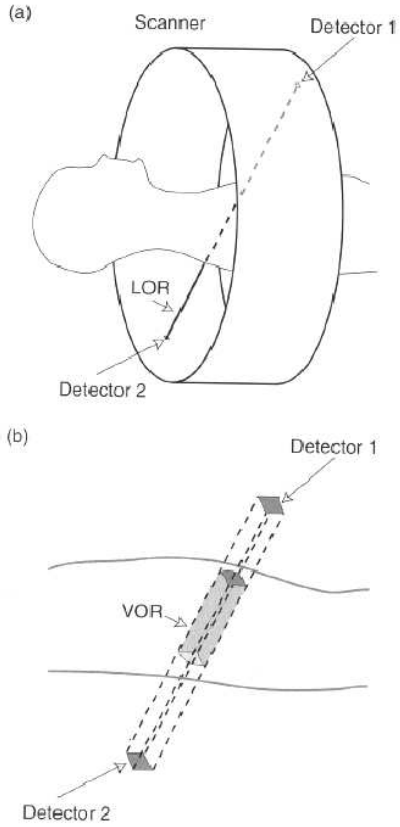

Figure 1.5: (a) Overall scheme with the line of response (LOR) that joins detector 1 and 2. (b) Detail of the sensitive region scanned by the two detectors that defines the volume of response (VOR) [19].

LOR Histogram The natural parametrization of PET data uses the two indices (d_1, d_2) of the detectors in coincidence or the index of the associated LOR (l_{d_1,d_2}). Storing the coincidences for each LOR corresponds to the LOR histogram way of organizing the data. The main advantage of the LOR histogram format is to take full benefit of the nominal spatial resolution of the scanner. The generalization from 2D to 3D imaging using LOR histogram can be done immediately. But, the natural parametrization is poorly adapted to analytic algorithms. This is the principal reason why the raw data are normally interpolated into an alternative sinogram parametrization (explained in the next section). Another reason to use the sinogram is that this parametrization is more compact and smaller than the LOR histogram. When the $N_{events} << N_{LOR}$, there is an approach to reduce data storage and processing time. This format consists of recording the LOR index or detector indices of each coincident event in a sequential data stream called a list-mode data set. Additional information such as the time or the energy of each detected photon can also be stored.

Sinogram For 2D imaging the considered LORs are the ones lying within a specified imaging plane. The acquired data are collected along a LOR through a 2D object $f(x, y)$ as shown in figure 1.6 and the equation 1.1 is written as a line

integral. In 2D, the line integral acquisition model can be expressed by the use of a rotated coordinate system. The rotated coordinates (subscript r) are related to the original coordinates by:

$$\begin{bmatrix} x \\ y \end{bmatrix} = \begin{bmatrix} \cos\phi & -\sin\phi \\ \sin\phi & \cos\phi \end{bmatrix} \begin{bmatrix} x_r \\ y_r \end{bmatrix} \tag{1.2}$$

With this notation the equation 1.1 can be compactly rewritten as:

$$p(x_r, \phi) = \int_{-\infty}^{\infty} f(x, y) dy_r \tag{1.3}$$

where the location of the LOR is described by x_r and ϕ, and $p(x_r, \phi)$ is the integral of $f(x, y)$ along the LOR.

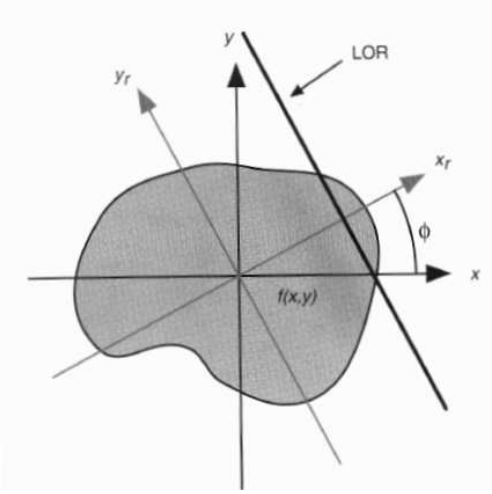

Figure 1.6: Two dimensional LOR example. The value of $f(x, y)$ is integrated along the LOR to obtain $p(x_r, \phi)$ [19]

For a fixed direction, ϕ, the set of line-integral data for all x_r forms a projection of $f(x, y)$ as indicated in figure 1.7. The collection of all projections for $0 \leq \phi < \pi$ as 2D function of x_r and ϕ has been termed a sinogram by the Swedish scientist Paul Edholm because the set of LORs passing through a fixed point (x_o, y_o) lies along a sinusoid described by $x_r = x_o \cos\phi + y_o \sin\phi$. This relationship is illustrated in figure 1.8. A sinogram for a general object will be the linear superposition of all sinusoids corresponding to each point in the object.

The line-integral transform of $f(x, y) \rightarrow p(x_r, \phi)$ is called the X-ray transform [20] which in 2D is the same as the Radon transform. The X-ray transform is a basis for a model of the data acquisition process of several modalities (gamma cameras, SPECT, X-ray imaging systems), not only for PET, and non-medical imaging modalities.

In fully 3D imaging the two dimensional line-integral data for all imaging planes perpendicular to the scanner or patient axis (direct planes), as well as the line-integral data lying on oblique imaging planes that cross the direct planes, are included. This type of data is typically acquired by PET scanners to increase

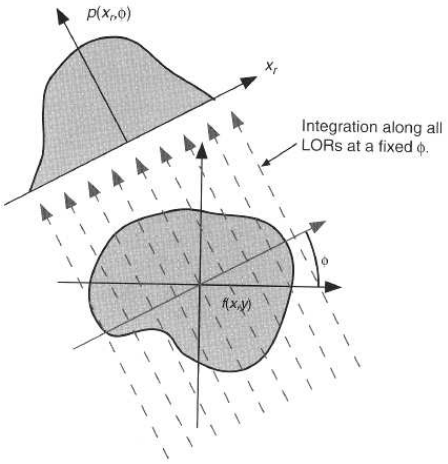

Figure 1.7: A projection formed from integration along all parallel LOR at an angle ϕ [19].

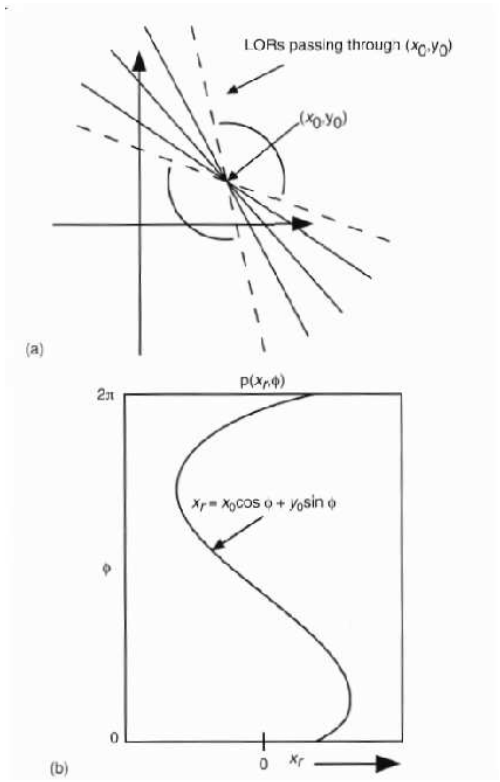

Figure 1.8: (a) Relation between LORs passing through a fixed point (x_o, y_o) and (b) the values of the sinogram $p(x_r, \phi)$ for a fixed point [19].

sensitivity and lower the statistical noise associated with photon counting, thus improving the signal-to-noise ratio in the reconstructed image.

For the X-ray transform of a three-dimensional object, four parameters are needed to parameterize the LOR shown in figure 1.9: Two angles (ϕ, θ) to define the unit vector $\hat{z}_r = (\cos\phi\cos\theta, \sin\phi\cos\theta, \sin\theta)$ parallel to the LOR, and

two coordinates (x_r, y_r) to locate the intersection of the LOR with the plane perpendicular to $\hat{z}_r(\phi, \theta)$.

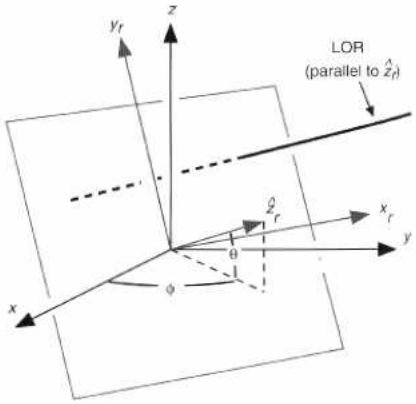

Figure 1.9: Parametrization of a 3D LOR for the X-ray transform using a rotated coordinate frame [19].

By using the constraint $\hat{\mathbf{x}}_r \cdot \hat{\mathbf{z}} = 0$ and the definition of θ as the co-polar angle, the rotated coordinates are related to the original coordinates by

$$\begin{bmatrix} x \\ y \\ z \end{bmatrix} = \begin{bmatrix} -\sin\phi & -\cos\phi\sin\theta & \cos\phi\cos\theta \\ \cos\phi & -\sin\phi\sin\theta & \sin\phi\cos\theta \\ 0 & \cos\theta & \sin\theta \end{bmatrix} \begin{bmatrix} x_r \\ y_r \\ z_r \end{bmatrix} \tag{1.4}$$

This choice of rotated coordinates and θ as the co-polar angle is customary because the equivalent 2D acquisition, or the direct planes, corresponds to $\theta = 0$. Using the coordinate transform of equation 1.4, the line integral projections along the LOR, located by (x_r, y_r, ϕ, θ) are easily expressed as:

$$p(x_r, y_r, \phi, \theta) = \int_{-\infty}^{\infty} f(x, y, z) dz_r \tag{1.5}$$

For a fixed direction, $\hat{z}_r(\phi, \theta)$, the set of line-integral data for all (x_r, y_r) forms a two-dimensional projection $p(x_r, y_r, \phi, \theta)$ of $f(x, y, z)$, as illustrated in figure 1.10. The full projection data set is a four-dimensional function, so the X-ray transform of $f(x, y, z) \rightarrow p(x_r, y_r, \phi, \theta)$ has increased the number of dimensions by one and this will cause redundancies in the data.

Analytical Methods

Analytic methods typically neglect noise and complicating physical factors in an effort to obtain frameworks that yield explicit inversion formulas for the reconstruction problem. Analytic methods usually produce solutions that are relatively practical to compute. The Filtered Back Projection (FBP) method is an example of this category of image reconstruction approaches referred to as analytic methods to distinguish them from iterative methods. FBP is a mathematical technique based on an idealized model of PET acquisition that ignores many

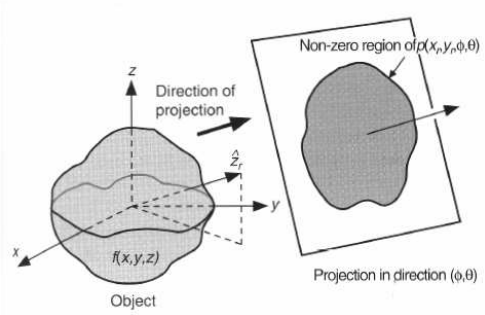

Figure 1.10: Illustration of a 2D line-integral projection $p(x_r, y_r, \phi, \theta)$ of a 3D object $f(x, y, z)$. The projection is formed from the set of all LORs parallel to $\hat{\mathbf{x}}(\phi, \theta)$ [19].

significant features of real data. Specifically, FBP assumes that the number of detected coincidence events travelling along a particular direction approximates an integral of the radiotracer distribution along that line, that is, the parallel projection $p(x_r, y_r)$ defined in figure 1.7. Introducing FBP based on the line-integral model means that there are important effects not considered, such as noise, attenuation, scatter, and detector size. Suboptimal, but reasonable results can be obtained in practice using FBP, even if attenuation and scatter are not accounted for[1]. However, noise must always be accounted for in some way, and this is usually achieved in FBP by smoothing the projections prior to reconstruction or by smoothing the image afterward.

The Central Section Theorem The central section theorem (also known as the central slice or projection slice theorem) is the most important relationship in analytic image reconstruction. In this section, the derivation of the two-dimensional version will be done first, which is then easily extended to the three dimensional X-ray transform. For all the results presented here, the imaging process must be shift-invariant, which allows the use of the Fourier transforms. The meaning of the shift invariance here is that the projections of the scanning of a shifted object are also shifted, but are otherwise identical to the projections of the unshifted object. Shift-invariance is a natural property of ideal two-dimensional imaging. For fully three-dimensional imaging situation is somewhat more complicated.

The definition of the one-dimensional Fourier transform and the inverse transform are the starting point of the 2D central section theorem derivation:

$$\begin{aligned} F(\upsilon_x) &= F_1\{f(x)\} = \int_{-\infty}^{\infty} f(x) e^{-i2\pi x \upsilon_x} dx \\ f(x) &= F_1^{-1}\{F(\upsilon_x)\} = \int_{-\infty}^{\infty} F(\upsilon_x) e^{+i2\pi x \upsilon_x} d\upsilon_x \end{aligned} \tag{1.6}$$

where the adopted notation is capital letters for Fourier transformed functions,

[1]Usually, scatter and attenuation are taken into account before the reconstruction by including corrections in the sinogram.

and, in general, the operator $F_n\{f(x)\}$ for the n-dimensional Fourier transform of $f(x)$, $F_n^{-1}\{F(\upsilon_x)\}$ for the inverse n-dimensional Fourier transform, and υ_x as the Fourier space conjugate of x.

The one-dimensional Fourier transform of a projection is given by:

$$P(\upsilon_{x_r}, \phi) = F_1\{p(x_r, \phi)\} = \int_{-\infty}^{\infty} p(x_r, \phi) e^{-i2\pi x_r \upsilon_{x_r}} dx_r \tag{1.7}$$

An important step is the introduction of the definition of $p(x_r, \phi)$ from equation 1.3,

$$\begin{aligned} P(\upsilon_{x_r}, \phi) &= \int_{-\infty}^{\infty} p(x_r, \phi) e^{-i2\pi x_r \upsilon_{x_r}} dx_r \\ &= \int_{-\infty}^{\infty}\int_{-\infty}^{\infty} f(x, y) e^{-i2\pi x_r \upsilon_{x_r}} dx_r dy_r \\ &= \int_{-\infty}^{\infty}\int_{-\infty}^{\infty} f(x, y) e^{-i2\pi (x\cos\phi + y\sin\phi)\upsilon_{x_r}} dx dy \\ &= F(\upsilon_{x_r}\cos\phi, \upsilon_{x_r}\sin\phi) \end{aligned} \tag{1.8}$$

where $F(\upsilon_x, \upsilon_y) = F_2\{f(x, y)\} = \int_{-\infty}^{\infty}\int_{-\infty}^{\infty} f(x, y) e^{-i2\pi(x\upsilon_x + y\upsilon_y)} dx dy$. Because the Fourier transform is invariant under rotation, it is obtained from the equation 1.2:

$$\begin{bmatrix} \upsilon_x \\ \upsilon_y \end{bmatrix} = \begin{bmatrix} \cos\phi & -\sin\phi \\ \sin\phi & \cos\phi \end{bmatrix} \begin{bmatrix} \upsilon_{x_r} \\ \upsilon_{y_r} \end{bmatrix} \tag{1.9}$$

Equation 1.8 can be more concisely expressed using equation 1.9:

$$P(\upsilon_{x_r}, \phi) = F(\upsilon_x, \upsilon_y) \mid_{\upsilon_{y_r}=0} \tag{1.10}$$

Equation 1.10 is the key to understand tomographic imaging. It shows that the Fourier transform of a one-dimensional projection is equivalent to a section, or profile, at the same angle through the center of the two-dimensional Fourier transform of the object. This is illustrated in figure 1.11. It is known that any function is uniquely determined by its Fourier transform (that is, it can be computed via the inverse Fourier transform), the central slice theorem indicates that if we know $P(\upsilon_{x_r}, \phi)$ at angles $0 \leq \phi < \pi$, then it is possible somehow to determine $F(\upsilon_x, \upsilon_y)$ and thus $f(x, y)$.

To derive the central section theorem for the X-ray projection of a 3D object, first the two-dimensional Fourier transform is computed with respect to the first two (linear) variables:

$$P(\upsilon_{x_r}, \upsilon_{y_r}, \phi, \theta) = \int_{-\infty}^{\infty}\int_{-\infty}^{\infty} p(x_r, y_r, \phi, \theta) e^{-i2\pi(x_r\upsilon_{x_r} + y_r\upsilon_{y_r})} dx_r dy_r \tag{1.11}$$

If $F(\upsilon_x, \upsilon_y, \upsilon_z)$ is the three-dimensional Fourier transform of $f(x, y, z)$

$$F(\upsilon_x, \upsilon_y, \upsilon_z) = \int_{-\infty}^{\infty}\int_{-\infty}^{\infty}\int_{-\infty}^{\infty} f(x, y, z) e^{-i2\pi(x\upsilon_x + y\upsilon_y + z\upsilon_z)} dx dy dz \tag{1.12}$$

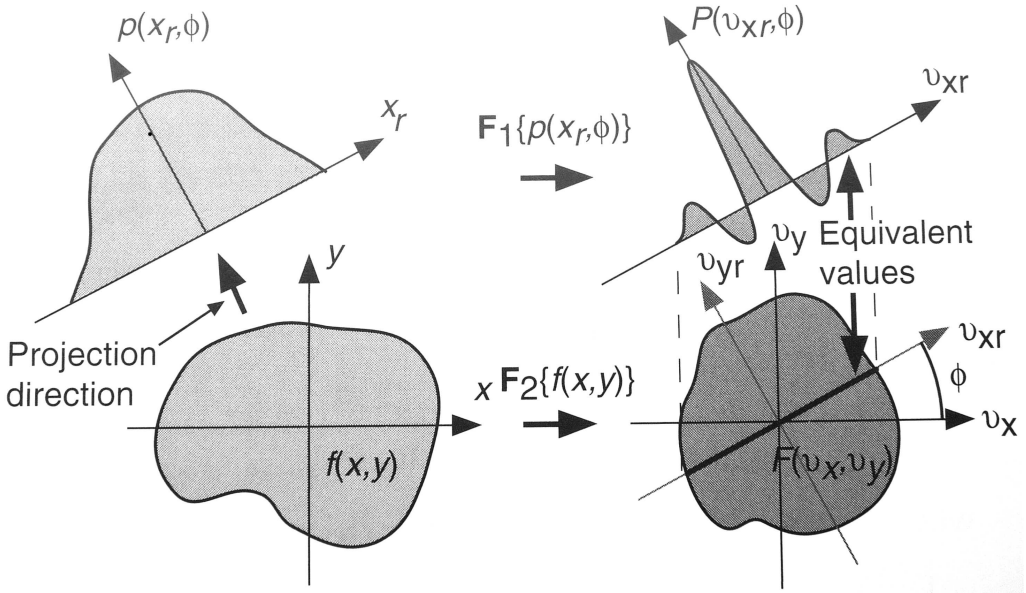

Figure 1.11: 2D central section theorem, showing the equivalency between the 1D Fourier transform of a projection at angle ϕ and the central section at the same angle though the 2D Fourier transform of the object [19].

then by using a derivation similar to equation 1.8, the three-dimensional version of the central section theorem for X-ray projections is obtained:

$$P(\upsilon_{x_r}, \upsilon_{y_r}, \phi, \theta) = F(\upsilon_x, \upsilon_y, \upsilon_z) \mid_{\upsilon_{z_r}=0} \tag{1.13}$$

where from equation 1.14 the relationship between $(\upsilon_{x_r}, \upsilon_{y_r}, \upsilon_{z_r})$ and $(\upsilon_x, \upsilon_y, \upsilon_z)$ is

$$\begin{bmatrix} \upsilon_x \\ \upsilon_y \\ \upsilon_z \end{bmatrix} = \begin{bmatrix} -\sin\phi & -\cos\phi\sin\theta & \cos\phi\cos\theta \\ \cos\phi & -\sin\phi\sin\theta & \sin\phi\cos\theta \\ 0 & \cos\theta & \sin\theta \end{bmatrix} \begin{bmatrix} \upsilon_{x_r} \\ \upsilon_{y_r} \\ \upsilon_{z_r} \end{bmatrix} \tag{1.14}$$

The meaning of the three-dimensional central section theorem for the X-ray projection is analogous to the two-dimensional case: A two-dimensional Fourier transform of a projection perpendicular to $\hat{\mathbf{z}}(\phi, \theta)$ is equivalent to a section at the same orientation thought the three-dimensional Fourier transform of the object. This is illustrated in figure 1.12.

There are two major differences between 2D and 3D PET imaging that affects the reconstruction derived from standard Fourier deconvolution techniques: Data redundancy and spatial variance. These differences complicate 3D image reconstruction.

To illustrate the data redundancy of 3D PET imaging, consider that in normal 2D PET imaging of a volume (using septa), there is enough information to reconstruct the tracer distribution. In performing 3D imaging of the same volume, we

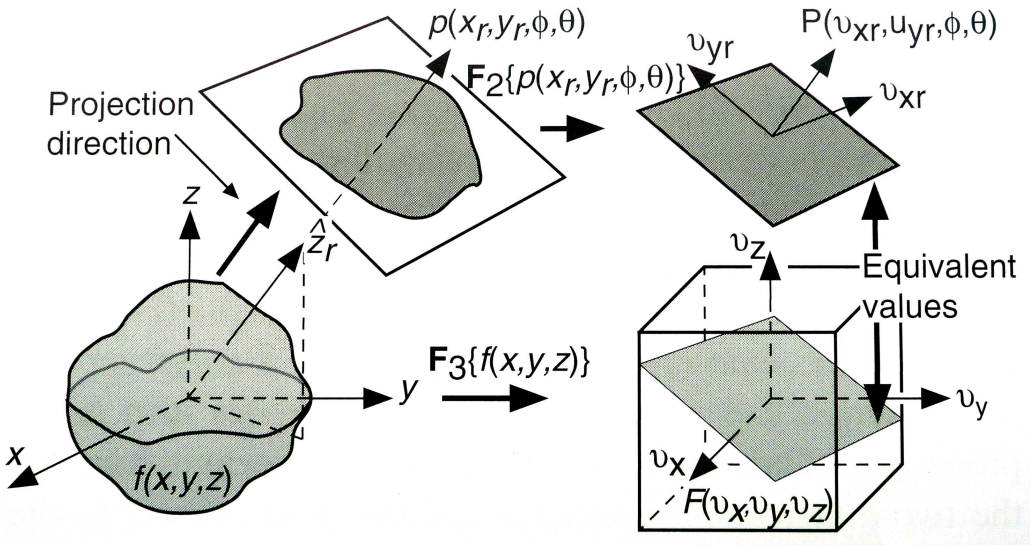

Figure 1.12: 3D central section theorem for X-ray transforms, showing the equivalency between the 2D Fourier transform of a projection in direction $\hat{z}(\phi, \theta)$ and the central section at the same angle though the 3D Fourier transform of the object [19].

collect a super-set of the 2D data, therefore the additional data must consist of redundant information. The key point of 3D PET imaging is that the collection of this redundant information along the additional LORs, if used properly, can improve the image signal-to-noise ratio by reducing the statistical noise.

The shift variance of 3D PET can be understood by considering figure 1.13, which illustrates how a projection is truncated due to the finite axial extent of the scanner. To develop the theory and algorithms required to reconstruct the tracer distribution, it is necessary to assume that $p(x_r, y_r, \phi, \theta)$ is known for all (x_r, y_r). In other words, it is necessary to measure all the LORs parallel to $\hat{\mathbf{z}} = (\cos\phi\cos\theta, \sin\phi\cos\theta, \sin\theta$ (defined in figure 1.9) and crossing the region D_f, where D_f is the support of the object, that is, where $f(\mathbf{x}) \neq 0$. If the projections are not truncated, they are said to be complete. If all projections were complete, the sensitivity of the scanner would be independent of the position in the field-of-view and the reconstruction problem would be stationary (shift-invariant) and could be solved using standard Fourier deconvolution techniques. The 2D reconstruction problem, with a multiring scanner operated with the septa extended, is shift-invariant provided the small effects such as the parallax error are neglected or corrected. In contrast, the 3D problem is not shift-invariant because the solid angle subtended by the scanner decreases when one moves away from the center of the field-of-view along the scanner axis. Truncation increases the complexity of the reconstruction because filtered-backprojection, being based on Fourier deconvolution, cannot be applied to incomplete data. For the impractical case of a nontruncated spherical scanner ($\Theta_D = \pi/2$), the scanner response would be spatially invariant, although the issue of data redundancy would remain.

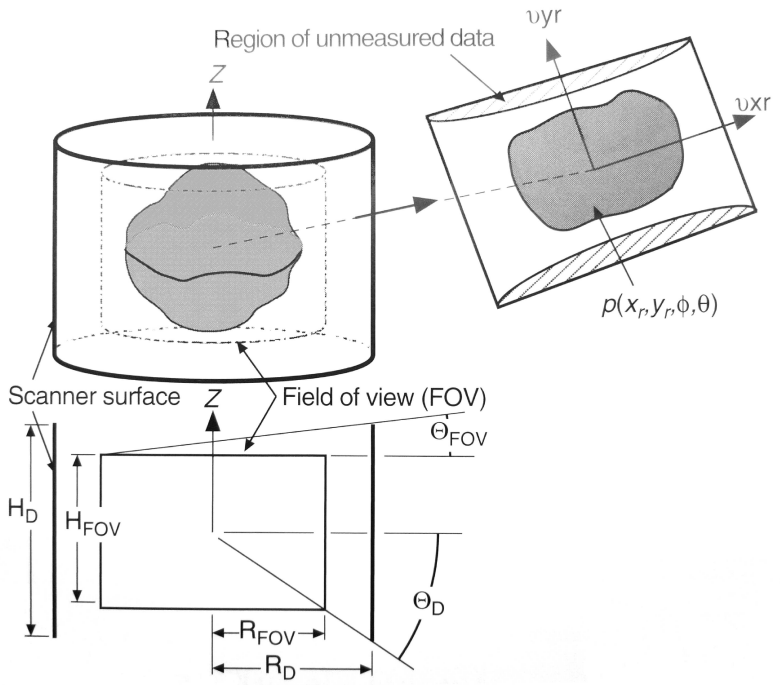

Figure 1.13: Illustration of the region of complete data acquisition for a 3D PET scanner [19].

Two-Dimensional Image Reconstruction

In most cases, the reconstruction of PET data is based on the filtered backprojection (FBP) approach for parallel projections. This algorithm originated from work in a number of fields, including radio astronomy and electron microscopy. A similar approach, modified to incorporate divergent as opposed to parallel projections, is currently used in computed tomography (CT). The implementation for PET requires two steps:

1. *Convolution or filtering:* Each projection $p(x_r, \phi)$ at a given ϕ is convolved with a function (kernel) $h(x_r)$ to yield a modified projection $p_F(x_r, \phi)$, where:

$$p_F(x_r, \phi) = \int p(x'_r, \phi) h(x_r - x'_r) dx'_r \tag{1.15}$$

The kernel is the inverse Fourier transform of the ramp function, $\mid \upsilon_{x_r} \mid$, related to the Jacobian of the transformation to polar coordinates (υ_{x_r}, ϕ). In practice, for reasons to be discussed below, it is necessary to limit the high-frequency behaviour of the ramp by multiplying by a low-pass window function $W(\upsilon_{x_r})$, such that $h(x_r)$ is given by

$$h(x_r) = \int \mid \upsilon_{x_r} \mid W(\upsilon_{x_r}) e^{+2\pi i x_r \upsilon_{x_r}} d\upsilon_{x_r} \tag{1.16}$$

The convolution may be equivalently performed in Fourier space where the convolution operation reduces to a simple multiplication ([21]). Thus:

$$\begin{aligned} p_F(x_r,\phi) &= \int_{-\infty}^{\infty} P_F(\upsilon_{x_r},\phi)e^{+i2\pi x_r \upsilon_{x_r}} d\upsilon_{x_r} \\ P_F(\upsilon_{x_r},\phi) &= \mid \upsilon_{x_r} \mid W(\upsilon_{x_r}) \int_{-\infty}^{\infty} p(x_r,\phi)e^{-i2\pi x_r \upsilon_{x_r}} dx_r \end{aligned} \tag{1.17}$$

The Fourier transform of the convolving function $h(x_r)$, i.e. $\mid \upsilon_{x_r} \mid W(\upsilon_{x_r})$, is called a filter, and hence equation 1.17 is referred to as the filtering step and $p_F(x_r,\phi)$ as filtered projections.

2. *Backprojection:*

   The reconstruction $f_R(x,y)$ of the tracer function $f(x,y)$ is formed from the filtered projections by redistributing the filtered projection value $p_F(x_r,\phi)$ uniformly along the straight line (x_r,ϕ):

$$f_R(x,y) = \int_0^{\pi} p_F(x\cos\phi + y\sin\phi,\phi)d\phi \tag{1.18}$$

   This operation is called backprojection since formally it is the reverse of the projection process, the value of $f_R(x,y)$ at the point (x,y) being obtained by summing the contributions.

In practice, PET images are reconstructed from sinograms using discretized versions of equations 1.17 and 1.18. The discretization of these expressions can be found in [22].

An important feature of the kernel $h(x_r)$ that appears in equation 1.15 is its dependence on the distance $x_r - x'_r$ rather than on the separate coordinates x_r and x'_r. This property relates to the fact that the kernel is shift-invariant, meaning that all projections values are filetered using the same kernel. Any translation of the tracer distribution $f(x,y)$ results in a corresponding translation of the projection data $p(x_r,\phi)$, without modifying the form of equation 1.3. The simple form of equation 1.17 is then a direct consequence of the shift-invariance of $h(x_r)$. In practice, however, shift-invariance is only approximately satisfied due to the sensitivity variations within a LOR and to differing LOR cross sections. Nevertheless, these variations are, in general, small, and shift-invariance is a reasonable approximation for the reconstruction of direct and cross plane sinograms. Unfortunately, shift-invariance is not satisfied in the case of three-dimensional acquisition, but this will be discussed in the next section.

Three-Dimensional Image Reconstruction

For a tomograph comprising multiple rings of detectors, a 3D image of the tracer distribution $f(x,y,z)$ can be built up by stacking a set of independent 2D slices. Each slice is reconstructed independently of the adjacent slices. However, this procedure is no longer possible when coincidences are acquired between all

ring of detectors. A full 3D acquisition necessitates a full 3D reconstruction algorithm in order to correctly incorporate the sinograms for the oblique LORs. The problem, therefore, is to recover the tracer concentration $f(x, y, z)$ from the line integrals defined by equation 1.5 modified to the 3D case.

Reconstruction of the tracer distribution $f(x, y, z)$ from the integrals $p(x_r, y_r, \phi, \theta)$ is therefore a problem of inverting the X-ray transform in the three dimensions. Unlike the 2D case, in the 3D the Radon transform is not equivalent to the X-ray transform, equation 1.5. Whether or not the inversion is possible depends upon the set of line integrals which have been measured by the tomograph. Assume initially that the line integrals are measured for a limited set of directions $0 \leq \phi < \pi$ and $-\Theta_c \leq \theta < \Theta_c$, but for all coordinate pairs (x_r, y_r) for which the straight line (x_r, y_r, ϕ, θ) intersects the 3D field of view. This means that, while not all possible parallel projections are measured because of the limited range of θ, those projections which are measured are complete.

Although not all possible line integrals through the field of view are available (since $\mid \theta \mid < \Theta_c < \pi$), the solution of the equation 1.5 is nevertheless unique, and can be obtained by straightforward generalisation of equations 1.15 to 1.18 above

1. *Convolution or filtering*: Each 2D parallel projection is convolved with a kernel $h(x_r, y_r, \theta)$, independent of ϕ, to give the filtered projection $p_F(x_r, y_r, \phi, \theta)$:

$$p_F(x_r, y_r, \phi, \theta) = \int\int p(x'_r, y'_r, \phi, \theta) h(x_r - x'_r, y_r - y'_r, \theta) dx'_r dy'_r \qquad (1.19)$$

   As for the 2D case, this filtering operation may be more efficiently performed using the Fourier convolution theorem than by implementing equation 1.19 directly.

2. *Backprojection*: The 2D filtered projections are backprojected by redistributing the values $p_F(x_r, y_r, \phi, \theta)$ uniformly along the line (x_r, y_r, ϕ, θ) so as to form the reconstructed image:

$$f_R(x_r, y_r, \phi, \theta) = \int_0^{\pi} d\phi \int_{-\Theta}^{\Theta} \cos\theta \, p_F(x_r, y_r, \phi, \theta) d\theta \qquad (1.20)$$

   with $x_r = -x \sin\phi + y \cos\phi$ and $y_r = -x \cos\phi \sin\theta - y \sin\phi \sin\theta + z \cos\theta$.

   The expressions in equation 1.20 for the projection coordinates (x_r, y_r) ensure that the line (x_r, y_r, ϕ, θ) passes through the point (x, y, z). Thus, as in the 2D case, the reconstructed value $f_R(x, y, z)$ at the point (x, y, z) is obtained by summing the contributions from all the backprojection lines (x_r, y_r, ϕ, θ) which pass through (x, y, z). In analogy to the equation 1.17, the convolution kernel $h(x_r, y_r, \theta)$ may be expressed as the Fourier transform of a filter function $H(\upsilon_{x_r}, \upsilon_{y_r}, \theta)$ multiplied by a low-pass window function $W(\upsilon_{x_r}, \upsilon_{y_r})$:

$$h(x_r, y_r, \theta) = \int\int H(\upsilon_{x_r}, \upsilon_{y_r}, \theta) W(\upsilon_{x_r}, \upsilon_{y_r}) e^{2\pi i (x_r \upsilon_{x_r} + y_r \upsilon_{y_r})} d\upsilon_{x_r} d\upsilon_{y_r} \quad (1.21)$$

where $(\upsilon_{x_r}, \upsilon_{y_r})$ are frequency space cartesian coordinates corresponding to the projection coordinates (x_r, y_r). Equivalently, polar coordinates (ρ, α) can be defined by:

$$\upsilon_{x_r} = \rho \cos\alpha, \ \upsilon_{y_r} = \rho \sin\alpha, \ with \ \rho^2 = \upsilon_{x_r}^2 + \upsilon_{y_r}^2 \quad (1.22)$$

An appropriate filter function $H(\upsilon_{x_r}, \upsilon_{y_r}, \theta)$ was published by Colsher [23] expressed in frequency space polar coordinates on the projection plane as:

$$\begin{aligned} H(\rho\cos\alpha, \rho\sin\alpha, \theta) &= \frac{\pi\rho}{\arcsin\frac{\sin\Theta}{Z}} \quad \text{if } Z \geq \sin\Theta \\ &= 2\rho \qquad\qquad\quad \text{if } Z < \sin\Theta \end{aligned} \quad (1.23)$$

where $Z = \sqrt{\cos^2\alpha + \sin^2\alpha \sin^2\theta}$ and $\mid \theta \mid \leq \Theta_c$.

As in the 2D (equation 1.16), the filter function is proportional to the modulus of the frequency, ρ. In addition, since equation 1.19 is a convolution equation, the measured data set $p(x_r, y_r, \phi, \theta)$ is required to be shift invariant.

Unfortunately, in practice, the 3D data set acquired by a multi-ring PET tomograph does not satisfy the conditions for shift-invariance. This has been explained in section 1.1.2, page 34. Under these conditions, the filtered backprojection algorithm cannot be applied to reconstruct the data.

If, however, some angle Θ_c can be defined such that, for $\mid \theta \mid \leq \Theta_c$, say, the corresponding parallel projections are completely measured, then the algorithm could successfully be applied to a subset of the 3D data, rejecting those partially-measured projections with angles $\mid \theta \mid > \Theta_c$ ([23], [24]). Indeed, this was the condition under which the algorithm was originally derived earlier in this section, that all projections for $\mid \theta \mid \leq \Theta_c$ were completely measured. From figure 1.14, it can be seen that, as the tracer distribution extends axially from the centre, the angle Θ_c for which all projections are completely measured becomes progressively smaller. Finally, when the tracer distribution covers the full axial extent of the tomograph, $\Theta_c \approx 0$.

One of the simplest solutions to the problem of how to incorporate the oblique LORs from a multi-ring tomograph into a 3D reconstruction using filtered backprojection is based on the following idea ([25], [26], [27]): since the projections which give rise to shift-variance are incomplete, and it is desired to include them in a filtered backprojection reconstruction, why not complete these projections before including them. Then the reconstruction will again involve only completely-measured projections and can be performed, as outlined earlier in this section, by 3D filtered backprojection.

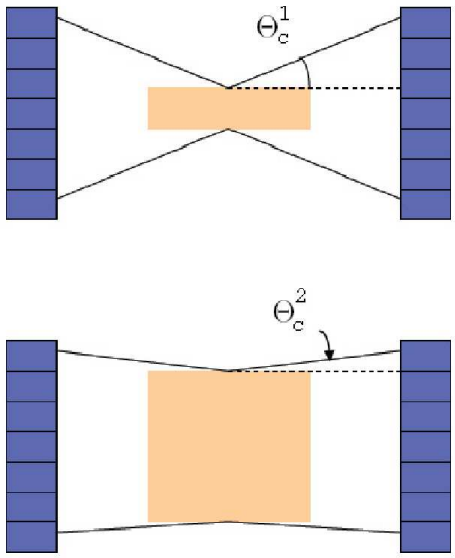

Figure 1.14: The dependence of the angle Θ_c on the axial extent of the tracer distribution ($\Theta_c^1 > \Theta_c^2$)

The problem of how to complete the partially-measured projections can be resolved by using the one set of complete projections that are measured, i.e. those for $\theta = 0$, to reconstruct an initial image using the 2D algorithm described in the previous section. With this initial image, it is then possible to simulate the projection process mathematically and create the unmeasured parts of a projection by "forward projecting" along LORs that do not exist in the actual tomograph. The procedure is equivalent to increasing the effective axial extent of the tomograph such that all projections for $\mid \theta \mid \leq \Theta_c$ are complete, where Θ_c is the maximum acceptance angle of the tomograph.

The steps in the algorithm are therefore as follows:

1. Reconstruct a first estimate of the image using only the direct and cross plane sinograms ($\theta = 0$) and a 2D reconstruction technique such as equations 1.17 and 1.18 above.

2. Based on this image estimate, reproject the non-existant LORs in order to complete the partially-measured projections for $\mid \theta \mid > 0$. If desired $\mid \theta \mid$ can extend out the maximum acceptance angle of the tomograph. However, at these angles the number of measured LORs may be small compared with the number that have been obtained by reprojection.

3. With a set of complete projections for all $\mid \theta \mid \leq \Theta_c$, reconstruct a final image incorporating all sinograms using equations 1.19 to 1.23 above.

In the ideal situation of continuously-sampled and noise-free data, the final image from step 3 will be identical to the initial estimate from step 1. It is only in

the presence of statistical noise that the incorporation of the additional oblique LORs serves to improve the signal to noise of the final 3D reconstruction.

Iterative Methods

While the analytic approaches typically result in fast reconstruction algorithms, accuracy of the reconstructed images is limited by the approximations implicit in the linear-integral model on which the reconstruction formulae are based. In contrast to the analytical methods, an iterative model-based approach can simply model the mapping from source to detector without requiring explicit line-integral or other models. The simplest iterative methods use on-the-fly computation of forward and backprojection with the same linear-interpolation-based method as is commonly used in FBP. A more flexible approach, which allows more accurate modelling of the physical detection process, is to precompute and store the projection matrices that define this mapping.

Iterative algorithms are based on the attempt to maximize or minimize a target function determined by the particular algorithm used. The target is reached through several analytic processes called iterations. A major advantage of this type of algorithm is the possibility of incorporating different a priori information, such as noise component, attenuation, or characteristics of detector nonuniformity, for more accurate image reconstruction; however, it must be pointed out that inclusion of additional parameters means increase in processing times. Depending on the method, different numbers of iterations are required to reach the target function, keeping in mind that too many iterations can easily lead to noise amplification with image quality deterioration. For this reason, it is important to perform an accurate evaluation of the number of iterations needed to obtain the best image quality.

Data and Image Model

The PET reconstruction problem[1] can be formulated as the following estimation problem: "Find the object distribution $\mathbf{f}$, given (1) a set of measurements $\mathbf{d}$, (2) information (in the form of a matrix $\mathbf{P}$) about the imaging system that produced the measurements, and, possibly, (3) a statistical description of the data and (4) a statistical description of the object (figure 1.15)".

Indeed, under the assumption that the imaging process is linear, the PET reconstruction problem is like any linear inverse problem of the following form:

$$d_i = \int_{R^D} f(\mathbf{x}) p_i(\mathbf{x}) d\mathbf{x} \quad i = 1, ..., I \tag{1.24}$$

where $\mathbf{x}$ is a vector denoting spatial coordinates in the image domain, d_i represents the ith measurement, and $p_i(\mathbf{x})$ is the response of the ith measurement to a source at $\mathbf{x}$. In 2D slice imaging, $D = 2$ and $\mathbf{x} = (x, y)$; in 3D imaging, $D = 3$ and $\mathbf{x} = (x, y, z)$. The point spread function (PSF) $p_i(\mathbf{x})$ can represent the effects of attenuation and all linear sources of blur. A good example of how various effects can be incorporated in the PSF can be found in [28].

[1] like any emission tomography (ET) problem

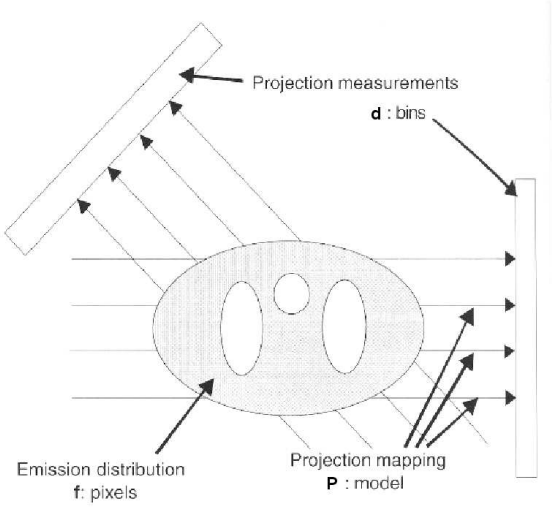

Figure 1.15: A general model of tomographic projection in which the measurements are given by weighted integrals of the emitting object distribution

What distinguishes tomography from other problems described by this linear model is that d_i are projections (organized either in the sinogram or LOR histogram format). In the ideal 2D Radon model on which FBP is based, $p_i(\mathbf{x})$ is a delta function along the LOR described by the detectors in coincidence (L_i), in which case the measurements are simply line integrals of the form $d_i = \int_{L_i} f(\mathbf{x}) d\mathbf{x}$.

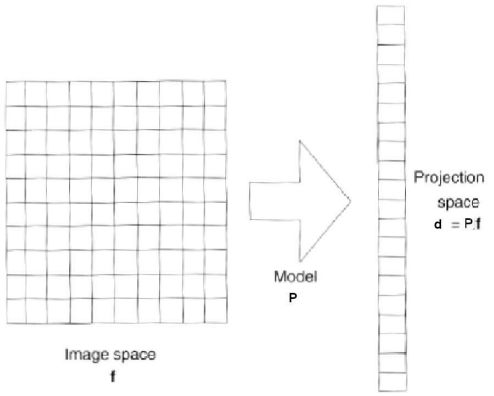

Figure 1.16: A discrete model of the projection process

For computing purposes, the reconstructed image cannot be represented in the continuous domain; instead, a sampled version of the images is estimated

and described in a discrete domain by column vector $\mathbf{f}$ (figure 1.16). Thus, each measurement in equation 1.24 can be approximated by the following system of linear equations:

$$d_i = \mathbf{p}_i^T \mathbf{f} \quad i = 1, ..., I \tag{1.25}$$

which can be summarized by a single matrix equation as follows:

$$\mathbf{d} = \mathbf{P}\mathbf{f} \tag{1.26}$$

Here, $\mathbf{p}_i$ is the ith row of $\mathbf{P}$, and each element of $\mathbf{f}$, denoted by f_j, $j = 1, ..., J$, represents one pixel in the image space. In this general notation, $\mathbf{f}$ may represent either a 2D slice image or a 3D volume image, and complicated imaging systems can be readily represented within this approach by appropriate definition of $\mathbf{P}$. The word pixel refers to elements of the image domain, although it should be understood to encompass the term voxel, which is an element of a volume image. Note that the measurement or projection space is also discrete, with the projection data represented by the vector $\mathbf{d}$. The elements of $\mathbf{d}$ are referred to here as projection bins or simply bins, and every projection measurement is represented by one bin. This bin can belong to the LOR histogram or to the sinogram, depending on the organization of data.

Considering the randomness in the projection data, due to the variability inherent in the photon-counting process used in PET, equation 1.26 should be written as:

$$E[\mathbf{d}] = \mathbf{P}\mathbf{f} \tag{1.27}$$

where $E[]$ denotes the expected value.

Photon emissions are known to obey the Poisson distribution, and photo detections also obey the Poisson distribution, provided that detector dead time can be neglected and that no correction factors have been applied to the data. In this case, the number of events detected in the projection bins are independent of one another. Thus, the probability law for $\mathbf{d}$ is given by:

$$p(\mathbf{d}; \mathbf{f}) = \prod_{i=1}^{I} \frac{\bar{d}_i^{d_i} e^{-\bar{d}_i}}{d_i!} \tag{1.28}$$

where $\bar{d}_i$ is the ith element of $E[\mathbf{d}] = \mathbf{P}\mathbf{f}$:

$$\bar{d}_i = \sum_{j=1}^{J} p_{ij} f_j \tag{1.29}$$

Although is not exact for real imaging systems, the Poisson model is a good description of raw PET data and is the most commonly used model in the PET field. However, other probability models are often used. For example, when a PET imaging system internally corrects for random coincidences by subtracting an estimated randoms contribution, the statistics can be described by a shifted Poisson model [29]. Gaussian models, which are used in cases in which the mean

number of events is reasonably high, are also often used because of their practical advantages.

In writing equation 1.24, it was ignored the fact that the activity distribution in the patient is actually a function of time. This fact is not considered in a static PET study, in which all the counts measured during the imaging session are summed together and used to produce a single static image of the patient. In this case, $f(\mathbf{x})$ in equation 1.24 should be interpreted as the time average of the spatiotemporal activity distribution $f(\mathbf{x}, t)$. Whereas the static study is concerned only with the spatial distribution of the tracer, gated studies and dynamic studies also measure temporal variations of the tracer concentration. In a PET study, there are two types of temporal variations of interest: (1) fluctuations caused by physiological interactions of the tracer with the body and (2) cardiac motion, which helps assess whether the heart is functioning normally. Other temporal variations, including respiratory motion, voluntary patient motion, and the steady decline of activity associated with radioactive decay, are effects to be corrected for, if possible. For time-sequence imaging, as in the case of dynamic or gated studies, the imaging model may be expressed as follows:

$$d_{ik} = \frac{1}{\tau_k} \int_{l_l} dt \int_{R^{D+1}} d\mathbf{x} f(\mathbf{x}, t) p_i(\mathbf{x}, t) \quad i = 1, ..., I; \quad k = 1, ..., K \tag{1.30}$$

where l_k is the time interval of duration τ_k during which the kth frame of the data is acquired.

System Matrix In the equation 1.26, $\mathbf{P}$ is a $I \times J$ matrix called system matrix, which describes the imaging process, and can include attenuation and any linear blurring mechanisms. Each element of $\mathbf{P}$ (denoted by p_{ij}) represents the mean contribution of pixel j in the object to bin i in the projections. It is in the specification of $\mathbf{P}$ that the model of the projection process can become as simple or as complex as we require because the intensity of a projection bin is a weighted sum of intensities of the image pixels. To represent the Radon case, the matrix elements are defined so that a projection bin receives contributions only from pixels that are intersected by a given line and the contributions of pixels that do not intersect the line are set to zero. The linear model can also represent a more realistic case wherein a projection bin receives contributions from many pixels, each weighted according to the relative sensitivity of the projection bin to each pixel. These contributions are affected by physical factors such as attenuation, detector response, and scatter and can be estimated from knowledge of the system design and measurement of the patient attenuation distribution. There are several methods to build the system matrix and they will be summarized in chapter 3. This chapter is dedicated to the creation of the system matrix for a dedicated small animal PET scanner.

General Components and Structure of Iterative Algorithm

Any method for image reconstruction is composed of two related but distinct components. The first component, which is called criterion, is the statistical basis or governing principle for determining which image is to be considered as the best

estimate of the true image. The second component, which it is called algorithm, is the computational technique used to find the solution specified by the criterion. In other words, the criterion is a strategy, and the algorithm is a set of practical steps to implement that strategy.

Most iterative reconstruction algorithms fit the general model shown in figure 1.17. The process is begun with some initial estimate $\mathbf{f^0}$ of the pixel intensity values in the image. A projection step is applied to the current image estimate $\mathbf{f^n}$, which yields a set of projection values $\mathbf{\hat{d}^n}$ that would be expected if $\mathbf{f^n}$ where the true image. The predicted projections $\mathbf{\hat{d}^n}$ are then compared with the actual measured data $\mathbf{d}$ to create a set of projection-space error values $\mathbf{e_d}$. These are mapped back to the image space through a back-projection operation to produce image-space error values $\mathbf{e_f}$ that are used to update the image estimate, which becomes the new estimate $\mathbf{f^{n+1}}$. This process is repeated again and again until the iteration stops automatically or is terminated by the user. Each of the repetition is called iteration. At the conclusion of the process, the current image estimate is considered to be the final solution.

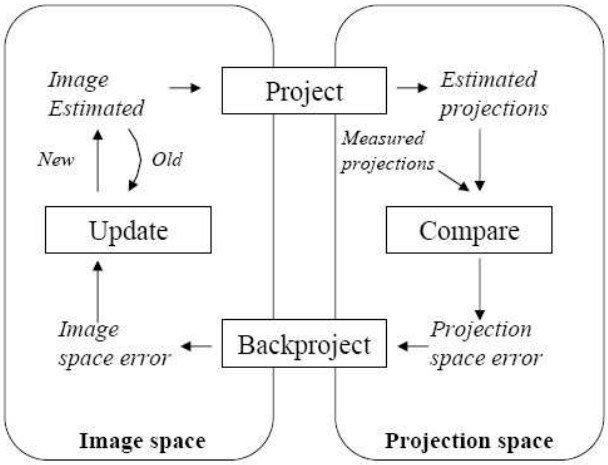

Figure 1.17: Flowchart of a generic iterative reconstruction algorithm

The details of the projection, comparison, backprojection, and update steps have not been specified because, principally, it is in these steps where the individual reconstruction algorithms differ. The power of iterative methods lies in the use of this feedback loop to improve the reconstructed image, in comparison to the FBP that uses only the backprojection portion of the loop and there is no feedback about the image estimate.

The Maximum-Likelihood Expectation-Maximization Algorithm

Numerous iterative algorithms are present in literature, some based on methodologies of numeric linear algebra and others based on statistical approaches. To the latter class belongs the maximum-likelihood expectation maximization (MLEM), which is the standard algorithm and is able to estimate accurately radiotracer distribution. The MLEM is based on the maximization of the loga-

rithm of a Poisson-likelihood target function [17], this is the maximum-likelihood (ML) criterion, and the method uses the expectation maximization algorithm (EM). The attempt is to obtain a reconstructed slice whose forward projection generates a projection dataset almost equal to the original one. When applied to the PET reconstruction problem (or indeed to any linear inversion problem with Poisson noise), the MLEM framework yields the following simple iterative equation, which is easy to implement and understand:

$$f_j^{m+1} = \frac{f_j^m}{\sum_{i=1}^{I} p_{ij}} \sum_{i=1}^{I} p_{ij} \frac{d_i}{\sum_{b=1}^{J} p_{ib} f_b}, \tag{1.31}$$

The main feature of its reconstruction algorithm is to update the image during each iteration by using a multiplicative factor assessed as the ratio between the original acquired projections and the newly estimated ones. Advantages of this iterative method are the fact that all reconstructed values will be positive because a nonnegativity condition is imposed on the original data, the count preservation at each iteration, and the algorithm is simple to implement by a computer. The main disadvantage is the large number of iterations required to converge to an optimal solution and then the long processing times (one or two orders of magnitude more processing time than FBP), hampering its applicability in clinical routine. Another shortcoming of MLEM algorithm is that it provides very noisy reconstructed images. As the iteration process advances, the noise in the image increases. However, one should keep in mind that the MLEM algorithm can perform much better than FBP.

To overcome the problem of slow convergence rate, the ordered-subsets expectation maximization (OSEM) algorithm was proposed in 1994, which is now the most widely used iterative reconstruction method in whole-body PET imaging [18].

The OSEM is a modified version of MLEM (the target is still the maximization of the log-likelihood function) with the main difference being that projections are grouped into subsets having projections uniformly distributed around the volume to be imaged. Within each iteration the target function is updated as many times as the number of subsets, proportionally accelerating convergence. An optimization of subsets and iterations number is required when the method is applied to real, noisy data, because the algorithm can cycle without converging to the MLEM function.

Finally, a few words about spatial resolution achieved with the different reconstruction algorithms. Shift invariant linear imaging systems are often characterized by their PSF. Noiseless data from a point source will produce an image of the PSF so that the measurement of the full-width-at-half-maximum (FWHM) of the PSF is a measure of system resolution. This measurement is useful for images reconstructed using filtered backprojection since the reconstruction procedure is linear. For non-linear estimators, such a ML, the PSF is spatially variant and object dependent. Therefore, the PSF can only be examined locally and with a specific object [30].

1.1.3 Image Degradation and Compensation

Parallax Error

The parallax error results from the uncertainty of the depth of interaction of the gamma rays in the crystal and affects the PET image resolution. The gamma rays travel some (unknown) distance in the crystal (or adjacent crystals) before an interaction occurs. If the source is located near the center of the FOV, gamma rays enter the two detectors at near-normal angle. The depth of interaction does not affect the positioning accuracy of the coincidence LOR defined by the two detectors. When the source is off-center, the gamma rays enter the detectors at an oblique angle that increases with the radial offset of the source. Depending on the DOI, the detector in which the interaction occurs may not be the same detector that initially intercepts the gamma ray. If the design of the detector can identify the depth of interaction, the coincidence LOR can be accurately defined. However, if the detector is not capable of providing DOI information and only assumes a predetermined depth as the interaction point, there is a finite probability that the coincidence LOR is mispositioned. The loss of radial resolution can be seen in figure 1.2 as the source is moved away from the center of the FOV. This parallax error caused by the DOI effect depends on four factors: (a) the radius of the system, (b) the total depth of the detector, (c) the radial offset of the source, and (d) the detector material.

Scatter

When a positron annihilates in the body, there is a reasonable chance that one or both of the annihilation photons will scatter in the body (object scatter) or in the detector itself (detector scatter). At the energy of the annihilation photons (511 keV), the most likely type of interaction is Compton scattering in which the photon transfers some of its energy to loosely bound electrons and deviates form its initial path [31]. Since the coincidence LOR formed after one or both photons undergo Compton scattering is no longer colinear with the site of annihilation (figure 1.1), such events degrade the PET measurement. Scatter results in generally diffuse background counts in reconstructed PET images, reducing contrast and distorting the relationship between image intensity and activity concentration.

The proportion of accepted coincidences which have undergone Compton scattering is referred to as the scatter fraction and its magnitude depends on several factors, including the size and density of the scattering medium, the geometry of the PET scanner and the width of the energy-acceptance window (which is mainly determined by the energy resolution of the detectors). The scatter fraction typically ranges from about 15% in a ring tomograph with slice-defining septa (2D mode) to 40% or more for the same tomograph operated without septa (3D mode), [57], [58].

Although the underlying physics describing Compton scattering of annihilation photons is reasonably complex, there are several characteristics of the resul-

tant LORs which can be exploited to estimate their distribution and potentially correct the measured data. For example:

1. LORs recorded outside the object boundary can only be explained by scatter in the object (assuming that randoms have been subtracted) since LORs arising from unscattered trues must be colinear with the point of annihilation.

2. The scatter distribution is very broad and relatively featureless.

3. The portion of the energy spectrum below the photopeak has a large contribution from scatter events.

4. Scattered coincidences that fall within the photopeak are mainly due to photons that have only scattered once.

These various characteristics have given rise to a wide variety of approaches for estimating and correcting scattered coincidences in PET data. They can be broadly divided into four categories: empirical approaches [61], methods based on two or more energy windows [62] [63], convolution-deconvolution methods [59] [60], and model-based algorithms [64] [65]. The explanation of these approaches are out of the scope of this work and the author refer to the bibliography.

Random Coincidences

As it has been already explained, a PET acquisition consists in the simultaneous detection of two 511 keV photons. Considering the time of flight of the photons, the scintillation time and the processing electronics, it is necessary to accept the events with a time difference. As a consequence, two uncorrelated single detection events occurring sufficiently close together in time can be mistakenly identified as a true coincidence event arising from one annihilation. These are the random coincidences, also known as "accidental" or "chance" coincidences, they are the primary source of background noise and image distortion in a PET scanner.

As it was already mentioned, the fully 3D acquisition also leads to an increase in the axial extent of the random coincidence event FOV relative to the true coincidence FOV, which is even more significant for scanners with larger radial FOVs relative to the end-shield aperture.

Prior to correct for this effect, it is necessary to estimate their contribution. In the following paragraphs, some methods to estimate the random coincidences are presented.

Delayed-Window (DW) Method. In this method, random coincidences are estimated by measuring coincidences within a second time window that is delayed in time (delayed window). The delayed window has the same width as the time coincidence window and is opened after a time interval ΔT, which is much larger than its width. Therefore, it can be assumed that the singles found in the delayed window are uncorrelated with those in the prompt window.

Considering a uniform distribution of random coincidences in time, the number of these uncorrelated events (found in the delayed window) provides an estimation of the number of random coincidences in the prompt window. This method is an approximation as it counts singles that would have contributed to a true coincidence. Therefore it could be inaccurate when the ratio true coincidences to singles is not very small.

This method presents two potential drawbacks. First, the method increases the dead time of the scanner since it is necessary to measure delayed coincidences through dedicated electronics. Second, the estimate is noisy and the noise propagates directly into the data when the randoms are corrected.

Singles-Rate (SR) Method. The randoms rate between two detectors i and j, $\dot{R}_{ij}$, can be estimated using the well-known expression [104], [103], [3], [105]:

$$\dot{R}_{ij} = 2\tau S_i S_j, \tag{1.32}$$

where τ is the coincidence time window and S_i is the singles rate of detector i.

This relation is true provided that the singles rate is much larger than the rate of coincidence events, and that the singles rates are small compared to the reciprocal of the coincidence time window τ, so that deadtime effects can be ignored. This method has the advantage of utilizing high statistics singles measurements, thereby introducing low noise level in the data.

Time Histogram (TH) Fitting Method.

The histogram of the time difference of the prompts presents an almost flat tail [106]. This tail can be fitted to a linear function and it is possible to evaluate the number of double randoms by integrating the fitted function in the range between 0 and τ. The TH method is illustrated in figure 1.18.

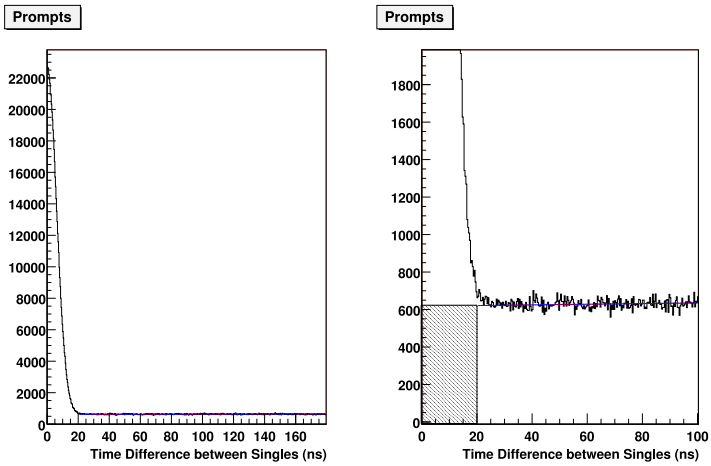

(a) (b)

Figure 1.18: Steps of the time histogram fitting method. (a) Time histogram of the prompts. (b) A zoom of the time histogram to show the integration of the fitted function in the corresponding time interval.

This method allows us to make an overall estimation of the total number of

randoms in the acquisition, but it is not useful for obtaining a random estimate for each LOR or element of the sinogram since there are not enough coincidence events in a single LOR or element of the sinogram for a useful histogram.

Normalization

The lines of response in a PET dataset have different sensitivities for a variety of reasons including variations in detector efficiency, solid angle subtended, summation of neighboring data elements... Information on these variations is required for the reconstruction of quantitative and artifact-free images – indeed, some algorithms require that these variations are removed prior to reconstruction. The process of correcting for these effects is known as normalization, and the individual correction factors for each LOR are referred to as normalization coefficients.

In general, the causes of sensitivity variations are summarized in the following:

- *Summing of adjacent data elements.* It is common practice to sum adjacent data elements in order to simplify reconstruction or to reduce the size of the dataset. This effect is fairly simple to account for, since the degree of summing is always known. However, it can complicate the process of correcting the other effects if the summing is performed prior to normalization.

- *Rotational sampling.* In a rotating system, LORs at the edge of the field of view are sampled just once per half-rotation, while those near the center are sampled many times. As a result, sensitivity falls as radius increases.

- *Detector efficiency variations.* In a detector system, detector elements vary in efficiency because of the position of the element in the block, physical variations in the crystal and light guides, and variations in the gains of the photomultiplier tubes. These variations result in substantial high-frequency non-uniformities in the raw data.

- *Geometric and solid angle effects.* Figure 1.19 shows that in a system with segmented detectors, the volumes that cover the detectors in coincidence close to the edge of the field of view are narrower and more closely spaced than those at the center. The narrowing of the VORs yields in a tighter acceptance angle and in reduced sensitivity, although in the transaxial plane this effect is partially compensated for by the fact that the separation between opposing detectors is less towards the edge of the FOV, so that the acceptance angle increases when the LORs are closer to the FOV border. The narrowing of the VORs also results in reduced sampling distance. However, this effect is easily describable analytically and can be corrected for at reconstruction time, this process is known as “arc-correction”. Arc correction may not be an issue for systems that employ continuous detectors.

  An effect that is relevant for systems employing either continuous or discrete detectors, and that is not so easy to describe analytically, is related to the

angle of incidence of the LOR at the detector face. A photon entering a crystal at angle will usually have more material in its path than one entering normally, thus having an increased probability of interaction. In the case of a ring scanner, this results in measurable changes in sensitivity as the radial position of the LOR is increased and is known as the radial, or tansaxial, geometric effect.

- *Time window alignment.* In order for coincidence detection to work efficiently, timing signals from each detector must be accurately synchronized. Asynchronicity between detector pairs results in an offset and effective shortening of the time window for true and scatter (but not random) coincidences. This, in turn, results in variations in the sensitivity to true and scatter coincidences.

- *Structural alignment.* In a ring tomograph, the accuracy with which the detectors are aligned in the gantry can affect LOR efficiency. Such variations will manifest in different ways depending on the exact design of the tomograph, the detectors, and any casing in which the detectors are contained.

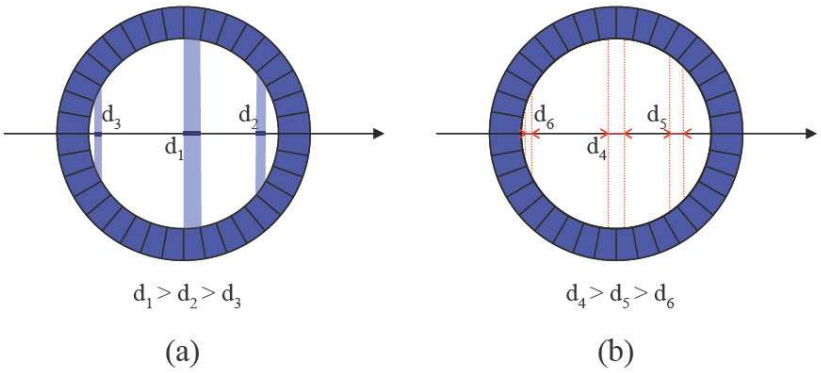

Figure 1.19: (a) The VORs are narrower as the radial distance increases. (b) At the edges of the FOV, the LORs are more closely spaced compared to the ones at the center.

The simplest approach to normalization is to illuminate all possible LORs with a planar or rotating line positron source (usually ^{68}Ge). Once an analytical correction for non-uniform radial illumination has been applied, the normalization coefficients are assumed to be proportional to the inverse of the counts in each LOR. This process is known as "direct normalization" [66]. Problems with this approach include:

1. In order to obtain adequate statistical quality in the normalization dataset, scan times are long; typically several hours.

2. The used sources must have a very uniform activity concentration or the resultant normalization coefficients will be biased.

To reduce normalization scan times, variance-reduction techniques can be applied. However, in order to implement these, the normalization coefficients must be factored into a series of components, each reflecting a particular source of sensitivity variation (described above). This approach is known as component-based model for normalization. A drawback of this approach is that the accuracy of the normalization is dependent on the accuracy of the model used to describe the tomograph. However, it has the advantage that a more intelligent treatment of the different properties of scattered and true coincidences is possible, which can be very helpful in 3D imaging.

Although the plane sources have been suggested as the ideal geometry for PET normalization [131], [134], the sources which have been used for normalizing 3D PET systems are:

- Plane source using ^{68}Ge in [134]
- Uniform 20 cm diameter cylinder, usually containing ^{68}Ge in [135]
- ^{68}Ge transmission scanning rod sources in 2D used in [133]
- ^{68}Ge transmission scanning rod sources in 3D used in [136]
- a line source of ^{68}Ge which oscillates across the transaxial field of view, emulating a plane source [138]

When the normalizaton is acquired with transmission ring or rod sources, one concern is that the location of the sources relative to the detectors are very different to that when imaging an object in the centre of the tomograph (this applied to both 2D and 3D acquisitions). But, little difference is observed between rod sources and a uniform cylinder. It is clear that using a uniform cylinder for the normalization data will include a significant amount of scatter in this measurement; what is not clear, however, is whether this is a good thing or not. Scatter in the measurement means that the energy spectra from the detectors will be similar to that from a subject having a scan. The consequences of a large number of scattered coincidences being recorded in the normalization data has not been studied in great detail.

Attenuation

Attenuation is the loss of true events due to scatter and absorption and its correction is the most important correction in clinical PET. The attenuation factor can be as high as 45 for a 40 cm diameter man and 7 for the human brain, but only 1.6 for a rat and 1.25 for a mouse, which is still non negligible if absolute quantification of the radiotracer concentration is required [67]. However, one of the most attractive features of PET is the relative ease of applying accurate and precise corrections for attenuation, based on the fact that attenuation depends only on the total thickness of the attenuation medium.

The most obvious effect of attenuation is the overall loss of counts. The result is increased noise and inaccurate quantitation of radioactivity distributions. Although the noise effects cannot be remedied, quantitative accuracy can be recovered with attenuation correction.

Another effect of attenuation correction is to introduce nonuniformities into reconstructed images. For example, radiation emitted from the middle of the body is more likely attenuated than radiation emitted near the edge. The resulting images will, therefore, show artificially depleted radioactivity deeper in the body. On the contrary, the outer contour of the body shows an artificially high amount of radioactivity because of the radiation emitted tangentially to the outer body contour is not attenuated.

A coincidence event requires the simultaneous detection of both photons arising from the annihilation of the positron. If a photon is either absorbed within the body or scattered out of the field of view, a coincidence will not occur. The probability of detection, therefore, depends on the combined path of both photons. Since the total path length is the same for all such sources lying on the line that joins two detectors, the probability of attenuation is the same for all such a sources, independent of source position (see figure 1.20). Therefore, the problem of correcting for photon attenuation in the body is that of determining the probability of attenuation for all sources lying along a particular line of response.

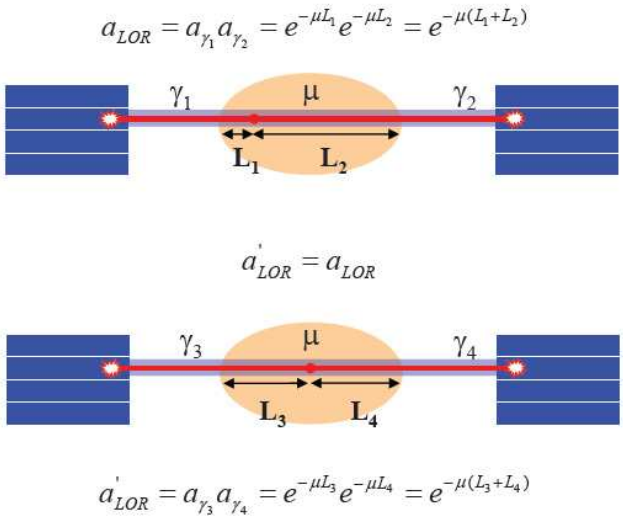

Figure 1.20: Attenuation of annihilation γ-rays depends only on the total thickness ($L=L_1+L_2=L_3+L_4$) of the absorber, that is, it is independent of the position of the source relative to the absorber.

To assess the probability of attenuation is necessary to implement transmissive acquisitions to estimate the attenuation factors. Transmission measurements are routinely performed in PET to correct for attenuation of the annihilation photons within the body. These measurements can be performed using several different source and detector configurations. Actually, available scanners use two different kinds of transmission sources:

1. ^{68}Ge, which is a β^+-emitter and the transmission data are collected as coincidence events [68], [69].

2. ^{137}Cs, in this case the source is a γ-emitter of 662 keV and the transmission data are collected using single events. When using this source, an additional step is necessary in order to account for energy difference (662 vs. 511 keV) [70].

In the case of PET/CT scanners, the measurement of transmission data is performed using the CT examination. The resulting data are taken at an energy that is very different from 511 keV, so the data must be scaled to use for the attenuation correction of the emission data.

Dead Time Correction

In general, PET scanners have a finite deadtime and associated count losses. The deadtime is the length of time required for a counting system to fully process and record an event, during which additional events cannot be recorded. As a result, the measured count rate is systematically lower than the actual count rate. Such count losses are significant, however, only at "high" count rates (i.e., greater than the inverse deadtime expressed in seconds). For multi-detector ring PET systems, deadtime count losses are generally minimal at clinical administered activities. Nonetheless, a real-time correction for deadtime count losses is routinely applied to the measured count rates. Most commonly, this is performed by scaling up the measurement count rate, either per LOR or globally, based on an empirically derived mathematical relationship between measured and true count rates.

Compensation for image degradation phenomena

Once the values for correcting the above mentioned degradation factors have been estimated using one of the methods described above, the estimated values are usually subtracted or multiplied to the prompts. In many clinical implementations, the prompts are pre-corrected prior to the reconstruction step. The pre-correction of the data is necessary when the analytical reconstruction methods are used. Nevertheless, when working in the iterative framework, it is possible and recommended to reconstruct directly the prompts data introducing the corrections within the reconstruction algorithm. In the iterative framework, the statistical model of the emitted and detected data obeys the Poisson distribution. When correction factors are applied to the raw data, this assumption is no longer valid. For example, in the case of random coincidences correction, the subtraction technique can be problematic and can reduce the accuracy of the image reconstruction, as discussed in [112]. The reason of the reduction in accuracy is that the iterative algorithms which have been developed using pre-corrected data (described by a shifted Poisson model [29]) are approximate in nature.

The expression of the MLEM algorithm with the relevant corrections included [112] is the following:

$$f_j^{m+1} = \frac{f_j^m}{\sum_{i=1}^{I} \epsilon_i a_i p_{ij}} \sum_{i=1}^{I} \epsilon_i a_i p_{ij} \frac{d_i}{\sum_{b=1}^{J} \epsilon_i a_i p_{ib} f_b + s_i + d_{r,i}}, \tag{1.33}$$

where

$$d_i(f) = d_{t,i} + s_i + d_{r,i} = \sum_{j=1}^{J} \epsilon_i a_i p_{ij} f_j + s_i + d_{r,i}. \tag{1.34}$$

Considering that the data are organized as a LOR histogram and the index i counts for the LORs, $d_{t,i}$ is the number of true coincidences at i, s_i refers to the number of scatter coincidences i, $d_{r,i}$ represents the random coincidences i, p_{ij} is the element of the system matrix corresponding to LOR i and voxel j, and f_j is the value of the voxel j at the image. The normalization (ϵ_i) and the attenuation (a_i) correction are multiplicative and they appear multiplying the elements of the system matrix p_{ij}. The variables I and J correspond to the total number of LORs and the total number of voxels, respectively.

1.1.4 Image Quality

The ability to obtain images that help achieve a desired goal is the way to test an image reconstruction algorithm, a correction method or to validate the use of an specific system matrix. Therefore, the image evaluation is called task-based assessment. For example, if the task is quantitative, such a measurement of tracer concentration in a given image region, then the reconstruction algorithm, correction method or system matrix should be judged by its quantitative accuracy. Lesion detectability is another interesting task for our case and is one of the major application of PET, then an algorithm, correction method or system matrix is considered to perform well if it produces images that lead to accurate diagnosis. Finally, if the task requires the ability to visualize small objects, the spatial resolution would be the corresponding metric.

The following figures-of-merit (FOM) were employed in this work to quantify the quality of the reconstructed images, keeping in mind quantitative, lesion detectability, and visibility of small details tasks:

1. Root Mean Square Error: A comparison between the emitted source and the reconstructed image was performed using the root mean square error (ϵ_{rms}) defined as:

$$\epsilon_{rms} = \left[\frac{1}{M} \sum_{m=0}^{M} (f_m^{(k)} - f_m)^2 \right]^{\frac{1}{2}} \tag{1.35}$$

   where M is the total number of voxels, m is the voxel number, $f_m^{(k)}$ and f_m are the counts in the reconstructed image at k iteration and the number of photon pairs emitted in the voxel m, respectively. Both are normalized to the average voxel value.

2. Spatial Resolution: The full width at half maximum (FWHM) and full width at tenth maximum (FWTM) of the radial and tangential profiles of a point source were determined by linear interpolation.

3. Discrepancy: The activity within a region of interest (ROI) was obtained by summing the voxels in the ROI in the reconstructed images. The activity found for this ROI in the reconstructed image (A_{ROI}), was compared with the activity within the ROI in a reference image (A^{ref}_{ROI}). The discrepancy (D) was calculated as

$$D(\%) = 100\frac{A_{ROI} - A^{ref}_{ROI}}{A^{ref}_{ROI}}, \tag{1.36}$$

4. Mispositioned Events (ME): The number of events found within a ROI, where there should be no activity, were counted and divided by the total reconstructed counts in the image

$$ME(\%) = 100\frac{Events_{NoAct-ROI}}{Events_{all}}. \tag{1.37}$$

The ideal ME value would be zero.

5. Signal-to-Noise Ratio (SNR): This is given by

$$SNR = \frac{|\mu_{ROI_1} - \mu_{ROI_2}|}{\sigma_{ROI_2}}, \tag{1.38}$$

where μ_{ROI_1} and μ_{ROI_2} are the averages of the reconstructed voxels within two ROIs defined on the image, and σ_{ROI_2} is the standard deviation of the voxels of second ROI.

6. Background Noise ($\bar{\sigma}_{bkg}$): This is the normalized standard deviation of the voxel values within a background ROI (standard deviation divided by the average).

7. Contrast Recovery Coefficient (CRC): This is the value of the contrast between two ROIs normalized to the expected value for the contrast, C_{ideal}:

$$CRC = 100\frac{\frac{\mu_{ROI_1}}{\mu_{ROI_2}} - 1}{\frac{a_{ROI_1}}{a_{ROI_2}} - 1}, \tag{1.39}$$

where a_{ROI_1} and a_{ROI_2} are the activity concentration in the first and second ROIs respectively (see figure 1.21).

1.1.5 Monte Carlo Simulations

Monte Carlo (MC) methods are numerical calculation methods based on random variable sampling. The technique of random sampling to solve mathematical problems has been known since 1770. Only with the advent of quantum mechanics in which matter-radiation interactions were interpreted using cross sections as

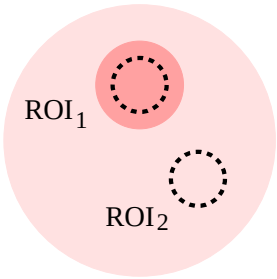

Figure 1.21: Example of ROI definition in a phantom that consists of a background area and inside of it a hot region. The ROI_1 and ROI_2 are drawn in the areas under study of the phantom.

probabilities, the random sampling technique [2] was applied to nuclear physics. In the early 1960s, the Monte Carlo method was used by H.O. Anger to simulate the physical response of his new scintillator camera. Since then, thanks to the possibility of modelling different physical processes independently, the method has been applied in medical radiation physics to a wide range of problems that could not be easily addressed using experimental or analytical approaches. Nuclear Medicine Imaging, that deals with radioactive decay, the emission of radiation energy through photons and particles, and the detection of these quanta and particles in various materials, can benefit from the MC method. The simulation of the above mentioned processes based on the MC method are known as Monte Carlo simulations.

In Nuclear Medicine and particularly in Single Photon Emission Computed Tomography (SPECT) and PET, the use of Monte Carlo methods has the advantage of using general purpose codes developed for high energy physics or dosimetry. High-energy processes (>1 MeV), secondary and low-energy radiations could be neglected as they were not involved in SPECT and PET. On the other hand, the similarity of physical and geometrical characteristics of most emission tomographs suggested specific models to be developed, thus favouring the creation of codes dedicated to simulations of emission tomography configurations.

Several SPECT/PET dedicated Monte Carlo software packages were developed for simulating a variety of emission tomography studies. Among them, public domain codes have been made available in last years, allowing the use of the Monte Carlo method by the whole scientific community and even in the clinical environment. Several topics were addressed by Monte Carlo simulations in both PET and SPECT, among which optimisation of imaging system design (including detector, collimator, and shield design), development of correction methods for improved image quantitation, evaluation of correction techniques (scatter/randoms/attenuation correction, partial volume effect), development and assessment of image reconstruction algorithms, receiver operating characteristic studies [3], pharmaco-kinetic modelling. Two types of Monte Carlo codes can be

[2] named "Monte Carlo method" because the Monte Carlo casino was the most famous centre for playing games involving random drawing.

[3] This analysis is done to assess how well the medical images allow a human observer to

Table 1.3: Main Monte Carlo codes currently available for SPECT and PET simulations

Generic Codes	
	EGS4 (radiation dosimetry) [32] MCNP (radiation dosimetry) [33] ITS (high energy physics) [34] GEANT 3 (high energy physics) [35] GEANT 4 (high energy physics) [36]
Dedicated codes	
SPECT only:	SIMIND [37] SimSPECT (derived from MCNP) [38] [39] MCMATV [40] [41]
PET only:	PETSIM [42] [43] EIDOLON [44] Reilhac [45] PET-EGS [46]
SPECT and PET:	SIMSET [47] [48]
Dedicated based on Generic codes:	
SPECT and PET:	GATE (based on GEANT 4) [49] [50]

used for simulating SPECT and PET: 1)general purpose code, which simulate particle transportation and were developed for high energy physics or for dosimetry, 2)dedicated codes, designed specifically for SPECT or PET simulations. Table 1.3 summarises the main codes currently available. General-purpose packages include well-validated physics models, geometry modelling tools and efficient visualization utilities. However, it is quite difficult to tailor these packages to PET and SPECT. On the other hand, the dedicated Monte Carlo codes developed for PET and SPECT suffer from a variety of drawbacks and limitations in terms of validation, accuracy and support.

All Monte Carlo codes share some common components, such as random number generator, rules to sample probability distributions, and sets of probability density functions. The features that make the codes different are related to the accuracy, flexibility, efficiency and ease to use of the codes.

One of the limitations is that because the results are based on a computer model, the accuracy of the results will depend on the accuracy of the model. The question one should always ask is whether the model includes all the factors one would expect to affect the measurement in real situations (normalization correction, decay time).

A major advantage of simulations in nuclear medicine imaging is that they allow studies of parameters that are not measurable in practice (for example,

perform the specified task. The study plots the trade-off of false-positive and true-positive for an observer.

random coincidences in our case). In addition, in a computer model it is possible to turn off certain effects, such as photon attenuation and scattering in the phantom.

Another fundamental requirement in MC simulations is access to random numbers. In theory, a random number cannot be predicted or calculated. Despite this, the most common approach in computer simulations is to use a computer program to obtain randomly distributed numbers. These pseudo-random numbers are calculated from previous numbers, which implies that there must be a original number (seed) to initiate the random number sequence. Thus, starting two simulations with the same initial value will in the end produce the same result, even through random numbers are involved. Furthermore, because simulations are performed on digital machines that use numbers limited to a known range (2, bytes, 4 bytes, 8 bytes, etc.), there is always a chance that a random number sampled during the simulation will be equal to the initial value. The result will then be a repetition of the random number sequence, which may have serious consequences for the accuracy of the results. Therefore, for Monte Carlo simulations, it is crucial that the generators have good randomness properties. This is particularly important for large-scale simulations done on high-performance parallel computers.

GATE

GATE, the Geant4 Application for Tomographic Emission, is a Monte Carlo simulator that combines the advantages of the general-purpose Geant4 simulation code [52] and of specific software tool implementations dedicated to emission tomography. Indeed, GATE takes the advantage of the well-validated physics models, of the geometry description, and of the visualisation and 3D rendering tools offered by Geant4. Furthermore, GATE integrates specific components to facilitate its use in the PET/SPECT domain.

One distinctive and original feature of GATE is the modelling of time-dependent processes; synchronized with the evolution of the source activities and spatial distributions [53]. Moreover, GATE includes a coherent management of parallel multiple sources with independent time-profiles and locations.

The code comprises a large number of software components allowing it to model various aspects of nuclear medicine experiments: geometry, movement, detection, data output, etc. Users can choose among these components and assemble them interactively to set up simulations according to their own requirements by using a scripting language. In addition, the users may specify any number of radioactive sources with different propierties (radioisotope, position, activity), which may overlap each other, as well as the detector geometry (for example, natural radioactivity of the lutetium). GATE computes the full gamma tracking from the vertex point to the end of the gamma range in the experimental area with Compton scattering, Rayleigh diffusion, and photoelectric effects. A number of modules are available for modelling the detection process, going from the detection of the gamma-rays by the scintillating crystals (singles) to the de-

tection of coincidences in PET. Random events are tagged and may be processed independently from the true coincidences. Scattering events in detector or in phantom can be tracked and stored in a list mode file output.

LHC Computing Grid Project

Although variance reduction techniques have been developed to reduce computation time, the main drawback of the Monte Carlo method is that it is extremely time-consuming. For example, one needs to track hundreds of millions of particles to obtain the statistics required for image reconstruction studies. Consequently, a large amount of CPU time (weeks or even months) may be required to obtain useful simulated data sets. As distributed or parallel computers are becoming increasingly accessible to computational scientists, problems that may otherwise be computationally prohibitive can be performed much faster than with a scalar machine. Additionally, among all simulation techniques of physical processes, the Monte Carlo method is probably the most suitable one for parallel or distributed computing since photon histories are completely independent from each others.

The LHC Computing Grid Project (LCG) was born to prepare the computing infrastructure for the simulation, processing and analysis of the data of the Large Hadron Collider (LHC) experiments [54]. The LHC, which has been constructed at the European Laboratory for Particle Physics (CERN), is the world's largest and most powerful particle accelerator. The case of the LHC experiments illustrates well the motivation behind Grid technology. The LHC accelerator started operation in September 2008, and the experiments that will use it (ALICE, ATLAS, CMS and LHCb) will generate enormous amounts of data. The processing of this data will require large computational and storage resources and the associated human resources for operation and support. It was not considered feasible to fund all of the resources at one site, and so it was agreed that the LCG computing service would be implemented as a geographically distributed Computational Data Grid. This means that the service will use computing and storage resources, installed at a large number of computing sites in many different countries, interconnected by fast networks. LCG-2 Grid middleware will hide much of the complexity of this environment from the user, giving the impression that all of these resources are available in a coherent virtual computer centre. The users of a Grid infrastructure are divided into Virtual Organisations (VO), abstract entities grouping users, institutions and resources in the same administrative domain. The LCG-2 VOs correspond to real organisations or projects, such as the four LHC experiments; other VOs exist in the context of EGEE, like the community of biomedical researchers, etc.

There is a Grid facility at the IFIC (Instituto de Física Corpuscular) consequence of a cooperation between the University of Valencia and CSIC (Consejo Superior de Investigaciones Cientficas). Two VOs are using this facility, the ATLAS project and the IFIC. The IFIC VO is meant for researchers at IFIC that want to use the Grid resources. At the IFIC, there are 192 PCs connected with a fast Ethernet. Each PC is a AMD Athlon of 1.2/1.4 GHz with 1 GByte SDRAM

and a harddrive UDMA100 of 40 GByte. Through a collaboration between the IFIC and the Klinikum rechts der Isar, we have been able to employ the computational resources of this facility to run distributed Monte Carlo simulations.

1.2 Why small animal PET scanners?

Many of the traditional medical imaging technologies, including PET, are being adapted for use in small laboratory animal imaging. PET can be viewed as an in vivo counterpart to autoradiography, tissue detection and other techniques that involve imaging or counting excised tissue samples taken from animals into which a radioactively labeled tracer has been introduced prior to sacrifice. The advantage of a non invasive imaging technique such as PET is that the entire time course of the biodistribution or a radiolabeled tracer can be determined in a single living animal. Furthermore, that animal can be studied again at a later time, permitting longitudinal, within-subject study designs to follow disease models and interventions over periods of days, weeks, and even months. Because the same animal is used at every time point, each animal serves as its own control and variability due to interanimal differences is effectively removed. Therefore, a single animal studied multiple times by PET may in some instances provide the same data that would have required tens of animals using traditional invasive techniques that requires sacrifice of the animal. This clearly is in keeping with the desire to reduce the number of laboratory animals used in experiments, but equally important, it has the potential to dramatically reduce the cost of experiments and to speed up the availability of results. It may also improve the quality of the data (because of the within-subject design), although this has yet to be unequivocally demonstrated.

A large number of positron-labeled compounds have been synthetized [8] thus enabling a wide range of biological processes to be measured quantitatively, noninvasively and repeatedly using PET [9]. Combined with the very high sensitivity of radiotracer methods, this flexibility to interrogate living biological systems at the level of specific enzymes, proteins, receptors, and genes makes PET extremely attractive for studies in laboratory animals.

A final important advantage of using medical imaging techniques such as PET in small animal models of disease is that imaging provides a bridge between the animal model and human studies. A valid concern in the use of animal models relates to how well that model predicts what will happen in the human. Techniques such as PET provide the opportunity to perform exactly the same experiments in mouse and human, facilitating direct comparison and appropriate interpretation of the animal model data.

1.3 Challenges of small animal PET

Challenges common to all imaging techniques include (a) the design of probes or probing techniques that are highly specific to the biological processes of interest,

(b) optimization of imaging systems to provide the highest sensitivity and image resolution, and (c) minimization of perturbation to the biological processes under observation so that the experimental outcomes correlate to the biology and not the probing process. There are a number of issues that must be carefully considered in animal PET studies. Some of these have much in common with designing and optimizing PET scanners for human imaging; others are problems specific to small animal imaging. The underlying challenge, as always, is to obtain as many counts as possible and to localize these counts as accurately as possible. Accurate localization of counts depends primarily on the spatial resolution of the detectors and the ability to remove or correct phenomena such as scatter, accidental coincidences, and pile-up that are incorrectly positioned. Maximizing the number of detected counts requires injection of the maximum radioactivity possible based on mass and specific activity considerations, and using an imaging system with high-efficiency detectors and large solid-angle coverage. The system must be able to run at high counting rates so that no counts are lost due to dead time and it must also have a narrow timing window to minimize accidental coincidences. The first challenge to PET imaging technology clearly comes from the vast difference in physical size between the subject for which clinical PET systems have been developed, the human (weight ∼70 kg), and the laboratory rat (weight ∼300 g). This represents more than 200 fold decrease in volume. Laboratory mice, at 30 g, account for another order of magnitude decrease in volume. Therefore to achieve similar image quality and to address the same biological questions in mice that can currently be studied in humans, PET system must be developed with similar improvements in spatial resolution. This suggest a reconstructed spatial resolution <1 mm in all directions (<1 μl in volume) as opposed to the ∼10 mm (∼1 ml in volume) reconstructed image resolution typical in human whole body studies. This stringent requirement calls for new approaches in both detector materials and design.

The absolute detection sensitivity of the imaging instrument (the fraction of radioactive decays that result in a detected event) must be at least as good, and preferably much better than, the typical PET scanner. Whole-body human PET scanners detect on the order of 0.3-0.6% of the coincident annihilation photons in two-dimensional mode and 2-4% in 3D acquisition mode [10], [11]. For sensitivity it is clearly not possible to use the previous argument. Even with perfectly efficient detectors and complete solid angle coverage around the animal, the best we can hope to achieve is about 200-fold increase in 2D mode and 30-fold increase in 3D mode. An approach to compensate for the sensitivity problem is to use more sophisticated reconstruction algorithms that make better use of the available counts. Iterative algorithms that accurately model the physics of the scanner and the statistics of the raw data will probably play an important role in very-high-resolution PET studies because they can produce improvements in either resolution or signal-to-noise relative to analytic reconstruction algorithms. Another approach can be to inject larger amounts of radioactivity, but there are some fundamental issues that limit how far the dose can be raised and we will discuss them below. One might be tempted to think that because laboratory

animals are not subject to the same radiation exposure rules and procedures applicable to humans, the injected activity per gram of tissue could be adjusted upward, thereby increasing the detected counts per resolution element and overcoming some of the sensitivity challenges outlined above. However, the whole idea of a tracer kinetic experiment is that the mass levels are sufficiently low so as not to perturb the biological system under study. For a given specific activity of radiotracer [0], the injected mass is linearly proportional to the injected activity. There are many circumstances in which the tracer mass will limit the amount of radioactivity that can be injected into a mouse in the range of 0.037 to 3.7 MBq [16]. The amount of mass that can be injected without violating tracer principles must be carefully determined on a case by case basis. There are cases in which relatively large amounts of radioactivity can be injected into an animal, in these cases dead time and count rate performance may become the limiting factor. Other factors, such as energy resolution, dead time characteristics, the ability to perform attenuation correction, and imaging field of view, pose different constraints to the design of detector and system and need to be taken into consideration.

The accuracy of the biological models derived from animal PET experiments depends on the quantitative accuracy of imaging. PET data needs to be corrected, notably for normalization, attenuation, scatter, and dead time, to achieve quantitative images. The implementation of these correction techniques can be affected by the choices of the system design. Compromises in performance characteristics are often necessary, and should consider the targeted applications of the system, the availability and cost of technologies, and the ease and cost operation.

1.4 Overview of this work

The following work has been dedicated to a specific small animall PET called MADPET-II, developed at the Klinikum rechts der Isar in Munich. Unique features of MADPET-II are the crystals distribution in two radial layers and the individual crystal read out by an avalanche photodiode. Chapter 2 discusses at length the design and main features of this scanner. MADPET-II performance allows us to obtain high sensitivity preserving high spatial resolution. High sensitivity is achieved by using a FOV as large as the inner diameter of the scanner, reducing the low energy threshold (LET) and introducing triple events. At the same time, high spatial resolution is obtained providing DOI and reconstructing images with LOR-based 3D iterative techniques (MLEM) with a Monte Carlo system matrix. Two chapters of this thesis are reserved to study in more detail two of the above mentioned elements, the generation of the Monte Carlo system matrix (chapter 3) and the introduction of the triple events (chapter 5).

In general, small animal PET scanners are aimed at radiopharmaceutical stud-

[0] the fraction of the molecules in the tracer solution which are radiolabeled at a given time and it is expressed in units Bq/g becquerels per gram or, more commonly, in concentration units of Bq/mol becquerels per mole

ies. For these studies, it is very important that the reconstructed images provide quantitative information about the activity within the subject under study. Several corrections must be taken into account in order to obtain realistic estimates of the activity distribution. Among the latter, this thesis has focused in the random coincidence correction (chapter 4) and normalization (chapter 6).

All the chapters of this thesis have a common denominator which is the use of simulations based on Monte Carlo techniques. We have taken advantage from the benefits of the Monte Carlo method and suffered its limitations. First of all, we are able to simulate a scanner which is very complex due to the dual layer configuration. Another advantage of the Monte Carlo technique is that it allows studies of effects that depend on parameters that are not measurable in practice. For example, we could test the validity of the random coincidences estimation methods using the information related with the annihilation that is provided by the simulation toolkit. In addition, in a computer model it is possible to switch on and off certain effects according to the focus of interest. For example, the scatter and attenuation inside the object was left aside when investigating the random coincidences to focus on the detector and system effects. For the normalization study, we need a realistic simulation of the source and thus, we simulate the source within the container, including the attenuation and scatter within the object, and as well, the decay of the activity. An important limitation of the Monte Carlo technique is the computing time required for the simulations. We have partially solved this problem by using the symmetries of the scanner and the distributed computers at the Grid facility in IFIC.

After the description chapter of the MADPET-II scanner, the outline of this work is as follows:

- Chapter 3 presents the creation of the Monte Carlo system matrix.
- Chapter 4 investigates the random coincidences correction.
- Chapter 5 includes the triple events for generating the images.
- Chapter 6 studies different approaches of normalization.

At the end of each chapter the conclusions are explained in English. The last chapter summarizes the main conclusions in Spanish.

Chapter 2

MADPET-II

2.1 Objectives of the system

MADPET-II is a small animal scanner for radiopharmaceutical studies. The concept and design of MADPET-II improves both spatial resolution and sensitivity compared with conventional technology. These goals are achieved by modifying traditional detector designs that may degrade the performance of the imaging device:

- Individual crystal readout in contrast to block detector. Block detectors are replaced by individual crystal readout to avoid either event mispositioning (affecting spatial resolution) or count losses (reducing sensitivity) due to pile-up effects if multiple scintillation pulses are incident within a short time [71]. The event mispositioning or count losses may result when using block detector, since every photodetector in a block reads the scintillation light from many crystals, more important at high incident gamma ray flux. Additionally, with its individual crystal readout, the system can differentiate those photons depositing some energy in a single crystal from those undergoing interactions in more than one unit (inter-crystal scatter, ICS). Block detectors assign to such ICS photon the LOR resulting from the weighted average over all the energy depositions within a block. This mispositioning of the coincidence may lead to a resolution degradation. On the contrary, MADPET-II can distinguish and, if desired, disregard ICS coincidences. However, the contribution of ICS events to the sensitivity can be significant and the degradation of spatial resolution due to the ICS events can be solved by using an algorithm to identify the primary LOR.

- Crystals in dual-layer arrangement as compared to one layer. As it was explained in the introduction (see section 1.1.1) shorter crystals provide better DOI information, thus better spatial resolution. On the contrary, the sensitivity is reduced for these crystals. To achieve high spatial resolution it is necessary to use small crystals and to compensate for the decrease of sensitivity a second layer of crystals is included. The two radial layers offer the advantage of quantified, "binary" DOI information. Therefore,

the dual-layer configuration fulfil at once the requirements of high spatial resolution and high sensitivity.

- Singles list-mode acquisition unlike acquired data in sinogram format or coincidence events in list-mode. The singles list-mode acquisition provides a tremendous amount of flexibility in generating images, because all the parameters of interest can now be adjusted post-acquisition in software [73]. Consequently, several images with different applied lower energy thresholds or coincidence timing windows can be generated from a single data set acquired in a single scan. It is also possible to use intelligent algorithms in the coincidence sorting stage that will decide to include or reject certain types of coincidence events based on user-defined criteria such as high resolution or high sensitivity.

2.2 System Description

Front-end architecture

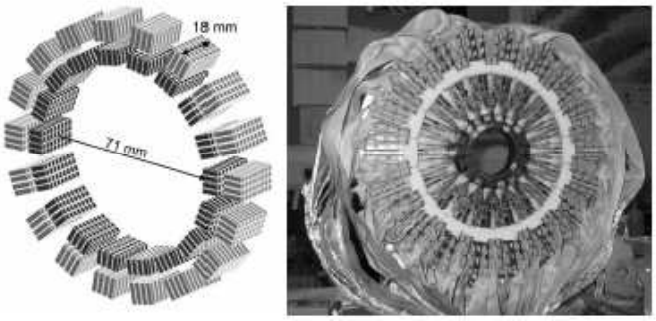

Figure 2.1: Crystal distribution of the MADPET-II scanner as reproduced by Monte Carlo simulations (left) and the arrangement of the 18 dual layer detector modules in the complete system (right).

MADPET-II consists of 18 dual layer detector modules arranged in a ring (see figure 2.1). The axial and radial extent of the tomograph is 18.1 and 71 mm respectively, allowing for mouse and rat imaging. Each detector module consists of two layers: Front and back. For each dual layer detector module, the front layer contains a 4×8 array of 2×2×6 mm LSO crystals, each optically isolated (using a 3M Radiant foil) and coupled one-to-one to a monolithic 4×8 avalanche photodiode (APD) array (Hamamatsu), shown in figure 2.2. The back layer is read out independently, and is similar to the front layer, apart from the radial size of the LSO crystals, which is 8 mm in this case. The APD pixel sensitive area is 1.6×1.6 mm^2 and the interspacing between units is 0.3 mm. The coupling between each

individual crystal and the corresponding photodetector was achieved by means of UV cured optical adhesive (DELO photobond, Germany) with a refractive index of 1.6. The complete scanner has 1152 individual crystals, each read out by its own independent electronic channel. Therefore, the system consists of 1152 fully independent electronic channels. The energy and time resolution of the current system are 21% at 511 keV [72] and 10 ns at a single channel [113], respectively.

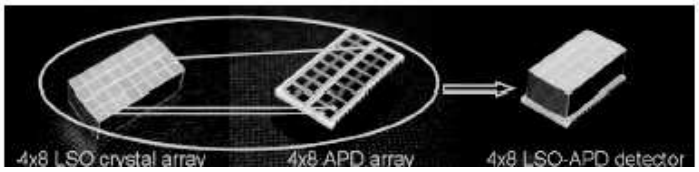

Figure 2.2: Photo of the 4 × 8 LSO array (left), the 4 × 8 APD array (center) and the one-to-one coupled detector array (right).

Pre-processing and data acquisition

The front-end signals are transferred via approximately 5 m long differential lines to the processing electronics which are placed remotely in order to avoid interference with the detectors. Pre-processing of analog signals from the resulting 1152 individual channels is performed using 72, 16-channel low noise Charge Sensitive Preamplifiers (CSPs) followed by differential line drivers, both implemented in Application Specific Integrated Circuits (ASICs) using JFET/CMOS technology [75].

The data acquisition system has been developed at the Technical University, Munich (TUM), in collaboration with Mixed-Mode GmbH (Munich, Germany), to read out signals from MADPET-II [72]. As it was already mentioned, the system features individual crystal readout, therefore no use of light sharing, signal multiplexing or any type of data reduction is performed. To achieve the goal of processing signals from 1152 channels independently, an ASIC containing the analog signal processing electronics has been developed and is mounted on a board (referred to hereafter as "PET board"). This ASIC was designed for time and energy discrimination and more detailed description of it can be found in [113] and [74]. The digitization of the analogue signals is done under Field Programmable Gate Arrays (FPGAs) control by analogue to digital converters (ADCs) and time to digital converters (TDCs) mounted on the PET boards for the extraction of the digital pulse height (energy) and time information respectively. After all the complete electronic path from the front-end, 2x32 bit words are written to disk in list-mode format with information about time stamp, energy and channel number for each single event. The coincidences are sorted post-acquisition in software.

Identification of Coincidences

Emulating the measurements performed with MADPET-II, each simulation produces an output file listing the detected singles and coincidences are sorted after acquisition according to the detection time [73]. Unlike the measurements, more information about the single event than time, energy and channel number is available in the simulation files. The sorting starts with the first single of the list which opens the first time coincidence window (prompt window), where τ is the window width. Then, the number of singles within τ is determined. This procedure is repeated until the end of the singles list.

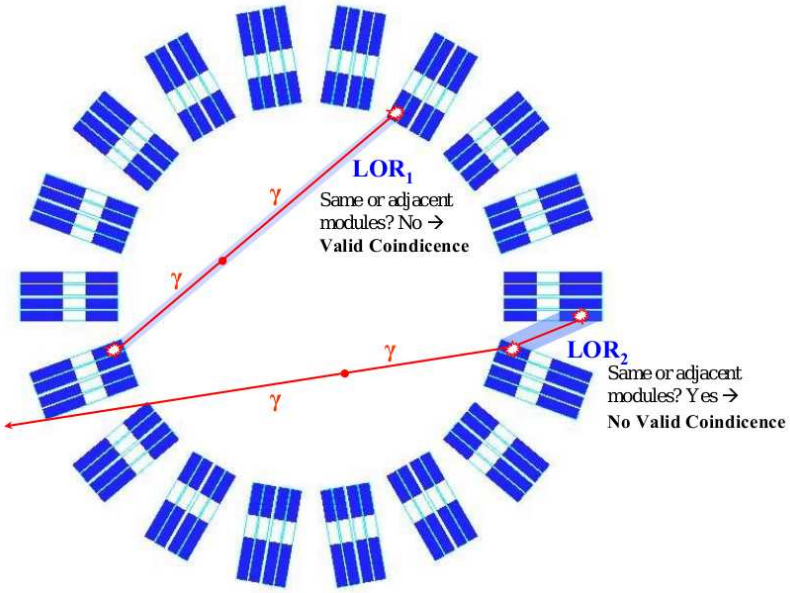

Figure 2.3: Two examples of possible coincidences in MADPET-II. The coincidence characterized by the LOR_1 is a valid coincidence because satisfies the geometrical condition. Whereas, the LOR_2-coincidence, defined by two crystals from adjacent modules, do not satisfy the geometrical condition. Thus, this coincidence would be excluded.

Coincidences are organized according to the following criteria:

1. The number of singles m in τ are counted, excluding the one that opens the window. The case $m = 1$ is considered a double coincidence (*double*) while $m = 2$ is a triple coincidence (*triple*). In this work, values of m higher than 2 were not classified (*multiple coincidences*).

2. To exclude coincidences arising from the same annihilation photon through ICS, a geometrical condition is applied (see figure 2.3). Most of the singles

produced by the same photon are usually detected within the same dual-layer module or in adjacent ones. Coincidences that involve singles detected in the same (or adjacent) dual-layer module are labeled as not physically meaningful (NP) and are not taken into account for image reconstruction purposes. Coincidences that involve different, non-contiguous modules are considered as valid coincidences because the LOR described by the single events is physically meaningful. If two singles are detected in two non-contiguous dual-layer modules and within the time coincidence window, this double coincidence is considered a prompt. In the case of $m = 2$, a triple, the geometrical condition must be satisfied by at least two singles.

3. Using the information provided by GATE (`EventID`), a random or true coincidence can be identified. If all singles within τ, including the one that opens the time coincidence window, have the same EventID, all come from the same annihilation process, and this coincidence is labeled as a *true* (double or triple true coincidences depending on m). A random coincidence is identified when at least one single has a different EventID than the others (double or triple random coincidences depending on m).

The complete procedure for coincidence sorting is outlined in figure 2.4.

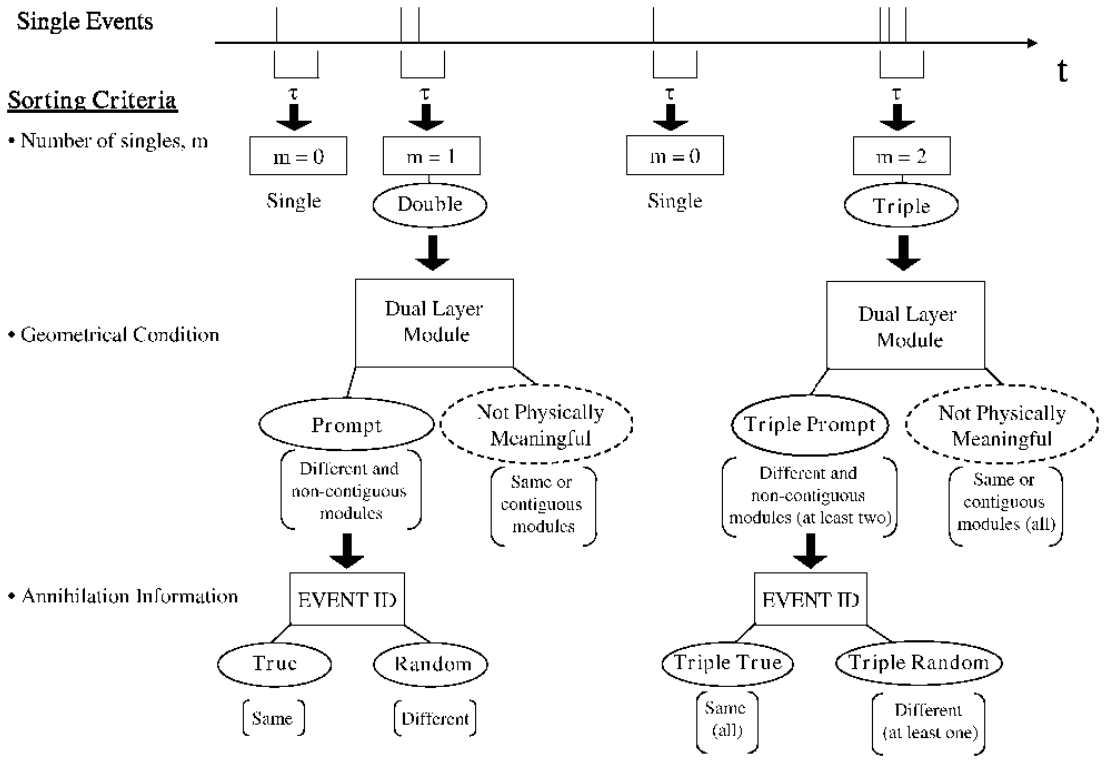

Figure 2.4: Outline of the coincidence sorting process. The horizontal axis represents the time evolution, and each vertical line marks the time of a single event.

Inter-Crystal Scatter

Inter-Crystal (IC) scatter takes place when a photon deposits its energy in more than one crystal due to Compton scatter. MADPET-II with its individual readout of the LSO units and when working at LETs lower than 255 keV [1] has the ability of discriminating the different crystals involved in the detection of a photon that has undergone several interaction in more than one unit. Leading to the case of a triple or multiple coincidence coming from the same two-photons annihilation process (triple or multiple true coincidence). For simplicity, an example of a possible triple true coincidence that could take place when measuring with MADPET-II, is presented in figure 2.5.

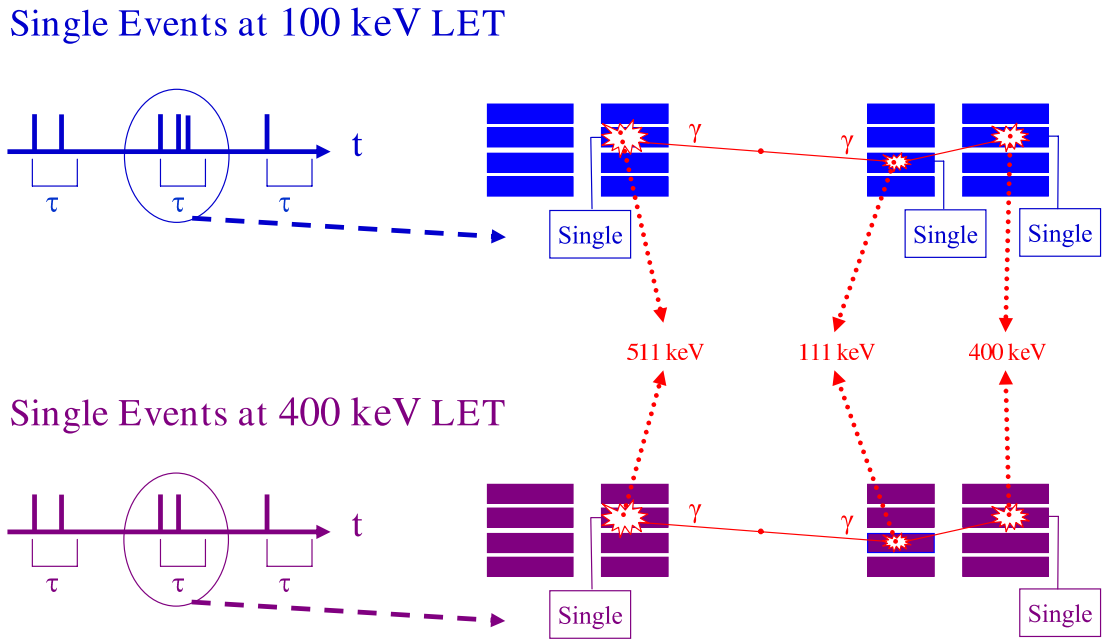

Figure 2.5: Triple coincidence arising from the same annihilation event in MADPET-II. At 100 keV LET MADPET-II is able to measure the IC scatter and the output is a triple coincidence. By contrast, at a higher LET (400 keV), although the IC scatter occurs, the system cannot detect it (hidden IC scatter).

2.3 Image Reconstruction

Given the small size of the MADPET-II inner diameter, a FOV as large as the inner diameter of the detector ring (71 mm) should be reconstructed to allow rat and mouse imaging. Under these circumstances, the effect of crystal penetration worsens the spatial resolution. To solve this problem, a fully 3D iterative reconstruction technique (MLEM) is used with a Monte Carlo system matrix [109].

[1] In the case of perfect energy resolution, if the LET is higher than the half of the energy of the annihilation photon, MADPET-II would never detect two energy depositions from the same photon.

The coincidence data were organized in LOR histogram, to keep the spatial information. Additionally, all the studied corrections in this thesis were applied within the reconstruction algorithm (see section 1.1.3).

2.3.1 Simulations with GATE

In this work we have used extensively Monte Carlo techniques by means of GATE for studying various aspects related to the image reconstruction process. For these simulations, the geometry and main characteristics of MADPET-II have been emulated. In order to speed up the simulations, two photons of 511 keV emitted in opposite directions were generated for each annihilation event, instead of creating the positron and posterior the annihilation. A time resolution of 10 ns and energy resolution of 21% at 511 keV were included to reproduce the response of the scanner. The low energy threshold was set to 100 keV, while the upper energy threshold was at 700 keV.

Chapter 3

System Matrix for MADPET-II

As it was already explained in the introduction (section 1.1.2), iterative reconstruction algorithms require the computation of the system matrix (SM) $\mathbf{P}$, which represents the imaging process. This chapter is dedicated to show how the SM can be built by means of Monte Carlo techniques, and the high quality images that provide the combination of a Monte Carlo SM with an iterative reconstruction algorithm MLEM. The comparison of two different system matrices for a different energy window in terms of image quality is also presented in order to decide which energy window produces the best results.

3.1 Monte Carlo System Matrix

In PET, the elements of the system matrix, p_{ij}, represent the probability of detecting an annihilation event emitted from the image voxel j by the LOR i defined by a detector pair. The probability depends on the range of the positron, the non-collinearity of the annihilation photons, the scatter and attenuation of the photons within the object to image, the scatter of the photons in the detector ring, the efficiency of the scintillator crystals, etc. If one wants to include all involved effects, even for the case of 3D small animal PET, the system matrix becomes huge. Sparseness and symmetries can be use to reduce the size to more reasonable proportions. Additionally, factoring the system matrix in components that account for the different physical effects is another way to handle the size problem [76], [77]. The decomposition could be done as follows:

$$\mathrm{P} = \mathrm{P}_{det.eff}\mathrm{P}_{det.scatter}\mathrm{P}_{att}\mathrm{P}_{geom}\mathrm{P}_{positron} \tag{3.1}$$

From the last expression, one can see that there are factors that depend on the scanner ($\mathrm{P}_{det.eff}$, $\mathrm{P}_{det.scatter}$, and P_{geom}), on the object (P_{att}) and on the radio-isotop being used ($\mathrm{P}_{positron}$).

As first approximation, the elements of the system matrix could be assessed by computing the intersection of the LOR with each voxel; this simplified model allows that the weights of the SM can be calculated on-the-fly [78]. More precise methods consider the position of the voxel relative to the detectors [79], or use analytical models or empirical kernels to correct for parallax error [80], [81], [82].

The correct way of calculating the SM would be to make a set of measurements of a point source within the scanner. However, this would take a huge amount of time to acquire good statistics and the need of having the system running before testing the reconstruction algorithm. Nevertheless, a simplified approach of the correct way was performed by [83] (an the extension to fully 3D PET in [84]), making a reduced number of point source measurements and extracting in a very elaborate manner the overall SM. Our approach for high resolution 3D PET in order to increase the reconstruction quality is to use Monte Carlo techniques [85] [86], in this way the forward process of the measurement is precisely modelled.

Monte Carlo simulations allow to obtain a realistic complete response of MADPET-II, before the system was built, providing a way to check some features and to optimize the image reconstruction algorithm and corrections. Therefore this is the chosen approach for MADPET-II. However, there are some limitations in our choice. One of these limitations is that the matrix elements are affected by statistical noise, due to the random processes involved in a MC simulation. The effect of the noise propagation into the image from the elements of the SM could be reduced by increasing the number of simulated events [110]. Another limitation is related to the storage of the SM elements, due to the number of LORs and image voxels, the size of the SM will be very large. To overcome this drawback, optimization of the format in which the SM is stored in relation to the calculations used in the reconstruction algorithm is necessary. Finally, a general limitation of the MC simulations, because of the results are based on a computer model, the accuracy of the results will depend on the accuracy of the model. GATE is the simulation code employed in this work and there are several publications that validate the model in which is based [87], [88], [89], [90], [91], [92], [93].

3.2 Generation of the System Matrices

As we have mentioned, the SM has been built using MC simulations (MCSM) by means of the software named GATE. The FOV has a cylindrical shape whose radius is 35 mm ($R_{FOV} = 98\%R_{scanner}$) and is 20 mm long. The FOV is discretized in 140×140×40 cubic voxels of 0.5×0.5×0.5 mm^3 volume and centered at the middle of the scanner (figure 3.1). An individual simulation for each voxel that belongs to the cylindrical FOV is performed to generate the SM. In total, from the 784000 voxels that form the cubic array, a number of 615200 voxels fit into this FOV. For the simulations, the voxels are considered cubic sources of 0.5-mm side. Within each voxel, 2 million positron annihilations were created. This number was chosen for two reasons. The first one was to increase the statistics of a previous MCSM [109]. The second was to obtain the MCSM in a reasonable time. To speed up the computations, the annihilations were emulated sending two photons back-to-back, without considering the emission of the positron, the positron range, and the non-collinearity.

After the simulation of an individual voxel the output contains the single

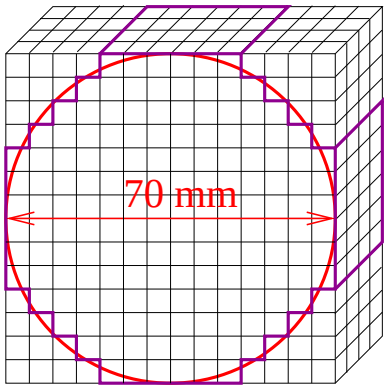

Figure 3.1: Representation of the FOV inside of a 3D array of voxels. The voxels, whose center is inside of the red circle, are for image reconstruction.

events detected at 100 keV LET [1]. First of all, a LET higher than 100 keV is applied to the singles list. Coincidences were sorted according to the detection time t and the criteria explained in chapter 2. If the number of the singles within τ (m) is 1 and this single belongs to the same annihilation (same `EventID`) as the single that opens the time window, a LOR is assigned to this coincidence if the geometrical condition is satisfied. Then, we obtain the number of detected coincidences in that LOR i for each voxel j, c_{ij}. The c_{ij} are called non-normalized coefficients or weights of the SM. The probabilities of the SM (p_{ij}) are calculated dividing c_{ij} between the 2 million simulated annihilations:

$$p_{ij} = c_{ij}/2 \cdot 10^6. \tag{3.2}$$

In our approach, the non-zero elements c_{ij} are stored and the corresponding p_{ij} are calculated in the reconstruction algorithm. In this way, the storage of the SM is reduced by using integers for the non-normalized coefficients (c_{ij}).

We focus on two different situations to build the SM:

- Considering double true coincidences (double trues) for a LET of 200 keV (SM-200).
- Working double trues and 400 keV LET (SM-400).

These two LETs are interesting for the MADPET-II scanner because they represent two different frameworks. At 200 keV LET, inter-crystal scatter (photons that undergo Compton scatter and deposit its energy in more than one crystal) is present and can be measured by MADPET-II (due to its individual crystal readout). On the contrary, increasing the LET to 400 kev makes that the inter-crystal scatter is not detected. Additionally, at lower LET the sensitivity of the scanner is higher. But, the spatial resolution could be affected by the increase of

[1] In a real acquisition, to maximize the flexibility of MADPET-II, a very low energy threshold is set in hardware. Our intention in the simulations was to mimic the measurements and, therefore, they are done with the same LET.

scattered events in the scanner [2]. Therefore, our goal is to determine under which circumstances (inter-crystal scatter and higher sensitivity versus no scatter and lower sensitivity) the reconstructed images with higher quality are obtained.

By using MC simulation to generate the SM, the elements of the created SM include the factors that account for the geometry of the scanner and the scatter in the detector ($P_{det.scatter}$ and P_{geom}). The factor $P_{det.eff}$ is studied in chapter 6 and it needs from measurements to obtain the coefficients. In the case of small animal PET, as MADPET-II, the noncolinearity of the two photons coming from the annihilation is negligible (resolution loss is $0.0022 \times 70 \approx 0.015$ mm). Related to the range of the positron, if we consider ^{18}F studies, the positron range for this radio-isotope is in the sub-millimetre. Therefore, the $P_{positron}$ can be set equal to the identity matrix. In any case, if necessary, the range of the positron can be included in the model a posteriori. Finally, P_{att} is object-dependent and the attenuation factors can be calculated or measured for each object being scanned.

3.2.1 Matrix Symmetries

It is possible to increase the statistical quality of $\mathbf{P}$ by applying the symmetries inherent in the combination of MADPET-II system and the voxelized FOV (see figure 3.2). Considering the transaxial plane and a centered grid, the value related to the weight p_{ij} corresponding to voxel j (purple square at the top right) and LOR i (top right solid line) is the same as for p_{kl}, where k and l are the values of the LOR and the voxel after the reflections about the Y axis. These elements can also be reflected about the X axis to obtain p_{mn} and p_{op}. Additionally, four more identical values can be found after reflection about the OXY plane. The voxels corresponding to 1/8 of the whole FOV were simulated (see figure 3.7) and by exploiting the mentioned symmetries, all the elements of the SM can be obtained. In this way, the necessary time to reproduce the SM and the space to store it is reduced by 8 times.

3.2.2 Use of Grid

After using the symmetries, the number of voxels to be simulated is 76900. Thus, realistic simulations to build the SM would take approximately 534 days (considering that the simulation of a voxel would need, in average, 10 minutes) in a single CPU computer. However, these simulations are excellent candidates for the parallel solution to the computational problem, because there is no need of inter-process communication. Providing that we have access to the Grid resources at the IFIC (143 PCs), the simulations to generate the SM have been performed fully in these computers. The time necessary for these simulations was 90 days. As we can see, the theoretical, linear speed-up is not achieved due to many factors. The most important factor is that these PCs are shared between the users of two VOs, ATLAS and IFIC. The users of the ATLAS VO have a 70% priority

[2] Also in the object, but this has not been studied in this thesis

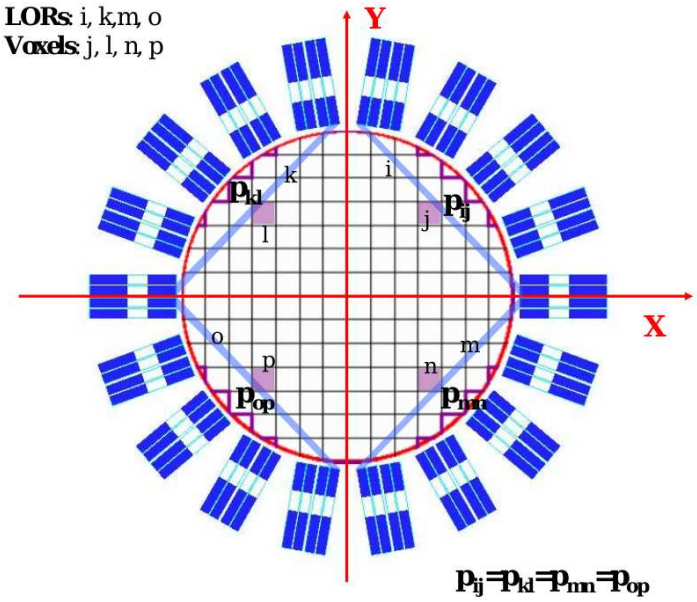

Figure 3.2: Symmetries in MADPET-II system for a cartesian voxelized FOV.

in use, whereas the users at the IFIC VO only 30%. Other factors are the time spent in the submission of the job and getting the output data, and there is a limit in the number of jobs that a user can send. Nevertheless, we speed up in a factor of almost 6, that makes a "reasonable" time to obtain the data for the SM.

3.2.3 Storage of the System Matrix

As we have already mentioned, the size of system matrix in the case of 3D acquisition is very large. Taking into account that the SM is a sparse matrix, it is possible to save some space by storing only the non-zero elements. Nevertheless, the precalculated non-zero elements of the SM need to be stored in large files that cannot be loaded into the RAM and, therefore the reconstruction algorithm needs a lot of time to read the elements of the SM from file for each iteration. Through a collaboration with computer scientists at the TU-Munich, a format was developed to optimize the storage of the SM in order to make faster the reconstruction algorithm. This format had a header, where relevant information about the SM is provided, like the maximal LOR number or the emitted annihilations (all the information contained in the header is shown in figure 3.3). An LOR array follows the header, where an offset for a given LOR is stored. This offset indicates the address, where the information related to this LOR (the corresponding voxels and weights) is found. When the LOR has no entries the offset is the same that the previous one. After the LOR array comes an structure that is repeated as many LOR with entries. The structure contains the maximum

non-normalized weight for this LOR (c_{ij}^{max}), then $c_{ij}^{max}+1$ offsets into the voxel data and the voxel data for this LOR. The first offset corresponds to the address where the voxels that have $c_{ij}=1$ can be found. The second indicates where the voxels, that have a non-normalized weight of 2 counts, start and so on. Finally, the voxel data for this LOR follows the voxel offsets. With this new format the disk space is notably reduced and the reconstruction time is feasible.

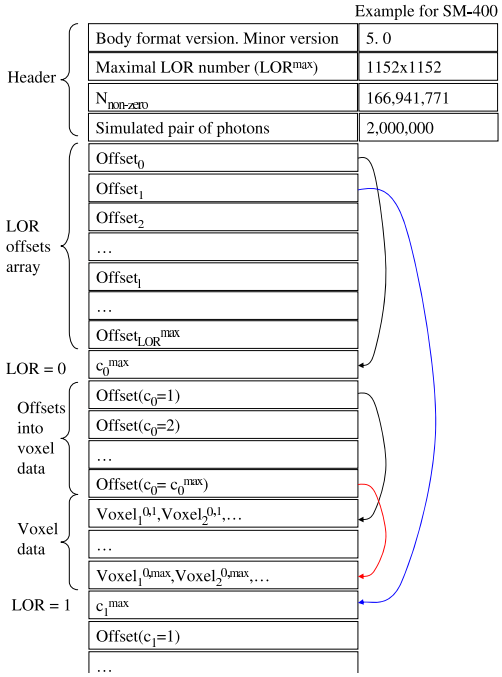

Figure 3.3: Schema of the optimized format employed to store the system matrix. The color lines are drawn to show where the offsets (memory addresses) are pointing. After the header, there is an array of LOR offsets. This array has $\text{LOR}^{max}+1$ elements, each pointing to the memory position where the information related to the corresponding LOR is stored. As an example, in the figure is shown the first black arrow that is starting at Offset_0 and ending at the position in which the maximum number of counts for the 0-LOR is found. The same is indicated with the blue arrow for the Offset_1 for the 1-LOR. The structure and information that is stored for each LOR is the following: first the maximum number of counts for this LOR (c_{LOR}^{max}), then another array of c_{LOR}^{max} offsets, and finally the voxel data. The second black arrow in the figure is indicating where the voxels that have one count for the 0-LOR are saved. The red arrow points to the voxels with maximum counts for the 0-LOR.

3.3 Characterization of the System Matrices

We have employed the following parameters to characterize the two system matrices, prior to evaluation of the quality of the reconstructed images that the SMs provide,

- The number of non-zero matrix elements, $N_{non-zero}$.
- The mean relative error, defined as

$$\bar{\sigma}_{rel} = \frac{\sum_{i=0;j=0}^{I-1;J-1} \frac{\sigma_{c_{ij}}}{c_{ij}}}{N_{non-zero}}\,, \tag{3.3}$$

  where $\sigma_{c_{ij}}$ is the standard deviation of the detected counts (c_{ij}) by the LOR i emitted from voxel j. Assuming that the detection of the photons is a Poisson process, it is possible to write $\sigma_{c_{ij}} = \sqrt{c_{ij}}$.
- The sensitivity is defined as the ratio between the true coincidences detected by the scanner for a voxel at the center of the FOV (j_c) and the emitted annihilations (N_{ea})

$$S = 100\frac{\sum_{i=0}^{I-1} c_{ij_c}}{N_{ea}}\,. \tag{3.4}$$

- Disk space occupied by the SM in the optimized format.

3.4 Effect of the Low Energy Threshold on Image Reconstruction

3.4.1 Simulated Sources

To study the image quality obtained by using the two system matrices (SM-200 and SM-400), the following sources have been simulated:

- A Derenzo-like phantom was used for visual analysis of the image quality. This phantom consists of 6 sectors containing 20 mm long rod sources with diameters of 1, 1.3, 1.5, 1.8, 2.4 and 3.2 mm and rod separation twice the diameter. The rod sources were spread within a cylinder of 62 mm diameter (see figure 3.4). The activity concentration of this source was 2.52 MBq/cm^3. The acquisition time of the simulation was 900 s (the detected events were 1.15×10^8 and 4.38×10^7, for 200 keV and 400 keV LET, respectively).
- Point sources covering half of the radial FOV were simulated to estimate parameters related to the spatial resolution. The point sources were spherical distributions of 0.125 mm radius. The sources were separated by a distance of 5 mm. The activity of each source was 1.85 MBq and the simulation was acquired during 120 s.
- Hot-cold-background (HCB) phantom was employed to analyse quantitatively the quality of the images reconstructed using both SMs. This phantom is a 3.7-MBq cylindrical source of 20 mm long and 30 mm radius (background region). There are two rods inside the cylinder. One of the

rods does not contain activity (cold rod) and the other has 1.54 MBq (hot rod). The centers of the rods are situated at (0,-15,0) and (0,15,0) mm, for the cold and hot regions respectively. Both rods are cylinders of 10 mm radius and 19.5 mm. The activity concentration ratio between the hot rod and the background was 1:3 and the acquisition time is 600 s. Inside the hot-cold-background source three regions of interest (ROI) were defined, a hot, cold and background ROI corresponding to the hot rod, cold rod and background regions respectively (figure 3.5). The three ROIs are 8 mm long cylinders with diameters of 16 mm. These ROIs were used to quantify the quality of the reconstructed images based on the figures-of-merit described in section 1.1.4.

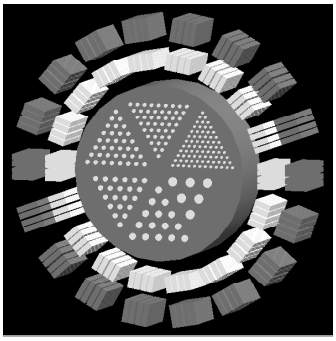

Figure 3.4: Derenzo-like phantom simulated using GATE to investigate the quality of the reconstructed images. The phantom is organized in 6 sectors. Each sector is made up of 20 cm long rod sources with diameters of 1, 1.3, 1.5, 1.8, 2.4, and 3.2 mm and rod separation twice the diameter.

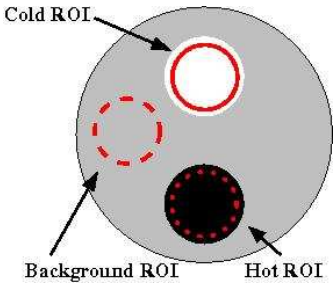

Figure 3.5: Hot, cold, and background ROIs in the hot-cold-background source. All ROIs are 8 mm long cylinders with diameters of 16 mm. Diameter of the source cylinder is 60 mm, and diameter of rods is 20 mm.

In order to focus on the image quality that the SMs can provide, there was no attenuation media in the simulated sources, therefore we do not reproduce the scatter, nor attenuation within the object. Another reason that supports this approximation is that the contribution of the object scatter for a small animal PET scanner is small in comparison to the detector scatter ([94], [95], [96], [97]).

3.4.2 Image reconstruction

As we have mentioned, we use MLEM reconstruction algorithm to reconstruct the images combined with the Monte Carlo SM. The code employed for this purpose was optimized in order to run in a reasonable time using the large file, where the SM was stored. All the sources described in this section were reconstructed using this algorithm. Additionally, as we were interested in quantifying the spatial resolution, the point sources were reconstructed using the 3D Reprojection Algorithm (FBP3D) that implements Kinahan and Rogers FBP algorithm with reprojection of the missing data [27], provided by the open source Software for Tomographic Image Reconstruction (STIR, [100]).

3.4.3 Figures-of-Merit

The system matrix is the basis of the iterative algorithm. Therefore, to estimate which is the SM that provides better images for MADPET-II, we need to use FOMs according to the tasks that MADPET-II was designed for:

1. Quantitation: For the evaluation of the images according to this task, the discrepancy, the mean square error, and the misspositioned events, defined at the introduction (section 1.1.4, 57), were employed for the hot-cold-background phantom, using the known emitted source as a reference.

2. Lesion Detectability: Computing the CRC vs. the background noise or the SNR for the hot-cold-background phantom (the hot region would simulate the lesion among the background activity) can reflect the performance that may be achieved for this task (defined in section 1.1.4, 57).

3. Small details visibility was assessed by means of the FWHM and the FWTM (used to express the spatial resolution as presented in section 1.1.4, 57) for the reconstructed images of point sources using MLEM and FBP3D.

3.5 Results: Comparison of the System Matrices

3.5.1 Characteristics of the System Matrices

From the 153.8×10^9 total emitted annihilations to generate the SM, 1.49×10^9 detected coincidences were found in the SM at 200 keV LET and 5.44×10^8 for the 400 keV LET case. Taking into account the voxels that are inside the FOV, from where the annihilations were emitted, the mean valued of detected events per voxel is 19510.8 and 7128.4 for 200 keV and 400 keV LET, respectively. The average of the detected events per LOR, considering only the LORs that at least have one detected event, is 3206.56 for the 200 keV LET case and 2128.41 for 400 keV LET case. The number of LORs with at least one detected event was 464886 and 255885, for 200 keV and 400 keV LET, respectively.

For the SM at 200 keV LET, the maximum number of detected events per LOR and per voxel was 97 and the average of detected events over the nonzero elements was 2.72. This can be understood due to the fact that over 71% of the non-zero matrix elements were related to only one detected pair of photons per LOR and per voxel, i.e. $c_{ij} = 1$. This situation is not so extreme in the case of 400 keV LET, where the maximum was found to be 59, the average was 3.26 counts per voxel and LOR and the percentage of elements with one count was 43%. This situation can be very well seen in the figure 3.6. In these plots the contribution from a voxel to an specific LOR is represented (c_{ij}), then the left-right and up-down symmetries were applied to obtain the complete LOR. In the plots corresponding to the 200 keV LET case, voxels spread from all over the FOV contribute to the LOR, whereas in the situation of 400 keV LET, the voxels are concentrated in the area defined by the LOR.

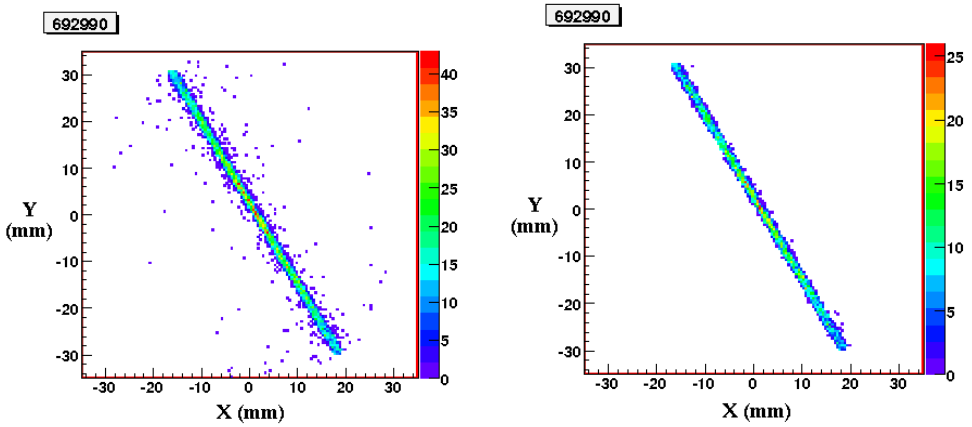

200 keV 400 keV

Figure 3.6: Plots corresponding to the contribution of each voxel that belongs to a certain slice to a specific LOR represented in the label of the plot. The complete LOR has been drawn by using the symmetries, because only the voxels that belong to 1/8 of the FOV were simulated.

The situation seen in the plots at 200 keV LET is a consequence of the LET used. Setting the low energy threshold at 200 keV allows that photons that have scattered previously in other detector crystal could produce a detected event only depositing a part of its initial energy. This produces a contribution from a voxel out of the LOR volume to this LOR. As it can be seen from the values, these contributions had very low probability, the values of these elements usually were 1 or 2 detected annihilations per voxel and LOR.

Finally, to end up with the characterization of the two SMs, the main properties of the SMs are shown in table 3.1. In this table, it can be seen that the statistical quality of the SMs at 400 keV LET is higher than at 200 keV, although the number of detected events is less. This is due to the elements with one count in the SM at 200 keV. Indeed, for 200 keV LET, if the elements with one count are

Table 3.1: Properties of the calculated probability matrices

SM-LET (keV)	$N_{nonzero}$	$\bar{\sigma}_{rel}$ (%)	S (%)	Disk space (GB)
200	546159653	0.85	1.50	2
400	166941771	0.72	0.57	0.6

removed, the $\bar{\sigma}_{rel}$ is reduced to 0.45%. Under these circumstances, reconstructed images of point sources removing the noisiest elements for the SM ($c_{ij} = 1$) were performed and the FWHM was found to be smaller. Nevertheless, no further effects on the quantification with other sources were studied. This evaluation was beyond the scope of this thesis and it would need deeper and more systematic analysis. As it was expected, the sensitivity at 200 keV LET is higher than in the case of 400 keV LET.

The statistical quality of the SM plays an important role in the noise properties of the reconstructed images. For a dedicated analysis of the later we refer the reader to [110]. In [110], there is a prediction in the number of detected coincidences necessary to obtain a reasonable image quality for the MADPET-II scanner. The proposed value of the detected coincidences is $\approx 2.3 \times 10^9$. Considering that the given detected coincidences for SM-200 and SM-400 are for 1/8 of the FOV, we have reached the number of detected events that above it the quality of the SM is barely improved.

3.5.2 Sensitivity Matrix

The sensitivity matrix is obtained summing the SM elements, p_{ij} over the LORs for a specific voxel j, representing the detection probability of an annihilation emitted from this voxel by the whole system. The sensitivity matrix elements S_j are calculated as follows

$$S_j = \sum_{i=0}^{I} p_{ij} \tag{3.5}$$

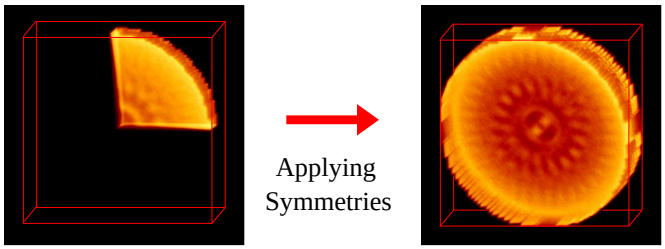

Figure 3.7: Applying symmetries to obtain the sensitivity matrix for the whole FOV.

To get the sensitivity matrix for the whole FOV, the symmetries were applied to the simulated data, as it can be seen in figure 3.7. These calculations were

performed for both cases, 200 and 400 keV LET. The sensitivity matrix for the voxels that belong to the central slice are represented in figure 3.8 for the studied cases. The two pictures on the left are normalized to the same maximum, the one corresponding to the 200 keV case. From these images is obvious that the scanner at 400 keV LET is less sensitive, as we expected. As a consequence of lower sensitivity at 400 keV LET, the sensitivity matrix shows higher noise for this LET, as it can be seen in the most right plot. On the other hand, the sensitivity matrix of both cases has the same flower-like structure and two internal rings, this is more visible on the two extreme plots. This structure is due to the association of the crystals in 18 modules and the empty spaces (no detector crystals) between them. Indeed the petals of the flower shape are 18, like the number of modules. And the rings are coincident with the missing sampling due to the distance between detector modules, shown in figure 3.10 at the left by the area under the blue lines. Another common characteristic is that the value of the sensitivity matrix is increasing radially from the center to the edges of the FOV. The reasons of this behaviour are that the voxels towards the FOV edge have larger solid angle (see figure 3.9) and more effective crystal thickness. The increase of the effective crystal thickness can be understood qualitatively, thinking in an ideal detector ring (figure 3.10 at the right) and considering that the probability of detection is proportional to the distance travelled by the photon within the detector ring. The annihilation photons leaving a voxel at the center of the ring pass through the ring, all covering the same distance, the width of the ring. Whereas, the annihilation photons emitted from a voxel at the edges of the FOV travel across the ring a larger distance than the width of the ring. Which means, the photons from the edge of the FOV have a higher probability to be detected.

3.5.3 Spatial Resolution

The point sources covering half of the radial FOV and the Derenzo-like phantom were used to study and compare the spatial resolution attained with the two SMs. The reconstructed images of both phantoms are shown in figures 3.11, 3.12, and 3.13. As we can see from the figure of the Derenzo-like phantom, there is no substantial differences between the reconstructed images using the SMs at 200 keV LET and at 400 keV LET, not only in the reconstructed images, but also in the profiles through the sectors of 2.4- and 1.5-mm diameter rods (at the left) and 3.2 and 1.3 rods diameter (at the right). For both SMs, the smallest rod structure of the Derenzo-like phantom that can be identified is the corresponding to the 1.5 mm rods diameter. It is possible to distinguish the 8 rods of the 1.5 mm diameter rods sector from its profile for the two studied cases of SM.

To quantify the spatial resolution across the radial FOV, the projections of the point sources were reconstructed using FBP. As first step the sources were reconstructed using FBP without any rotation during the acquisition, because the scanner is not meant to rotate. The results of this first step can be seen in the first row of figure 3.13. Due to the gaps between the detectors there are null elements

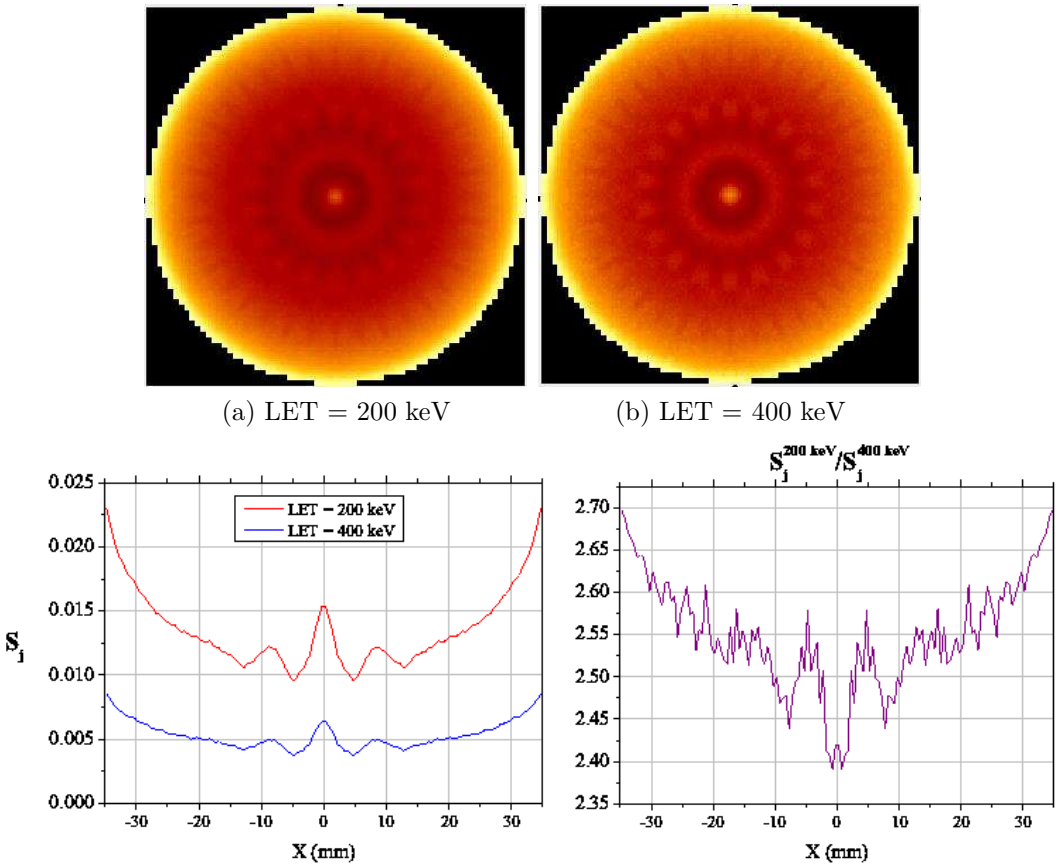

Figure 3.8: Top: Sensitivity Matrix of the central slice for the two studied cases. Bottom: Profiles of the sensitivity matrices (left) and the ratio of both profiles (right).

in the sinogram and these missing data are creating the "star" artifacts that we can see in these images. The artifacts prevent from calculating the FWHM (neither the FWTM) from these images to quantify the spatial resolution. The second step, done in order to solve this problem, was to rotate the scanner during the simulation (it can be done also by rotating the source). This was proposed in [98] and [99] to recover the missing data. By doing this, the reconstructed images shown in the second row of figure 3.13 were obtained. Although, there are still some artifacts due to the non-uniformity in the sensitivity of the LORs and to remove them it is necessary to normalize. However, it is still possible to asses the spatial resolution for these images.

As we have mentioned that we plan to reconstruct the images using MLEM and the Monte Carlo SM, the corresponding reconstructed images using MLEM and the two SMs are also presented in figure 3.13 and the FWHM and FWTM were also calculated from the profile of these images to compare with the results obtained using FBP. The point sources in the MLEM reconstructed images are perfectly visible and there are no artifacts close to them. Only the two point sources closest to the edge of the FOV are blurred. For these images there is

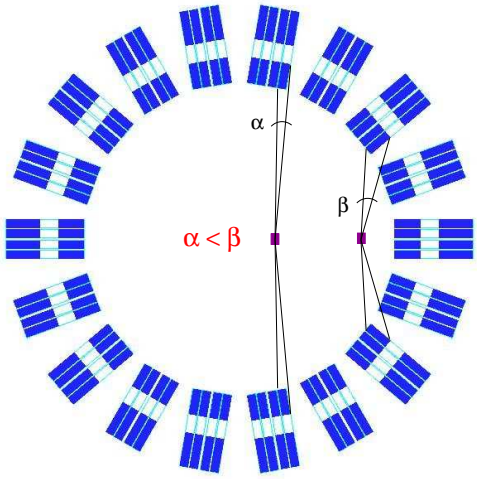

Figure 3.9: The solid angle seen by the voxels increases as the voxels are closer to the edge of the FOV. In this figure it is shown the solid angle for a central voxel (α) and for a excentrical voxel (β). The solid angle for the voxel closer to the edge of the FOV is larger than the one for the central voxel.

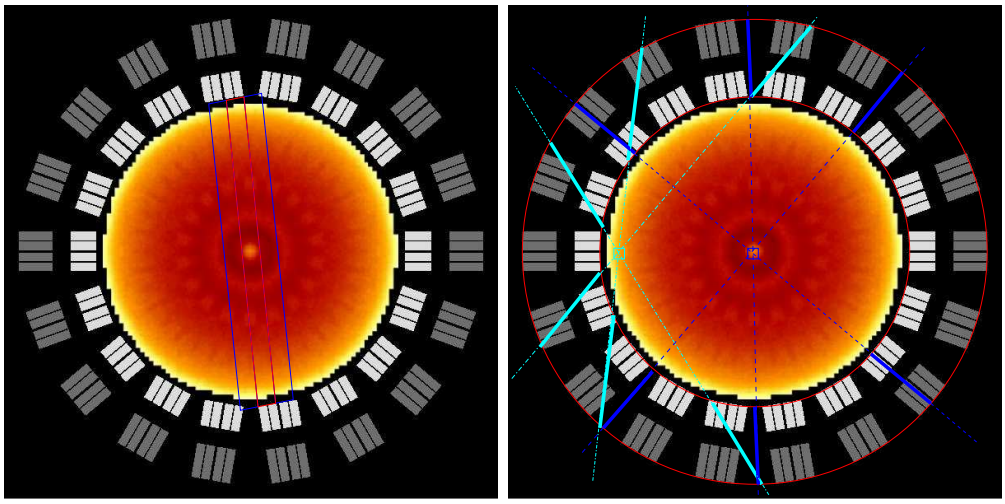

Figure 3.10: Graphical explanation of the flower-like shape of the sensitivity matrix (left) and the increase of S_j towards the edge of the FOV (right). In the image at the right, it is observed that the central black ring is coincident to the undersampled areas due to the space between detectors (dark-blue lines). On the left, it is shown the intersection of the photon pair path with an ideal detector ring. The cyan lines correspond to cases that the incidence is not perpendicular, whereas the dark blue lines are for the orthogonal incidences. Considering that the probability of detection is proportional to the travelled distance of the photon in the detector, the voxels closer to the edge have higher probability.

a slight difference between the reconstructed images using the SM at 200 keV LET and 400 keV LET, the point sources are blurrier for the case of 200 keV LET, more obvious at the edges of the FOV. The reason of this behaviour can

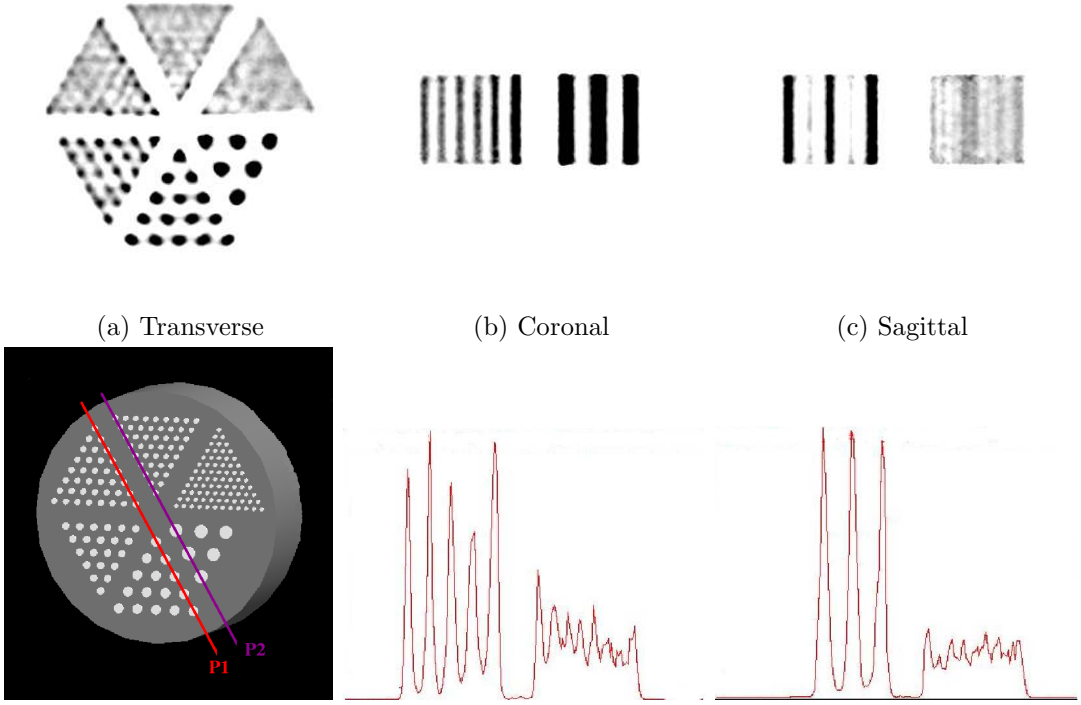

(a) Transverse (b) Coronal (c) Sagittal

(d) P1 (e) P2

Figure 3.11: Reconstructed images (top) and profiles (bottom) of the Derenzo phantom, using 100 iterations of MLEM at 200 keV LET.

be predicted from the figure 3.6: Due to the lower LET, there are contributions from voxels outside the tube defined by the two detectors and these elements of the SM make that the point sources at 200 keV LET are slightly more spread. This is an example of limitation in the ability of the SM to compensate for the degradation effects. Although the detector scatter is modelled on both SMs, the results achieved for the 400-SM are better than for 200-SM, because the detector scatter is more notable at 200 keV LET.

The profiles of the second and third row of the figure 3.13 were used to calculate the FWHM and the FWTM, and the calculated values versus the radial position are represented in figure 3.14. In general the values of the FWHM and FWTM are always slightly better for the reconstructed images at 400 keV LET. The reason is what we have pointed out in the previous paragraph, related to the increase of detector scatter when working at 200 keV LET. Comparing FBP and MLEM reconstructed images is obviously better the combination of MLEM with the Monte Carlo SM, this was already seen in the figure 3.13. Nevertheless, there are two points corresponding to the FBP reconstructed images that show lower FWHM compare to the MLEM reconstructed images, as we can see in the plot of the figure 3.14. The reasons of this unexpected behaviour are different for the different point sources. When reconstructing using the FBP algorithm provided

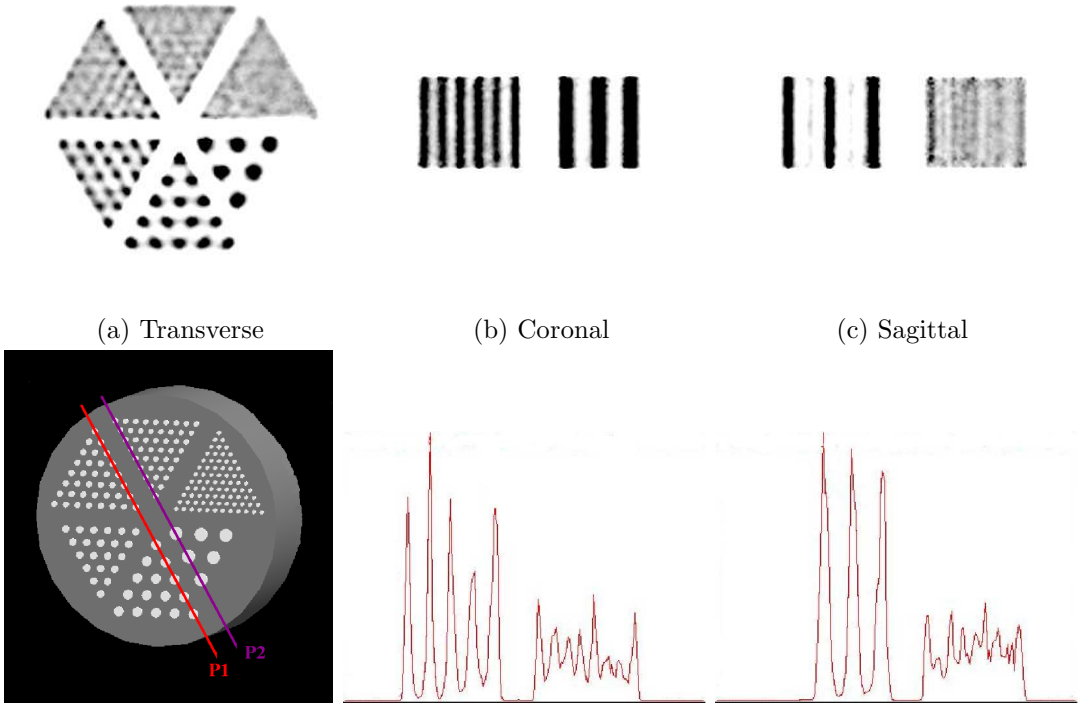

(a) Transverse (b) Coronal (c) Sagittal

(d) P1 (e) P2

Figure 3.12: Reconstructed images (top) and profiles (bottom) of the Derenzo phantom, using 100 iterations of MLEM at 400 keV LET.

by STIR, the zero position should be at the center of the bin. In this way the point source at the center is fully contained in the central voxel. Whereas in the MLEM reconstructed images, the central point source is shared between the two most central pixels. This is the reason of the smaller value of the FWHM for the FBP in the central point source. The second unexpected values corresponds to the 6th point source and the reason in this case is the artifact observed in the image. This artifact is producing a second lower peak in the profile of this point source and this creates that the linear interpolation is done before this second lower peak, making narrower the FWHM. In the FWTM plot, it is more visible the difference between the reconstructed images at 200 keV and 400 keV LET.

3.5.4 Quantification

The Hot-cold-background phantom was used to determine the quantification and lesion detectability capabilities of these two SMs. The reconstructed images and the corresponding activity distribution are shown in the figure 3.15. At first sight, the main difference between the reconstructed images of both LETs is the higher noise of the image at 400 keV LET, due to the lower sensitivity at this LET. This can be seen, not only in all the views of the reconstructed image (transversal,

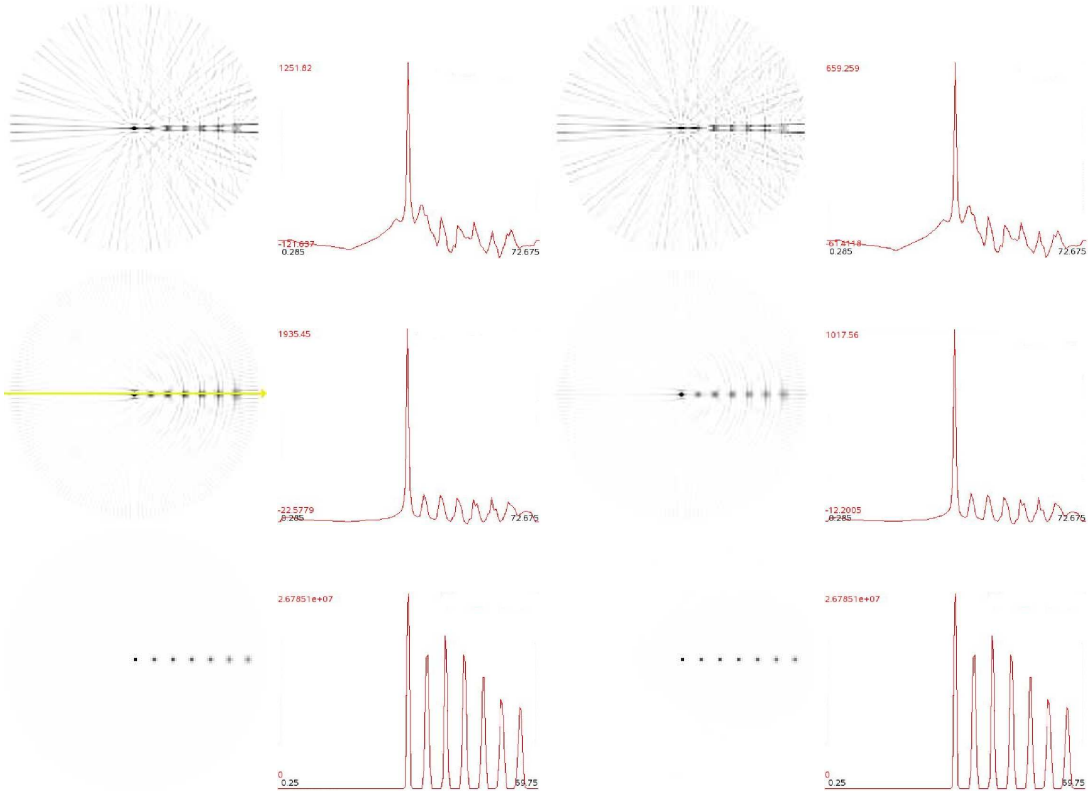

Figure 3.13: Reconstructed images and profiles of the point sources using FBP without rotation, FBP with scanner rotation (20 steps of 1^o) and 100 iterations of MLEM for 200 (left) and 400 (right) keV LET.

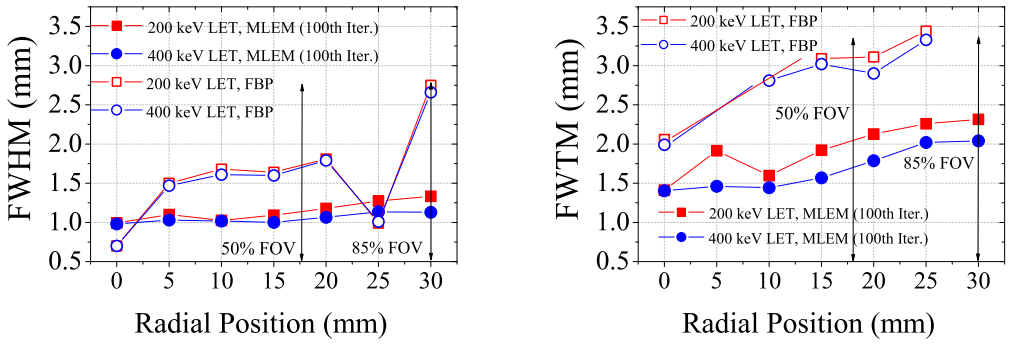

Figure 3.14: FWHM (left) and FWTM (right) as a function of the radial position from the profiles of the reconstructed images using FBP with scanner rotation (20 steps of 1^o) and 100 iterations of MLEM for 200 and 400 keV LETs.

coronal and sagittal), but also in the profile shown at the last column of the figure 3.15.

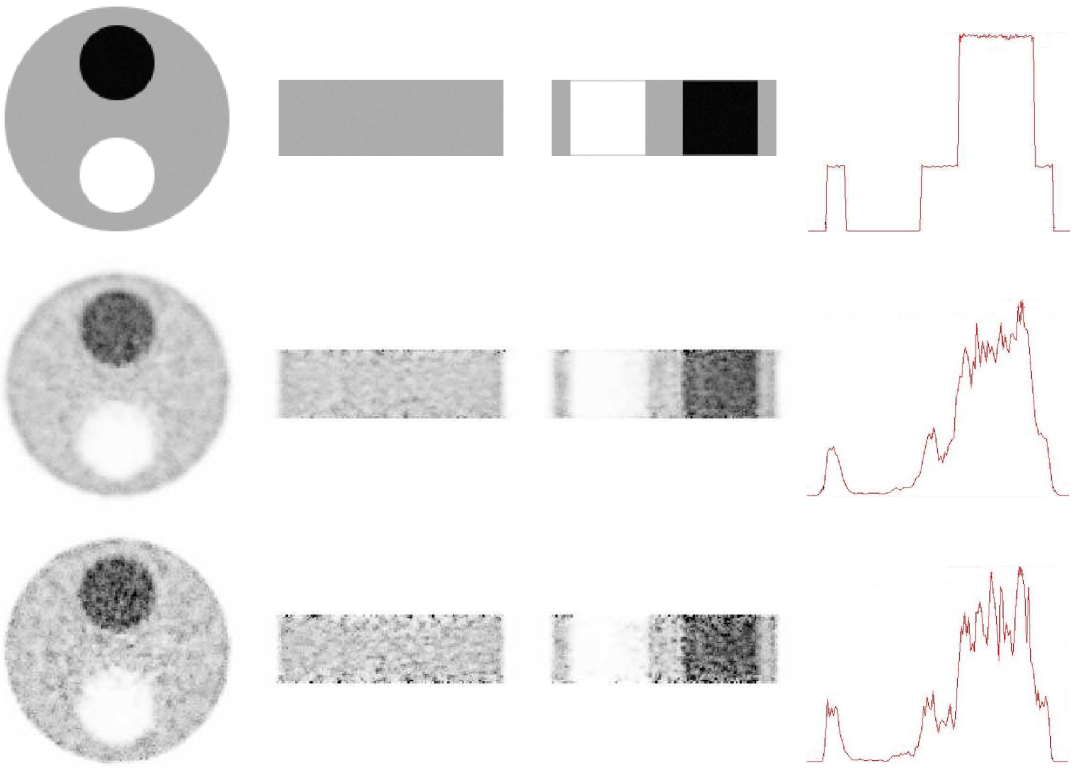

Figure 3.15: Emitted source (top) and reconstructed images of the hot-cold-background phantom (view: transversal, coronal and sagittal), using 100 iterations of MLEM for 200 (center) and 400 (bottom) keV LET.

According to the analyzed FOMs (except for the ME) the 200 keV SM provides a superior image quality than the 400 keV LET SM. The reason of this behaviour is the higher noise of the SM at 400 keV LET. The noise is higher because the 400-SM and the LOR histogram for this LET have less counts than the 200 keV LET. In order to compensate for the lower number of counts, we should increase the number of simulations for the SM to get the same counts per LOR than at 200 keV and the time of the acquisition of the hot-cold-background source.

At figure 3.16 the ϵ_{rms} is represented for the different iterations. The reconstructed images are compared to the emitted source to obtain ϵ_{rms}. It is observed that this error is higher for the case of 400 keV LET, as we expected. Comparing the absolute reconstructed activity to the absolute emitted activity in the hot and background ROIs (figure 3.17) using the discrepancy ($D(\%)$), it is observed that we can recover the emitted activity using both SMs (the maximum discrepancy value is 1%), but the SM at 200 keV LET provided closer values to the reference. Looking at the plots of the figure 3.19, it is also seen that the reconstructed images at 400 keV LET show worse results due to the higher noise: The SNR is lower in the plot at the left and the background noise ($\bar{\sigma}_{BKG}$) is bigger at the right plot on the figure 3.19. The CRC has been also plotted for different iterations,

but it is not shown here, because the same information can be seen in the right plot of the figure 3.19. For both cases, the CRC reaches its maximum at the 30th iteration (the first point of the right plot at the figure 3.19 corresponds to the 10th iteration) and there are no big changes from this iteration. Related to the ME, despite that the difference is small, the reconstructed images at 200 keV LET show higher values, which means higher number of mispositioned events. The reason of these barely higher values is the contribution of voxels outside the tube of response, like in the spatial resolution section.

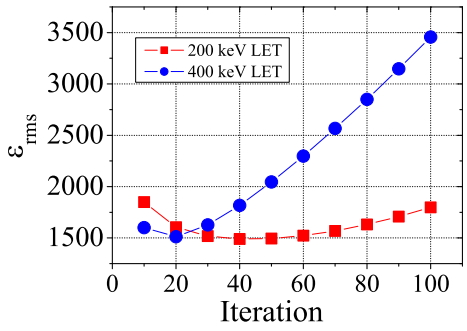

Figure 3.16: Root mean square error of the reconstructed images using MLEM for 200 (red) and 400 (blue) keV LET compared to the emitted source.

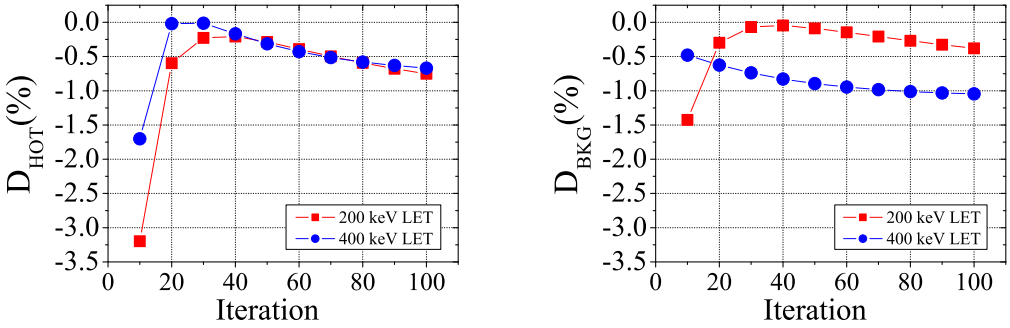

Figure 3.17: Discrepancy of the activity of the reconstructed images calculated using true coincidences and the emitted source within the hot (left) and background (right) ROI for 200 and 400 keV LETs as a function of the number of iterations.

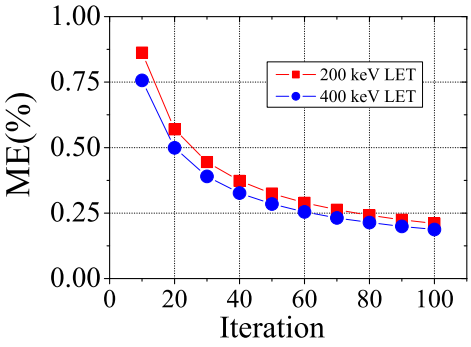

Figure 3.18: Mispositioned Events within the cold ROI for 200 and 400 keV LETs as a function of the number of iterations.

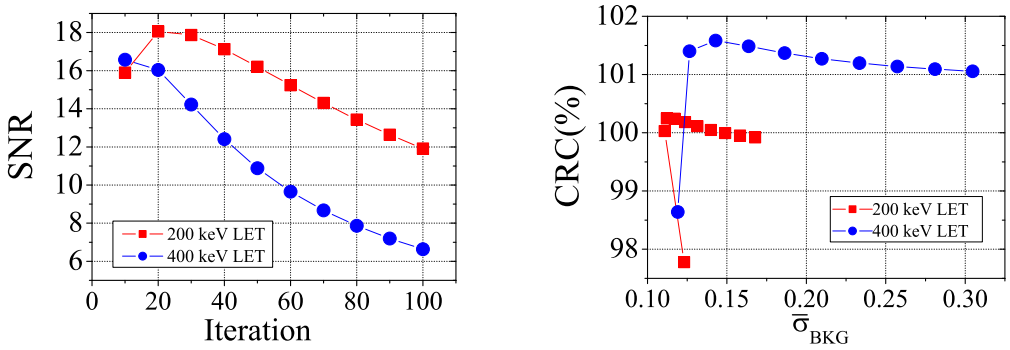

Figure 3.19: SNR for 200 and 400 keV LETs as a function of number of iterations (left) and CRC versus $\bar{\sigma}_{BKG}$ for both LETs (right).

3.6 Conclusions

In this chapter we have shown how the system matrix for MADPET-II using Monte Carlo techniques by means of GATE can be generated. One of the obstacles that this task poses is the computing time. In order to reduce this time, the symmetries of the system and distributed computing have been employed. One of the characteristic of MADPET-II is the flexibility of the acquired data granted by the singles list mode. This facilitates the sorting of coincidences by software using different parameters. Among the parameters that we can vary post-acquisition in MADPET-II, we have focused on the low energy threshold. The main reason is because the LET plays a very important role in the sensitivity of the scanner. By lowering the LET, we have a gain in the sensitivity but, at the same time, there is an increase of detected scattered photons in the

detector and in the object [3]. The increase of scatter can deteriorate the spatial resolution. The main aim of this chapter was to analyze the images at different LETs, chosen as 200 and 400 keV. For each LET the detectors of the scanner responds differently, thus requiring specific system matrices, denoted by SM-200 and SM-400 throughout this chapter.

Some words about the obtained sensitivity matrices are appropriate before discussing the results of the reconstructed images. We have used the same simulation time to build the two SMs and, as a consequence of the higher sensitivity at 200 keV LET, the sensitivity matrix at this LET is less noisy than at 400 keV LET. For a fair comparison between both SMs, we would need to increase the time of the simulations for the SM-400 to achieve the same noise level. It is nevertheless interesting to contrast the performance of the SM-200 and the SM-400 when the same time has been invested in creating both.

Let us now turn to the analysis of the reconstructed images. In terms of spatial resolution, there are almost no observable differences in the Derenzo reconstructed images, and the smallest rods that can be distinguished in both cases are the ones of 1.5 mm diameter. When assessing the FWHM of the reconstructed point sources, some differences appear for the point sources at the edges of the FOV. The SM-400 provides better spatial resolution (smaller values of the FWHM) for the point sources close to the edge of the FOV. From this result, we can conclude that the detector scatter present in the SM-200 has a higher impact on the reconstructed image resolution than on the overall image noise. The statistical noise is higher for 400-SM, but the noise introduced by the detector scatter due to mispositioning of the events is notably less and this produces a better FWHM, FWTM and ME.

When analyzing the FOMs for quantitation and lesion detectability, the SM-200 gives better performance. Clearly, the higher statistical noise in the SM and also in the input LOR histogram at 400 keV LET are the factors which produce this outcome. The conclusion of this part is that higher sensitivity, which means lower statistical noise for the same acquisition time, is very important for quantitation of the activity distribution and lesion detectability.

The statistical noise in the input LOR histogram can be reduced by increasing the acquisition time in the measurement at 400 keV LET. This was not studied, but it is important to keep in mind that there are examinations which are bounded to short time frames, like in the dynamic studies for pharmacokinetic modelling. In addition, it is very important to know the concentration of the tracer for these studies and a lower LET provides more accurate information for the activity distribution. On the other hand, for static studies, where we are not limited to short time frames, working at 400 keV LET would provide better images in terms of visibility of the small details. For the quantitative analysis at 400 keV LET, simulations with longer running time for the system matrix are required to reach the performance of the SM-200.

[3] As we have already mentioned in the section 3.4.1, the scatter of the photons inside the object for a small animal PET scanner has a less important effect for the reconstructed images than the scatter in the detector, and has not been considered in this work.

From the results shown in this chapter, we can conclude that the flexibility provided by the singles list-mode output of MADPET-II is a very useful feature, because one can adapt the low energy threshold to the type of study in order to obtain the best results for the specific task.

Chapter 4

Random Coincidences Correction

An accidental or random coincidence (*random*) takes place when two photons coming from different annihilations are detected within the same time coincidence window and mistakenly assigned as coincidence event (*prompt*). Random coincidences can contribute substantially to the background in PET. Accurate estimates of radioactivity distributions within a patient or rodent from PET images cannot be provided unless the effect of these coincidences is taken into account in a quantitative manner [3]. Several methods are commonly used for randoms correction. They have been explained in the introduction, section 1.1.3. The goal of this chapter is to investigate the validity of the techniques for random coincidence estimation for various low energy thresholds (LETs). For this investigation, simulated list-mode data for MADPET-II are used as input. The simulations have been performed using the GATE simulation toolkit. Since the GATE simulations allow random and true coincidences to be distinguished, a comparison between the number of random coincidences estimated using the standard methods, and the number obtained using GATE is performed. The random coincidence correction can be applied in two different ways. One can subtract the estimated randoms from the prompts before the reconstruction. Or the randoms correction is applied in the reconstruction algorithm. We compare the two approaches in this chapter. The last part of the chapter is dedicated to the effect of the activity on the randoms estimation methods and correction. Most of the results shown in this chapter are published in [101].

4.1 Randoms Estimation Methods for MADPET-II

There are several methods to estimate random coincidences. The most common technique is to acquire single events arriving within a delayed-coincidence window defined such that the probability of a true coincidence is zero [3]. The method is based on the assumption of constant time distribution of random coincidences. This technique provides an accurate but noisy estimation for random coincidences [103]. A second method, called "singles-based" [103] estimation of

random coincidences, calculates the mean random coincidence rate $\dot{R}_{ij}$ for each line of response (LOR) (or sinogram element related to detectors i and j) by using a relationship between the singles rate in these detectors and the time coincidence window width, as explained in section 1.1.3. A third method uses the timing histogram of the prompt coincidences [106], which shows an almost flat tail and this tail can be fitted to a linear function. As it was shown in section 1.1.3, the total number of random coincidences can be obtained integrating the fitted function within the corresponding time interval. In what follows, these three random estimation methods for different low energy thresholds applied to the small animal PET scanner MADPET-II were investigated. In the case of the DW method, two different modalities were used and they are explained in the following section.

4.1.1 Approaches to the Delayed Window method

Two approaches have been implemented for this method. In the first approach (which we call DW), the singles list-mode data were processed using two time windows of the same size separated by a time interval (ΔT). The first window was the time coincidence window and the second was the delayed window. For randoms estimation, the number of singles m found in the delayed window was counted and classified according to the conditions (i) and (ii) described in section 2.2. Condition (ii) was applied to the single that opened the prompt window and the single or singles found within the delayed window.

In the second approach (DW'), the singles data were duplicated by delaying the time information of each single by a fixed amount ΔT, as presented in [114]. Then, the delayed singles were added to the original data stream. The delayed singles carry a flag that distinguishes between original (not delayed) and duplicated (delayed). The combined data stream was sorted with only one time window (time coincidence window). Only non-delayed singles can open the time coincidence window. Within this window, the singles n carrying a delayed flag were counted. After the geometric condition is applied to the LOR described by the single that opens the window and the delayed singles, $n = 1$ refers to the case of double randoms while $n = 2$ corresponds to triple randoms. In this work, the cases $n > 2$ has not been considered.

Schemes representing the two approaches are presented in figure 4.1.

4.1.2 Simulations to study the performance

In this study, several sources were used to compute the total number of randoms (figure 4.2 and table 4.1). The sources represent various geometries, namely a point-like source (*Small Sphere*), a planar source (*Plane*), a linear source (*NEMA Rat-like*), and a cylindrical source (*Hot-Cold-Background*). The small sphere and plane source were chosen to see the influence of the source geometry in the random estimation methods. The Rat-like source was based on the National Electrical Manufacturers Association (NEMA) NU2-2001 Performance Measurements of Positron Emission Tomographs, with the source dimensions scaled down to the

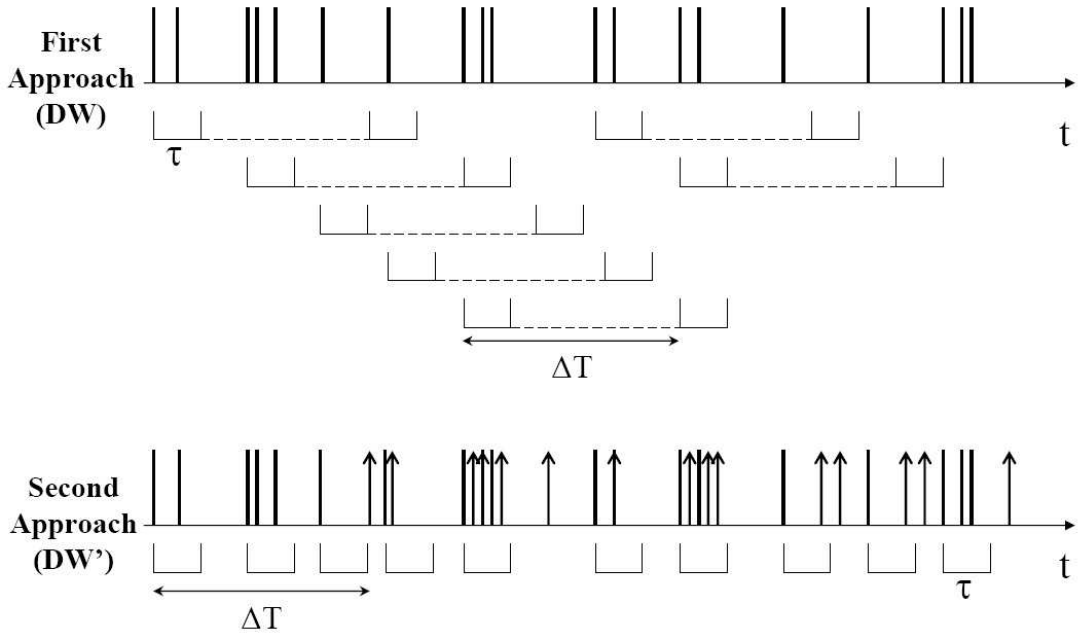

Figure 4.1: Two different approaches of the randoms estimation methods based on the delayed window concept. The first approach uses only the original singles chain. The second approach employs the original and the delayed singles chain (top). The horizontal line in both approaches shows the time evolution of the measurement (bottom). The time coincidence window is denoted with τ. The delay applied to the delayed window is expressed with ΔT. The solid vertical lines (|) represent the singles of the original chain. The arrows (↑) are the singles of the delayed chain.

size of a standard rat. The NEMA rat-like source is a line source situated at 17.5 mm offset from the central axis with radius and length 1.05 and 140 mm respectively.

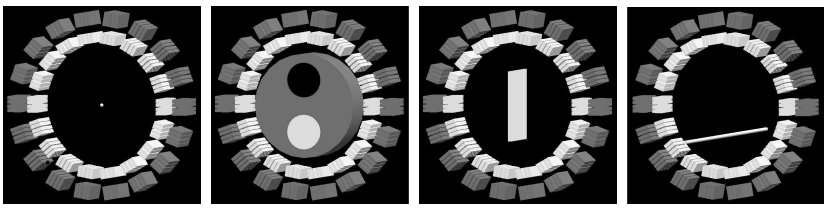

Figure 4.2: Various source geometries simulated with GATE to study randoms estimation methods (see table 4.1 for dimensions).

The hot-cold-background source (figure 4.2b) was simulated, not only to analyse the performance of random coincidences estimation methods, but also to study the effects of the methods on the reconstructed image. This source was a 20 mm long, centred cylinder of 60 mm diameter without attenuation media and filled

Table 4.1: Simulated sources.

	Source	*Position*	*Dimensions*(mm)	$A(MBq)$	$T(s)$
a	Small Sphere	centered	$r = 1$	3.7	60
b	Hot-Cold-Back.	centered	$r = 30, h = 20$	$3.7 + 1.59$	600
c	Plane	centered	$x = 2, y = 40.3,$ $z = 26.5$	3.7	60
d	Rat-like	17.5 mm offset	$r = 1.05, h = 140$	3.7	60

with activity (background, 3.7 MBq). Inside this cylinder two rods were placed, a cold rod without activity, and a hot rod with 3 times the activity concentration of the background (1.59 MBq). Both rods had the same dimensions (19.5 mm length and 20 mm diameter). The hot rod was located in the lower half of the cylinder while the cold rod was in the upper half (see figure 4.2b). For image reconstruction purposes, the acquisition time for this source was 600 s. Inside this source three ROIs were defined like in the previous chapter (figure 3.5). The three ROIs were cylinders, whose dimensions were 8-mm height and 16-mm diameter. These ROIs were used to quantify the quality of the reconstructed images based on the figures-of-merit described in section 1.1.4.

To investigate the influence of the activity in the random estimation methods, simulations for various activity concentrations within the hot rod and background keeping constant the 3:1 ratio were carried out. The total activity of the background cylinder ranged from 3.7 MBq to 111 MBq.

The expression for MLEM in equation 1.31 (page 48) with the MCSM presented in chapter 3 was used for obtaining the reconstructed images from these simulations. For this study, in order to focus on random correction, the simulated object has no attenuation media. Therefore, there is nor scatter, neither attenuation in the object and it is not necessary to take them into account, $s_i = 0$ and $a_i = 1$. Several reconstructions of the same set of data (double coincidences) were performed for the different values of the random coincidences obtained using the DW and SR methods, for two LETs (200 keV and 400 keV) and for 100 iterations. Additionally, the case of using pre-corrected data (DW or SR) for reconstruction has been studied. These images are referred to as DWSub or SRSub respectively.

4.1.3 Figures-of-Merit

To quantify the quality of the reconstructed images, the following figures-of-merit were employed (all of them defined in section 1.1.4):

1. Discrepancy (D), calculated using the hot and background ROIs defined in figure 3.5; the reference is the reconstructed image obtained employing only the true coincidences. The reconstructed images with and without randoms correction are compared to reference.

2. Mispositioned Events(ME)

3. Signal-to-Noise Ratio (SNR)
4. Background Noise ($\bar{\sigma}_{bkg}$)
5. Contrast Recovery Coefficient (CRC)

4.2 Results

In this paragraph we describe the outline of the results part of this chapter. When studying the DW and SR randoms estimation methods for MADPET-II data at lower LET, it was observed an overestimation in the number of random coincidences. The randoms overestimation is presented in the section 4.2.1 for different sources simulated with GATE. We have seen that this overestimation decreases for LETs higher than 255 keV and it is reduced when the single events which have undergone a Compton interaction in crystals before being detected are removed from the data. These two facts lead us to infer that the overestimation is due to the inter-crystal scatter (explained in section 4.2.2). Including triple coincidences could be a possible solution to solve this problem and some data that support this option are shown in section 4.2.3. The effect of this overestimation on the reconstructed image is studied for a hot-cold-background source with 3.7 MBq totat activity in the background region and 1.59 MBq total activity in the hot region in section 4.2.4. Finally the last section (4.2.5) is dedicated to analyze the effect on the overestimation when changing the source activity.

4.2.1 Overestimation of the Random Coincidences

In figure 4.3, the total number of double randoms (d_r) obtained from the simulations of the planar source using GATE information, d_r^{gate}, is compared with the double randoms estimated using the DW, DW', SR, and TH methods ($d_r^{dw}, d_r^{dw'}, d_r^{sr}, d_r^{th}$, respectively), by calculating the ratio d_r^{method}/d_r^{gate}. Ideally, this ratio should be 1. The graphs show that the number of randoms for the DW, DW', and SR methods is higher than d_r^{gate}. It can be seen that the overestimation of randoms is higher for lower LETs. In the case of LETs higher than 250 keV, the agreement between d_r^{dw}, $d_r^{dw'}$, and d_r^{sr} with d_r^{gate} is better and is not changing largely when varying the LETs. For the case of TH, the estimated randoms are slightly lower than d_r^{gate}, unlike the other methods. The observed overestimation for DW and SR does not change substantially for the different τ values, except the curves of the SR method at the two lowest LETs (100 and 150 keV). Therefore τ was set to 20 ns in the analysis that follows, which is twice[1] the time resolution at a single channel of the system to ensure that almost all the double true coincidences are within this window.

As an aside, it is interesting to calculate the ratio between the total number of double randoms in the simulation, d_r^{gate}, and the prompts, d_p, for the different

[1]The width of the time coincidence window is traditionally chosen to be twice the system's measured time resolution

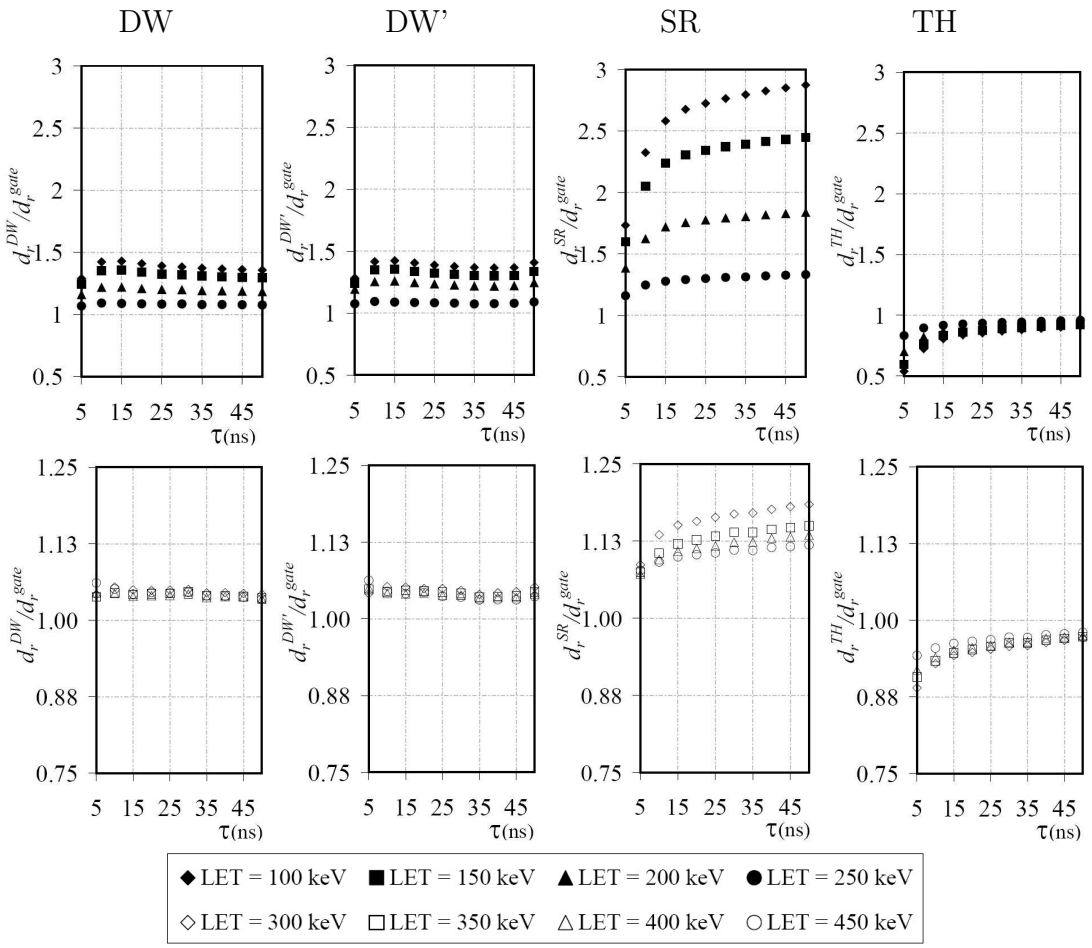

Figure 4.3: Ratio between d_r estimated with DW, DW', SR, and TH methods and d_r obtained using GATE information as a function τ for a planar source and for different LETs.

sources. This ratio is presented in figure 4.4. It is observed in these plots that the percentage of randoms is increasing for higher LETs for the same source. Comparing the sources, the point source is the one that has the lowest value of this ratio. This can be explained as follows. In general, we could differentiate two types of random coincidences. One type would be the random coincidences created because one of the photons is not detected although it has passed through the detector crystals. The other type would correspond to the case in which the photon is not detected because there is not detector in its path[2]. Considering the point source at the center of the FOV, only the first type of random coincidences is geometrically possible and they are less probable. The source with higher percentage of randoms is the NEMA rat-like, due to the fact that almost all the activity of the source is outside the FOV. Comparing the plane source with the Hot-cold-background source, the latter has higher ratio of randoms because it has

[2]In both types, it is necessary that a second annihilation is produced and one of the photons goes undetected.

higher activity than the plane.

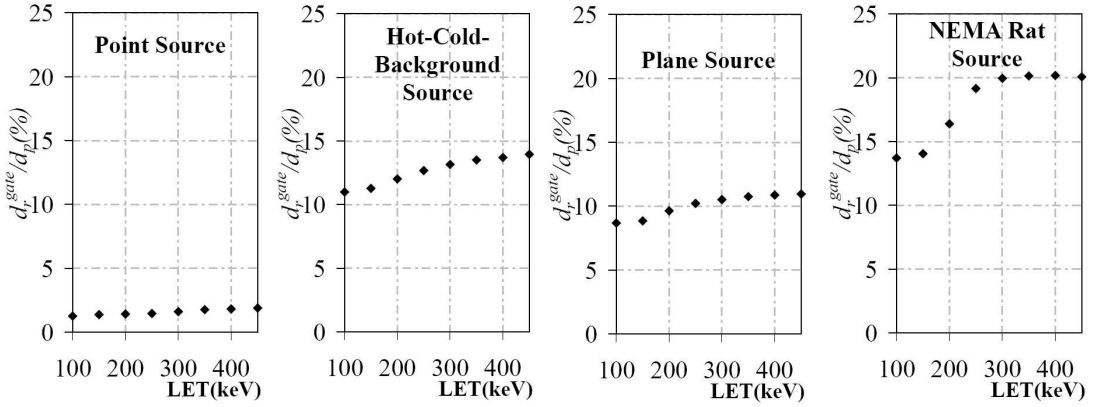

Figure 4.4: Ratio between d_r obtained with GATE and the prompts d_p in the simulations for different LET, all the sources, and τ=20 ns.

In figure 4.5 the ratios d_r^{method}/d_r^{gate} for τ = 20 ns and different LETs are plotted for the point, hot-cold-background, plane, and NEMA rat-like sources. For all randoms estimation methods, the mismatch between estimated randoms and those simulated was largest at lower LETs and decreased when the LET was increased, becoming roughly constant (approaching to 1) for LETs higher than 255 keV. In addition, the mismatch depends on the radial and axial extension of the source, being larger for the smallest source (small sphere) and smaller for the most extended source (NEMA Rat-like source).

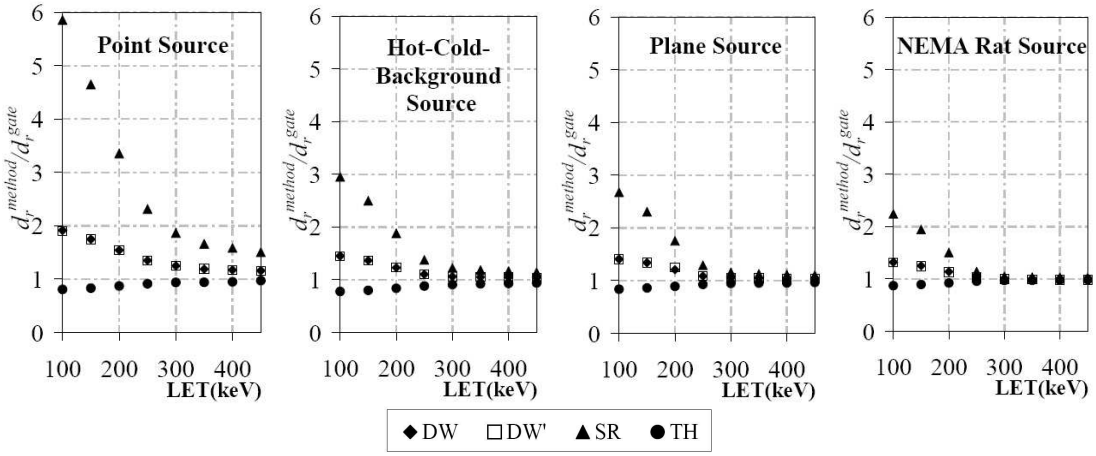

Figure 4.5: Ratio between d_r estimated with DW, DW', SR, and TH methods and d_r obtained using GATE information for different LET and for all sources (τ=20 ns).

Both DW and DW' methods yield the same results. This was expected because both are based in the assumption of uniform distribution of the random coincidences and the two approaches differ mainly in the way of organizing the

data. In the DW, only the original singles chain is used with two time windows (coincidence and delayed time window). Whereas in the DW', the sum of the original plus the delayed singles chain is employed with only one time window. The effect of varying the delay in the DW' method is shown in figure 4.6. For different values of ΔT (150, 200, 300 and 500 ns), the number of double randoms was compared with the number of double randoms for the reference delay, which is $\Delta T = 100$ ns. As illustrated in figure 4.6, the randoms estimation is almost independent of the delay. The discrepancy between the values obtained for different delays and the reference is smaller than 2% for all LETs.

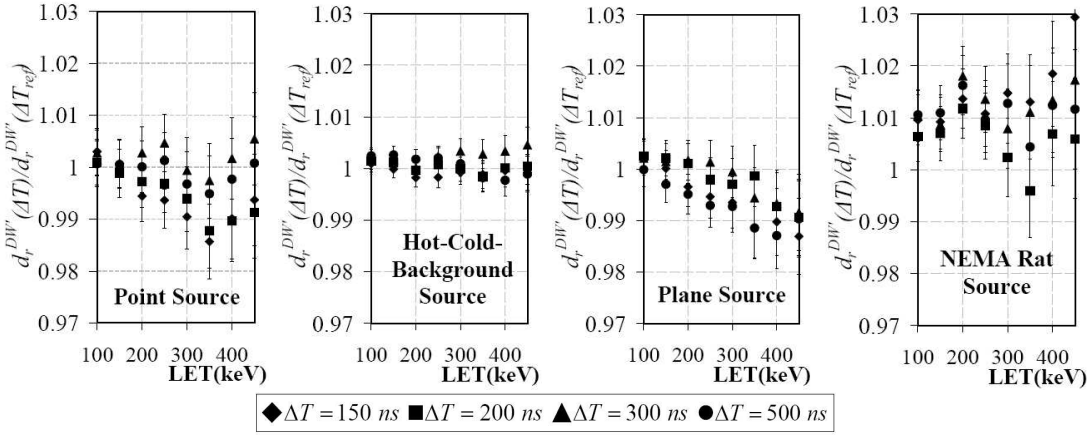

Figure 4.6: Ratio between randoms estimated using the DW' method with some delay, ΔT, and the reference delay ($\Delta T = 100$ ns).

4.2.2 Effect of the Inter-Crystal Scatter

Photons that have undergone a Compton interaction in different crystals (IC scatter) are present in the data for LETs lower than 255 keV [108]. For example, for 200 keV LET, the number of scattered singles in the front layer is 9-10% (external rings) to 20-21% (central rings) higher than the number of singles that have been detected without a previous Compton interaction in a crystal, for all the studied sources. These IC scatter singles coming from one annihilation photon increase the singles rate in a crystal producing a direct effect on the SR method, because singles that not only produce double coincidences but also triple and multiple coincidences were used in this method. In order to apply the method, one needs to use all the singles in each channel. These triple coincidences could be both trues and randoms for a LETs lower than $m_e/2 \simeq 255$ keV. But the triple true coincidences rarely[3] occur at a LET higher than 255 keV and hence the triple coincidences can only be randoms. In addition, if IC scatter singles are present, the probability of finding a single in the delayed window increases. In relation to the TH method, it is necessary to open a wider time window (100 ns) and

[3]Triple true coincidences at higher LET than 255 keV could be possible due to the energy resolution. In an ideal detector, these coincidences would not take place above 255 keV LET.

to find only prompts (two singles in two non-contiguous modules) to make the time histogram. In the presence of IC scatter singles, there are more triples and multiples (more than 3 singles in the time window), consequently the number of double randoms estimated with the TH method is less than the number of randoms obtained with GATE. The latter facts suggest that the IC scatter could have an impact on the random estimation methods. To test this possibility, the effect of removing the IC scatter singles from the singles data was analyzed and the modified data were processed again. To identify the IC scatter singles, the GATE variable `ComptonCrystal` defined in section 2.2 was used. The singles from the initial data that had `ComptonCrystal` equal to zero were the ones being analyzed in this section. By doing this, the results shown in figures 4.7, 4.8, and 4.9 were obtained. The mismatch for the DW and DW' methods almost disappears (figure 4.7), and that for the SR method is substantially reduced (figure 4.8). Thus, the effect of IC scatter is notable when using DW and SR methods at lower LETs. These results also show that the IC scatter impact is considerably reduced at high LETs (above 255 keV, where there is no possibility than a photon produces more than one single). The results also improve in the case of the TH method (figure 4.9), although the mismatch obtained with IC scatter was not as high as for the other methods.

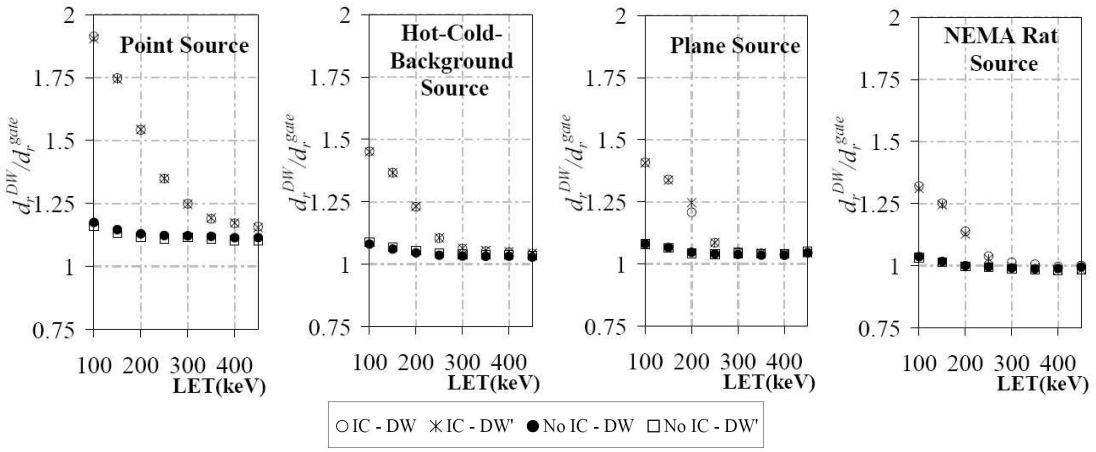

Figure 4.7: Ratio between d_r estimated with DW and DW' methods and with GATE (τ =20 ns, ΔT =100 ns), for several LETs and with and without IC scatter events.

4.2.3 Including triple random coincidences

A possible approach for random estimation applied to MADPET-II for low LETs would be to estimate the percentage of IC scatter singles present in the measurement and remove it, previous to coincidence sorting. However, this strategy implies a substantial decrease in sensitivity. Another approach, which will be examined in more detail in chapter 5, would be to include the triple prompts (defined in section 2.2) in the coincidence sorting. The results shown in figure

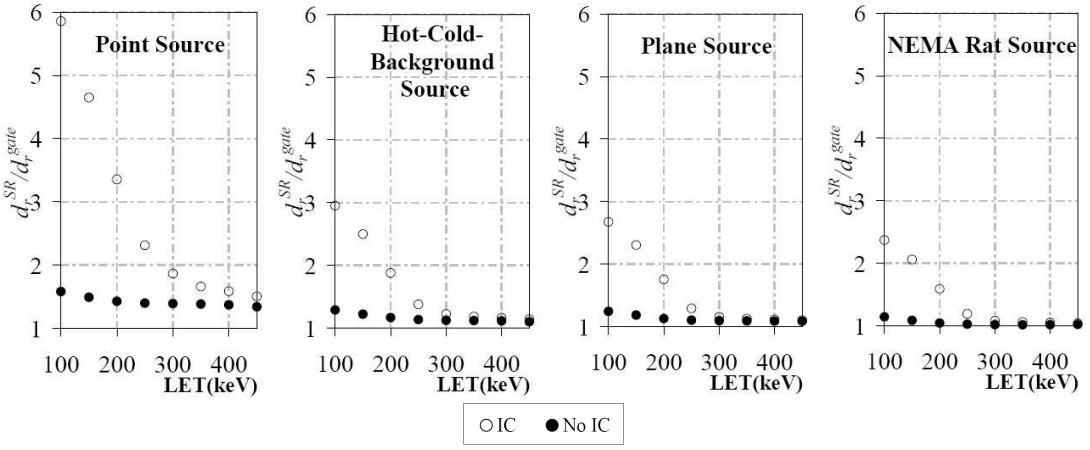

Figure 4.8: Ratio between d_r estimated with SR method and with GATE, for several LETs and with and without IC scatter events (τ =20 ns).

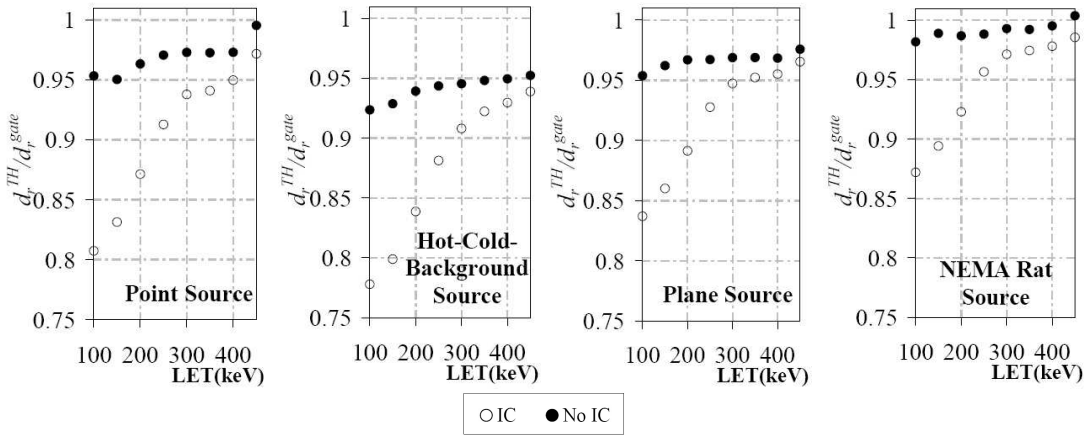

Figure 4.9: Ratio between d_r estimated with TH method and with GATE for τ of 20 ns, for several LETs and with and without IC scatter events.

4.10 motivate this approach. In this figure the total number of triple (two singles found in the delayed window, t_r^{DW}) and double randoms estimated with DW, and the total number of triple (t_r^{gate}) and double randoms obtained using GATE information is compared. The mismatch is dramatically reduced for LETs higher than 200 keV as compared with the data with IC scatter of figure 4.7. Thus, the estimation of random coincidences (combining double and triple randoms) using the DW method is closer to the values obtained with GATE information for the combined double and triple random coincidences. The posterior random correction involving these triple prompts should be addressed elsewhere. In the case of the SR method, in order to take into account the triple randoms, either a new expression for the random coincidences rate should be derived or the singles should be sorted differently. Both options are beyond the scope of this work and will not be further discussed. In the rest of the chapter, we focus only in doubles (prompts, trues, and randoms) and the triple coincidences are studied in more

detail in chapter 5.

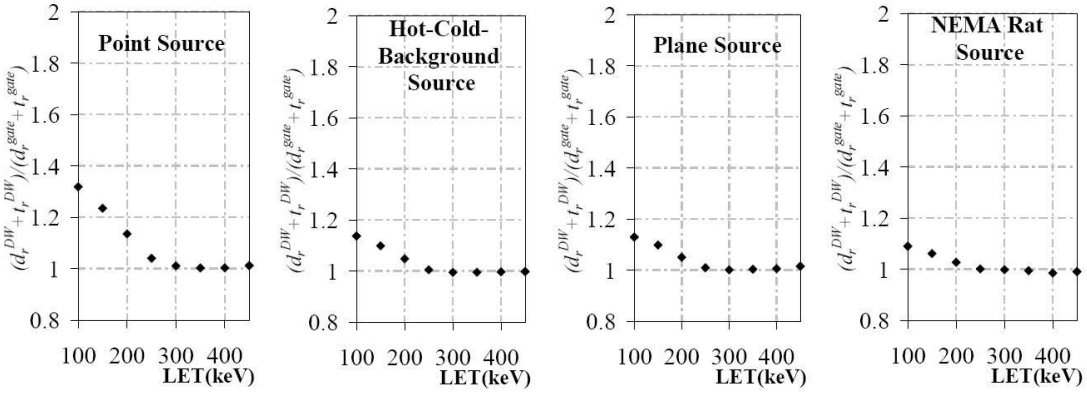

Figure 4.10: Including triple random events in the estimation of the randoms. Ratio between the total number of triple and double randoms estimated with DW, and the total number of triple and double randoms obtained using GATE information. The y-axis range has been chosen in accordance to that of figure 4.7 to make more visible how the overestimation is reduced when the triple randoms are included.

4.2.4 Quantification of the reconstructed activities

The analysis was done for two LETs: 200 and 400 keV. For the 200 keV LET, we have seen that the overestimation of randoms is present for both the DW and SR methods, whereas the overestimation is not important for either method at 400 keV LET. The hot-cold-background source was chosen for this analysis. As we have calculated in the previous section, for this source the randoms to prompts ratio was 12% for 200 keV LET and 14% for 400 keV LET, the overestimation of randoms for 200 keV LET was 23% for the DW method and 87% for the SR method. In the case of 400 keV LET, the overestimation was 5% and 16%, respectively. These values are summarized in the first row of tables 4.2 and 4.4.

Figures 4.11 and 4.12 show no appreciable effects of overestimation of randoms, similar to previous results [115]. It is observed that the reconstructed images obtained at 400 keV LET are noisier than the ones obtained at 200 keV LET, due to the higher sensitivity of the scanner at the lower LET. At 400 keV LET, the reconstructed image, corrected for randoms within the algorithm and using the SR method, is the closest to the reconstructed image using double trues, and shows less noise.

However, the overestimation does effect the quantification of the images. In figure 4.13 the results for the discrepancy, $D(\%)$ (defined in section 1.1.4), are shown. As expected, without randoms correction (prompts), there is an overestimation of the activity measured in both ROIs. In the hot ROI the discrepancy is 3% for 200 keV and 3.3% for 400 keV LET. In the background ROI, the overestimation is higher, ranging between 7% (200 keV LET) and 8.3% (400 keV LET).

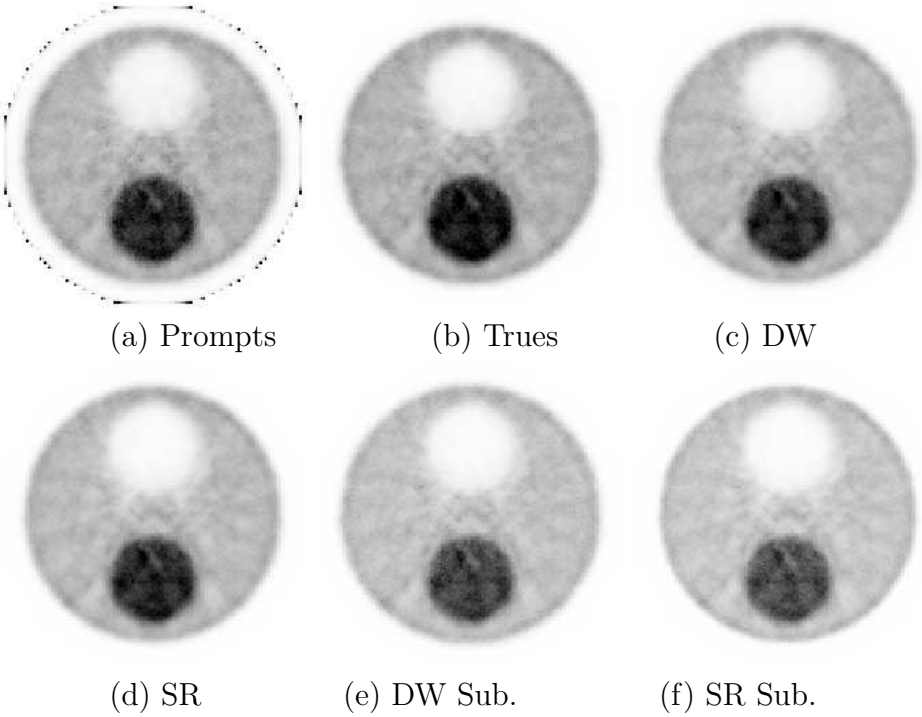

(a) Prompts (b) Trues (c) DW

(d) SR (e) DW Sub. (f) SR Sub.

Figure 4.11: Reconstructed images of the hot-cold-background phantom, using 50 iterations of MLEM, and a 200 keV LET. (a) No correction for randoms, (b) double trues only, (c) randoms corrected using DW method, (d) randoms corrected using SR method, (e) pre-corrected data using DW method, and (f) pre-corrected data using SR method.

Reconstructed images corrected using the DW and SR methods give an underestimation of activity in both ROIs for 200 keV. This underestimation is notably reduced for a LET of 400 keV, at which the discrepancy is around 1% or less for both ROIs. Therefore, the higher number of random coincidences estimated using the SR and DW methods at 200 keV LET produces images with lower activity than actually emitted. In figure 4.13, it is also observed that correcting for randoms within the reconstruction algorithm gives results with a smaller discrepancy value (filled squares for SR and filled circles for DW) than using pre-corrected data (empty squares and circles in the case of SR and DW, respectively) for higher iterations.

In the analysis of the cold ROI, the discrepancy could not be calculated since the standard deviation of the pixel values within the cold ROI was higher than the average value. For this reason, the ME is presented as the FOM to study this ROI. The results are given in figure 4.14. For 200 keV LET, the ME shows the lowest value for SR due to the higher overestimation obtained in the number of randoms. Independent of the number of iterations, the ME values for the different corrections (SR, DW, Sub. SR, and Sub. DW) are equal or smaller than the reconstructed images using trues at 200 keV LET. The randoms overestimation in cold regions should yield negative values in the reconstructed images of these

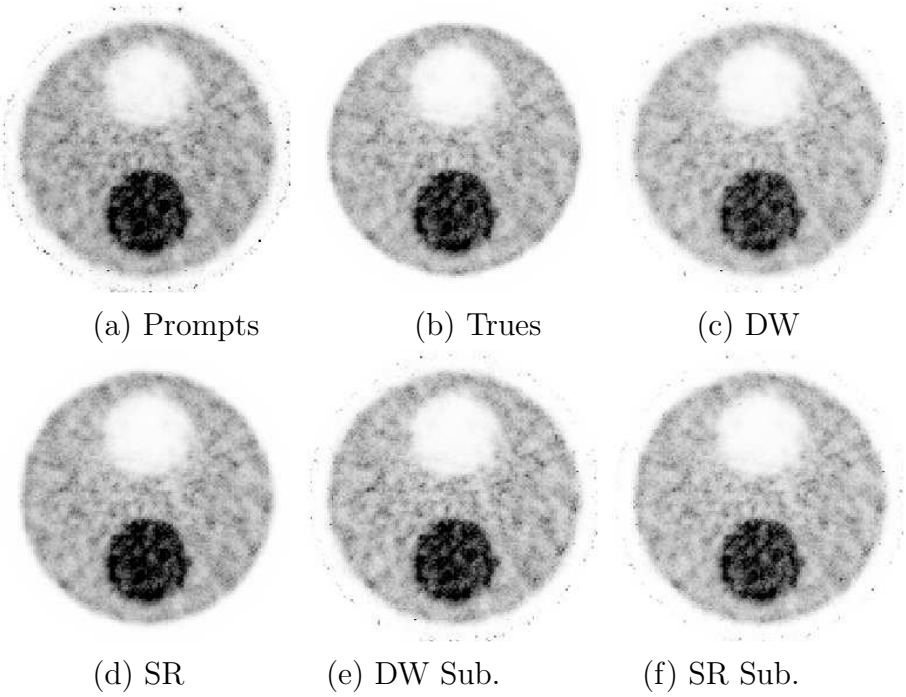

(a) Prompts (b) Trues (c) DW

(d) SR (e) DW Sub. (f) SR Sub.

Figure 4.12: Reconstructed images of the hot-cold-background phantom, using 50 iterations of MLEM, and a 400 keV LET. (a) No correction for randoms, (b) double trues only, (c) randoms corrected using DW method, (d) randoms corrected using SR method, (e) pre-corrected data using DW method, and (f) pre-corrected data using SR method.

regions, but this does not happen with the MLEM algorithm, which can only generate positive values. Therefore, the effect of the overestimation using this algorithm in the cold regions apparently goes in the right direction, though this is a misleading result. The values of ME at 400 keV LET for the trues and the corrected reconstructed images are very close. The highest values of ME are always for the non-corrected images (prompts), both at 200 keV and 400 keV LET, in agreement with the well-known fact that randoms are an important source of background noise.

In addition to the discrepancy and the mispositioned events in the reconstructed activity, the SNR, CRC, and $\bar{\sigma}_{bkg}$ values defined in section 1.1.4 have been calculated. They are presented in figures 4.15 and 4.16. From these FOM values, the images that yield better results are the ones corrected using DW at 200 keV LET and SR for 400 keV LET. Like for the D and the ME, in the case of the 400 keV LET shown in figure 4.16, images corrected with SR or DW yield almost the same CRC as images with only double trues. But, the SNR at 400 keV LET (figure 4.15) shows slightly different results for the different methods. The latter is a consequence of the different levels of noise in the reconstructed images, being higher when precorrecting and for the DW method. To summarize the results of the studied FOMs for 400 keV LET, differences among the correcion methods can only be seen in terms of noise (SNR, $\bar{\sigma}_{bkg}$). The correction

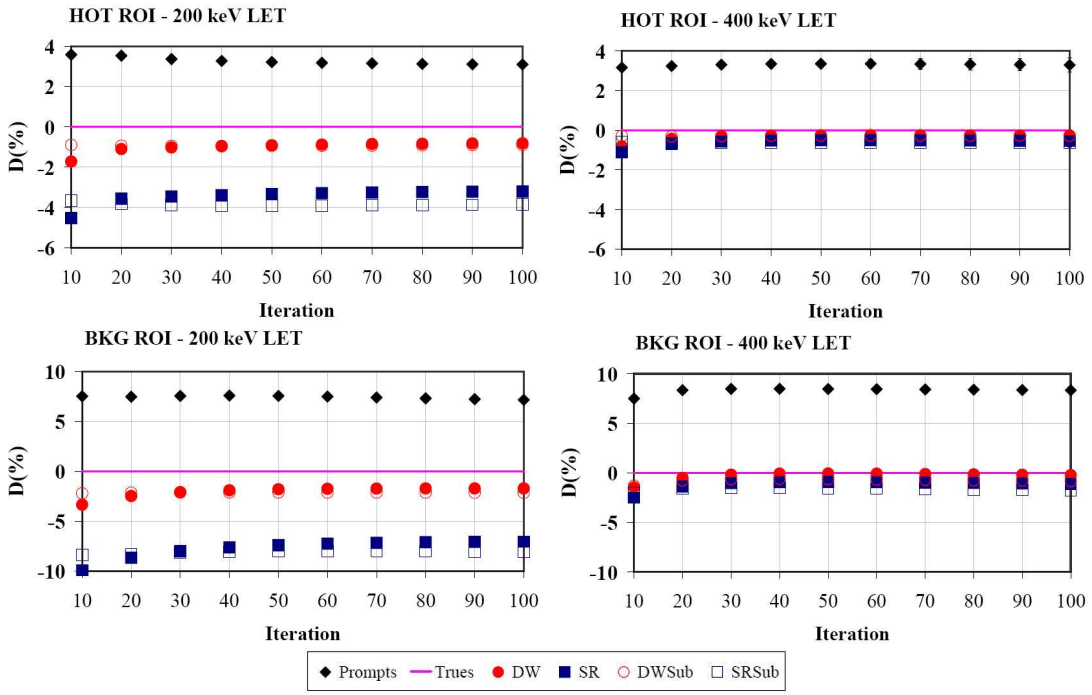

Figure 4.13: Discrepancy in the activity of the reconstructed images calculated within the hot (upper row) and the background (lower row) ROI for LET 200 (left column) and 400 (right column) keV as a function of number of iterations.

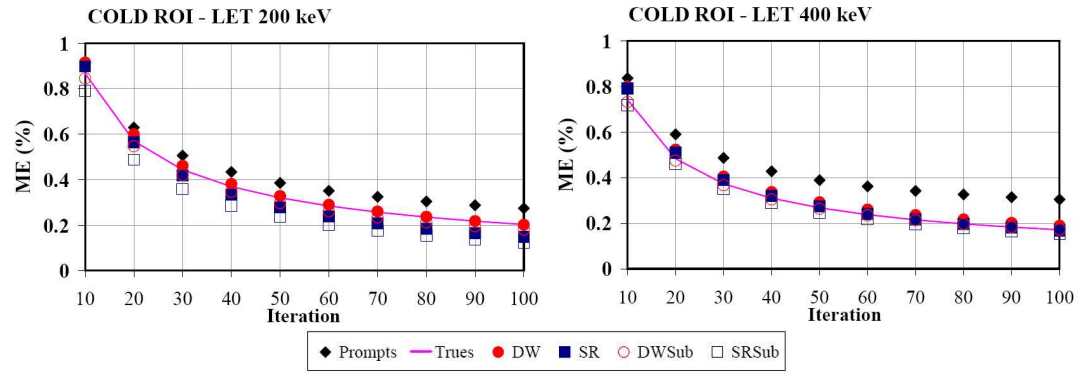

Figure 4.14: Mispositioned Events within the cold ROI for LET 200 (left) and 400 (right) keV as a function of number of iterations. Ideally, $ME = 0$

methods provide almost the same performance considering the contrast (CRC) and reconstructed activity (D, ME).

Considering 200 keV LET, the behaviour of the images varies according to the different randoms correction methods used. The better CRC values achieved using SR correction are mainly due to higher contrast. But, the contrast is higher due to overestimation. For example for the hot-cold-background source, overestimation causes the activity in the background to be 7% lower compared with trues and in the hot region 3% lower in relation to trues for the SR method at 200

keV LET. Consequently, the CRC is higher than 100% (approximately 106%). The same effect can be seen for SR when using pre-corrected data (SRSub), but the images are noisier due to the precorrection. In the case of the DW method, a similar outcome is observed, but less pronounced. In general, when comparing pre-corrected data to data corrected within the reconstruction algorithm, although there is not a remarkable difference, the pre-corrected reconstructed images are worse, mainly in terms of SNR and noise.

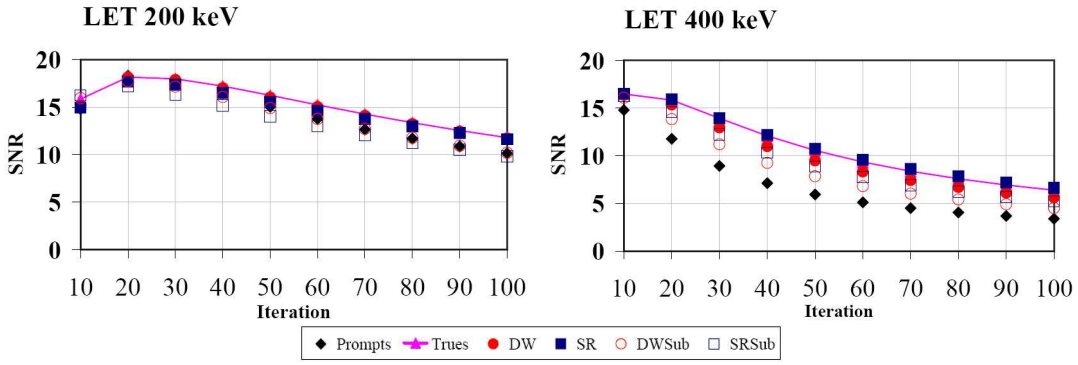

Figure 4.15: SNR for LET 200 (left) and 400 (right) keV as a function of the number of iterations.

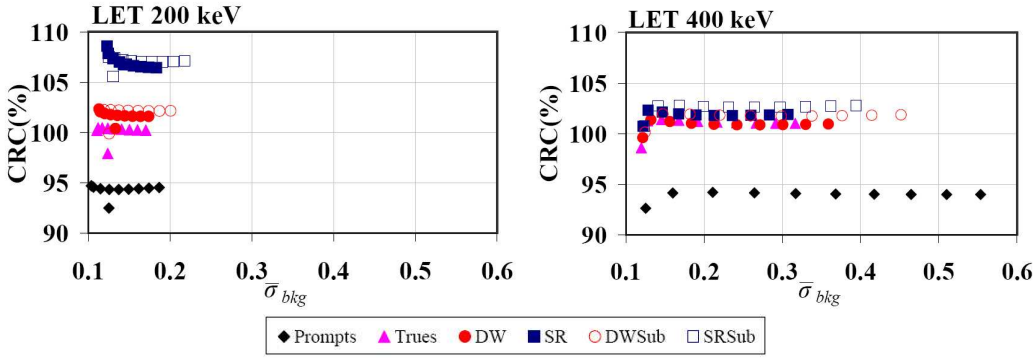

Figure 4.16: Comparison of CRCs versus $\bar{\sigma}_{bkg}$ for LET 200 (left) and 400 (right) keV. Ideally, CRC=100 % and $\bar{\sigma}_{bkg}$=0.

4.2.5 Effect of the activity on the overestimation of randoms

In this section we discuss the dependence of the overestimation of randoms on the source activity. For this part, we have focused on one source, the hot-cold-background, two LETs (200 and 400 keV) and two random estimation methods, SR and DW. To run all the simulations in a feasible time, the acquisition time in the simulation has been reduced to compensate the increase of activity, keeping the number of emitted events and the simulation time[4] constant. The results are shown in figure 4.17. As we can see from the figure 4.17, the randoms overestimation in the case of the DW is constant with the activity, whereas in the case of the SR increases notably. The probability of having triple (and also multiples) random coincidences goes up as the activity raises, although these triple random are considered negligible to develop the expression used in the SR method [104]. At 400 keV LET, the triple randoms represent 1% of the sum of double and triple coincidences when the activity of the background is 3.7 MBq, whereas at 74 MBq background activity, the percentage of triple randoms over the sum of triples and doubles is 12%. In the case of 200 keV LET, the ratios between triple randoms and the sum of triple and double coincidendes are 3% and 25% for 3.7 and 74 MBq of background activity, respectively. Therefore, these triple random coincidences, present in both 200 and 400 keV LETs, produce the increase of the overestimation for higher activities in the SR method.

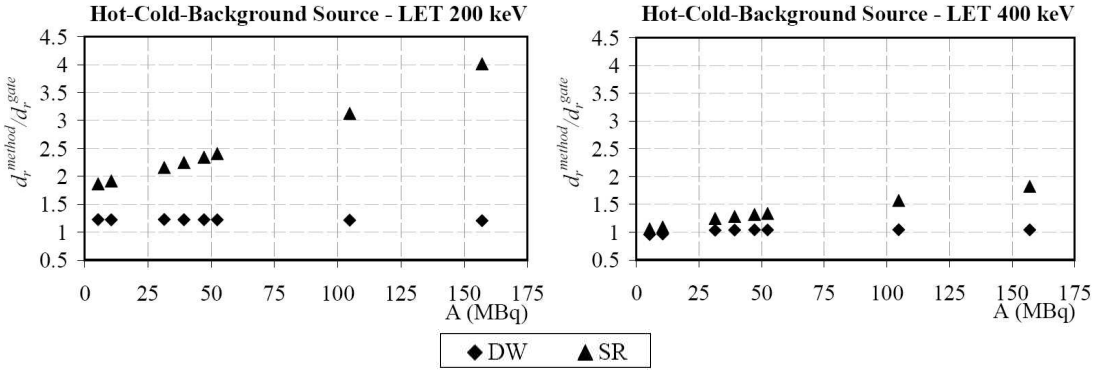

Figure 4.17: Ratio between d_r estimated with DW and SR methods and d_r obtained using GATE information for the hot-cold-background source and for the different activities (τ=20 ns).

Next we consider the effect of the activity in the randoms corrected images. We have selected three reference values among those shown in the figure 4.17. These correspond to a total activity of the background region of 11.1, 27.75 and 74 MBq. The reconstructed images for these activities can be seen in the figures 4.18 for the 200 keV LET case, and 4.19 for the 400 keV LET. The first

[4]The time that the simulation is running on the computer.

interesting feature of these images is that, as a consequence of not correcting for randoms (first column: prompts), there are artifacts in the image, not only the high intensity voxels at the edge of the FOV, but also a ring-flower like structure inside of the hot-cold-background phantom. This structure is similar to a reconstructed image where all the LORs have the same value (figure 4.20b). The random coincidences add background noise in the data and thus, the use of the constant LOR histogram. The artifact becomes more important as the activity increases, because the random coincidences rate increases as the square of the activity. For the trues reconstructed images (second column of figures 4.18 and 4.19), slight differences between them are noticeable. These differences are due to the less statistics in the input data as the activity increases (see table 4.3 and 4.5). The original double trues at lower activities may become triple randoms at higher activities, thus the reduction in double trues as the activity increases. Also it can be seen that the images at 400 keV are noisier than the others at 200 keV, as a consequence of the lower sensitivity at this LET.

For the DW reconstructed images (third column of both figure 4.18 and 4.19), those with 74 MBq of background activity and both LETs show blurred edges of the background, hot and cold regions. This is more obvious for the case at 200 keV LET than at 400 keV. The plots in figure 4.17 show that the overestimation of the DW method is almost constant with the activity for both LETs. Therefore, one could expect that the overestimation has the same effect on the images at 74 MBq than at 3.7 MBq. But, due to the fact that the random coincidences increase as the square of the activity, the outcome of the overestimation is higher for higher activities, as we can see in tables 4.2 and 4.4 in the percentage of the randoms for the DW method. This is the reason of the lowest quality of the DW-images at 74 MBq. Looking at the table 4.3, one can see that the d_t^{gate} at 74 MBq is slightly lower than the d_t^{DW} at 27.75 MBq, and observing the reconstructed images there are some differences in them. The edges of the phantom structure are blurrier in the case of DW method and 27.75 MBq. Thus, the overestimation for the DW at 27.75 MBq is removing important information for the reconstruction and it is affecting to the quality of the reconstructed image (it is more obvious the case of SR method at 11.1 MBq, that has almost the same trues than the simulation, d_t^{gate}, at 74 MBq, but the SR reconstructed image is worse).

Finally, the reconstructed images corrected using the SR estimation (fourth column) are strongly affected by the overestimation, up to the point that the source cannot be properly reconstructed, as it is the case for the background activity of 27.75 and 74 MBq at 200 keV LET and 74 MBq at 400 keV LET. Indeed the SR corrected image for 74 MBq at 200 keV LET shown in figure 4.18 corresponds to the 20th iteration; further iterations lead to an image in which all the voxels have zero intensity. Thus for the SR method, the combination of the increase of both the overestimation and the random coincidences with the activity produces poorly reconstructed images.

After the qualitative analysis of the reconstructed images, we present relevant FOMs for these corrected images. In the figure 4.21, the plots of the discrepancy versus the iteration number for the DW corrected images are shown. At 200 keV

Table 4.2: Percentage of randoms ($P_r(\%) = d_r^{gate}/d_p$), randoms overestimation ($O^{method}(\%) = d_r^{method}/d_r^{gate} - 1$), and percentage of estimated randoms ($P_r^{method}(\%) = d_r^{method}/d_p$) for the DW and SR methods obtained for the different activities at 200 keV LET.

$A_{BKG}(MBq)$	$T(s)$	$P_r(\%)$	$O^{DW}(\%)$	$P_r^{DW}(\%)$	$O^{SR}(\%)$	$P_r^{SR}(\%)$
3.70	600	**12.2**	23.0	**15.0**	87.3	**22.8**
11.10	200	**29.4**	22.7	**36.1**	96.3	**57.7**
27.75	80	**51.1**	22.3	**62.4**	122.4	**113.5**
74.00	30	**73.6**	21.2	**89.3**	204.8	**224.5**

Table 4.3: Total trues in the simulation (d_t^{gate}) and total trues after randoms substraction (d_t^{method}) for the DW and SR methods obtained for the different activities at 200 keV LET.

$A_{BKG}(MBq)$	d_t^{gate}	d_t^{DW}	d_t^{SR}
3.70	24.9×10^6	24.1×10^6	21.9×10^6
11.10	23.3×10^6	21.1×10^6	14.0×10^6
27.75	20.5×10^6	15.8×10^6	< 0
74.00	14.5×10^6	5.9×10^6	< 0

Table 4.4: Percentage of randoms ($P_r(\%) = d_r^{gate}/d_p$), randoms overestimation ($O^{method}(\%) = d_r^{method}/d_r^{gate} - 1$), and percentage of estimated randoms ($P_r^{method}(\%) = d_r^{method}/d_p$) for the DW and SR methods obtained for the different activities at 400 keV LET.

$A_{BKG}(MBq)$	$P_r(\%)$	$O^{DW}(\%)$	$P_r^{DW}(\%)$	$O^{SR}(\%)$	$P_r^{SR}(\%)$
3.70	**14.1**	4.7	**14.8**	16.0	**16.4**
11.10	**33.1**	4.5	**34.5**	18.7	**39.3**
27.75	**55.3**	4.4	**57.7**	27.6	**70.6**
74.00	**76.8**	4.3	**80.1**	53.1	**117.5**

Table 4.5: Total trues in the simulation (d_t^{gate}) and total trues after randoms substraction (d_t^{method}) for DW and SR methods obtained for the different activities at 400 keV LET.

$A_{BKG}(MBq)$	d_t^{gate}	d_t^{DW}	d_t^{SR}
3.70	8.6×10^6	8.6×10^6	8.4×10^6
11.10	8.3×10^6	8.1×10^6	7.5×10^6
27.75	7.7×10^6	7.3×10^6	5.0×10^6
74.00	6.2×10^6	5.3×10^6	< 0

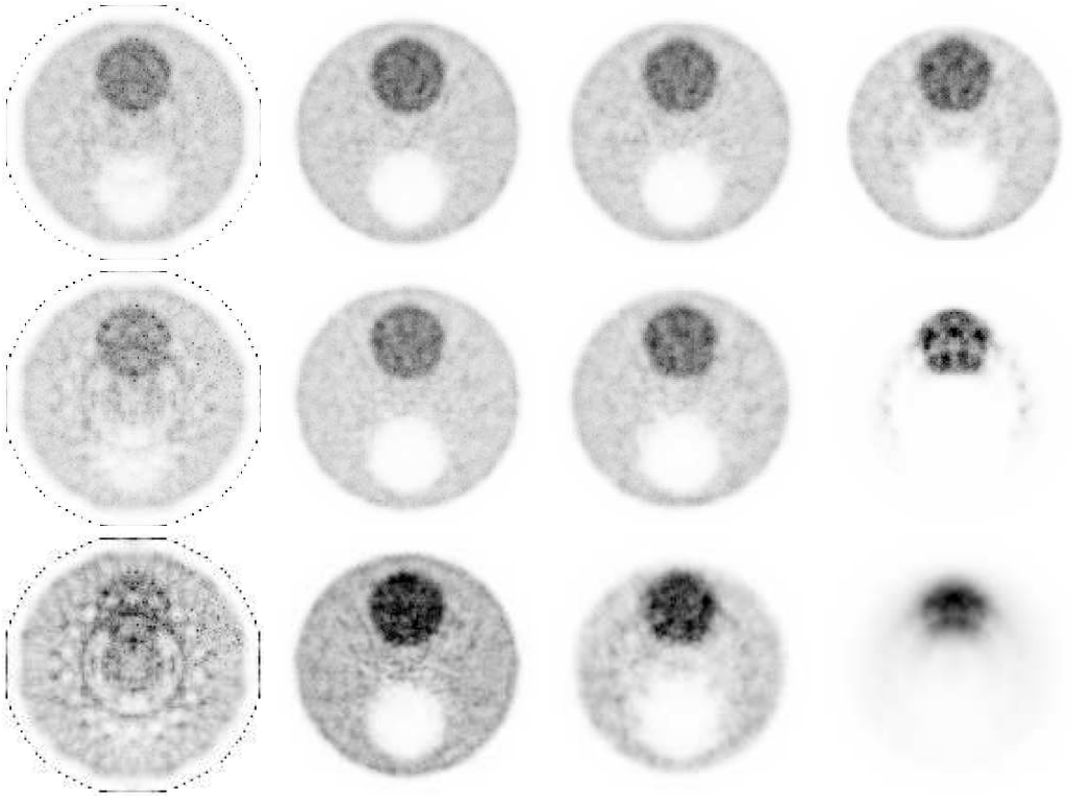

(a) Prompts (b) Trues (c) DW (d) SR

Figure 4.18: Reconstructed images of the hot-cold-background phantom, using 100 iterations of MLEM, and at 200 keV LET for different activities: First row correspond to $A_{BKG} = 11.1$ MBq; Second row, $A_{BKG} = 27.75$ MBq; Third row, $A_{BKG} = 74$ MBq. The SR corrected image for 74 MBq corresponds to the 20th iteration, because the image of the 100th iteration has value zero for all the voxels.

LET (two most left plots), it is observed that, although the overestimation in the DW method is almost independent of the activity, the discrepancy is negatively increasing with the activity due to the higher percentage of the random coincidences. As we have seen before, the overestimation affects more to the background region than to the hot one. From figure 4.17 we know that the overestimation is around 5-4% for the DW method at 400 keV LET, and we hardly see an effect in the reconstructed images, except for the images with background activity of 74 MBq, where we found the biggest difference between the randoms percentage, P_r, and the estimated randoms percentage for DW method, P_r^{DW} (see table 4.4).

In the case of the SR method, the plots of the discrepancy for the hot and background ROIs are displayed in the figure 4.22. The behaviour observed in these plots is expected from the increase of the overestimation and the poor quality of the reconstructed images as the activity increases. In the SR method, an increase in the activity yields an increment of the overestimation for both LETs (increase of the triple coincidences that are not accounted for in the SR

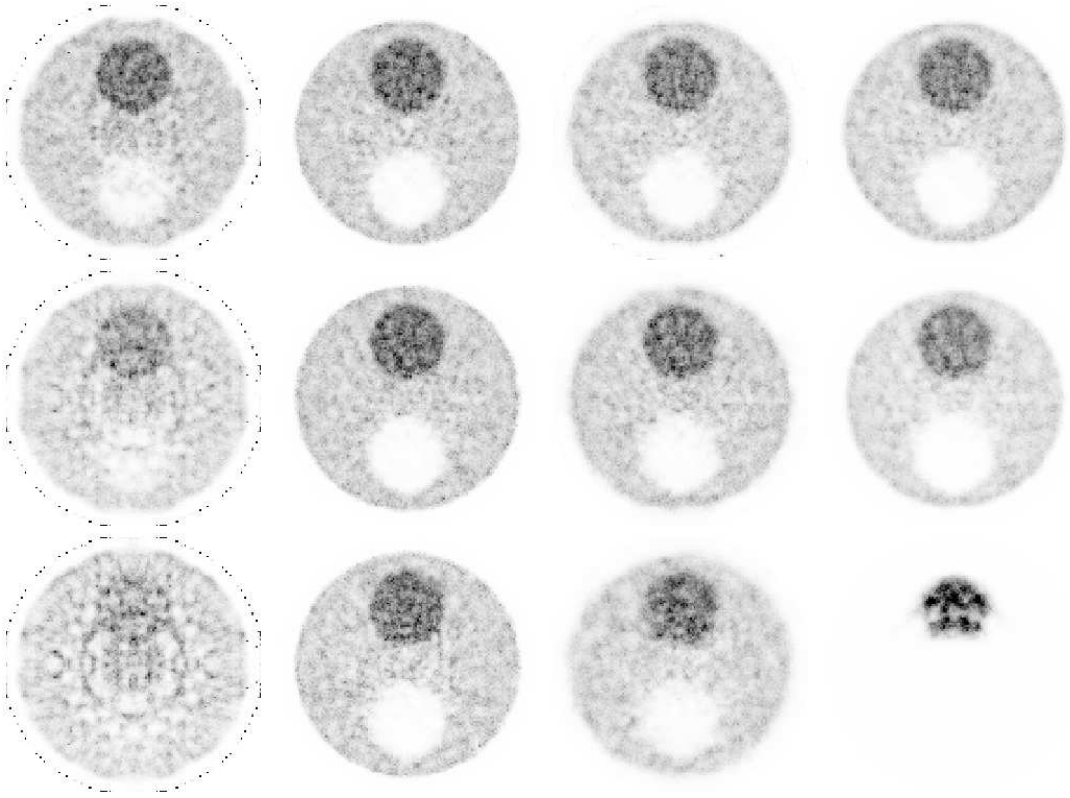

(a) Prompts (b) Trues (c) DW (d) SR

Figure 4.19: Reconstructed images of the hot-cold-background phantom, using 100 iterations of MLEM, and a 400 keV LET for different activities: First row correspond to $A_{BKG} = 11.1$ MBq; Second row, $A_{BKG} = 27.75$ MBq; Third row, $A_{BKG} = 74$ MBq

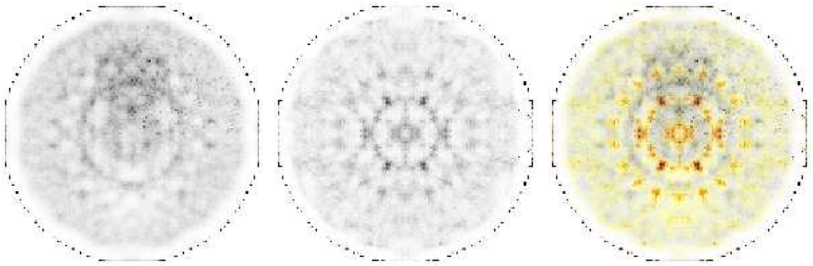

(a) Prompts (b) Constant LOR histogram (c) Combination of both images

Figure 4.20: (a) Reconstructed image of the hot-cold-background phantom, using 100 iterations of MLEM, and a 200 keV LET for a background activity of 74 MBq. (b) Reconstructed image of a uniform LOR histogram after 100 iterations and at 200 keV LET. (c) Superposition of the previous images.

expression). This increment together with the higher randoms percentage leads to a poor quantification of the hot and background ROIs, being worse for the background and for the 200 keV LET. The discrepancy values of the reconstructed

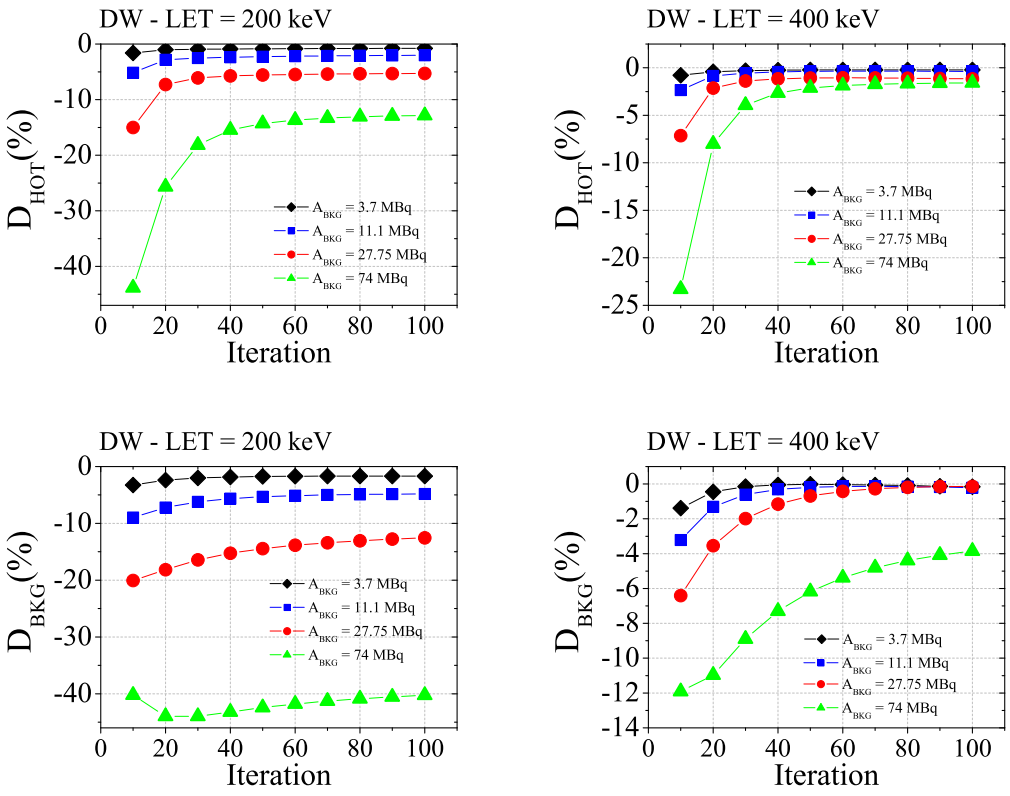

Figure 4.21: Discrepancy of the hot (top row) and background (down) ROI for the DW method and both LETs (200 keV at the left column and 400 keV at the right one) plotted versus the iteration number.

images of the 74 MBq background activity at 200 keV for both ROIs were not plotted because all the images were zero after the 20th iteration.

To end up with the part of the analysis for different activities, the CRC versus the normalized background noise for these images is given in figure 4.23. The main effect of the overestimation is to increase the CRC, as it was also observed in figure 4.16. In the case of 400 keV LET and the DW method, since the overestimation is very small and almost constant, the CRC is close to 100% for all the studied activities, except for the highest one where the randoms overestimation produce the highest increment in the random percentage. When the LET is 200 keV for the corrected images using the DW method, the CRC is above 100 % for all the activities, due to the fact that the overestimation is higher as compared to the one at 400 keV LET. In the same way, for the SR method and both LETs, as the overestimation is higher than in the DW method and going up with the activity, the CRC is always higher than 100 %, even for the lowest activity and 400 keV. In the SR method, for the activities 27.75 MBq and 74 MBq at 200 keV LET the CRCs is above 300 % and it has not been plotted. The same happens at 400 keV LET and SR method, but only for the background activity of 74 MBq.

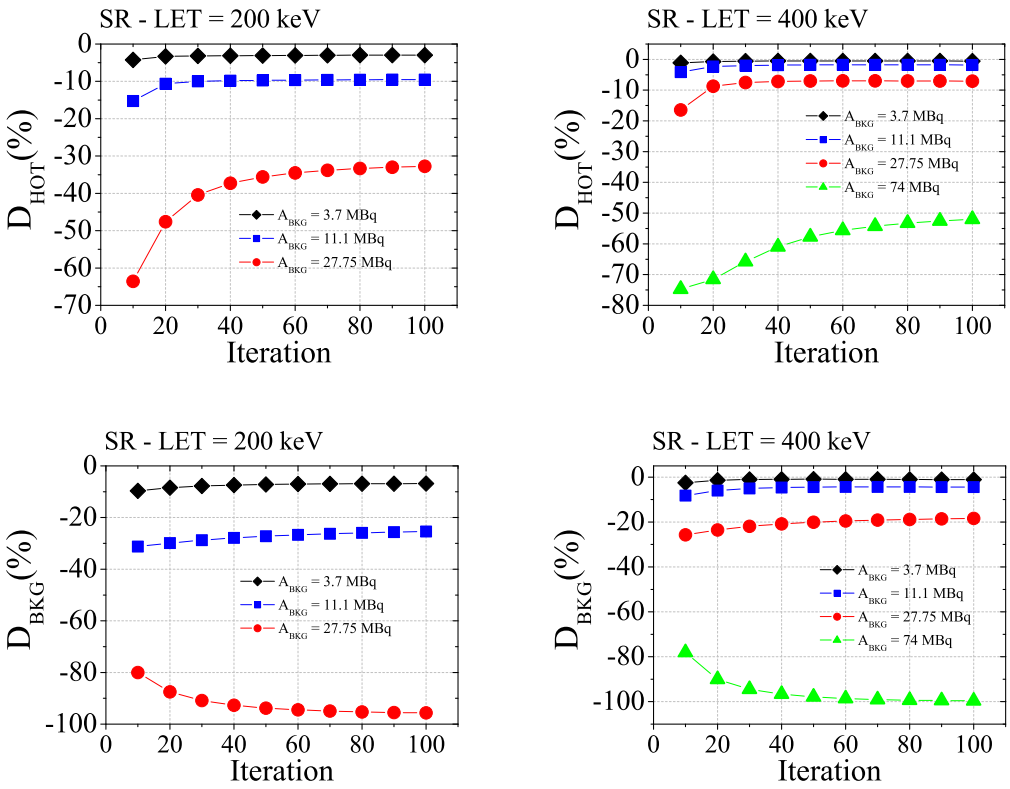

Figure 4.22: Discrepancy of the hot (top row) and background (down) ROI for the SR method and both LETs (200 keV at the left column and 400 keV at the right one) plotted versus the iteration number.

4.3 Conclusions

Delayed window and singles rate methods have been used in this chapter to estimate the random coincidences for MADPET-II at various low energy thresholds. For LETs lower than 255 keV, a notable overestimation of the random coincidences is observed, being higher for the SR method than for the DW method. The overestimation found in the DW and DW' methods cannot be explained from the chosen delay. It was found that this overestimation is mainly caused by inter-crystal scatter, which plays an important role at these LETs. These results were presented for a total activity of 3.7 MBq. When increasing the source activities, the overestimation goes up for the SR method, while it remains constant for the DW method. This behaviour of the SR method is explained by the increment in the number of triple random coincidences. Images obtained by compensating for randoms in the reconstruction algorithm were in general improved in terms of SNR, noise levels and in the determination of the absolute activities than the images made with pre-corrected data. Only in the ME, the pre-corrected images show better results. In general, for all the LETs studied, the DW method is

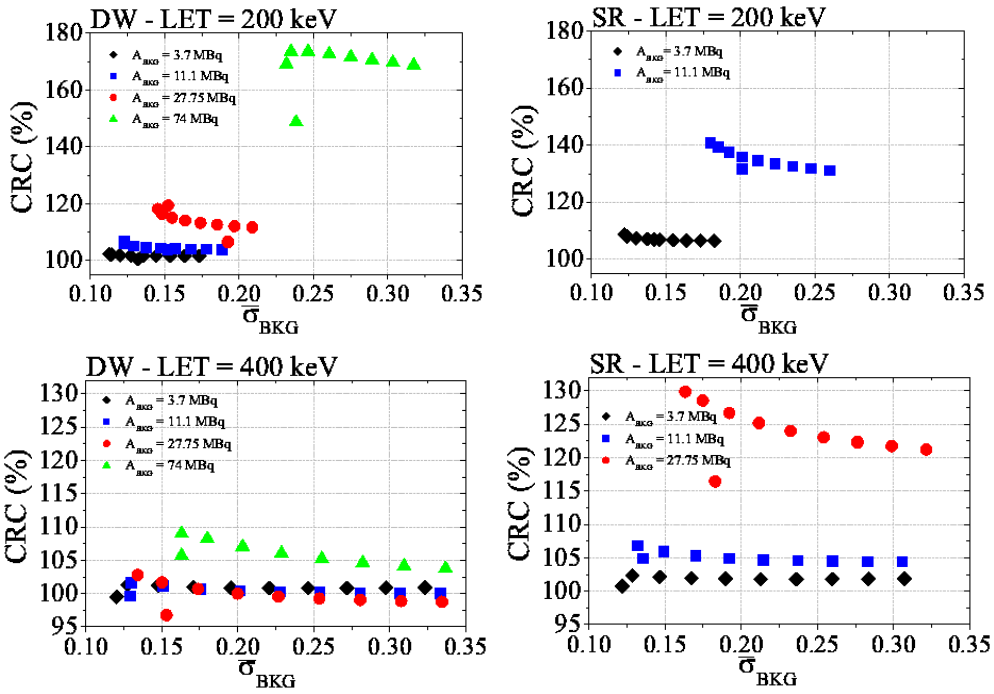

Figure 4.23: $CRC(\%)$ versus $\bar{\sigma}_{BKG}$ for both randoms estimation methods (DW on the left column and SR at the right), for both LETs (200 keV LET at the top row and 400 keV LET at the bottom), and for different activities.

more accurate for assessing the absolute activity of reconstructed images due to the lower randoms overestimation, although the difference with SR at 400 keV is not very important for the lower studied activities. The observed discrepancies for the corrected images at the lowest activity (2%-4% in the worst case) are not a major issue, considering that the accuracy of the activity concentrations in the attenuation uncorrected images is -26.4% for the mouse-sized phantom and -38.5% in the rat-sized phantom [116]. But from the dependence of the overestimation with the source activity, we have seen that the discrepancies are larger for higher activities. At 200 keV LET, the reconstructed images do not show a remarkable difference in terms of noise for the lowest source activity. When the source activity increases, the overestimation produces an increase in the noise of the SR-images at 200 keV LET. At 400 keV LET the reconstructed images using SR show less noise for all the studied activities. The question of the most appropriate LET is still open. With a LET lower than 255 keV ($\simeq m_e/2$), there is an underestimation of the reconstructed activity, but the sensitivity is higher and the reconstructed images are less noisy. Working at these LETs, the DW is preferred. The noise in the resultant images could be reduced using randoms variance reduction techniques as discussed in [102]. For higher LET, quantification is not an issue, but the sensitivity of the system is reduced and the images are noisier; therefore the SR method is the most appropriate for the lower activities because it shows images with less noise. For higher activities and the SR

method, the overestimation has a higher effect on the reconstructed images and, as a consequence, must be corrected for. Future work should investigate how the overestimation in the number of estimated randoms can be corrected using DW and SR methods. Although this study was performed using the MADPET-II geometry, the results are expected to be valid for other systems with finely granulated crystals.

Chapter 5

Triple Coincidences

A triple coincidence can be produced when three singles are found in the same time coincidence window. These three singles could come mainly from one annihilation or from two annihilation that occur simultaneously or within a very short time. In order to have three singles consequence of one annihilation, one of the photons must suffer a Compton interaction and deposit its energy in two crystals (IC scatter). If the system has the ability of differentiating these two depositions (MADPET-II has it), it is possible to obtain a triple coincidence out of the annihilation into two photons. In this chapter, we are interested in this type of triple coincidences and they will be presented in the next section. In the second type that we mentioned, the triple coincidence occurs when one of the photons from the two annihilations is not detected. Because this situation implies two annihilations, this would be a triple random coincidence and they should be included as random coincidences. Other combinations with more than two annihilations can take place that lead to a triple random coincidences, these are rare for the activities of this study and not considered here (0.5 % of the triple coincidences are formed by three singles from three different annihilations at 3.7 MBq and a LET of 200 keV). Finally, the positron annihilation into three photons could also generate a triple coincidence. But this is very suppressed (the yield of the three photon is 0.5% in water [119]) and therefore not accounted in this thesis.

The contribution of the triple coincidences consequence of IC scatter can be used to increase the system efficiency. But, when the primary path of IC scatter is not properly identified, the spatial resolution could worsen. Therefore, these events have been investigated previously by our group in [108]. In the referred paper, it was found out that the combination of individual crystal readout, a low energy threshold and an appropriate recovery scheme, the system efficiency was increased without any major worsening of the spatial resolution when including these triple coincidences. There was no study of the triple random coincidences in [108] because GEANT-3 did not provide time information of the detection process, as it does GATE. In this chapter we resort to this kind of triple coincidences due to the problem found on the random coincidences estimation methods, more important at lower LETs. As it was pointed out in the previous chapter (section

4.2.3), the combination of double and triple random coincidences for the DW method leads to a better estimation.

The goal of this part is to include the triple coincidences in the randoms estimation methods and in the image reconstruction process and determine if the triple events, when working a lower LETs, solve the overestimation problem and produce images with higher quality.

5.1 Triple Coincidences in MADPET-II

As we have already seen in the section 2.2 (page 72), triple true coincidences (same annihilation process) can be detected by MADPET-II. This type of events takes place when one of the annihilation photons delivers its energy in two crystals, whereas the other photon interacts only with one crystal (figure 2.5).

One of the question that arises when handling with triple coincidences is which is, among all possibles LORs, the one related to the original trajectory. To identify the right LOR is important to minimize the spatial resolution degradation. Several algorithms were proposed and studied to identify the primary path of the IC scatter event and then, take the corresponding LOR in [118], [120], [121], [122], [123], [108], [124], [125], [126], [127] and [128]. From the proposed identification algorithms, we have used in this work the *Maximum Energy algorithm* (ME). Although this algorithm has not the highest identification fraction (IF), it is easy to implement and shows less dependence with the energy resolution.

The first step when working with triple coincidences is to differentiate between the two singles related to the IC scatter event and the single related to the non-scattered photon (or, at least, the photon that has generated only one single) using a geometrical condition. We named the last one *reference single*. The second step is to apply the ME algorithm to the two singles that belong to the IC scatter. The crystal of the single that has delivered the highest energy is taken in combination with the crystal of the reference single to form the LOR. An schema of these two steps can be seen in figure 5.1.

5.2 System Matrix for the triple coincidences

The purpose of this chapter is to include the triple coincidences in the image reconstruction process, in the frame of a iterative reconstruction algorithm (in contrast to [108] where an analytic framework was used). Therefore, a system matrix that accounts for this kind of coincidences should be built by using Monte Carlo techniques, continuing with our approach. As we mentioned in chapter 3, computing a 3D system matrix (even employing symmetries and distributed computing) would take several months. Especially if triple coincidences are taken into account, due to the number of possible combinations. For this reason, generating a 2D-system matrix (only for a transversal slice of the FOV, but the emission is in 3D) is a faster way to check, that the introduction of the triples coincidences provide reconstructed images with the same quality than without and improve

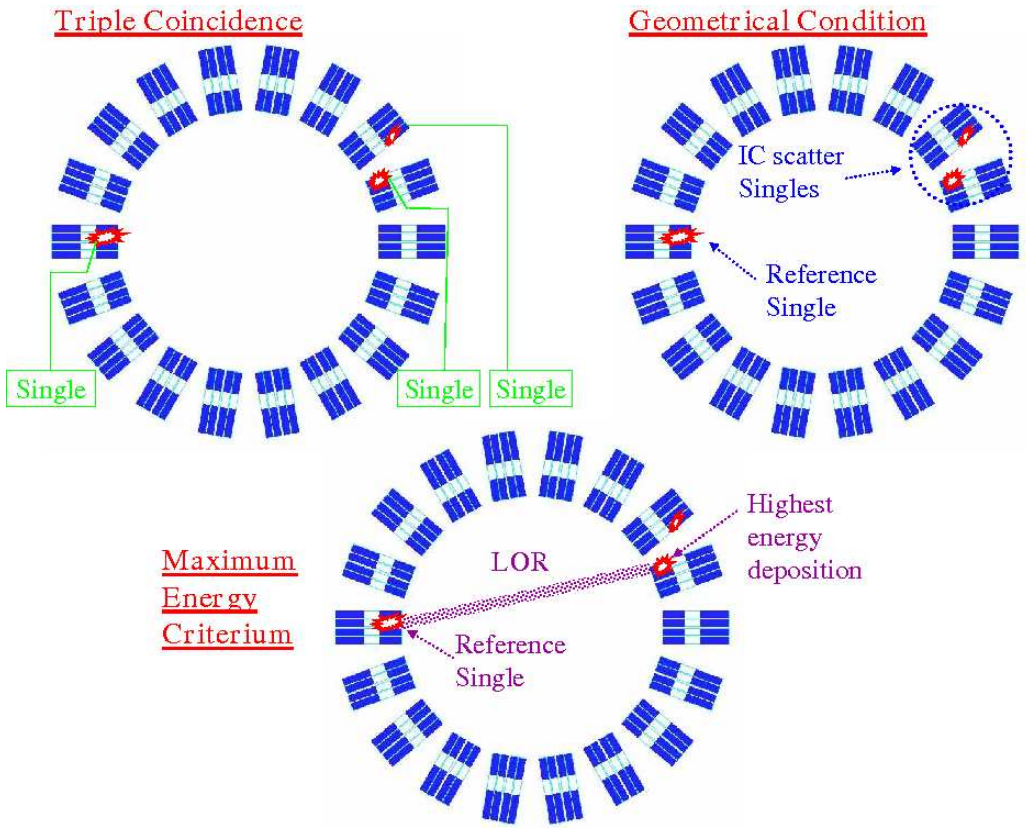

Figure 5.1: Different steps in the procedure of assigning LOR to a triple coincidence. After the triple coincidence is detected, the first step is to identify which is the reference single and which are the IC scatter singles, by employing a geometrical condition. In the second step, the most energetic single from the two singles that were identified as IC scatter, is used in combination of the reference single to assign the LOR.

the results of the random coincidences corrected images. We use the prefix *2D* in the SM to highlight the fact that the SM is only for one transversal slice, although the emission is in 3D and the complete scanner is employed for the detection.

A central plane of the FOV was chosen to create the SM for the triple coincidences (figure 5.2). We have used the simulations previously done for the chapter 3. But we only employed the simulations of the voxels that belong to this central plane. The output files of these simulations were processed again, but in a different way: only triple true coincidences were considered ($m = 2$ and all the singles had the same EventID) and the LOR was assigned using the ME algorithm explained in the previous paragraph. After processing data in the simulations, the triple true coincidences in the LOR i coming from the voxel j, $c_{ij}^{triples}$, are obtained. It is possible to calculate the elements of the doubles and triples SM by adding these new counts, $c_{ij}^{triples}$, to the ones obtained for the double coincidences case, $c_{ij}^{doubles}$.

For consistency with the previous chapters 3 and 4, we compare the SM, the

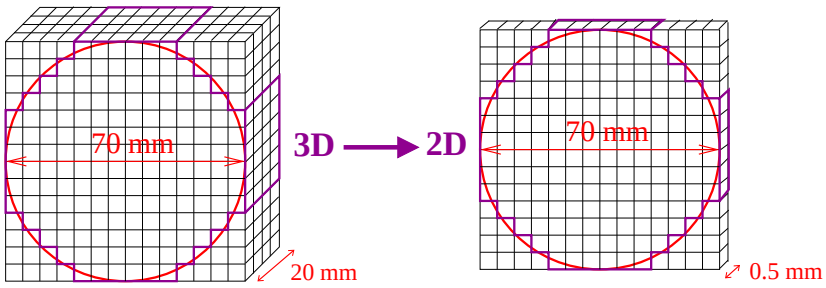

Figure 5.2: As a proof-of-concept, the SM only for a central plane of the whole FOV (2D) was taken to evaluate the inclusion of the triple coincidences.

randoms overestimation and the reconstructed images for the cases of double coincidences ($P^{doubles}$) and double and triple coincidences ($P^{dou+tri}$) at 200 keV LET.

5.3 Random estimation method

The DW and SR random estimation methods were modified to include the triple random coincidences, as we will explain in the next two sections.

5.3.1 Delayed Window method

Using this method, a triple random coincidence was considered when two singles were found in the delayed window, as explained in chapter 4. In order to use the estimation method to correct and reconstruct images, we need to define some criteria to obtain the LOR for the estimated triple random coincidence. We have used either these two criteria to assign the corresponding LOR: maximum distance (MD) and maximum energy (ME). The MD criterion calculates the distance between the single that opens the time coincidence window and the two singles that are found in the delayed window. The combination of detectors that provides the maximum distance is the one taken to define the LOR. On the other hand, the ME criterion chooses the single among the two singles within the delayed window that has the highest energy deposition. As we are handling with random coincidences, there is no reason that supports one condition more than the other. The criteria were applied to the two singles within the delayed window, and the single that opens the time coincidence window was considered the reference. The maximum distance condition uses the crystals combination of the reference single with that single in the delayed window that yields the longest LOR. The maximum energy criterium was applied to the two singles that were in the delayed window: to define the LOR, the highest energetic single within the delayed window was combined with the reference single. The random coincidences estimated using MD or ME condition for the DW method will be named as $DWmd$ and $DWme$, respectively.

5.3.2 Singles Rate method

In this case the modification implies to filter the original singles chain. The filter works as follows: from all those singles found within the same time coincidence window and related to the same or adjacent modules[1], only the single fulfilling the ME is further used. An example is shown in figure 5.3. The first two singles (green) correspond to a valid coincidence (satisfies the geometrical condition) and are not filtered. But, if a non-physically meaningfull double is found (purple), only the most energetic single is kept (as we can see in the filtered single events). If a triple coincidence contained two singles detected in the same or adjacent modules (red), these two were also converted into one using again the ME criterium. After processing and screening all the events, we applied the SR expression to the filtered event chain. We refer to this new sorting as *SRns*.

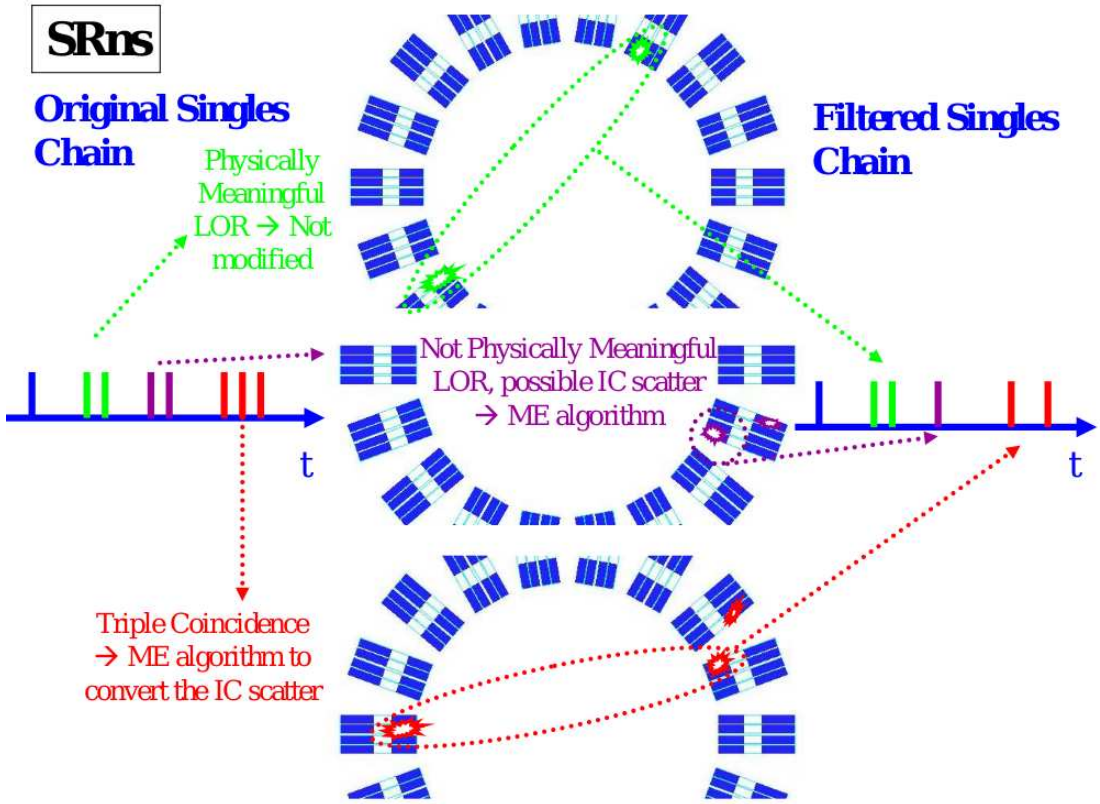

Figure 5.3: Filtering the original singles chain in such a way that almost all the possible IC scatter singles are converted into one single. Some examples of the procedure are depicted in this figure like in the case of a non physically meaningful coincidence (purple), which is converted into one single. On the other hand, a physically meaningful coincidence is not modified (like the case in green). Lastly, in the situation of a triple coincidence, the IC scatter singles become one single (red).

[1]These singles correspond to the ones that define a non-physically meaningfull LOR.

5.4 Simulated sources

We want to address the following objectives with the simulated sources employed in this chapter:

- Evaluate the spatial resolution degradation when including the triple true coincidences and the primary path recovery algorithm.
- Validate the modified DW and SR methods to compensate for triple random coincidences.
- Include the estimated triple random coincidences aimed at reducing the overestimation and obtaining better agreement between the randoms corrected reconstructed images and the reconstructed images with true coincidences.

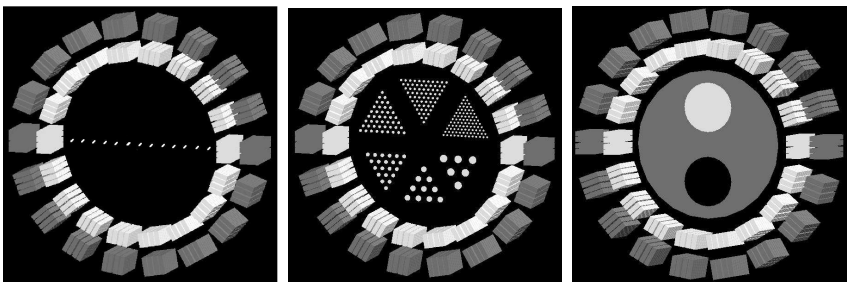

(a) (b) (c)

Figure 5.4: Various sources simulated with GATE to study the introduction of triple coincidences in the image reconstruction process (see table 5.1 for source dimensions).

The simulated sources for this study (see figure 5.4) were confined to the transversal plane in which the doubles and triples SMs was calculated. Therefore the axial dimension of these sources was 0.5 mm to fit into the axial voxel size of the SMs.

Related to the spatial resolution degradation, we have used two sources: the horizontal capillaries that cover the radial FOV and a Derenzo phantom (figures 5.4a and 5.4b). The Derenzo-like phantom was used for qualitative analysis of the image. Like in the chapter 3, this phantom consists of 6 sectors. Each sector contains 0.5 mm long rod sources with diameters of 0.8, 1.0, 1.2, 1.6, 2.4 and 3.2 mm and rod separation twice the diameter. The rod sources were spread within a disc of 62 mm diameter. The total activity of this source was 22.2 MBq. The acquisition time of the simulation was 300 s (number of detected events for doubles and doubles and triples). The horizontal capillaries were employed to assess quantitative values related to the spatial resolution. This source is composed of small cylindrical sources of 0.5 mm long and 0.25 mm radius. They are extended covering the radial FOV and the separation distance between them is 5 mm.

Table 5.1: Simulated sources used in this triple coincidences study.

	Source	*Position*	*Dimensions(mm)*	*A(MBq)*
a	Horizontal Capillaries	Radial FOV	$r = 0.25, h = 0.5$ $d_{Cap} = 5$	9.62
b	Derenzo	centered	$r = 0.4, 0.5, 0.6, 0.8$ $r = 1.2, 1.6, h = 0.5$	22.2
c	Hot-Cold-Bkg	centered	Cyl.:$r = 30$ Rods: $r = 10$,$h = 0.5$	3.7/1.59(3:1)

The second and third points of the previous list were studied simulating a hot-cold-background phantom. This phantom has the same structure than in chapters 3 and 4, excepting the axial dimension, which is reduced to 0.5 mm.

5.5 Figures of merit

The possible spatial degradation was studied calculating the FWHM and FWTM (characterized in section 1.1.4) of the line profiles of the reconstructed capillaries for the true coincidences (double true coincidences in the case of $P^{doubles}$, and double and triple trues for $P^{dou+tri}$). To see the effect on the quantification of the images when adding the triple coincidences, the following figures-of-merit were employed (all of them defined in section 1.1.4, page 57):

1. Discrepancy (D), calculated using the hot and background ROIs defined in figure 3.5, but with the axial dimension set to 0.5 mm; the reference is the reconstructed image obtained employing only the true coincidences. The reconstructed images with and without randoms correction are compared to the reference.

2. Background Noise ($\bar{\sigma}_{bkg}$)

3. Contrast Recovery Coefficient (CRC)

5.6 Results and Discussion

5.6.1 Characterization of System Matrices

The values presented in this section correspond to the SM related to the voxels belonging to a central slice of the FOV. Using these 2D-system matrices, the disk space needed to store the SMs is not a problem. Therefore, the full SM (not 1/4 of it) can be saved in a binary file that contains the values of the triplet voxel (j), LOR (i) and the corresponding counts for this combination of voxel-LOR, c_{ij}. The emitted gamma-ray pairs for this case were 30.760×10^9 (2 million of 511 keV photon pairs for each voxel, 15380 voxels belong to this FOV), the sum of the c_{ij}

Table 5.2: Properties of the calculated 2D probability matrices at 200 keV LET

	$N_{nonzero}$	$\bar{\sigma}_{rel}$ (%)	S (%)	Disk space (GB)
Doubles	159,699,164	0.84	1.50	1.8
Doubles & Triples	187,994,856	0.84	1.80	2.2

coefficients for the case of the doubles at 200 keV (total detected photons pair) was 4.58×10^8. When including the triple true coincidences (0.93×10^8 detected at 200 keV), the value of the sum was 5.51×10^8 (20% more compare to only double true coincidences). Considering the LORs that have non-zero counts, the average number of counts per LOR was 829.395 for doubles only, whereas for doubles and triples the average increased to 994.806. The elements of the SM with one detected event ($c_{ij} = 1$) was also higher when the triples were accounted for, 1.09×10^8 compared to 1.30×10^8. In both cases, it represented the 69% of the total of non-zero elements. The maximum (average) of the coefficients was 85 (2.87) for the SM with doubles only and 91 (2.93) for doubles and triples.

The summary of the main properties of this special case of SMs is shown in table 5.2. In this table, it is observed that the statistical quality of both SMs is equal. This means that when including the triples, not only the maximum and average were increased, but also the number of non-normalized elements with one count (indeed, the percentage of these elements is the same for both SM). As it was expected, the sensitivity at 200 keV LET taking into account the triples is higher than in the case of only doubles at the same LET.

In GATE there is no variable that informs about if the single was created from one of the annihilation photon or the other. Therefore, when handling with triple coincidences in GATE, it is not always possible to identify which is the reference single[2]. For this work, in order to decide which was the reference single we have employed a geometrical condition. This geometrical condition is supported by the fact that, for around 95% of the triple true coincidences, two of the three singles are detected in the same (75-80%) or adjacent (20-14%) modules and a third single elsewhere. Therefore the geometrical condition to determine the reference single was the one that gave the most common combination when using triple true coincidences and the reference single was the third one (afterwards with the two closest detected singles the ME condition was applied). If the geometrical condition was not satisfied, the two most energetic singles were chosen to assign the LOR. The triple prompts were classified according to this schema. Although the way we process the triples introduces some uncertainty, this degradation effect is also taken into account in the SM. Therefore, the degradation will be partially compensated during the reconstruction. Because the model is not perfect (statistical noise), the SM cannot remove completely the mispositioning.

We have also calculated the sensitivity matrix for these two cases. In figure

[2]The reference single can be distinguished only in the cases, in which it has undergone only a photoelectric effect. In this cases, the `ComptonCrystal` variable is zero.

5.5 we observe the same structure of the sensitivity matrix for the doubles and triples and for only the doubles at 200 keV. The main difference is the increase of the sensitivity when adding the triples. The increase of sensitivity when including triples is shown clearly in the profiles of figure 5.5. We have also calculated the ratio of these matrices and, as expected, the values are in the range of [1.18,1.22].

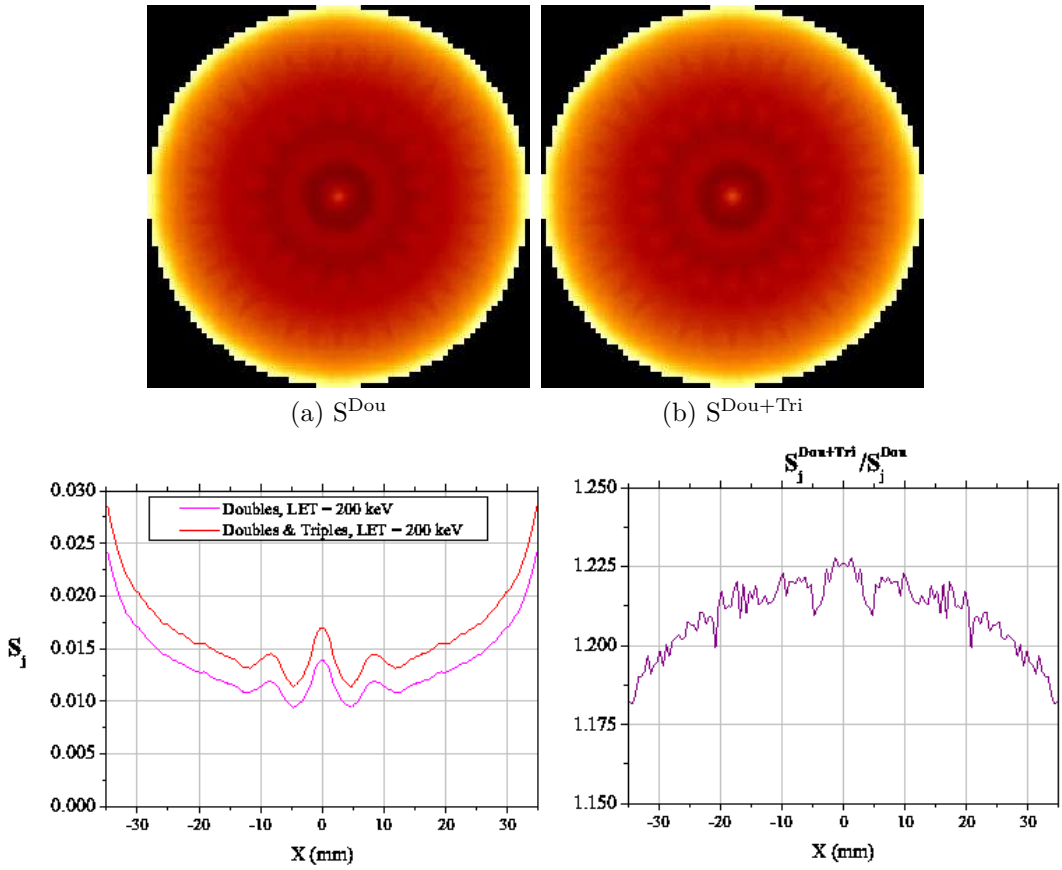

(a) S^{Dou} (b) $S^{Dou+Tri}$

Figure 5.5: Top: Sensitivity Matrix of the central slice for the two studied cases. The one for the doubles is at the left (S^{Dou}) and the one for doubles and triples is at the right ($S^{Dou+Tri}$). Bottom: Profiles of both sensitivity matrices (left) and ratio of the two sensitivity matrices (right).

5.6.2 Effect on spatial resolution

In this section we examine if there is some degradation of the spatial resolution by including the triple coincidences. Besides, we are interested in the validation of the proposed schema for processing the IC scatter events. In figure 5.6, we present the reconstructed images of the Derenzo phantom for both cases, employing true coincidences. We observe that, when adding the triple coincidences to the data, no degradation of the spatial resolution is visible. On the contrary, the rods of 1.2 mm, which are not visible in the case of doubles, can be distinguished in the region close to the center in the reconstructed image using doubles and triples.

These observations lead us to think that the increase of the sensitivity when using the triple coincidences together with the modelling of the uncertainty introduced by the recovery algorithm in the SM produce images with higher quality.

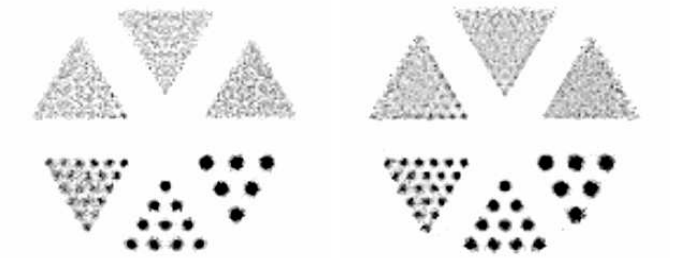

Figure 5.6: Reconstructed images of the Derenzo phantom after 100 iterations for the two system matrices and 200 keV LET (left: only doubles; right: doubles and triples).

The reconstructed horizontal capillaries have been used for determining the spatial resolution (figure 5.7). There is no important differences between the reconstructed images of the capillaries using the two SMs. In the figure 5.8 the line profiles of the images are shown. From these line profiles the FWHM and FWTM were calculated (figure 5.9). The value of the FWHM varies slightly around 1 mm within the 70% of the radial FOV for both SMs. The FWHM reaches its maximum, 1.12 mm at the position corresponding with the 85% of the FOV. A slight difference between the two images is found at the edges of the FOV and this difference can be quantified using the FWTM. Only the last capillary of the reconstructed image with triples has higher FWTM than the image obtained only with doubles. The rest of the capillaries, on the contrary, show a lower FWTM in the case of doubles and triples than only doubles. In general, this quantitative result supports the same reasoning that we got from the Derenzo images: Not only there is no spatial degradation of the image when adding the triples, but also the reconstructed images employing doubles and triples show better quality in terms of spatial resolution. And this improvement is due to a higher sensitivity combined with modelling the recovery schema within the SM.

Figure 5.7: Reconstructed images of the capillaries extended through the radial FOV after 100 iterations for the different system matrices at 200 keV LET (left: only doubles; right: doubles and triples.)

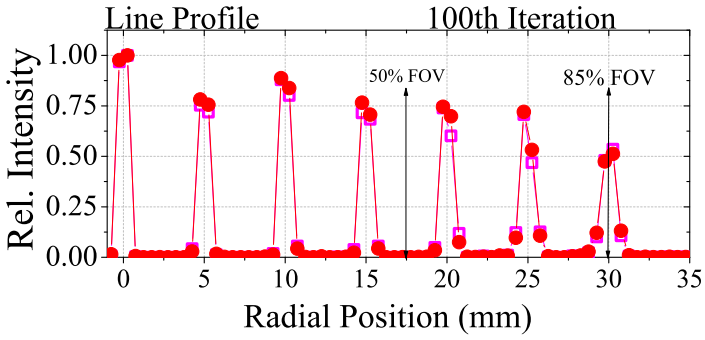

Figure 5.8: Line profile of the reconstructed images of the capillaries after 100 iterations for the two system matrices at 200 keV LET (pink open squares: only doubles; red circles: doubles and triples).

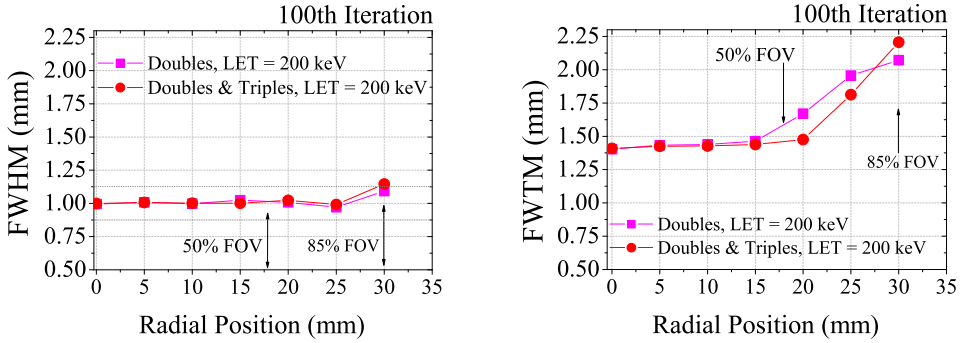

Figure 5.9: FWHM and FWTM of the line profiles versus the radial position which covers almost the entire FOV for the two studied cases.

5.6.3 Random coincidences correction

The reconstructed images of the hot-cold-background phantom (shown in figure 5.4c) obtained using the SM with only doubles at 200 keV LET are presented in figure 5.10, whereas the images for the doubles and triples case are in figure 5.11. Before focusing on the random coincidences correction, it is necessary to confirm that using the true coincidences (figures 5.10b and 5.11b), the reconstruction algorithm together with the SM can recover the emitted activity. In the table 5.3 the absolute reconstructed activities of the hot-cold-background phantom using the true coincidences are presented. A very good agreement between the emitted and the reconstructed activity with the two different SMs is observed for the hot and background ROIs (defined in figure 3.5 and reduced the axial size to 0.5 mm).

Once that we have assured that there is no deterioration of the reconstructed images when including the triple coincidences and that we can obtain the same (or even better) results by adding the triples, we continue with the random coincidences correction. As we saw in the previous chapter, there was an overestimation of the number of randoms when using DW and SR methods. This overestimation

Means and standard deviations of absolute ROI values		
	Hot (μCi/cc)	Bkg (μCi/cc)
Simulated Activity	273.3±0.4	90.8±0.3
Doubles	270±13	90±6
Doubles & Triples	270±11	90±5

Table 5.3: Means and standard deviations of absolute ROI values from reconstructed images using only true coincidences (50th iteration) for the two system matrices at 200 keV LET.

Randoms percentage and overestimation DW and SR			
	R(%)	$O^{DW}(\%)$	$O^{SR}(\%)$
Doubles	8	30	120
Doubles & Triples	10	8	29

Table 5.4: Result of the randoms estimation methods: the percentage are given for randoms and overestimation for DW and SR for the Hot-Cold-Background phantom (described in table 5.1).

was more important at LET lower than 255 keV. In table 5.4, the values of the overestimation of randoms for DW and SR methods and the percentage of randoms in the hot-cold-background phantom used in this chapter are summarized. The overestimation considering triple random coincidences is notably reduced for both methods, from 30% to 8% in the DW method and from 120% to 29% using the SR technique. This first result related to the randoms estimation method is very important, because we are interested in obtaining a good agreement between the estimated random coincidences and the "real" random coincidences. The second step to validate the modifications done to the DW and SR methods (DWmd, DWme and SRns) is to analyze the randoms corrected reconstructed images (figures 5.10c, 5.10d, 5.11c, and 5.11d).

From visual inspection of the randoms corrected images, there is no appreciable difference among them. Therefore, the modifications applied to the DW and SR methods to include the triple randoms do not produce any artifact on the image. The last step in our analysis is to quantify these images using $D(\%)$ for the hot and background ROIs, $CRC(\%)$, and $\bar{\sigma}_{BKG}$.

From the first set of plots that corresponds to $D(\%)$, represented versus the number of iterations, it is observed that the main effect of the overestimation is to produce images with lower activity than emitted (top row), as we have already seen it in the previous chapter. This effect is more important for the SR method and for the background ROI. At the second row of this set of plots, as a consequence of the overestimation reduction by the inclusion of the triples, there is a better agreement between the activities obtained with trues and randoms corrected for both methods.

Finally, in the plots of the figure 5.13, a previous result observed in chapter 4 is also reproduced here for this hot-cold-background phantom and almost corrected

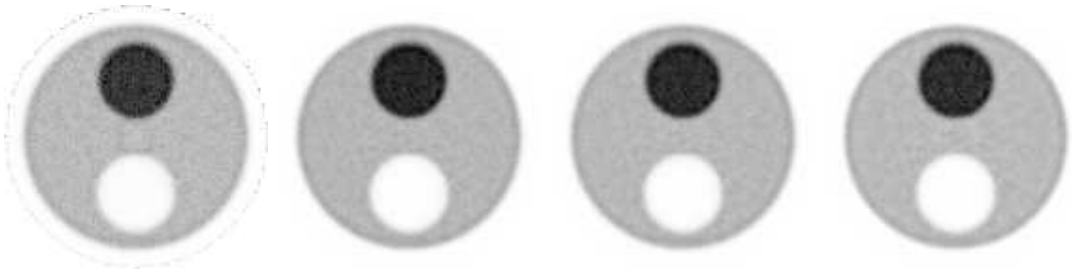

(a) Prompts (b) Trues (c) DW (d) SR

Figure 5.10: Reconstructed images of the Hot-Cold-Background phantom after 50 iterations for the system matrix for doubles at 200 keV LET. (a) Prompts; (b) Trues; (c) Corrected for randoms estimated using DW method; (d) Corrected for randoms estimated using SR method .

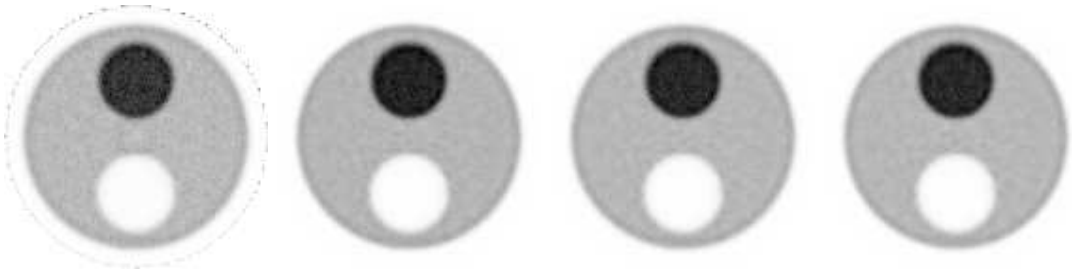

(a) Prompts (b) Trues (c) DWmd (d) SRns

Figure 5.11: Reconstructed images of the Hot-Cold-Background phantom after 50 iterations for the system matrix for doubles and triples at 200 keV LET. (a) Prompts; (b) Trues; (c) Corrected for randoms estimated using DWmd method (There is no difference in the reconstructed images using DWmd and DWme methods to estimate the triple randoms, therefore only the ones obtained with DWmd is presented); (d) Corrected for randoms estimated using SRns method .

when adding the triples. We refer to the fact that the CRC is higher than 100% due to the overestimation, this values are seen for the plot at the left. The highest value of the CRC is 105% and corresponds to the SR method. In the plot at the right, where the triple coincidences are considered, the values of the CRC are getting closer to 100% as one would expect. Another fact, consequence of the higher sensitivity when taking into account the triple coincidences, is that the noise is lower in these images.

5.7 Conclusions

The triple coincidences and their impact on the random coincidences methods have been studied in this chapter. The benefit of taking into account these type of events for reconstruction is to increase the sensitivity of the system. Additionally, in the previous chapter we have found that using triple coincidences could help us to solve the problem of the randoms overestimation. When including

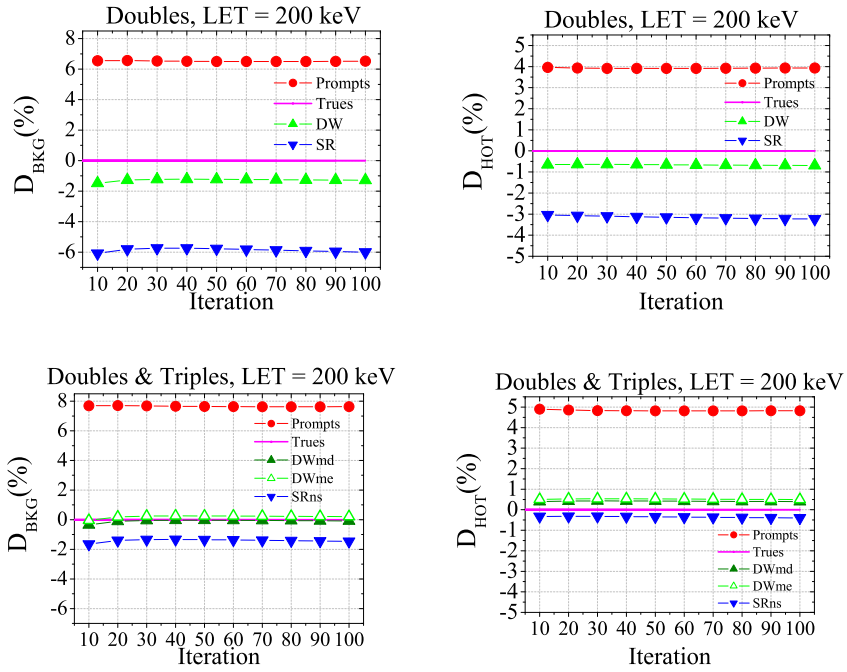

Figure 5.12: Analysis of the hot and background ROIs of images reconstructed with the two system matrices.

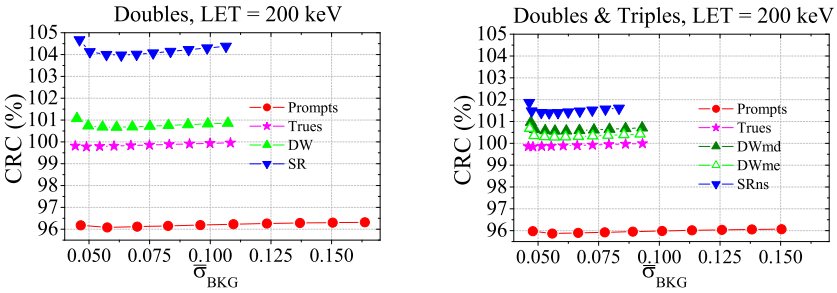

Figure 5.13: CRC versus the normalized standard deviation within the ROI in the background for randoms corrected and non-corrected images for the two studied cases.

triple coincidences, it is necessary to know how to process them in order to not deteriorate the quality of the reconstructed images.

First, we have confirmed that the sensitivity increases 20% at 200 keV LET when the triple coincidences are taken into account. Secondly, before starting with the randoms coincidence correction, it was important to verify that there is no degradation in the reconstructed images obtained using double and triple true coincidences. In order to do this, we have compared reconstructed images obtained with a SM that considers only double coincidences to a SM created with double and triple coincidences. In terms of spatial resolution, a Derenzo phantom and horizontal capillaries have been simulated and reconstructed with both SMs.

In the Derenzo images, we have found that not only there is no visual degradation, but also some rods of 1.2 mm close to the center, which were not visible for the SM with doubles, are identified in the SM with doubles and triples. In the horizontal capillaries, small differences are observed for the FWTM at the edges of the FOV. Additionally, the hot-cold-background phantom has been employed for testing the capabilities of recovering the emitted activity. The reconstructed images with both SMs are in good agreement to the emitted activity. Therefore, from these first results obtained from true coincidences (doubles and triples), there is no deterioration of the reconstructed images using doubles and triples. In addition we can conclude that better quality in terms of spatial resolution is achievable when including the triple coincidences in the processing and reconstruction.

Related to the random coincidence correction, considering the triple events requires to modify the estimation method to include these events. We have adapted DW and SR method and we have observed that, when including the triple randoms, the randoms overestimation (shown in the previous chapter) is notably reduced. Additionally, the randoms corrected reconstructed images with triples do not show any artifact that would discourage us of using the modified random estimation methods. On the contrary, there is no visual difference between them and the reconstructed images obtained with doubles only. From the quantitative analysis, we can infer that the introduction of the triples solves the underestimation of the activity and, due to the higher sensitivity, the noise in the images is lower.

Therefore, triple events are good candidates to be included in the reconstruction process, because not only increase the sensitivity of the system, but also reduce notably the randoms overestimation and improve the quantification of the reconstructed images at lower LET. Nevertheless, the approach presented in this chapter is a proof-of-concept, because all the results given here are for a 2D system matrix. Future work will be to confirm them with a 3D system matrix and larger objects.

Lastly, for this work we have only focus in a sorting algorithm that uses a single time coincidence window. Whereas there are other sorting algorithms that employs multiple time coincidence window. For further analysis on this issue we refer to [129], where a comparison between single and multiple time coincidence window sorting algorithms is done.

Chapter 6

Normalization Correction

The normalization correction in Positron Emission Tomography is necessary to obtain reconstructed images without artifacts and to assure proportionality between the intensity of the reconstructed image and the emitted activity (section 1.1.3, page 52). This correction depends on the algorithm employed for image reconstruction. In the case of analytical reconstruction, the algorithm requires that all the lines of response have the same sensitivity. In general this is not the case, there are geometric variations over the field of view and random and systematic variations in individual detector efficiencies. The normalization factors can be assessed by irradiating all the detectors with a known activity source. The ratio between the detected coincidences in each detector and the expected coincidences (if all the detectors would have efficiency equal to 1) provides the normalization factors. This technique is known as direct normalization and its accuracy is limited by the counts measured in the detectors, consequently by the time used to make the normalization measurement. Another technique was proposed in [117], in which the normalization factor for a LOR can be derived from the product of the efficiencies of the detectors that define this LOR. By doing this, the number of parameters to estimate is notably reduced, improving the statistical accuracy of the method. The authors present as well a variance reduction technique for computing the values of the efficiencies. Later on, in [131], a geometrical component was added to the previous model. In [133] the method was extended to fully 3D scanners and the authors developed an algorithm using the geometric mean to obtain the detector efficiencies and geometrical factors. All these methods are known as component-based normalization, to distinguish them from the direct normalization. When operating the PET scanner in 3D mode, object scatter increases notably and this situation must be taken into account when calculating the normalization factors. The latter has been addressed in [137], where a method to calculate the normalization factors for trues and scattered coincidences is developed. A more sophisticated component-based model can be found in [139], where the normalization coefficients are split into several factors which not only involve the crystal efficiencies and the geometry, but also the block profile and the crystal interference pattern. An extension of this model to include the time alignment factors and count-rate dependence was presented in [141]. All the ref-

erences presented up to this point apply the component-based approach to correct for efficiency inhomogeneities (normalize) in the case of analytical algorithms. In the framework of statistical image reconstruction, the normalization correction depends on the model or method used to generate the system matrix, and the normalization factors must account only for the effects that are not included in the system matrix and produce variations in the sensitivity of the LORs [142]. The component-based model can also be used in the statistical framework to calculate the normalization factors. This is the approach that we will apply in this chapter, and several methods to assess these factors will be analyzed.

6.1 Normalization for to MADPET-II

In this work, the MLEM algorithm combined with a Monte Carlo system matrix is used to reconstruct images for MADPET-II. All the geometrical factors are included in the Monte Carlo SM; therefore, when using the component-based model for normalization, only the detection efficiency of the LOR (ε_{LOR}) must be assessed. It is necessary to perform a measurement with the system in order to obtain the LOR efficiencies, called *normalization measurement*. We will describe how to estimate ε_{LOR} using *a priori* information from a Monte Carlo simulation combined with the normalization measurement. The first approach calculates the normalization factors using the coincidences in the normalization measurement. As in the direct normalization, when estimating the correction factors through coincidence measurements, the accuracy of the factors is limited by the number of coincidences. In order to improve the statistical quality of the normalization factors, we propose a second method to calculate them where singles instead of coincidences from the normalization measurement are used. Under the assumption that the component-based model is valid, we can split the efficiency of a LOR into two factors –the two individual efficiencies of the crystals that define the LOR ($\varepsilon_{crystal}$)–, and we can employ singles measurements to obtain these individual efficiencies. These two methods (coincidences-based and singles-based) will be applied to reconstruct images of MADPET-II and the validity of these approaches for the complete scanner will be investigated in a future work. For this chapter, we have tested these two approaches in the incomplete 384-channel prototype (see images in figure 6.2). When studying the effect of these normalization methods on the image reconstruction, it was necessary to rotate the source during the data acquisition to compensate for the missing angular sampling of the non-present channels.

6.1.1 Calculation of the normalization factors

The normalization factors are coefficients which are applied to the input data (sinogram or LOR histogram) to provide the mentioned correction. In the direct normalization, they are proportional to the reciprocal of the number of counts obtained in each sinogram element or LOR in the normalization measurement. In

this work, we use the following convention (similar to the direct normalization): we call normalization factors (NF_i) to the values that multiply the input data and efficiencies (ε_i) to the inverse of these factors ($\varepsilon_i = 1/NF_i$). The efficiencies modify the system matrix to account for normalization. Next we explain the calculation of the LOR efficiencies employing the two proposed methods, singles-based and coincidences-based.

Singles data: Crystal efficiencies

The singles list data from the simulation and measurement were histogrammed according to the different detectors after applying the low energy threshold of 400 keV. After analyzing the singles histograms, it was found that some of the detector crystals had no counts at all or very few in the measurements. Those detector crystals that have no counts are called dead channels (or dead crystals). On the other hand, when there are only few counts (less than 50% of the counts for the same channel in the simulation), we refer to it as a low efficiency crystal. Once the histograms for the measurement and for the simulations were done, the crystal efficiency factors were calculated as follows:

$$\varepsilon_k^{sin} = \frac{s_k^{meas} / \sum_j s_j^{meas}}{s_k^{sim} / \sum_j s_j^{sim}} , \tag{6.1}$$

where k indicates the crystal number and runs from 0 to 1151, s_k^{meas} is the number of singles for the crystal k in the measurement, and s_k^{sim} is the number of singles for the crystal k in the simulation. From the previous expression the corresponding LOR efficiency was obtained as:

$$\varepsilon_{i(k,l)}^{sin} = \varepsilon_k^{sin} \varepsilon_l^{sin} . \tag{6.2}$$

Coincidences data: LOR efficiencies

The coincidences are obtained by sorting the singles in the same way for simulated and measured data, as it was explained in section 2.2 (page 70). The delayed window method is applied to eliminate the random coincidences in the measurements. When handling the simulated data, no randoms estimation method was used, because it is possible to distinguish between true and random coincidences from the information provided by the simulation program. The LOR efficiencies then read:

$$\varepsilon_{i(k,l)}^{coin} = \frac{n_i^{meas} / \sum_j n_j^{meas}}{n_i^{sim} / \sum_j n_j^{sim}} , \tag{6.3}$$

where $i(k,l)$ refers to the LOR i defined by the crystals k and l. n_i^{meas} and n_i^{sim} are the number of coincidences in LOR i for the measurement and simulation, respectively.

6.1.2 How to apply the normalization

The calculated normalization factors can be applied directly to the input file of the reconstruction program, which is a LOR histogram, just by multiplying these factors by the number of the coincidences measured in each LOR. We refer to this method as direct normalization (DN).

A second approach is to modify the system matrix that is used in the MLEM algorithm by the efficiencies (ε_i). The resulting system matrix would contain the information of the detector efficiency: the MCSM elements, p_{ij}, are multiplied by the efficiencies ($\hat{p}_{ij} = \varepsilon_i p_{ij}$) and the new elements of the MCSM, $\hat{p}_{ij}$, take into acount the efficiencies of the LORs. The effect of this modification in the MLEM algorithm is:

$$f_j^{(n)} = \frac{f_j^{(n-1)}}{\sum_i \hat{p}_{ij}} \sum_i \frac{d_i}{\sum_k \hat{p}_{ik} f_k^{(n-1)}} \hat{p}_{ij} = \frac{f_j^{(n-1)}}{\sum_i \varepsilon_i p_{ij}} \sum_i \frac{d_i}{\sum_k \varepsilon_i p_{ik} f_k^{(n-1)}} \varepsilon_i p_{ij}. \tag{6.4}$$

We see that the efficiencies in the second factor are cancelled out, and the efficiencies only modify the sensitivity matrix[1]:

$$f_j^{(n)} = \frac{f_j^{(n-1)}}{\sum_i \varepsilon_i p_{ij}} \sum_i \frac{d_i}{\sum_k p_{ik} f_k^{(n-1)}} p_{ij}. \tag{6.5}$$

In order to liken the two approaches, we show in the next expression the resulting equation from applying directly the normalization factors (DN approach):

$$f_j^{(n)} = \frac{f_j^{(n-1)}}{\sum_i p_{ij}} \sum_i \frac{NF_i d_i}{\sum_k p_{ik} f_k^{(n-1)}} p_{ij} = \frac{f_j^{(n-1)}}{\sum_i p_{ij}} \sum_i \frac{d_i}{\varepsilon_i \sum_k p_{ik} f_k^{(n-1)}} p_{ij} \tag{6.6}$$

Comparing the expression in 6.5 to 6.6, it is obvious that the correction in both approaches acts differently.

To study the effect of the normalization, images were reconstructed in the following cases combining the two above explained approaches and the two ways of calculating the normalization factors (singles-based and coincidences-based):

1. No normalization is applied (NN).
2. Direct normalization with factors calculated from singles (DN-S).
3. Direct normalization using factors obtained from coincidence events (DN-C).
4. Normalization within the reconstruction algorithm operating with the coefficients from the singles, $\varepsilon^{sin}_{i(k,l)}$ (NRI-S).

[1]This is only possible when neither the random coincidences, nor scatter coincidences are corrected within the reconstruction algorithm

5. Normalization within the reconstruction algorithm employing the correction coefficients from the coincidences, $\varepsilon^{coin}_{i(k,l)}$ (NRI-C).

Additionally, in the NRI-S and NRI-C cases, we have explored the feasibility of reducing the scanning time by using a small part of the singles data stream for the NRI-S and of the coincidences for the NRI-C. In the case of the singles data, the normalization factors have been calculated using only 1/12 of the total singles. This approach was named NRI-SLS, where the acronym LS refers to the lower statistic employed to assess the normalization factors. The coincidences used for this lower statistic version NRI-CLS were 1/3 of the total coincidences. For all the studied cases for normalization, we have focused on data at 400 keV LET.

6.1.3 Normalization source

Different sources have been employed in the literature to calculate the normalization factors: In the case of 3D acquisitions [134] used a ^{68}Ge plane source, [135] a uniform 20 cm cylinder (commonly consisting of ^{68}Ge), [136] ^{68}Ge transmission scanning rod sources, and [143] a line source of ^{68}Ge which oscillates across the transaxial and an annular source. The advantages and disadvantages of using these different geometries have been shortly described in the introduction (section 1.1.3, page 52) and further details can be found in the references above (see also [130]).

For the case of MADPET-II, we have used an aqueous flood source contained in a plastic cover to generate a low-scatter planar distribution of activity that irradiates uniformly all the channels. The main two reasons of using this source are, on one hand, the presence of scatter is reduced notably in comparison to a cylindrical source. On the other hand, the different source activities viewed by each pair of detectors are more uniform in the case of the flood source than in the cylindrical source (see figure 6.1). This leads to a similar statistical quality of the normalization factors in the case of the flood source.

Measurement

The dimensions of the flood source are $1\times40\times25$ mm^3 and those of the plastic container $2.5\times50\times35$ mm^3 (see figure 6.2). The source covers 3 dual-layer modules at each side, in order to obtain nearly the same number of counts in all the detectors. The activity of the source at the beginning of the measurement was 7.96 MBq of F-18. The system records the singles for a defined number of detected events. For the normalization measurement, 12 sets of 60×10^6 counts at 100 keV LET were obtained and the 12 sets lasted approximately 43 minutes. The acquisition time of each set was known with 1 minute of error.

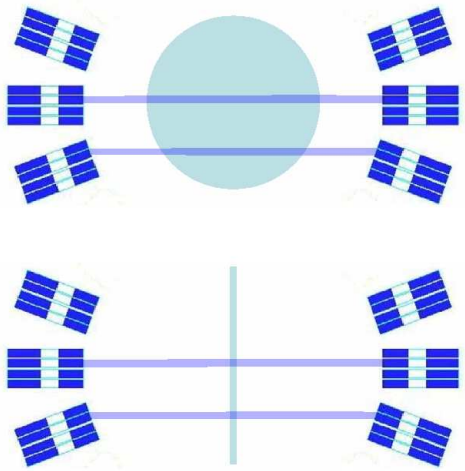

Figure 6.1: Examples of different source activities viewed by pair of detectors in the case of a cylindrical (top) and a flood (bottom) source. The activities seen by the LORs of the flood source are approximately equal. On the contrary, in the cylindrical source the area covered by the upper LOR is larger than the area of the lower LOR. This leads to higher number of counts in the upper LOR than in the lower LOR, as well as differencies in statistical errors.

GATE simulation

The simulations of the above mentioned measurement of the flood source were done using GATE. The decay constant of the F-18 was also included in the simulation to be closer to the measurement, mainly because the randoms were substracted to the prompts in order to calculate the normalization factors. In GATE the simulation can be done by setting either a fixed acquisition time or the number of emitted events. On the contrary, in MADPET-II the acquisition stops at a determined number of detected events. To reproduce the normalization measurement some calculations were done to obtain the measurement time of each set. The GATE acquisition times were slightly larger than the measurement times, to assure enough statistics in the simulation. This led to the need of normalizing the simulation and measurement data to the sum of the detected events in each case.

To speed up the simulations, only photons back-to-back were generated and the simulation code was executed in a Grid facility in order to emulate the measurement in a feasible time. The normalization measurement was split into simulations of 5 s acquisition time each and carried out on the various processors. Each parallel processor reads the same macro file at different time sets of the simulation and each generates its own simulation for the corresponding acquisition time. The activity in GATE is updated continuously throughout the simulation. Like in the simulations used for the SM, no inter-processor communication is

necessary while these simulations are taking place. Each processor produces the output data for each time set. Once all processors have finished, the output data are collected. Unlike the simulations for the system matrix, it was very important for the simulations of the normalization measurement to use different seeds in the random number generator for the various jobs sent to the Grid in order to obtain unequal sets of data.

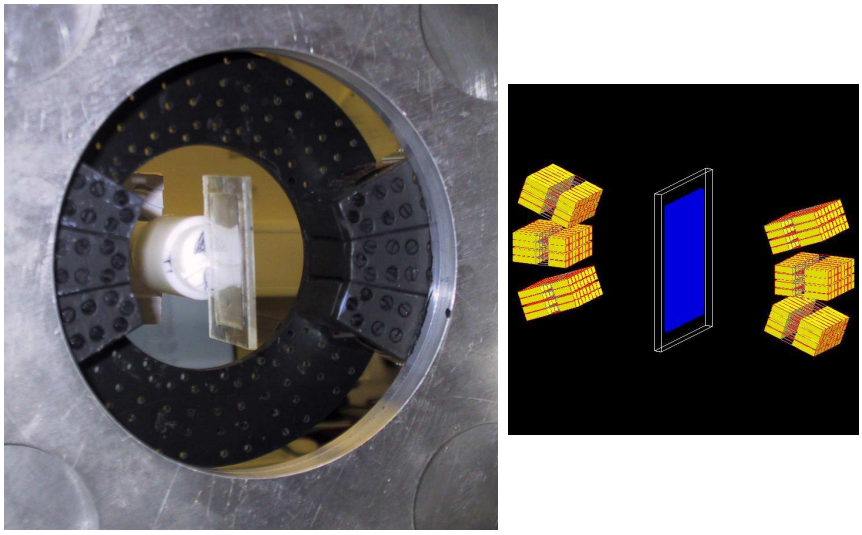

Figure 6.2: Planar source employed to obtain the normalization factors.

6.2 Effect on Image Reconstruction

6.2.1 Measured Phantoms

A homogeneously-filled cylindrical phantom was measured to compare the effect of the different normalization methods on the reconstructed images. The dimensions of the phantom were 23.55 mm diameter and 15 mm long. The activity of the source was 8.34 MBq and it was measured during 42 minutes. In the reconstruction of this phantom, the random coincidences were estimated using the DW method and presubtracted, neither attenuation, nor scatter correction were applied, and only the different modalities of normalization correction were used. When sorting the coincidences, the LET was set to 400 keV and the time coincidence window to 20 ns.

6.2.2 Figure-of-Merit: Relative Error

We expect to get more uniform images after the normalization. Therefore, to estimate the goodness of the proposed approaches we have used the relative error of the voxel values of a cylindrical ROI centered in the cylindrical phantom. The

relative error is defined as the ratio between the average voxel values and the standard deviation of these values:

$$\epsilon^{rel} = \frac{\sigma_y}{\hat{y}}. \tag{6.7}$$

6.3 Results

6.3.1 Efficiency Coefficients

Singles data

The measured and simulated singles data are represented in figure 6.3 for one of the 12 sets of the singles data in the normalization measurement and simulation. This set is the one used for the low statistic case (NRI-SLS). Each of the plots in the figure corresponds to the crystals in one ring of the MADPET-II scanner (144 crystals per ring). For these histograms, we have kept the numbering of the channels as in the complete system (1152 channels). The bins with 0 counts in measurement and in simulation are crystals not present in the 384-channel prototype. The first 72 bins in the histogram are related to the crystals in the front layer and the other 72 bins to the back layer. These plots compare the simulations with the measurements and some interesting features can be extracted from them. As it is seen in the plots, the front layer is more sensitive than the back layer [74]. The histogram from the simulated single events shows an structure due to the geometry, whereas in the measurement, the structure is not present due to the different intrinsic efficiencies of the crystals. The 384-channel prototype had some dead and low sensitivity channels. The dead channels were found when the number of detected events in the simulation is non-zero while in the measurement is zero. In this set there were four dead channels, in which no counts were detected in the measurement, and four crystals with very low sensitivity.

The same structure of in figure 6.3 is observed in the histograms of figure 6.4, where all the 12 sets from measurement and simulation were employed. The main difference between these two figures is the maximum number of events in each. Another difference, although less obvious, is that one of the channels considered dead was, in fact, a low efficiency channel, when all the data sets were considered. A third difference is that one of the channels of the fifth ring starts behaving like a low sensitivity channel. The last two differences can be also observed in the figures 6.6 and 6.7, where the efficiencies coming from the singles data for each LOR are represented for one data set of the measurement and for all data sets of the measuremet, respectively. In these plots, the white lines correspond to dead channels and the blue to low sensitivity channels.

The relative error associated for each channel in the measurement and the simulation is represented in the histograms at the top of figure 6.5. The histogram at the left corresponds to the low statistic case and the one at the right to the complete set of data. As expected, increasing the time of the measurement, the histogram moves to the left and it becomes narrower, meaning smaller relative

error. Nevertheless, for the singles case, the relative error of all the channels for measurement and simulation is below 1% for one set and for the complete data set (without considering the low efficiency crystals).

From the plots in figures 6.6 and 6.7, it is seen than the efficiency coefficients range from 0.75 to 1.5, without taking into account the dead and the low efficiency channels. Comparing both plots, one concludes that there is not a large difference between them, with the exception of the dead and low efficiency channels. Therefore, we would expect to obtain approximately the same results when using the coefficients of both cases, although in the low statistic case we have reduced the time for normalization measurement and simulation to 1/12.

Coincidences data

The coincidences histogram for the normalization measurement and simulation are shown in figures 6.8, for the low statistics case, and 6.9 for the complete set of data. As in the case of the singles data, there are more coincidences in the simulation than in the measurement. Namely, the number of coincidences in the simulation was 25% higher than in the measurement. The reason was pointed out in section 6.1.3: the acquisition times employed in the simulation were higher than in the measurement. To take into account this fact in the calculation of the efficiencies, the coincidences in the measurement and in the simulation were divided by the sum of coincidences in the measurement and simulation, respectively (see equation 6.3). Therefore, the values of the efficiencies in the plot of figure 6.11 are not always smaller than 1, as one would expect from the coincidence histogram in figure 6.9. Working with the coincidences histograms, we found 7 dead channels and one channel with very low sensitivity. Some of the low sensitivity channels in the singles data are converted into dead channels in the coincidences case, which is not unexpected[2].

Unlike singles-based case, where the efficiency coefficients represented in the plot for the low statistic set (figure 6.6) and the plot for the full set (figure 6.7) show the same structure, the case of the coincidences, the efficiency coefficients calculated from the low statistic data (figure 6.10) do not reproduce the same that is observed in figure 6.11, in which all the data sets are considered. Additionally, the distribution of the relative error associated to the counts detected by the LORs shown at the bottom of figure 6.5 is wider and has a higher central value for the low statistic case than for the complete set of data. From these first observations, larger differences are expected between the low statistic case and the full set of data when using coincidences instead of singles.

[2]The low efficiency channels detected some singles, but no coincidences. When using the coincidences to calculate the normalization efficiencies, the LORs defined by these channels do not have any coincidences and the value of the efficiency for these LORs is set zero.

6.3.2 Validity of the proposed methods

The efficiencies presented in the previous section have been used to normalize the data from a cylindrical phantom measured in the 6-module prototype. The reconstructed images of this phantom are shown in the figure 6.12. In the transverse slices for all the images, the reconstructed shape resembles more an hexagon than a circle. This "artifact" is due to the missing angular sampling in the 6 modules system, when only three rotation steps of 60^o are performed. The circular shape would be recovered by increasing the number of rotation steps. Therefore, for the complete MADPET-II system, this artifact will not arise. Another artifact, which is seen in the transversal slices like a circle shape, and in the coronal and sagittal slices like perpendicular lines, is present in all the cases except for the NRI-C one and not so strong in the DN-C. The origin of this artifact could be a possible mismatch between the simulated geometry of the scanner and the real one. This explanation would be in agreement with the fact that the distortion is not seen in the case of NRI-C and it is less clear in the DN-C: In the DN-C and NRI-C the geometrical coefficient that would account for the mismatch is included in the normalization factor but not in the NN case, neither in the cases of using singles data (DN-S and NRI-S), where the normalization takes into account only the intrinsic efficiencies of the crystals. The reconstructed images of the cylinder using NRI-SLS and NRI-CLS are not presented in figure 6.12 because they show similar behaviours as the ones from the NRI-S and NRI-C methods, respectively.

A quantitative analysis of these images was also done by means of the relative error. The results are shown in the table 6.1 for all the methods after the 30^{th} and 60^{th} iterations. The highest errors are produced by the NRI-CLS, NN, and DN-C approaches. One would anticipate that the highest error should appear in the NN case, because there is no correction, but is the NRI-CLS which shows the highest error. The reason of this result is clearly the low statistic quality of the data used to calculate the efficiencies. The result in the DN-C case is unexpected and has not a clear reason. One could figure out that the latter result is a combination of lower statistic quality due to the coincidences and the poor performance of direct normalization method. Without considering the NRI-CLS, the NRI methods show more uniform images (lower relative error) than the DN ones. As we have observed with the randoms correction in the chapter 4, when the correction is applied inside of the reconstruction algorithm, the images are less noisy. In this sense, we can conclude that the normalization should be addressed within the reconstruction algorithm. When comparing the images corrected by using singles or coincidences data, the former is preferred in terms of relative error. The NRI-S method, shows the lowest relative error in both iterations; also when employing 1/12 of the data, the modified method (NRI-SLS) is still providing a very low value for the error, even lower than in the NRI-C case. Therefore, it could be possible to reduce the normalization measurement time when using singles to calculate the normalization factors. On the contrary, for the coincidences-based methods, the time for the normalization measurement could not be shortened and in order to achieve the same results as with the singles-based, it should be

Table 6.1: Relative error of the voxel values inside a cylindrical ROI centered within the reconstructed cylinder at the 30th and 60th iteration for the different normalization approaches

Method	$\epsilon^{rel}(\%)$ 30^{th} iteration	$\epsilon^{rel}(\%)$ 60^{th} iteration
NN	17	27
DN-C	17	29
DN-S	16	26
NRI-C	12	19
NRI-CLS	20	34
NRI-S	9	14
NRI-SLS	10	15

increased.

6.4 Conclusions

Our analysis of the various singles- and coincidences-based methods does not allow us to decide which is the most appropriate to estimate the efficiencies. We nevertheless have found that normalization should be applied during the reconstruction process. This conclusion fully agrees with theory, that tells us that all corrections should be addressed in the MLEM reconstruction algorithm, based on Poisson statistics. Although being a preliminary result, we present in this section also the reconstructed images of a mouse heart obtained with the complete system. For these images, there was no normalization measurement available at the moment of writing this work. From the mouse measurement, it was possible to know the dead channels. We have checked the effect of taking into account the dead channels in the system matrix or not. In order to consider the dead channels into the SM, the elements of the SM that are related to the dead channels, were set to zero. The reconstructed images of the mouse heart are shown in the figure 6.13. In the first row, the images were reconstructed without modifying the SM. Whereas in the second row, the dead channels were accounted for. It is obvious from the images that the corrected ones have higher quality and less artifacts. This last result supports what the theory proposes and what we found in the 6-module system with the cylindrical phantom, i.e., the corrections should be performed within the reconstruction process.

Comparing the proposed methods, the reconstructed images are more uniform, but there is an artifact at the center when using the NRI-S. On the contrary, the NRI-C corrected images do not show this artifact, but they are noisier (higher relative error). Keeping in mind that the data come from the 384-channel prototype, there could be other reasons for the artifact that the commented mismatch, like for example misalignment in the rotation axis. Therefore, we expect that measurements and simulations in the complete scanner would provide the right

answer for this open question.

In terms of the acquisition time of the normalization measurement, it would not be necessary to increase this time when using the singles data. Whereas for the coincidence data, improvements in the uniformity of the reconstructed images are expected if the acquisition time would be raised.

Lastly, a few words about extracting the emitted activity from the reconstructed images. In principle, the reconstructed images should provide the emitted activity. But, the acquisition time of the measurement for the cylindrical source was known very rough (by 1 minute error between sets of measurements). This leads to a big error in the determination of the emitted activity (more than 20%). In addition, the reconstructed images are not corrected for attenuation. In [116], the difference between the emitted activity and the non-attenuation corrected reconstructed images of a 30 mm diameter mouse-like phantom is reported to be 25%. Therefore, at this level of the study, there are too many uncertainties and it makes no sense to compare the approaches in their ability to recover the emitted activity.

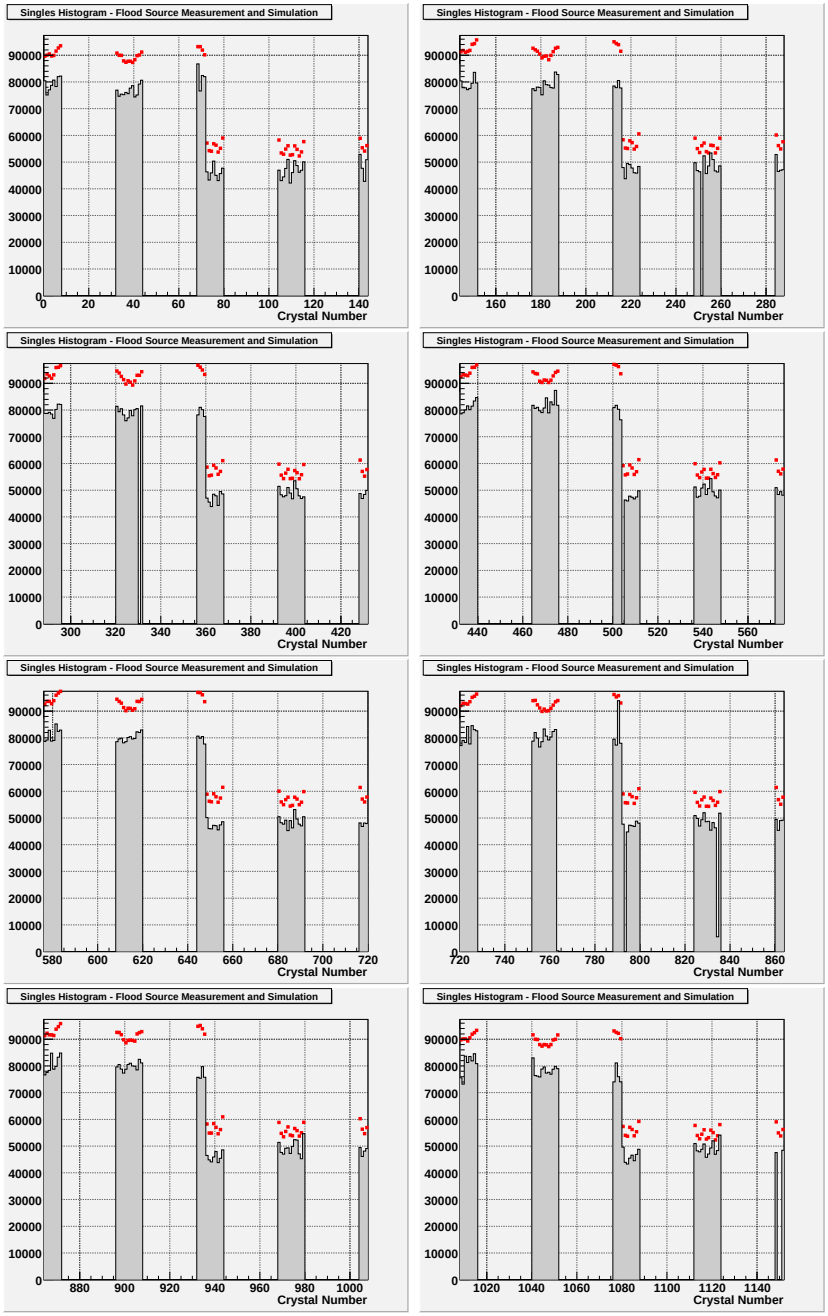

Figure 6.3: Singles histogram for measurement and simulation of the flood source in the 384-channel prototype for one set of data (low statistics case). The abcisas are the crystal number according to the numbering used in MADPET-II. Each histogram corresponds to one ring of crystals. Thus in each plot there are two distinguishable parts: the front layer and back layer crystals. The rear crystals always detect less than the front crystals, due to the front crystals screening. The red squares correspond to the simulations and the black line to the measurements. It can be seen that the singles histogram of the simulation presents almost the same pattern in all the plots. But the singles histogram of the measurements does not due to the crystal non-uniformities. The crystal numbers with zero values in simulation and measurement are the crystals no present in the 384-channel prototype.

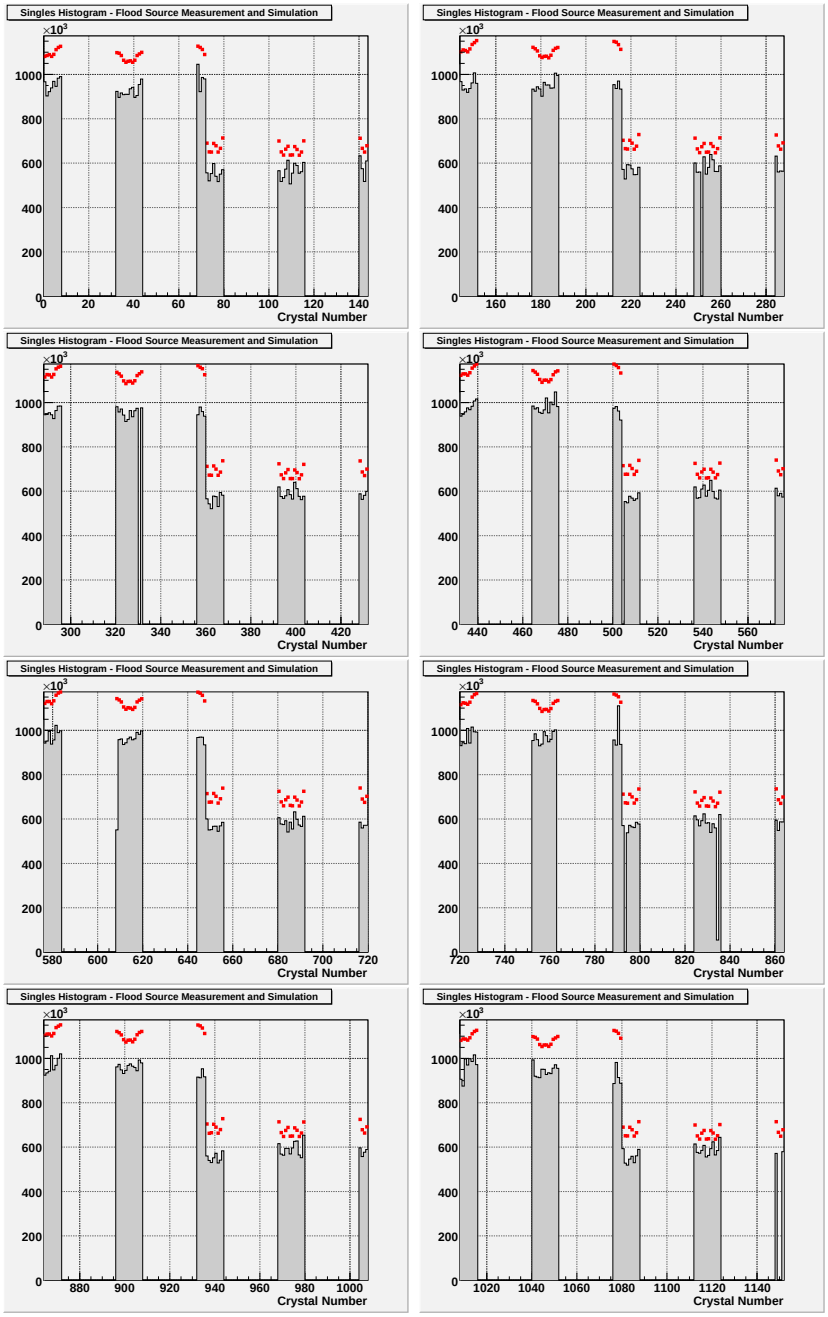

Figure 6.4: Singles histogram for measurement and simulation of the flood source in the 384-channel prototype for all the data sets. The abcisas are the crystal number according to the numbering used in MADPET-II. The red squares correspond to the simulations and the black line to the measurements. The crystal numbers with zero values in simulation and measurement are the crystals no present in the 384-channel prototype.

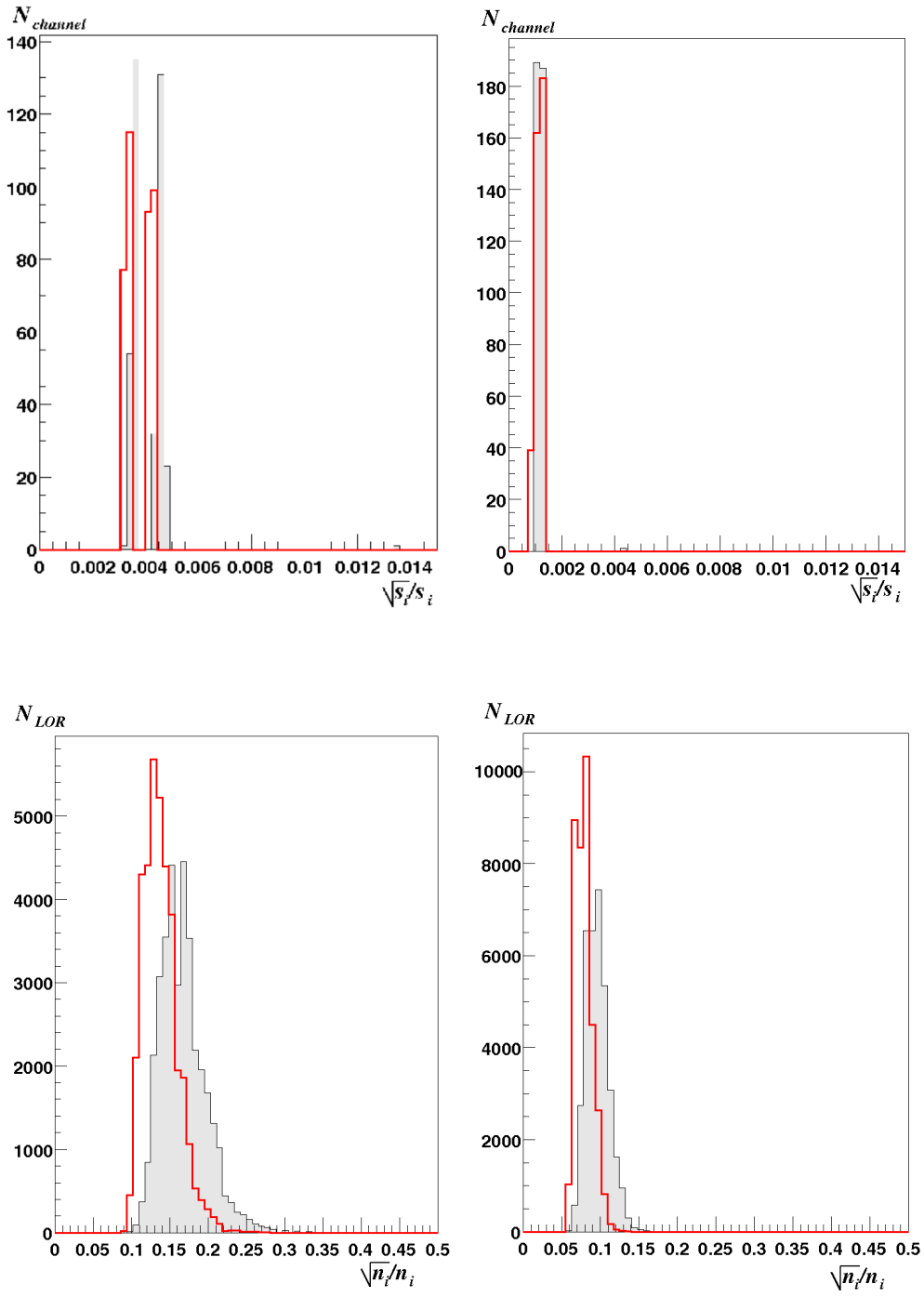

Figure 6.5: Top: Relative error histogram of the detected singles in the simulation (red) and in the measurement (black) for the normalization. Bottom: Relative error histogram of the detected coincidences in the simulation (red) and in the measurement (black) for the normalization. In both cases, the plots on the left correspond to the "low statistic" case (1/12 for the singles data and 1/3 for the coincidences data). The full set of measurements and normalization are shown on the right side.

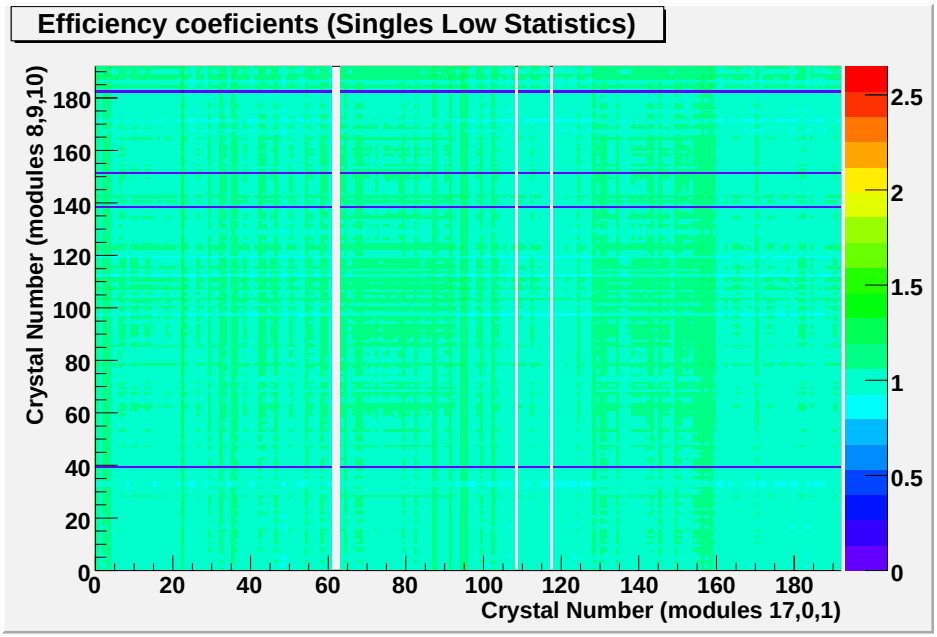

Figure 6.6: Efficiency coefficients for each LOR that belongs to the 384-channel prototype calculated from one set of the singles data. The crystal numbers do not correspond to the numbering used in MADPET-II, the numbering plotted was used in order to represent all the LORs in the graph in a compact way. In the abcisas, the first 64 crystals belong to module 17, the next 64 to module 0, and the last 64 to module 1. In each module the first 32 channels represent the crystals in the front layer, and the last 32 to the back layer. The same structure is followed in the ordinates, but the modules are different, the ones in front of the 17, 0 and 1. In this way, the first 64 crystal numbers are for the module 8, the next 64 for the module 9 and the last 64 for the module 10.

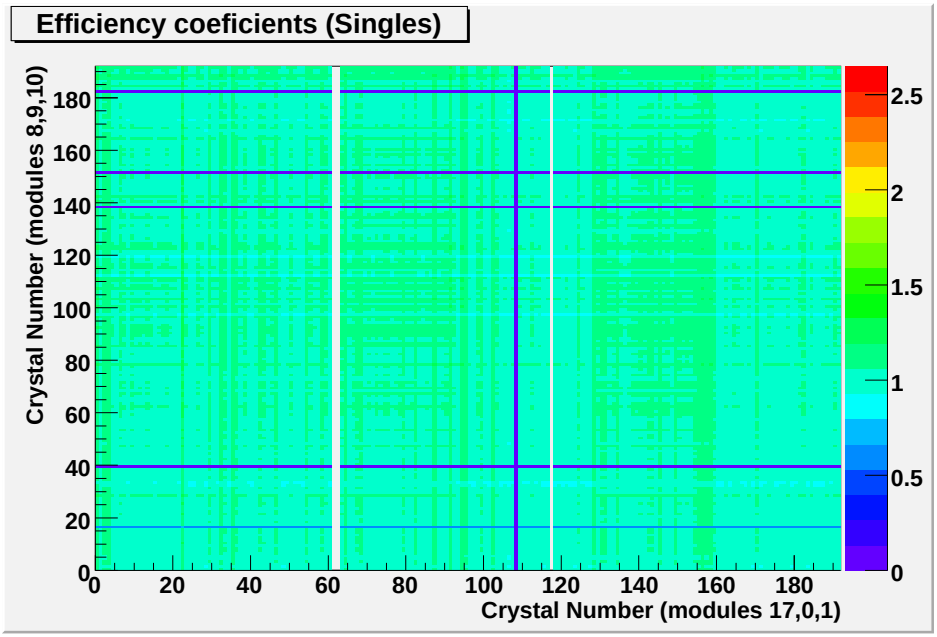

Figure 6.7: Efficiency coefficients for each LOR that belongs to the 384-channel prototype calculated from all the singles data. The numbering used in this histogram is explained in the caption of figure 6.6.

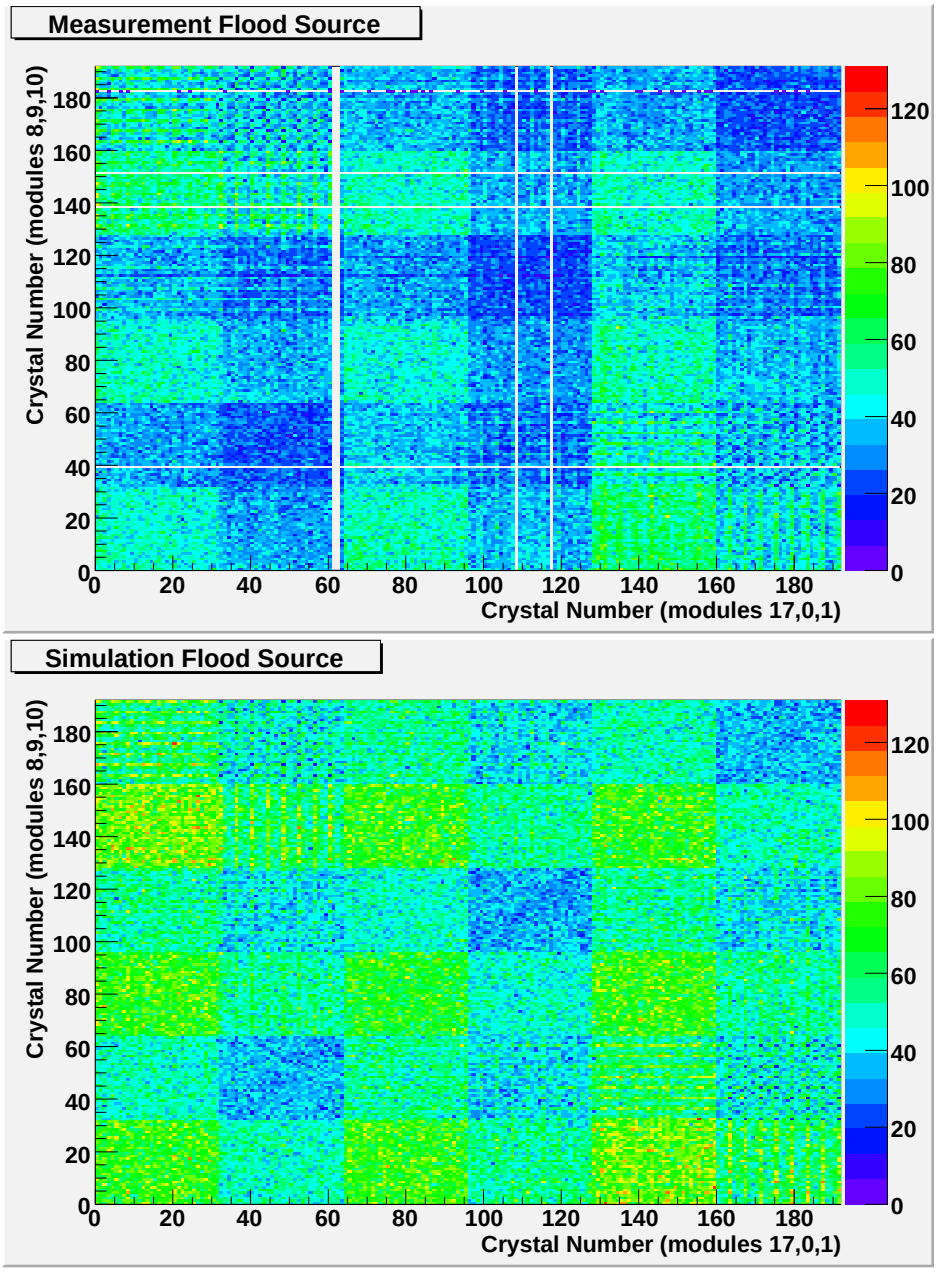

Figure 6.8: Low Statistics Coincidences histogram for measurement and simulation of the flood source in the 384-channel prototype. The numbering used in this histogram is explained in the caption of figure 6.6.

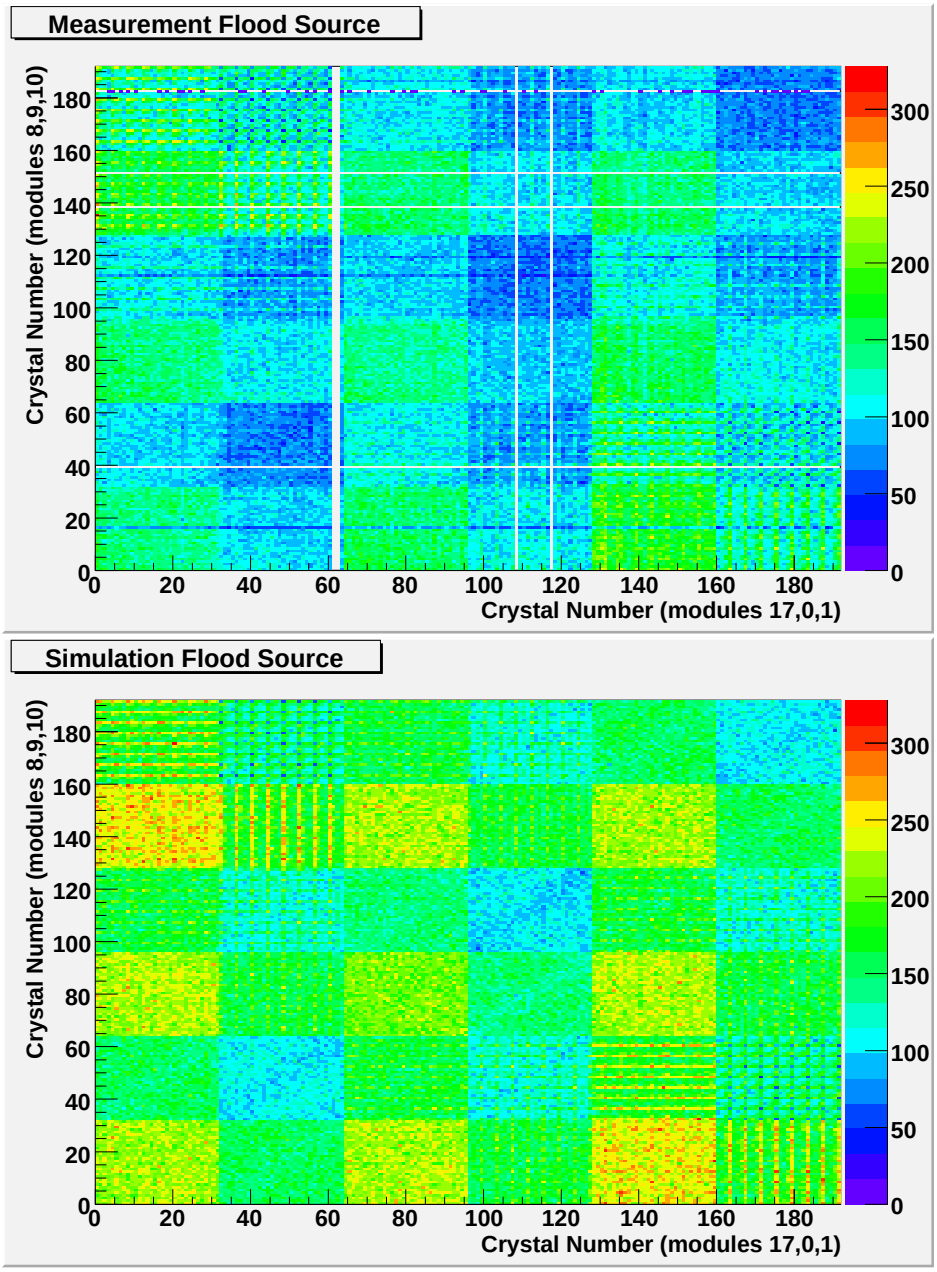

Figure 6.9: Coincidences histogram for measurement and simulation of the flood source in the 384-channel prototype. The numbering used in this histogram is explained in the caption of figure 6.6.

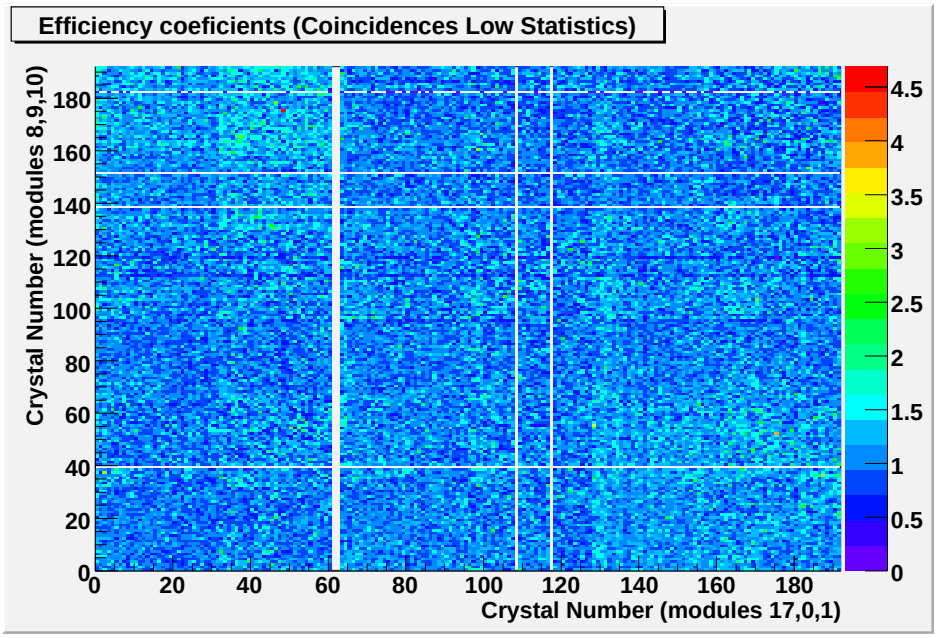

Figure 6.10: Efficiency coefficients for each LOR that belongs to the 384-channel prototype calculated from the low statistics coincidences data. The numbering used in this histogram is explained in the caption of figure 6.6.

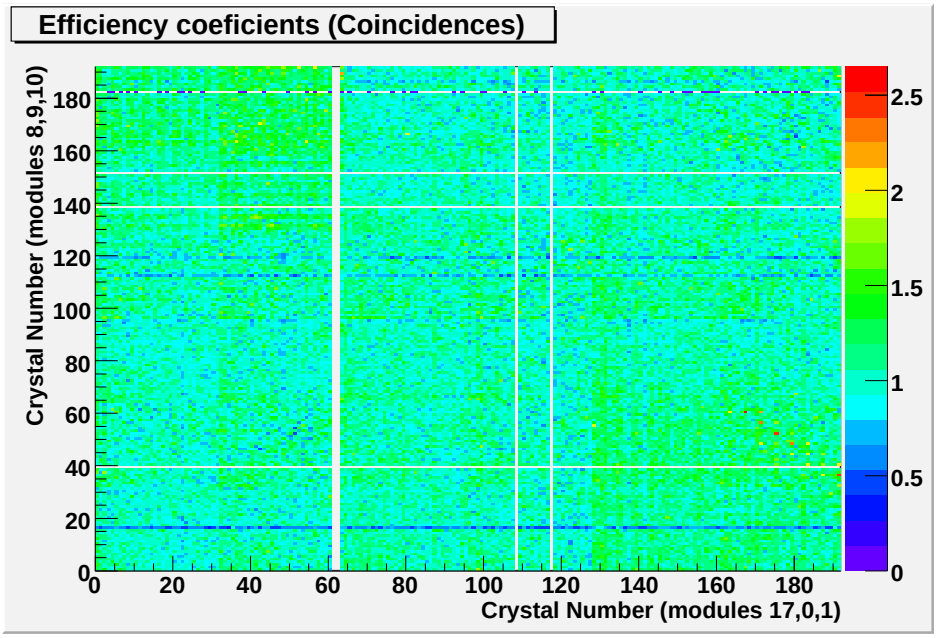

Figure 6.11: Efficiency coefficients for each LOR that belongs to the 384-channel prototype calculated from the coincidences data. The numbering used in this histogram is explained in the caption of figure 6.6.

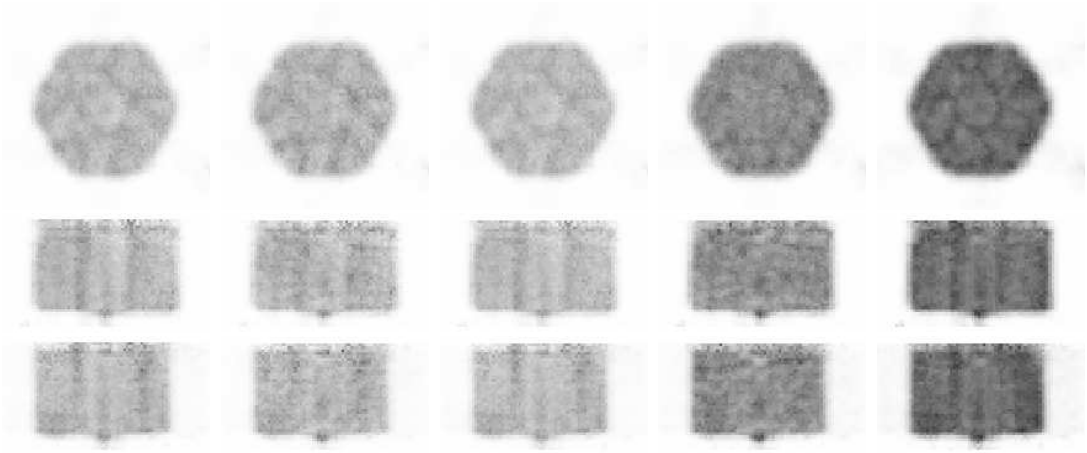

(a) NN (b) DN-C (c) DN-S (d) NRI-C (e) NRI-S

Figure 6.12: Reconstructed images of the cylindrical phantom, using 30 iterations of MLEM, and a 400 keV LET for different normalization approaches: First row corresponds to the transversal view; the coronal slices are at the second row; third row is the sagittal view. In the first column the images were not corrected (NN). The second and third columns correspond to the direct normalization, using coincidences (ND-C) and singles (ND-S) data. The normalization correction applied within the algorithm is shown in the last two columns, with coincidences data (NRI-C) and singles data (NRI-S)

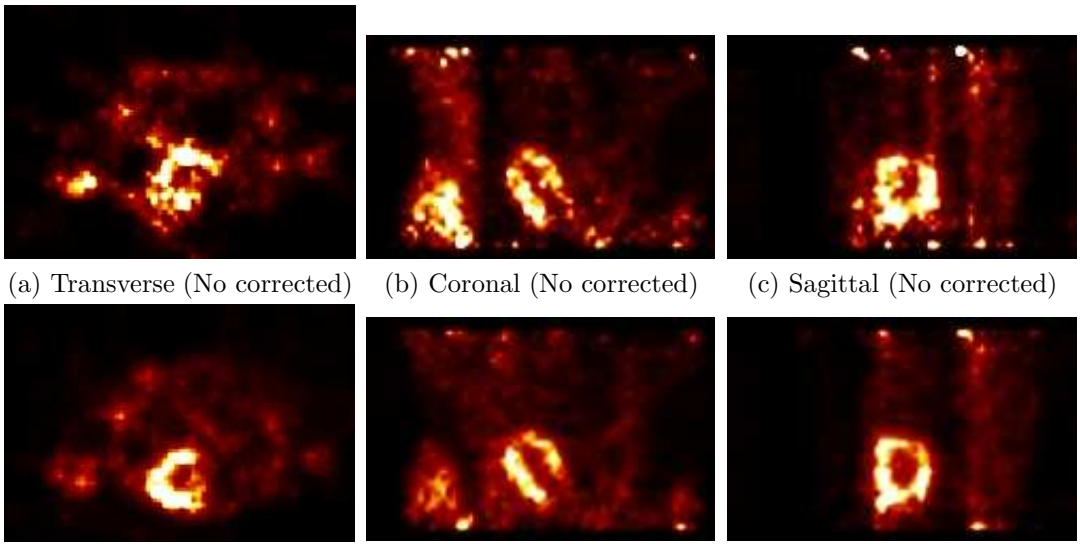

(a) Transverse (No corrected) (b) Coronal (No corrected) (c) Sagittal (No corrected)

(d) Transverse (Corrected) (e) Coronal (Corrected) (f) Sagittal (Corrected)

Figure 6.13: Reconstructed images of the mouse heart, using 50 iterations of MLEM, and a 400 keV LET. The first row correspond to the transversal, coronal and sagittal views when there is no correction applied. The images of the second row have been done taking into account the dead channels in the system matrix.

Conclusiones

Resumimos a continuación las conclusiones más relevantes que pueden extraerse de las discusiones de los capítulos precedentes.

Matriz del Sistema generada a partir simulaciones basadas en el método de Monte Carlo

En el capítulo 3 hemos mostrado como construir la matriz del sistema (SM) para MADPET-II usando técnicas de Monte Carlo a través del código GATE. Una de las limitaciones que tiene este método es el tiempo que tardan en ejecutarse las simulaciones. Para reducir este tiempo, se han utilizado las simetrías del sistema y las simulaciones se han distribuido en una granja de ordenadores. Una de las carácterísticas de MADPET-II es la flexibilidad a la hora de procesar los datos adquiridos, que viene garantizada por el formato en modo lista de los singles detectados. Esto facilita la clasificación de coincidencias por software cuando se desea utilizar distintos parámetros. De entre los parámetros que se pueden modificar después de la adquisición en MADPET-II, nos hemos centrado en el umbral de energía mínimo (LET). La principal razón es porque el LET juega un papel muy importante in la sensibilidad del escáner. Reduciendo el LET, se gana en sensibilidad pero, al mismo tiempo la dispersión en el objeto y en el detector es mayor. El aumento de dispersión puede empeorar la resolución espacial. El objetivo principal de este capítulo es analizar las imágenes reconstruídas para unos valores de LET de 200 y 400 keV. Los detectores del sistema responden de manera distinta para cada LET, por tanto se necesitan matrices del sistema específicas para cada LET. Nos referiremos a estas matrices con SM-200 y SM-400 para cada uno de los LET estudiados.

Antes de continuar con el analisis de las imágenes reconstruídas, es apropiado dedicar unas palabras a la sensibilidad que se obtiene con cada una de estas matrices. Se usó el mismo tiempo de simulación para construir ambas matrices y, como consecuencia de la mayor sensibilidad cuando trabajamos con un LET de 200 keV, la matriz de sensibilidad para este LET es menos ruidosa que a 400 keV. Si se deseara hacer una comparación justa entre ambas matrices, sería necesario incrementar el tiempo de las simulaciones para la SM-400 para alcanzar el mismo nivel de ruido en los datos. De todas formas es interesante hacer la comparación

para contrastar el comportamiento de ambas matrices cuando se ha empleado el mismo tiempo en generarlas.

En el análisis de las imágenes reconstruídas, en cuanto a la resolución espacial no se han observado diferencias en las imágenes reconstruídas del maniquíDerenzo y, en ambos casos, las capilares más pequeñas que se pueden distinguir son las de diámetro 1.5 mm. Las diferencias entre ambas matrices aparecen cuando se calcula la FWHM de las fuentes puntuales que se encuentran cerca del límite del campo de visión. De este resultado se puede concluir que la dispersión en los detectores presente en el caso de SM-200 afecta más a la resolución espacial que el ruido estadístico, que es mayor en el caso de SM-400.

Por otro lado, la matriz SM-200 produce mejores resultados en términos de cuantificación de la actividad y detección de lesión, como se observa del análisis de las correspondientes figuras de mérito (FOM). Claramente, el ruido estadístico más alto tanto en la SM y como en el histograma de LORes a la energía umbral de 400 keV es el factor que produce este resultado. La conclusión de esta parte es que una sensibilidad mayor, que implica menor ruido estadístico para el mismo tiempo de adquisición, es muy importante para cuantificar la distribución de actividad y para mejorar la detección de lesiones.

El ruido estadístico en el histograma de LORes se puede reducir aumentando el tiempo de adquisición en la medida a un LET de 400 keV. Esto no fue estudiado, pero es importante el tener en cuenta que hay medidas que están ligadas a tiempos de adquisición cortos, como estudios dinámicos para modelado farmacocinético. Además es muy importante conocer la concentración de trazador en estos estudios y, como hemos visto, bajos LET ofrecen información más precisa de la distribución de actividad. Por otro lado, en el caso de estudios estáticos, donde no estamos limitados a tiempos reducidos, trabajar con LETs de 400 keV proporcionaría mejores imágenes en cuanto a visualización de pequeños detalles. Para obtener los mismos resultados a nivel de cuantificación en el caso de SM-400, en comparación con el de SM-200, se necesitaría simular por más tiempo para obtener una matriz del sistema menos ruidosa.

De los resultados mostrados en este capítulo, se puede concluir que la flexibilidad que ofrece la adquisición en modo lista de sucesos singles del MADPET-II es una característica muy útil, porque permite adaptar el LET al tipo de estudio que se desea realizar y obtener los mejores resultados para esa tarea específica.

Corrección por coincidencias accidentales

Los métodos de la ventana restrasada (DW) y de la tasa de singles (SR) se han usado para estimar las coincidencias accidentales o random para varios valores de la energía umbral mínima. Para LETs menores de 255 keV, se observa una notable sobreestimación de las coincidencias random, siendo mayor para el método de SR que de DW. La sobreestimación encontrada en los métodos DW y su modificado DW' no se puede explicar a partir del retraso elegido para la

ventana temporal. El responable de esta sobreestimación es la dispersión que se da entre los cristales detectores, que es muy importante a bajas energías umbrales mínimas. Estos resultados se presentaron para una actividad total de 3.7 MBq. Si aumentamos la actividad, la sobreestimación aumenta para el método de SR, mientras que permanece constante para el método de DW. Este comportamiento del método SR es debido al incremento del número de coincidencias random triples para estas actividades. Las imágenes que se obtienen cuando la corrección por coincidencias random se aplica en el algoritmo de reconstrucción son mejores en términos del cociente señal-ruido, niveles de ruido y proporcionando valores de actividad absoluta (con alguna excepción en la que en ambos casos se comportan de la misma manera) que las imágenes reconstuídas con datos precorregidos. Sólo en el caso de ME (figura de mérito que mide sucesos que no han sido situados de manera correcta en la imagen reconstruída), las imágenes precorregidas muestran mejor resultados. En general, para todos los LETs estudiados, el método DW es más exacto para la obtención de la actividad absoluta de las imágenes reconstruídas, debido a la menor sobreestimación de coincidencias random, aunque la diferencia con SR a 400 keV no es muy importante para las actividades estudiadas más bajas. Las discrepancias observadas para las imágenes corregidas correspondientes a la actividad más baja (2%-4% en el peor caso) no suponen una cuestión importante, si consideramos que la exactitud de las concentraciones de actividad para imágenes no corregidas por atenuación es de -26.4% para un fantoma representativo de un ratón y -38.5% para un fantoma que representa una rata [116]. Sin embargo, la dependencia de la sobreestimación con la actividad de la fuente nos muestra que estas discrepancias son mayores para actividades más altas. A LET de 200 keV, las imágenes reconstruídas no presentan una diferencia sustancial en términos de ruido para la actividad más baja. Cuando la actividad de la fuente aumenta, la sobreestimación produce un aumento de ruido para las imágenes corregidas con el método SR a LET de 200 keV. A LET de 400 keV, las imágenes reconstruídas usando SR muestran un menor ruido para todas las actividades estudiadas. La pregunta sobre cuál es el LET más apropiado todavía queda sin contestar. Con LETs por debajo de 255 keV, hay una subestimación de la actividad reconstruída, pero las imágenes son menos ruidosas debido a la mayor sensibilidad. Trabajando a estos LETs, el método DW es el preferido. El ruido de las imágenes podría ser reducido usando técnicas de reducción de la varianza para las coincidencias aleatorias discutidas en [102]. Para LETs por encima de 255 keV, la cuantificación no supone un problema, la sensibilidad del sistema es menor y las imágenes son más ruidosas, por tanto el método SR es el más apropiado porque es el que muestra menor ruido. Para el caso de actividades más altas y para el método de SR, la sobrestimación tiene un efecto mayor y, por tanto, debe ser corregida. Por tanto, como trabajo futuro se debería estudiar cómo se puede corregir la sobrestimación en el número de coincidencias random usando los métodos de DW y SR para actividades altas. Aunque este estudio se ha llevado a cabo con la geometría de MADPET-II, se espera que los resultados sean válidos para otros sistemas formados por cristales finamente granulados.

Coincidencias triples

Las coincidencias tripes y su impacto en los métodos de estimación de coincidencias random se han estudiado en este capítulo. El principal beneficio de considerar este tipo de sucesos para la reconstrucción es que incrementa la sensibilidad del sistema. Además, en el anterior capítulo se encontró que las coincidencias triples podrían ser de ayuda para resolver el problema de la sobrestimación de coincidencias accidentales. Cuando se introducen las triples coincidencias, es necesario conocer cómo procesarlas para no deteriorar la calidad de las imágenes reconstruídas.

Primeramente se confirmó que la sensibilidad aumenta un 20% para un LET de 200 keV cuando se tienen en cuenta las coincidencias triples. Posteriormente, antes de empezar con la corrección por coincidencias random, era importante verificar que no se producía una degradación de las imágenes reconstruídas cuando se utilizaban coincidencias verdaderas tanto dobles como triples. Para hacer esto, se compararon las imágenes obtenidas usando una matriz del sistema que sólo contiene dobles coincidencias y las que se produjeron con una matriz del sistema que considera dobles y triples coincidencias. Para el análisis de la resolución espacial, se simuló un fantoma de Derenzo y unos capilares paralelos al eje del escáner y distribuídos horizontanmente, de manera que cubren el campo de visión del sistema. En el caso de las imágenes de Derenzo, no sólo no encontramos ningún tipo de degradación visula de la imagen, sino que además se pueden identificar algunas de las varillas de 1.2 mm de diámetro que se encuentran cerca del centro del campo de visión en el caso de la matriz del sistema que tiene dobles y triples coincidencias. En el caso de los capilares horizontales, pequeñas diferencias se observan en la FWTM para las fuentes situdadas cerca del límite del campo de visión. Para examinar las capacidades para recuperar la actividad emitida se ha usado el fantoma *hot-cold-background*. Es posible recuperar la actividad emitida en las imágenes reconstruídas de este fantoma con ambas matrices. Por tanto, a partir de estos primeros resultados obtenidos usando sólo coincidencias verdaderas (dobles y triples), podemos concluir que no existe deterioro de las imágenes reconstruídas usando dobles y tripes coincidencias. Además de que en términos de la resolución espacial, las imágenes donde se incluyen los triples muestran mayor calidad.

En cuanto a la corrección por coincidencias random, el considerar los sucesos triples nos lleva a tener que modificar la forma de estimar estas coincidencias para incluir estos sucesos. Hemos adaptado los métodos de DW y SR y hemos encontrado que al incluir las triples coincidencias, la sobrestimación de randoms (mostrada en en capítulo anterior) queda reducida notablemente. Además, las imágenes reconstruídas, corregidas por coincidencias random y con coincidencias triples, no muestran ningún artefacto consecuencia de la modificación de los métodos de estimación de coincidencias accidentales y que supusiera el no poder utilizar los métodos modificados. Al contrario, no existe ninguna apreciable diferencia visual entre ellas y las imágenes obtenidas usando sólo doble coincidencias.

Del análisis cuantitativo se obtiene que la introducción de las triples coincidencias resuelve la subestimación de la actividad y, al ser la sensibilidad mayor, el ruido de las imágenes es menor.

Por tanto, las coincidencias triples se presentan como buenas candidatas para ser incluídas en el proceso de reconstrucción porque, por un lado, aumentan la sensibilidad del sistema y por el otro reducen la sobrestimación de coincidencias random para bajos LET. Aunque no hay que olvidar que los resultados presentados aquíson para una matriz del sistema hecha para un solo corte del FOV. Por tanto, sería necesario confirmar estos resultados en una matriz del sistema en 3D y para objetos mayores.

Finalmente, en este trabajo nos hemos centrado en un único algoritmo para clasificar las coincidencias que usa una única ventana temporal de coincidencias. Existen otro tipo de algoritmos que utilizan múltiples ventanas de coincidencias y cambian la clasificación de lo que es una doble y triple coincidencia. Para un mayor análisis sobre esta cuestión referimos al trabajo [129], donde se hace una comparación entre métodos de clasificación que usan ventana temporal única y los que utilizan múltiples ventanas.

Normalización

Para resumir los resultados cuantitativos y cualitativos de esta parte, no es evidente cuál es el mejor método para estimar las eficiencias entre los métodos basados en singles y en dobles, pero lo que síqueda confirmado es que la normalización se debe de aplicar durante el proceso de reconstrucción. Esta última conclusión está de acuerdo con la teoría, que propone que todas las correcciones se deben de considerar durante el algoritmo de reconstrucción MLEM, basado en el modelo estadístico de Poisson. Aunque es un resultado preliminar, presentamos en esta sección las imágenes reconstruídas del corazón de un ratón que fue medido con el sistema completo. Para el sistema completo no hay medidas para realizar la normalización. Pero, de las medidas tomadas al corazón del ratón, fue posible conocer los canales muertos del sistema y hemos comprobado el efecto de tener en cuenta los canales muertos en la matriz del sistema o no tenerlos. Para contar con los canales muertos en la SM, los elementos de ésta que están formados por un canal muerto se hacen iguales a cero. Las imágenes reconstruídas del corazón del ratón se muestran en la figura 6.13. En la primera línea, las imágenes fueron reconstruídas sin modificar la matriz del sistema. Mientras que en la línea de abajo, los canales muertos se tuvieron en cuenta. Es obvio a partir de las imágenes, que las corregidas tienen una mayor calidad y presentan menos artefactos. Este último resultado apoya lo que la teoría propone y lo que hemos encontrado en el sistema de 6 módulos con la fuente cilíndrica: las correcciones se deben de llevar a cabo dentro del proceso de reconstrucción.

Comparando los métodos propuestos, las imágenes reconstruídas son más uniformes con el NRI-S, pero hay un artefacto en el centro de la imágen. Por el con-

trario, las imágenes corregidas usando NRI-C no muestran este artefacto, pero son más ruidosas (error relativo más grande). Como los datos vienen del sistema de 384 canales, podría existir otra razón para el artefacto que el comentado desajuste, como por ejemplo que el eje de rotación no estuviera bien alineado. Por tanto, esperamos que medidas y simulaciones del sistema completo nos proporcionen la respuesta a esta pregunta que queda abierta.

En términos del tiempo de adquisición de la medida de normalización, en caso de usar los singles, no sería necesario aumentarlo. Mientras que cuando se usan las coincidencias, se esperan mejoras en la uniformidad de las imágenes reconstruídas si se incrementara el tiempo de adquisición.

Finalmente, unas palabras relacionadas con la obtención de la actividad emitida a partir de las imágenes reconstruídas. En principio, las imágenes reconstruídas deberían proporcionar la actividad emitida. Pero el tiempo de adquisición de la medida de la fuente cilíndrica era conocido de manera muy imprecisa (1 minuto de error entre sets de medidas). Esto lleva a un gran error en el cálculo de la actividad emitida (mayor de un 20%). Además, las imágenes reconstruídas no se corrigieron por atenuación. En [116], la diferencia entre la actividad emitida y la actividad obtenida en las imágenes reconstruídas de un fantoma tamaño ratón de 30 mm de diámetro es 25%. Por tanto, al nivel que estamos en este estudio, hay demasiadas indeterminaciones y no tiene sentido comparar las diferentes propuestas en su capacidad para recuperar la actividad emitida.

List of Abbreviations

- **ADC**: Analog to Digital Converter
- **APD**: Avalanche PhotoDiode
- **ASIC**: Application Specific Integrated Circuit
- CRC: Contrast Recovery Coefficient
- **CSP**: Charge Sensitive Preamplifier
- **CT**: Computer Tomography
- D: Discrepancy
- **DN**: Direct Normalization
- **DN-C**: Direct Normalization Coincidences-based
- **DN-S**: Direct Normalization Singles-based
- **DOI**: Depth Of Interaction
- **DW**: Delayed Window
- **DWSub**: Delayed Window Subtracted (prior reconstruction)
- **DWmd**: Delayed Window maximum distance
- **DWme**: Delayed Window maximum energy
- **EM**: Expectation Maximization
- **FBP**: Filtered Back Projection
- **FOM**: Figure Of Merit
- **FOV**: Field Of View
- **FPGA**: Field Programmable Gate Array
- **FWHM**: Full Width Half Maximum

- **FWTM**: Full Width Tenth Maximum
- **GATE**: Geant4 Application for Tomographic Emission
- **HCB**: Hot-Cold-Background
- **IC**: Inter-Crystal
- **ICS**: Inter-Crystal Scatter
- **IF**: Identification Fraction
- **LCG**: LHC Computing Grid
- **LET**: Low Energy Threshold
- **LHC**: Large Hadron Collider
- **LOR**: Line Of Response
- **MADPET**: Munich Avalanche photoDiode Positrom Emission Tomograph
- **MC**: Monte Carlo
- **MCSM**: Monte Carlo System Matrix
- **MD**: Maximum Distance
- **ME**: Maximum Energy
- ME: Mispositioned Events
- **ML**: Maximum Likelihood
- **MLEM**: Maximum Likelihood Expectation Maximization
- **NEMA**: National Electrical Manufacturers Association
- NF: Normalization Factor
- **NN**: No Normalization
- **NRI**: Normalization within the Reconstruction of the Image
- **NRI-C**: Normalization within the Reconstruction of the Image, Coincidences-based
- **NRI-CLS**: Normalization within the Reconstruction of the Image, Coincidences-based with Low Statistics data
- **NRI-S**: Normalization within the Reconstruction of the Image, Singles-based

- **NRI-SLS**: Normalization within the Reconstruction of the Image, Singles-based with Low Statistics Data
- **OSEM**: Ordered Subsets Expectattion Maximization
- **PET**: Positron Emission Tomography
- **PMT**: PhotoMultiplier Tube
- **PSF**: Point Spread Function
- **ROI**: Region Of Interest
- **SiPM** Silicon PhotoMultiplier
- **SM**: System Matrix
- SNR: Signal-to-Noise Ratio
- **SPECT**: Single Photon Emission Computed Tomography
- **SR**: Singles Rate
- **SRSub**: Singles Rate Subtracted (prior reconstruction)
- **SRns**: Singles Rate new sorting
- **STIR**: Software for Tomographic Image Reconstruction
- **TDC**: Time to Digital Converter
- **TH**: Time Histogram
- **VO**: Virtual Organization
- **VOR**: Volume Of Response
- **1D**: 1 Dimensional
- **2D**: 2 Dimensional
- **3D**: 3 Dimensional

Bibliography

[1] Phelps M E, Hoffman E J, Mullani N A, Ter-Pogossian M M. 1975 Application of annihilation coincidence detection to transaxial reconstruction tomography. *J. Nuc. Med.* **16** 210-224

[2] Harper M D. 2004 Positronium: review of simmetry, conserved quantities and decay for the radiological physicist. *Med. Phys.* **31** 57-61

[3] Hoffman E J, Huang S-C, Phelps M E, Kuhl D E. 1981 Quantitation in positron emission computed tomography. IV. Effect of accidental coincidences. *J. Comput. Assist. Tomogr.* **5** 391-400

[4] Strother S C, Casey M E, Hoffman E J. 1990 Measuring PET scanner sensitivity: relating count rates to image signal-to-noise ratios using noise equivalent counts. *IEEE Trans. Nucl. Sci.* **37** 783-788

[5] Hoffman E J, Phelps M E. 1976 An analysis of some of the physical aspects of positron transaxial tomography. *Comput. Biol. Med.* **6** 345-360

[6] Moses W W, Derenzo S E. 1993 Empirical observation of resolution degradation in positron emission tomographs utilizing block detectors. *J. Nucl. Med.* **34** 101P

[7] Budinger T F, Derenzo S E, Huesman R H, Jagust W J, Valk P E. 1991 High resolution positron emission tomography for medical science studies. *Acta. Radiol.* **376** 15-23

[8] Fowler J S, Wolf A P. 1986 Positron emitter labeled compounds: Priorities and problems. In "Positron Emission Tomography and Autorradiography" (M. Phelps, J. Mazziotta, H. Schelbert, eds.), pp 391-450. Raven Press, New York

[9] Phelps ME. 2000 PET: The merging of Biology and Imaging into Molecular Imaging. *J. Nucl. Med.* **41** 558-564

[10] Bailey D L, Jones T, Spinks T J. 1991 A method of measuring the absolut sensitivity of positron emission tomographic scanners. *Eur. J. Nucl. Med.* **18** 374-379

[11] Chatziioannou A F, Cherry S R, Shao Y, Silverman R W, Meadors K, Farquhar T H, Pedarsani M, Phelps M E. 1999 Performance evaluation of microPET: A high-resolution lutetium oxy-orthosilicate PET scanner for animal imaging. *J. Nucl. Med.* **40** 1164-1175

[12] Marler J, McCauley T, Reucroft S, Swain J, Budil D, Kolaczkowski S. 2000 Studies of avalanche photodiode performance in a high magnetic field. *Nucl. Instrum. Methods A* **449** 311-313

[13] Buzhan P, Dolgoshein B, Filatov L, Ilyin A, Kantzerov V, *et al.* 2003 Silicon photomultiplier and its possible applications. *Nucl. Instrum. Methods A* **504** 48-52

[14] Georgievskya E A, Klemin S N, Filatov L A, Buzhan P J, Dolgoshein B A *et al.* 2003 The solid state silicon photomultiplier for a wide range of applications. *Proc. SPIE Int. Soc. Opt. Eng. (USA)* **5126** 3742

[15] Golovin V, Saveliev V. 2004 Novel type of avalanche photodetector with Geiger mode operation. *Nucl. Instrum. Methods A* **518** 560-564

[16] Hume S P, Gunn R N, Jones T. 1998 Pharmacological constraints associated with positron emission tomographic scanning of small laboratory animals. *Eur. J. Nucl. Med.* **25** 173-176

[17] Shepp L A, Vardi Y. 1982 Maximum likelihood estimation for emission tomography. *IEEE Trans Med. Imaging* **1** 113-121

[18] Hudson H M, Larkin R S. 1994 Accelerated image reconstruction using ordered subsets of projection data. *IEEE Trans Med. Imaging* **13** 601-609

[19] Wernick M N and Aarsvold J N. 2004 *Emission Tomography, The Fundamentals of PET and SPECT* (Elsevier Academic Press)

[20] Natterer F and Wübbeling F. 2001 *Mathematical Methods in Image Reconstruction* (SIAM, Philadelphia)

[21] Natterer F. 1986 *The mathematics of computerized tomography* (Wiley, New York)

[22] Townsend D W and Defrise M 1993 *Image Reconstruction methods in positron tomography* (Academic Training Lectures, CERN)

[23] Colsher J G. 1980 Fully three-dimensional Positron Emission Tomography *Phys. Med. Biol.* **25** 103-115

[24] Chu G and Tam K C. 1977 3D imaging in the positron camera using Fourier techniques *Phys. Med. Biol.* **22** 245-265

[25] Rogers J G, Harrop R, Kinahan P E. 1987 The theory of three-dimensional image reconstruction *IEEE Trans. Med. Imaging* **6** 239-243

[26] Kinahan P E, Rogers J G, Harrop R and Johnson R. 1988 Three-dimensional image reconstruction in object space *IEEE Trans. Nucl. Sci.* **35** 635-638

[27] Kinahan P E and Rogers J G. 1989 Analytic 3D Image Reconstruction using all detected events *IEEE Trans. Nucl. Sci.* **36** 964-968

[28] Qi J, Leahy R M, Hsu C, Farquhar T H and Cherry S R. 1996 Fully 3D Bayesian image reconstruction for the ECAT EXACT HR+' *IEEE Trans. Nuc. Sci.* **45** 1096-1103

[29] Yavus M and Fessler J A. 1996 Objective functions for tomographic reconstruction from randoms-precorrected PET scans *IEEE NSS MIC Conf. Rec.* **2** 1067-1071

[30] Leahy R M and Qi J. 2000 Statistical approaches in quantitative positron emission tomography *Statistics and Computing* **10** 147-165

[31] Compton A H. 1923 A quantum theory of the scattering of X-rays by light elements *Phys. Rev.* **21** 483-502

[32] Electron Gamma Shower (EGS) Monte Carlo Radiation Transport Code. http://pager.lbl.gov/egs/egs.html

[33] MCNP directory. http://www-xdiv.lanl.gov/XCI/PROJECTS/MCNP/

[34] Halbleib JA, Kensek RP, Mehlhorn TA, Valdez GD, Seltzer SM, Berger MJ. ITS Version 3.0: the integrated TIGER series of coupled electron/photon Monte Carlo transport codes. Sandia National Laboratories. Technical Report SAND91-1634, 1992

[35] GEANT 3 home page. http://wwwasd.web.cern.ch/wwwasd/geant/

[36] GEANT 4 home page. http://geant4.web.cern.ch/geant4/

[37] Ljungberg M, Strand SE. 1989 A Monte Carlo program for the simulation of scintillation camera characteristics *Comput. Methods Prog. Biomed.* **29** 257-272

[38] Yanch J C, Dobrzeniecki A B, Ramanathan C, Behrman R. 1992 Physically realistic Monte Carlo simulation of source, collimator and tomographic data acquisition *Phys. Med. Biol.* **37** 853-870

[39] Yanch J C, Dobrzeniecki A B. 1993 Monte Carlo simulation in SPECT: complete 3D modelling of source, collimator and tomographic data acquisition *IEEE Trans. Nucl. Sci.* **40** 198-203

[40] Smith M F. 1993 Modelling photon transport in non-uniform media for SPECT with a vectorized Monte Carlo code *Phys. Med. Biol.* **38** 1459-1474

[41] Smith M F, Floyd C D, Jaszczak R J. 1993 A vectorized Monte Carlo code for modelling photon transport in SPECT *Med. Phys.* **20** 1121-1127

[42] Thompson C J, Cantu J M, Picard Y. 1992 PETSIM: Monte Carlo program simulation of all sensitivity and resolution parameters of cilindrical positron imaging systems. *Phys. Med. Biol.* **37** 731-749

[43] Thompson C J, Picard Y. 1998 PETSIM: Monte Carlo simulation of positron imaging systems. In: Ljungberg M, Strand SE, King M, editors. Monte Carlo calculations in nuclear medicine. Bristol and Philadelphia: IOP Publishing, 233-248

[44] Zaidi H, Labbe C, Morel C. 1998 EIDOLON: Implementation of an environment for Monte Carlo simulation of fully 3D positron tomography on a high performance parallel platform *Parallel Comput.* **24** 523-536

[45] Reilhac A, Gregoire M C, Costes N, Lavenne F, Pierre C, Diou A *et al.* 1999 A PET Monte Carlo simulator from numerical phantoms: validation against the EXACT ECAT HR+ scanner. *IEEE NSS MIC Conf. Rec.* 1527-1536

[46] Castiglioni I, Cremonesi O, Gilardi M C, Bettinardi V, Rizzo G, Savi A *et al.* 1999 Scatter correction techniques in 3D PET: a Monte Carlo evaluation. *IEEE Tans. Nucl. Sci.* **46** 2053-2058

[47] Harrison R L, Vannoy S D, Haynor D R, Gillipsie S B, Kaplan M S, Lewellen T K. 1993 Preliminary experience with the photon history generator module of a public domain simulation system for emission tomography. *IEEE NSS MIC Conf. Rec.* 1154-1158

[48] SIMSET home page. http://depts.washington.edu/simset/html/simset_main.html

[49] GATE home page. http://opengatecollaboration.healthgrid.org/

[50] Jan S, Santin G, Strul D, Staelens S, Assié K, Autret D, Avner S, Barbier R, Bardiés M, Bloomfield P M, Brasse D, Breton V, Bruyndonckx P, Buvat I, Chatziioannou A F, Choi Y, Chung Y H, Comtat C, Donnarieix D, Ferrer L, Glick S J, Groiselle C J, Guez D, Honore P F, Kerhoas-Cavata S, Kirov A S, Kohli V, Koole M, Krieguer M, van der Laan D J, Lamare F, Largeron G, Lartizien C, Lazaro D, Maas M C, Maigne L, Mayet F, Melot F, Merheb C, Pennacchio E, Perez J, Pietrzyk U, Rannou F R, Rey M, Schaart D R, Schmidtlein C R, Simon L, Song T Y, Vieira J M, Visvikis D, Van de Walle R, Wiers E, Morel C. 2004 GATE: a simulation toolkit for PET and SPECT. *Phys. Med. Biol.* **49** 4543-4561

[51] Assié K, Breton V, Buvat I, Comtat C, Jan S, Krieguer M, Lazaro D, Morel C, Rey M, Santin G, Simon L, Staelens S, Strul D, Vieira J M, Van der Walle R. 2004 Monte Carlo simulation in PET and SPECT instrumentation using GATE *Nucl. Instrum. Methods A* **527** 180-189

[52] Agostinelli S, Allison J, Amako K, Apostolakis J, Araujo H, Arce P, Asai M, Axen D, Banerjee S, Barrand G, Behner F, Bellagamba L, Boudreau J, Broglia L, Brunengo A, Burkhardt H, Chauvie S, Chuma J, Chytracek R, Cooperman G *et al.* 2003 Geant4-a simulation toolkit *Nucl. Instrum. Methods A* **506** 250-303

[53] Santin G, Strul D, Lazaro D, Simon L, Krieguer M, Vieira Martins M, Breton V and Morel C. 2003 GATE: A Geant4-based simulation platform for PET and SPECT integrating movement and time management *IEEE Trans. Nucl. Sci.* **50** 1516-1521

[54] Worldwide LHC Computing Grid webpage. https://edms.cern.ch/file/454439//LCG-2-UserGuide.pdf

[55] Tai Y-Ch and Laforest R. 2005 Instrumentation Aspects of Animal PET *Annu. Rev. Biomed. Eng.* **7** 255-285

[56] Levin C S and Hoffman E J. 1999 Calculation of positron range and its effect on the fundamental limit of positron emission tomography system spatial resolution *Phys. Med. Biol.* **44** 781-799

[57] Cherry S R, Dahlbom M and Hoffman E J. 1991 3D PET using a conventional multislice tomograph without septa *J. Comput. Assist. Tomogr.* **15** 655-668

[58] Badawi R D, Marsden P K, Cronin B F, Sutcliffe J L and Maisey M N. 1996 Optimization of noise-equivalent count rates in 3D PET *Phys. Med. Biol.* **41** 1755-1776

[59] Bailey D L, and Meikle S R. 1994 A Convolution-Subtraction scatter correction method for 3D PET *Phys. Med. Biol.* **39** 411-424

[60] Bentourkia M, Msaki P, Cadorette J and Lecompte R. 1995 Assessment of Scatter Components in High-Resolution PET: Correction by Nonstationary Convolution Subtraction *J. Nucl. Med.* **36** 121-130

[61] Cherry S R, Meikle S R and Hoffman E J. 1993 Correction and Characterisation of Scattered Events in Three-Dimensional PET Using Scanners with Retractable Septa *J. Nucl. Med.* **34** 671-678

[62] Shao L, Freifelder R and Karp J S. 1994 Triple Energy Window Scatter Correction Technique in PET *IEEE Trans. Med. Imag.* **13** 641-648

[63] Grootoonk S, Spinks T J, Sashin D, Spryou N M and Jones T. 1996 Correction for scatter in 3D brain PET using a dual energy window method *Phys. Med. Biol.* **41** 2757-2774

[64] Ollinger J M. 1996 Model-based scatter correction for fully 3D PET *Phys. Med. Biol.* **41** 153-176

[65] Watson C C, Newport D and Casey M E. 1996 A single-scatter simulation technique for scatter correction in 3D PET. In "Fully Three-Dimensional Image Reconstruction in Radiology and Nuclear Medicine" (Eds P Grangeat and J L Amans, Kluwer Academic Publishers)

[66] Townsend D W, Sprinks T, Jones T, Geissbuhler A, Defrise M, Gilardi M C, Heather J. 1989 Three dimensional reconstruction of PET data from a multi-ring camera *IEEE Trans. Nucl. Sci.* **36** 1056-1065

[67] Lecomte R. 2008 Molecular PET Instrumentation and Imaging Techniques. In "Molecular Imaging in Oncology" (Eds Pomper M G and Gelovani J G, Informa Healthcare)

[68] Carroll L, Kertz P, and Orcut G. 1983 The orbiting rod source: Improving performance in PET transmission correction scans. In "Emission Computed Tomography - Current Trends" (Eds P D Esser, Society of Nuclear Medicine)

[69] Daube-Witherspoon M E, Carson R, and Green M. 1988 Postinjection transmission attenuation measurements for PET *IEEE Trans. Nucl. Sci.* **35** 757-761

[70] Karp J S, Muehllehner G, Qu H and Yan X H. 1995 Singles Transmission in Volume-Imaging PET with a Cs-137 Source *Phys. Med. Biol.* **40** 929-944

[71] Germano G and Hoffman E J. 1990 A Study of Data Loss and Mispositioning due to Pileup in 2-D Detectors in PET *IEEE Trans. Nucl. Sci.* **37** 671-675

[72] McElroy D P, Pimpl W, Pichler B J, Rafecas M, Schuler T and Ziegler S I. 2005 Characterization and Readout of MADPET-II Detector Modules: Validation of a Unique Design Concept for High Resolution Small Animal PET *IEEE Trans. Nuc. Sci.* **52** 199-204

[73] McElroy D P, Hoose M, Pimpl W, Spanoudaki V, Schuler T and Ziegler S I. 2005 A true singles list-mode data acquisition system for a small animal PET scanner with independent crystal readout *Phys. Med. Biol.* **50** 3323-3335

[74] Spanoudaki V. Development and performance studies of a small animal positron emission tomograph with individual crystal readout and depth of nteraction information and studies of novel detector technologies in medical imaging. *Dissertation*, Technische Universität München, 2008

[75] Pichler B J, Pimpl W, Buttler W, Kotoulas L, Böning G, Rafecas M, Lorenz E and Ziegler S. 2001 Integrated low-noise low-power fast charge-sensitive preamplifier for avalanche photodiodes in JFET-CMOS technology *IEEE Trans. Nuc. Sci.* **48** 2370-2374

[76] Mumcouglu E U, Leahy R M, Cherry S R. 1996 Bayesian reconstruction of PET images: methodology and performance analysis. *Phys. Med. Biol.* **41** 1777-1807

[77] Qi J, Leahy R M, Cherry S R, Chatziioannou A, Farquhar T H. 1998 High resolution 3D Bayesian image reconstruction using the microPET small-animal scanner. *Phys. Med. Biol.* **43** 1001-1013

[78] Siddon R L. 1985 Fast Calculation of the exact radiological path for three-dimensional CT array. *Med. Phys.* **12** 252-255

[79] Terstegge A, Weber S, Herzog H, Halling H. 1996 Resolution and better quantification by tube of response modelling in 3D PET reconstruction. *IEEE NSS MIC Conf. Rec.* **3** 1603-1607

[80] Selivanov V, Picard Y, Cadorette, Rodrigue S, Lecomte R. 2000 Detector response models for statistical iterative image reconstruction in high resolution PET *IEEE Trans. Nucl. Sci.* **47** 1168-1175

[81] Frese T, Rouze N C, Bouman C A, Sauer K, Hutschins G D. 2003 Quantitative comparison of FBP, EM and bayesian reconstruction algorithms for the IndyPET scanner *IEEE Trans. Med. Imag.* **22** 258-276

[82] Strul D, Slates B, Dahlbom M, Cherry S R, Marsden P K. 2003 An improved analytical detector response function model for multilayer small-diameter PET scanners *Phys. Med. Biol.* **48** 979-994

[83] Panin V Y, Kehren F, Rothfuss H, Hu D, Michel C, Casey M E. 2006 PET reconstruction with system matrix derived from point source measurements *IEEE Trans. Nucl. Sci.* **53** 152-159

[84] Panin V Y, Kehren F, Michel C, Casey M. 2006 Fully 3-D PET reconstruction with system matrix derived from point source measurements *IEEE Trans. Med. Imag.* **25** 907-921

[85] Verklerov E, Llacer J, Hoffman E J. 1988 MLE reconstruction of a brain phantom using a Monte Carlo transition matrix and statistical stopping rule *IEEE Trans. Nucl. Sci.* **35** 603-607

[86] Herraiz J L, España S, Vaquero J J, Desco M and Udías J M. 2006 FIRST: Fast Iterative Reconstruction Software for (PET) tomography *Phys. Med. Biol.* **51** 4547-4565

[87] Jan S, Comtat C, Strul D, Santin G, Trbossen R. 2005 Monte Carlo simulation for the ECAT EXACT HR+ system using GATE *IEEE Trans. Nucl. Sci.* **52** 627-633

[88] Bataille F, Comtat C, Jan S, Trbossen R. 2004 Monte Carlo simulation for the ECAT HRRT using GATE *IEEE NSS MIC Conf. Rec.* **4** 2570-2574

[89] Michel C, Eriksson L, Rothfuss H, Bendriem B, Lazaro D, Buvat I. 2006 Influence of crystal material on the performance of the HiRez 3D PET scanner: A Monte-Carlo study *IEEE NSS MIC Conf. Rec.* **4** 1528-1531

[90] Lamare F, Turzo A, Bizais Y, Le Rest CC, Visvikis D. 2006. Validation of a Monte Carlo simulation of the Philips Allegro/GEMINI PET systems using GATE *Phys. Med. Biol.* **51** 943-962

[91] Schmidtlein C R, Kirov A S, Bidaut L M, Nehmeh S A, Erdi Y E, Ganin A, Stearns C W, McDaniel D L, Hamacher K A, Humm J L, Amols H I. 2006 Validation of GATE Monte Carlo simulations of the GE Advance/Discovery LS PET scanner *Med. Phys.* **33** 198-208

[92] Jan S, Desbre A, Pain F, Guez D, Comtat C, Gurden H, Kerhoas S, Laniece P, Lefebvre F, Mastrippolito R, Trebossen R. 2005 Monte Carlo simulation of the microPET FOCUS system for small rodents imaging applications *IEEE NSS MIC Conf. Rec.* **3** 1653-1657

[93] Merheb C, Nicol S, Petegnief Y, Talbot J N, Buvat I. 2006 Assessment of the Mosaic animal PET system response using list-mode data for validation of GATE Monte Carlo modelling *Nucl. Instrum. Methods A* **A569** 220-224

[94] Lecomte R. 2004 Technology challenges in small animal PET imaging *Nucl. Instrum. Methods A* **527** 157-165

[95] Schäfers K P, Reader A J, Kriens M, Knoess C, Schober O, Schäfers M. 2005 Performance Evaluation of the 32-Module quadHIDAC Small-Animal PET Scanner *J Nucl Med* **46** 996-1004

[96] Yang Y, Cherry S R. 2006 Observations Regarding Scatter Fraction and NEC Measurements for Small Animal PET *IEEE Trans. Nucl. Sci.* **53** 127-132

[97] Lehnert W, Meikle S R, Newport D F. 2008 Count Rate Performance of the MicroPET Focus 220 Animal Scanner in Singles Transmission Scanning Mode *IEEE Trans. Nucl. Sci.* **55** 2493-2500

[98] Rafecas M. High Resolution Animal PET with Granulated Detectors: Pre-reconstruction Processing and Evaluation of Novel Design Options. *Tesis de Doctorado*, Universitat de València, 2001

[99] Böning G. Verbesserte statistische Bildrekonstruktion für die hochauflösende PET: Bestimmung der Systemmatrix aus Monte Carlo Simulationen, Validierung und Anwendung auf Tiermessungen, sowie Erweiterung für einen Doppellagen-Tomographen. *Dissertation*, Technische Universität München, 2002

[100] Software for Tomographic Image Reconstruction. STIR home page: http://stir.sourceforge.net/

[101] Torres-Espallardo I, Rafecas M, Spanoudaki V, McElroy D P and Ziegler S I. 2008 Effect of Inter-Crystal Scatter on Estimation Methods for Random Coincidences and Subsequent Correction *Phys. Med. Biol.* **53** 2391-2411

[102] Badawi R D, Millers M P, Bailey D L and Marsden P K. 1999 Randoms variance reduction in 3D PET *Phys. Med. Biol.* **44** 941-954

[103] Brasse D, Kinahan P E, Lartizien C, Comtat C, Casey M and Morel C. 2005 Correction Methods for Random Coincidences in Fully 3D Whole-Body PET: Impact on Data and Image Quality *J Nucl Med* **46** 859-867

[104] Evans R D. 1955 *The Atomic Nucleus* (McGraw Hill Book Co, New York), 791-793

[105] Yu D F, Fessler J A. 2002 Mean and variance of coincidence counting with deadtime *Nucl. Instrum. Methods A* **488** 362-374

[106] Knoll G F. 1999 *Radiation Detection and Measurement* (John Wiley & Sons, Inc.), 667

[107] Politte D G and Snyder D L. 1991 Corrections for accidental coincidences and attenuation in maximum-likelihood image reconstruction for positron-emission tomography *IEEE Trans. Med. Imaging* **10** 82-89

[108] Rafecas M, Boning G, Pichler B J, Lorenz E, Schwaiger M and Ziegler S I. 2003 Inter-crystal scatter in a dual layer, high resolution LSO-APD positron emission tomograph *Phys. Med. Biol.* **48** 821-848

[109] Rafecas M , Mosler B, Dietz M, Pogl M, Stamatakis A, McElroy D P and Ziegler S I. 2004 Use of a Monte Carlo-Based Probability Matrix for 3-D Iterative Reconstruction of MADPET-II Data *IEEE Trans. Nucl. Sci.* **51** 2597-2605

[110] Rafecas M, Boning G, Pichler B J, Lorenz E, Schwaiger M and Ziegler S I. 2004 Effect of Noise in the Probability Matrix Used for Statistical Reconstruction of PET Data *IEEE Trans. Nucl. Sci.* **51** 149-156

[111] Rafecas M, Torres-Espallardo I, Spanoudaki V Ch, McElroy D P and Ziegler S I. 2007 Estimating accidental coincidences for pixelated PET detectors and singles list-mode acquisition *Nucl. Instrum. Methods A* **564** 285-288

[112] Rahmim A, Cheng J Ch, Blinder S, Camborde M L and Sossi V. 2005 Statistical dynamic image reconstruction in state-of-the-art high-resolution PET *Phys. Med. Biol.* **50** 4887-4912

[113] Spanoudaki V Ch, McElroy D P and Ziegler S I. 2006 An analog signal processing ASIC for a small animal LSO-APD PET tomograph *Nucl. Instrum. Methods A* **564** 451-462

[114] Tetrault M A, Lepage M D, Viscogliosi N, Belanger F, Cadorette J, Pepin C M, Lecomte R and Fontaine R. 2005 Real Time Coincidence Detection System for Digital High Resolution APD-based Animal PET scanner *IEEE NSS MIC Conf. Rec.* 2850-2853

[115] Torres-Espallardo I, Rafecas M, Spanoudaki V, McElroy D P and Ziegler S I. 2006 Evaluation of different random estimation methods for the MADPET-II small animal PET scanner using GATE *IEEE NSS MIC Conf. Rec.* 3148-3150

[116] Chow P L, Rannou F R and Chatziioannou A F. 2005 Attenuation correction for small animal PET tomographs *Phys. Med. Biol.* **50** 1837-1850

[117] Casey M E and Hoffman E J. 1986 Quantitation in positron emission computed tomography: 7. A technique to reduce noise in accidental coincidence measurements and coincidence efficiency calibration *J. Comput. Assist. Tomogr.* **10** 845-850

[118] Boggs S E and Jean P. 2001 Event reconstruction in high resolution Compton telescopes *Astron Astrophys*, in press

[119] Abuelhia E, Kacperski K and Spyrou N M. 2006 Three-photon annihilation in PET: 2D imaging experiments *J. of Radioanal. Nuc. Chem.* **271** 489-495

[120] Comanor K A, Virador P R G and Moses W W. 1996 Algorithms to identify detector Compton scatter in PET modules *IEEE Trans. Nucl. Sci.* **43** 2213-2218

[121] LeBlanc J W, Clithorne N H, Hua C-H, Nygard E, Rogers W L, Wehe D K, Weilhammer P and Wilderman S J. 1998 C-SPRINT: A prototype Compton camera system for low energy gamma ray imaging *IEEE Trans. Nucl. Sci.* **45** 943-949

[122] Miyaoka R S and Lewellen T K. 2000 Effect of detector scatter on the decoding accuracy of a DOI detector module *IEEE Trans. Nucl. Sci.* **47** 1614-1619

[123] Oberlack U G, Aprile E, Curioni A, Egorov V and Giboni K L. 2000 Compton scattering sequence reconstruction algorithm for the liquid xenon gamma–ray imaging telescope (LXeGRIT) *Hard X–ray gamma–ray and neutron detector physics II* (SPIE) **4141**

[124] Rohe R and Valentine J D. 1995 A novel Compton scatter camera design for *in vivo* medical imaging of radiopharmaceuticals *IEEE NSS MIC Conf. Rec.* **3** 1579-1583

[125] Scannavini M G, Speller R D, Royle G J, Cullum I, Raymond M, Hall G and Iles G. 2000 Design of a small laboratory Compton camera for the imaging of positron emitters *IEEE Trans. Nucl. Sci.* **47** 1155-1162

[126] Schonfelder V, Hierner A and Schneider K. 1973 A telescope for soft gamma rays astronomy *Nucl Inst and Meth in Phys Res* **107** 385-394

[127] Shao Y, Cherry S R, Siegel S and Silverman R W. 1996 A study of inter–crystal scatter in small scintillator arrays designed for high resolution PET imaging *IEEE Trans. Nucl. Sci.* **43** 1938-1944

[128] Singh M. 1983 An electronically collimated gamma camera for single photon emission computed tomography. Part I: Theoretical considerations and design criteria *Med Phys* **10** 421-427

[129] Oliver J F, Torres-Espallardo I, Fontain R, Ziegler S and Rafecas M. 2008 Comparison of coincidence identification techniques in high-resolution PET *IEEE NSS MIC Conf. Rec.*, 4732-4735

[130] Bendriem B and Townsend D W. 1998 *The Theory and Practice of 3D PET* (Kluwer Academic Publishers), 86

[131] E. J. Hoffman *et al.* 1989 PET system calibrations and corrections for quantitative and spatially accurate images *IEEE Trans. Nucl. Sci.* **36** 1108-1112

[132] D. A. Chesler *et al.* 1990 Calibration of detector sensitivity in positron cameras *IEEE Trans. Nucl. Sci.* **37** 768-772

[133] M. Defrise *et al.* 1991 A normalization technique for a 3D PET data *Phys. Med. Biol.* **36** 939-952

[134] Stazyk M W, Sossi V, Buckley K R, Ruth T J. 1994 Normalisation measurement in septa-less PET cameras *J. Nuc. Med.* **31** 41P

[135] Kinahan P E, Townsend D W, Bailey D L, Sashin D, Jadali F, Mintun M. 1995 Efficiency Normalization techniques for 3D PET Data *IEEE NSS MIC Conf. Rec.* 1021-1025

[136] Casey M E, Gadagker H, Newport D. 1995 A component based method for normalization in volume PET *Proc. 3rd Int. Meeting on Fully Three-Dimensional Image Reconstruction in Radiology and Nuclear Medicine* 67-71

[137] Ollinger J M. 1995 Detector Efficiency and Compton Scatter in Fully 3D PET *IEEE Trans. Nucl. Sci.* **42** 1168-1173

[138] Bailey D L, Townsend D W, Kinahan P, Grootoonk S, Jones T. 1996 An investigation of factors affecting detector and geometric correction in Normalization of 3-D PET data *IEEE Trans. Nucl. Sci.* **43** 3300-3307

[139] Badawi R D, Lodge M A, Marsden P K. 1998 Algorithms for calculating detector efficiency normalization coefficients for true coincidences in 3D PET *Phys. Med. Biol.* **43** 189-195

[140] Oakes T R, Sossi V, Ruth T J. 1998 Normalization for 3D PET with a low-scatter planar source and measured geometric factors *Phys. Med. Biol.* **43** 961-972

[141] Badawi R D *et al.* 1999 Developments in component-based normalization for 3D PET *Phys. Med. Biol.* **44** 571-594

[142] Bai B *et al.* 2002 Model-based normalization for iterative 3D PET image reconstruction *Phys. Med. Biol.* **47** 2773-2784

[143] Vicente E *et al.* 2006 Normalization in 3D PET: Dependence on the Activity Distribution of the Source *IEEE NSS MIC Conf. Rec.* 2206-2209

[144] Torres-Espallardo I *et al.* 2007 Quantification Issues in Imaging Data of MADPET-II small animal PET scanner using a System Matrix based on Monte Carlo Techniques *IEEE NSS MIC Conf. Rec.* 4192-4197

¡Gracias!

¡Por fin he llegado a los agradecimientos! Aviso que serán un poco largos. Por un lado, aunque la investigación que se presenta en este trabajo se ha hecho en el grupo de MADPET-II bajo la supervisión de Sibylle Ziegler, los estudios de doctorado empezaron en el año 2000 en el grupo de Imagen Médica del José María Benlloch y acabarán en el departamento de Procesado de Imagen de la RWTH-Aachen de Til Aach. Por otro lado soy una persona que me encanta dar las gracias, junto con los buenos días y las felicitaciones en general, y no quiero que se me olvide nadie.

Primero quiero dar las gracias a las dos directoras de tesis Sibylle Ziegler y Magdalena Rafecas y decir que me siento orgullosa de haber tenido dos mujeres como directoras de tesis. A Sibylle le agradezco el que me diera la oportunidad de poder hacer el doctorado en su grupo. Durante el tiempo que estuve en Múnich fue difícil verla de mal humor. No importaba la cantidad de trabajo que llevara encima, ni la de gente que hubiera detrás de su puerta esperando algo de ella, siempre se comportó educadamente y con buenos modales. También he admirado su visión general del campo, que en muchas ocasiones me dejaba boquiabierta (aunque lo intentaba disimular). Cuando dejé el grupo, me quedé con la sensación que aún me quedaba mucho que aprender de ella. Pero gracias a la buena relación que mantenemos, todavía sigo descubriendo nuevas cosas a través de ella.

Antes de acabar físicas, ya habia oido hablar de Magdalena Rafecas a traves de Pepe Bernabeu. Me alegré mucho al saber que consiguió un contrato Ramón y Cajal en la Universidad de Valencia. Y gracias a que volvió a Valencia acabamos siendo directora y estudiante. He aprendido mucho de ella y siempre me ha sorprendido la capacidad que tiene para entender lo que yo le explico, escribirlo de manera coherente y que lo puedan entender otros.

Además de las directoras de tesis, también quiero agradecer a José María Benlloch, que fue el responsable de que empezara a preocuparme por los algoritmos de reconstrucción para un PET dedicado a animales pequeños. En aquellos tiempos conocí a Empar, Noriel, Jordi, Marcos, Nerina, Christoph y Kike. Todos ellos estudiantes de doctorado como yo, que me ayudaron en mis primeros momentos, con los primeros programillas y, posteriormente, con las simulaciones en el Grid. Y relacionado con las simulaciones que realicé en el Grid, quiero dar las gracias al grupo del Grid en el IFIC, especialmente a Javier y Alejandro.

Una persona fundamental en esta tesis y compañera de penurias y alegrías ha

sido mi querida amiga y anterior colega Virginia Spanoudaki. Durante una parte importante del doctorado estuvimos las dos mano a mano con Sibylle intentando entender nuestra querida MADPET-II. La pasión con la que trabaja y defiende su trabajo, su eficiencia, su profesionalidad, sus ganas por entender hasta el último detalle me han servido de referencia durante el tiempo que hemos compartido. Bien cerquita estaban Axel Martínez, Ralph Bundshuh, Axel Weber, Alexander Mann, M. José Martínez, Marc Huisman, Marisa y Thomas Wendler, con ellos he compartido divertidas comidas en la cafetería, interesantes seminarios, conferencias y fiestas de navidad. Me siento afortunada de haber podido disfrutar de una atmósfera tan acogedora en mi estancia en Múnich. Y, aunque fueron sólo unos pocos meses, me encantó trabajar con Jasmine, Gaspar, Arne, Sebastian, Astrid, Melanie y Josef.

Continúo con la parte relacionada con los ordenadores, tan fundamental para el campo de la imagen médica. El grupo de informáticos del departamento de Medicina Nuclear del Klinikum rechts der Isar me apoyó mucho desde el principio con las primeras instalaciones de GATE; por eso quiero dar las gracias a Mathias, Marcel y Ruppert. A través de la colaboración con el departamento de informática de la TU-Munich fue posible optimizar el formato de la matriz del sistema y tener imágenes reconstruídas en un tiempo razonable. Muchísimas gracias a Josef Weidendorfer, Tobias Klug y Carsten Trinitis.

Durante todos estos años he tenido la suerte de trabajar en hospitales, tanto cuando me dedicaba en exclusiva a la tesis, como cuando sólo podía hacerlo en mi tiempo libre. Colegas de hospitales en general y en particular, Pepe Pérez, Pepe Martí, Françoise, Juan Carlos, Agustín, Salvador y Vicente me han enseñado con su ejemplo a disfrutar de la física médica. Muy especialmente en esta última etapa quiero agradecer la frescura y alegría que ha traído mi nueva compañera del servicio de radioterapia del hospital universitario de Aquisgrán. Nuria, estoy convencida que vas a ser una física médica estupenda y mucho ánimo con la tesis que estás empezando.

Agradezco a los evaluadores de la tesis que con sus comentarios y correcciones han mejorado la calidad del manuscrito y a los miembros del tribunal el que hayan querido estar presentes en la defensa de la tesis. También quiero agradecer a Josep Oliver por encargarse de los trámites burocráticos relacionados con esta tesis que no he podido hacer por estar fuera de Valencia. Y a Enrique Giner por ayudarme desde el departamento de Física Atómica de la Universidad de Valencia con todos los pasos administrativos.

Voy a ir acabando con el apoyo emocional que es tan necesario para llevar adelante estos proyectos sin volverse loca: los amigos y la familia. Para mis chicas Rosi, Berta, Eva y Nerea: ¡muchísimas gracias guapas por estar cerquita y escuchar mis historias!. Más agradecimientos para aquellos con los que nos juntábamos para comidas, cenas y cafés como excusa para charlar y pasar un buen rato en Múnich, como Inma, Daniel, Mari Carmen, Emiliano, Ricard, Miguel, Timur, Eugeny y Pratik.

Ahora las gracias van para mi familia política que me cuidó como una reina este verano (y siempre que estoy en Alicante) cuando estaba acabando las últimas

correcciones de la tesis. Sigo con mi prima Tere que siempre encuentra momentos para escribirme, ponerme al día y mandarme cariño. Y tanto mis padres como mis hermanos-hermanas que me trasmiten la confianza que yo no tengo y me envían ánimos constantemente, sin los que no podría haber acabado la tesis. En momentos de dificultad, mi madre siempre estuvo presente con "hay que acabar lo que se empieza".

Como todos los que me conocen saben que me dejo siempre lo mejor para el final, quiero agradecer a Pedro el que estemos juntos. Muy importante para este trabajo fue que te animaras a ir de post-doc a Múnich. Tú has contribuído en este trabajo tanto apoyándome en momentos difíciles como mejorando el estilo y el inglés del texto. Como ahora tendré más tiempo, este invierno te podré preparar más pastelitos.

Thanks!

Finally I am in the acknowledgments! Although the research presented in this work was done in the MADPET-II group of Sibylle Ziegler, it has a long story since it started in 2000 in the Medical Image group of Jose María Benlloch and they will be finished at the Image Processing department of Til Aach at the RWTH-Aachen University. I feel grateful to all the people that have contributed to this thesis in its long way and this part is dedicated to the non-spanish speakers.

First of all, I want to thank my two PhD supervisors Sibylle Ziegler and Magdalena Rafecas and to say that I am proud of having two women as PhD supervisors. I really appreciate that Sibylle gave me the chance of doing the PhD in her group. While I was in Munich, it was difficult to see her in a bad mood. It did not matter how much work she had to do, how many people at her office's door waiting something from her, she was always very polite and helpful. I have also admired her wide general view of the field, several times I was blown away (although I tried not to show it). When I left the group, I had the feeling that there was still a lot to learn from her. But, as we keep a good relationship, I am still getting new things from her.

Before finishing my Physics studies, I have already heard about Magdalena Rafecas through Pepe Bernabeu. I was very happy when I knew that she came back to Valencia with a Ramón y Cajal contract. And then we became PhD supervisor and student. I have learnt a lot from her and I was always amazed of her ability to understand what I was saying and to write it in a coherent way.

As well as the PhD supervisors, I want to thank also José María Benlloch because he was the first to motivate me to think about the image reconstruction algorithms for a small animal PET. In the beginning of the PhD, I met Empar, Noriel, Jordi, Marcos, Nerina, Christoph, and Kike. All of them PhD students like me that helped me a lot in the first moments, with the first programs, and with the Grid simulations. Concerning the Grid simulations I would also like to thank the support from the Grid Group at the IFIC, specially Javier and Alejandro.

A very important person for this thesis and with whom I have shared suffering and happiness is my dear friend and former colleague Virginia Spanoudaki. During a considerable part of our PhD we were one-to-one with Sibylle trying to understand our dear MADPET-II. She was a reference for me in her way of working, always very professional and efficient. She likes to understand everything and this led us to create new theories, the pity was that we did not have time to write

them. I also admire her presentations, the passion she put when defending the group's work. Axel Martínez, Ralph Bundschuh, Axel Weber, Alexander Mann, M. José Martínez, Marc Huisman, Marisa, and Thomas Wendler were also very close and I have enjoyed with them lunch time, interesting seminars, conferences, and Christmas parties. I feel lucky to have had such a friendly atmosphere during my stay in Munich. Lastly, although it was only for a few months, it was a pleasure to work with the newcomers: Jasmine, Gaspar, Arne, Sebastian, Astrid, Melanie, and Josef.

I continue with the "computer assistance" which is fundamental for the medical imaging field. Matthias, Marcel and Ruppert of the IT section at the Klinikum rechts der Isar were very supportive since the very first GATE installation. Through a collaboration with computer scientists of the TU-Munich it was possible to optimize the format of the system matrix and to have reconstructed images in a feasible time. So, thank you very much Josef Weidendorfer, Tobias Klug, and Carsten Trinitis for aid with the high performance programming.

I would also like to thank the thesis referees because their comments and corrections have improved the quality of the manuscript, and the members of the committee that kindly agreed to come for the thesis defence.

There are more people to thank that have helped me in the administrative procedure (Josep Oliver and Enrique Giner) and moral support (from colleagues, family and friends) for this thesis. They understand Spanish and the last paragraphs of the acknowledgments written in Spanish are dedicated to them.